

AD-A113 959

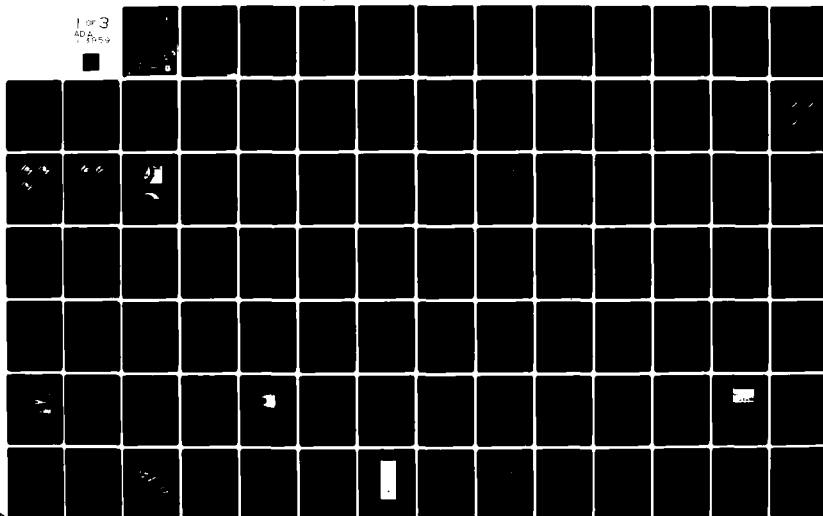
AIR FORCE GEOPHYSICS LAB HANSCOM AFB MA
PROCEEDINGS OF THE AIR FORCE GEOPHYSICS LABORATORY WORKSHOP ON --ETC(U)
OCT 81 R C SAGALYN, W N SPJELDOVIK, W J BURKE
AFGL-TR-81-0311

F/G 4/1

NL

UNCLASSIFIED

1 of 3
AD-A113 959



AD A113959

AFGL-TR-81-0311
ENVIRONMENTAL RESEARCH PAPERS, NO. 757



**Proceedings of the Air Force Geophysics
Laboratory Workshop on the Earth's
Radiation Belts: January 26-27, 1981**

Editors

**R. C. SAGALYN
W. N. SPJELDIK
W. J. BURKE**

21 October 1981

Approved for public release; distribution unlimited.

283 P
DTIC
ELECTED
APR 27 1982
K H

**SPACE PHYSICS DIVISION PROJECT 7601
AIR FORCE GEOPHYSICS LABORATORY
HANSCOM AFB, MASSACHUSETTS 01731**

AIR FORCE SYSTEMS COMMAND, USAF



82 04 27 128

DTIC FILE COPY

This report has been reviewed by the ESD Public Affairs Office (PA)
and is releasable to the National Technical Information Service (NTIS).

This technical report has been reviewed and
is approved for publication.

Alva T. Stair, Jr.
DR. ALVA T. STAIR, Jr.
Chief Scientist

Qualified requestors may obtain additional copies from the
Defense Technical Information Center. All others should apply
to the National Technical Information Service.

Unclassified

SECURITY CLASSIFICATION OF THIS PAGE (When Data Entered)

REPORT DOCUMENTATION PAGE		READ INSTRUCTIONS BEFORE COMPLETING FORM
1. REPORT NUMBER AFGL-TR-81-0311	2. GOVT ACCESSION NO. AD-A130554	3. RECIPIENT'S CATALOG NUMBER
4. TITLE (and Subtitle) PROCEEDINGS OF THE AIR FORCE GEOPHYSICS LABORATORY WORKSHOP ON THE EARTH'S RADIATION BELTS: JANUARY 26-27, 1981		5. TYPE OF REPORT & PERIOD COVERED Scientific. Interim.
		6. PERFORMING ORG. REPORT NUMBER ERP No. 757
7. AUTHOR(s) R. C. Sagalyn W. N. Spjeldvik* W. J. Burke		8. CONTRACT OR GRANT NUMBER(s)
9. PERFORMING ORGANIZATION NAME AND ADDRESS Air Force Geophysics Laboratory (PHG) Hanscom AFB Massachusetts 01731		10. PROGRAM ELEMENT, PROJECT, TASK AREA & WORK UNIT NUMBERS 62101F 76011203
11. CONTROLLING OFFICE NAME AND ADDRESS Air Force Geophysics Laboratory (PHG) Hanscom AFB Massachusetts 01731		12. REPORT DATE 21 October 1981
14. MONITORING AGENCY NAME & ADDRESS (if different from Controlling Office)		13. NUMBER OF PAGES 287
		15. SECURITY CLASS. (of this report) Unclassified
		15a. DECLASSIFICATION DOWNGRADING SCHEDULE
16. DISTRIBUTION STATEMENT (of this Report) Approved for public release: distribution unlimited.		
17. DISTRIBUTION STATEMENT* (of the abstract entered in Block 20, if different from Report)		
18. SUPPLEMENTARY NOTES *Nordmann Research Ltd Boulder, Colorado 80303 Work done in the Workshop by Emmanuel College was supported by Air Force Contract F19628-79-C-0102		
19. KEY WORDS (Continue on reverse side if necessary and identify by block number) Radiation belts Energetic particles Penetrating radiation wave-plasma interactions Magnetospheric modelling Microelectronic shielding Low energy plasma in magnetosphere Particle instrumentation		
20. ABSTRACT (Continue on reverse side if necessary and identify by block number) A two-day workshop on the earth's radiation belts was held on 26-27 January 1981 at the Air Force Geophysics Laboratory. The workshop reviewed the present state of knowledge of the radiation belts and the effects of energetic particles on microelectronic systems. From this perspective it is possible to define the instrumentation requirements of future missions into the radiation belts. Proceedings of the workshop presented here include: (1) reports on a tutorial session concerning the present level of understanding		

DD FORM 1 JAN 73 1473

Unclassified

SECURITY CLASSIFICATION OF THIS PAGE (When Data Entered)

Unclassified

SECURITY CLASSIFICATION OF THIS PAGE(When Data Entered)

20. Abstract (Continued)

of radiation belt measurements, dynamics, wave-particle interactions, and their effects on microelectronic elements, (2) specifications of the state-of-the-art instrumentation required to measure energetic particles, cold plasmas, magnetic fields, and waves, (3) overviews of existing statistical, numerical, and analytical models of the radiation belts, and (4) summaries of the sessions presented at the end of the workshop by the various session chairmen.

Accession For	<input checked="checked" type="checkbox"/>	<input type="checkbox"/>	<input type="checkbox"/>
NTIS GRA&I			
DTIC TAB			
Unannounced			
Justification			
By			
Distribution/			
Availability Codes			
Avail and/or			
Dist Special			
A			



Unclassified

SECURITY CLASSIFICATION OF THIS PAGE(When Data Entered)

Preface

The Earth's Radiation Belt Workshop, sponsored by the Air Force Geophysics Laboratory and Emmanuel College, was held on 26 and 27 January 1981 at AFGL. Many of the world's foremost space physics experimenters, theoreticians, data analysts, and modelers assembled to discuss the scientific and technological problems which influence the survivability of space systems in the radiation belts. The workshop consisted of four sessions: (1) Tutorial lectures on the general characteristics of the radiation belts and their effects on space systems, (2) State-of-the-art energetic particle measurements, (3) Subsidiary diagnostic measurements, and (4) Radiation belt modelling.

Topics covered in four tutorial lectures are the observational advances made over the past decade [D. J. Williams], the present theoretical understanding of radiation belt dynamics [M. Schulz], the relationships between plasma waves and particle populations in the belts [M. Ashour-Abdalla], and the effects of energetic particles on microelectronic systems [J. B. Blake]. Each of the topical sessions consisted of four or five invited presentations and several brief contributions. Generous amounts of time were allotted for discussion from the floor after each talk. The last half of the final session was dedicated to the presentation of summaries by the various session chairmen and to comments from the speakers.

In devising these proceedings it was decided to devote individual chapters to the tutorial lectures, to the topical sessions, and to the summaries of the chairmen. The only exception to this rule is Chapter 4 which combines the tutorial and contributed talks on the effects of energetic radiation on microelectronic systems. At the suggestion of several speakers the chapters are attributed to the session or

tutorial reporters. These chapters, which are based on tape recorded transcripts as well as the reporter's notes and leg-work, integrate talks with clarifying remarks and questions from the floor. To assist readers in pursuing topics of interest to greater depths, extensive references to the technical literature are provided. The Summary chapter is of two-fold importance. Obviously, the chapter gives a unifying overview of the meeting as a whole. More importantly, it provides the "least-filtered", immediate impressions of the workshop's thrusts and significance as seen through the eyes of session chairmen. Perhaps it is here that some of the speaker's recommendations and points of emphases best survive the smoothing effects of translation from spoken to written English.

Air Force interest in the radiation belts derives from operational needs to establish systems' reliability and lifetimes. Reliability is affected by soft errors induced by cosmic rays and by energetic, trapped particles. System lifetimes are limited by the cumulative deposition of energy by penetrating particles. The radiation belt data base presently used for reliability and lifetime engineering models was established more than a decade ago. The accuracy of these models for predicting radiation environments over the coming decade is inadequate. An updated data base is essential for accurate estimation of the reliability and operational longevity of future space systems. In this context, the Radiation Belt Workshop can be viewed as a first step in the direction of defining and implementing future Air Force systems needs.

It is easily recognized that due to the organizing activities of the Workshop's co-chairmen Rita C. Sagalyn and Paul L. Rothwell many of the world's foremost space scientists came together at AFGL to address questions related to past and future explorations of the earth's radiation belts. However, no meeting with over a hundred scientists in attendance can rise above anarchy without attention to myriad details prior to, during and after the event. These details were attended to under the coordination of Dr. Irving Michael of AFGL and Prof. M. Patricia Hagen of Emmanuel College. Preparatory details ranged from handling invitations and correspondence to arranging for local accommodations. To a large degree these were handled by Mary Outwater and Karen Leccese at AFGL and by Joan Drane at Emmanuel. At the meeting itself, programs and transportation were the responsibility of Jack Campbell of Emmanuel; registration and providing local information was done by Eileen MacKenzie of Emmanuel; David Knecht and Frank J. Pavlica of AFGL and Richard Laperriere of Northeastern University tape recorded the many talks; Airman Ivan Thomas kept the required audio and video equipment in working order. After the Workshop concluded it was still necessary to prepare these proceedings. The work of transcribing many hours of tape recordings was accomplished under Joan Drane's direction. As editors of the

proceedings, we give special thanks to Mary Outwater for her unfailing good humor and patience with the many changes and corrections introduced by us as the text evolved towards its final state.

Work done in the Workshop by Emmanuel College was supported by Air Force Contract F19628-79-C-0102.

The Editors

Contents

1. AN OVERVIEW OF RADIATION BELT ^D YNAMICS, William J. Burke	9
2. A THEORIST'S VIEW OF THE EARTH'S RADIATION BELTS, Michael Heinemann	47
3. THE ROLE OF WAVES AND COLD PLASMA IN THE DYNAMICS OF THE EARTH'S RADIATION BELTS, Delia E. Donatelli	69
4. RADIATION EFFECTS ON ELECTRONIC SYSTEMS Peter J. McNulty	99
5. STATE OF THE ART OF ENERGETIC PARTICLE MEASUREMENTS IN THE EARTH'S MAGNETOSPHERE Walther N. Spjeldvik	125
6. MAGNETIC FIELDS, LOW ENERGY PLASMA, AND WAVE MEASUREMENTS IN THE RADIATION BELTS William J. Burke, and David T. Young	209
7. MODELLING OF MAGNETICALLY TRAPPED RADIATION IN THE INNER MAGNETOSPHERE OF THE EARTH Walther N. Spjeldvik	245
8. SUMMARY AND COMPARISON OF RADIATION BELT MODELS, Stanley M. Kaye	271
9. A SUMMARY REVIEW OF THE RADIATION BELT WORKSHOP	279

Contents

1. Introduction	9
2. Ion Composition	12
3. Time Variations of Ions	13
4. Transport in the Radiation Belts	28
5. Electrons	33
6. Time Variations of Electrons	39
7. Concluding Remarks	43
References	44

PROCEEDINGS OF THE AIR FORCE GEOPHYSICS LABORATORY WORKSHOP ON THE EARTH'S RADIATION BELTS: JANUARY 26-27, 1981

1. An Overview of Radiation Belt Dynamics

by

William J. Burke
Air Force Geophysics Laboratory
Hanscom AFB, Massachusetts 01731

based on a tutorial lecture by

Donald J. Williams
NOAA Space Environment Laboratory
Boulder, Colorado 80303

1. INTRODUCTION

In this paper the current knowledge about the outer radiation zone is reviewed. A precise definition of the limits of this part of the magnetosphere does not exist, but one may visualize the region $3.5 \leq L \leq 8$. Emphasized in this overview is the radiation belt macrostructure and our evolving knowledge of it since 1970 as outlined in Table 1.

In terms of sources for the outer zone, it was generally assumed in the 1970 period that the solar wind was the primary source of particles. The question of whether or not there was direct access was debated. Primarily it was thought that electrons and protons convected earthward through the night-side plasma sheet and were injected into the trapping regions by some unknown process. By 1980 it was

(Received for publication 19 October 1981)

Table 1. Rough Evolution of Outer Zone Information, 1970-1980

	Level of Knowledge in 1970	Level of Knowledge in 1980
Sources	<ul style="list-style-type: none"> • Solar Wind via Plasma Sheet 	<ul style="list-style-type: none"> • Solar Wind • Ionosphere • Outer Zone
Transport	<ul style="list-style-type: none"> • $\vec{E} \times \vec{B}$ • Cross - L Diffusion 	<ul style="list-style-type: none"> • $\vec{E} \times \vec{B}$, E_{\parallel} • Cross-L Diffusion • Pitch Angle Diffusion
Time Variations	<ul style="list-style-type: none"> • Adiabatic • Non-Adiabatic 	<ul style="list-style-type: none"> • Adiabatic • Non-Adiabatic
Ion Composition	<ul style="list-style-type: none"> • Low Altitude > 1 MeV 	<ul style="list-style-type: none"> • Low and High Altitude ≥ 600 keV and ≤ 20 keV
Electron Pitch Angle Diffusion	<ul style="list-style-type: none"> • Weak Diffusion $j_0/j_{90} \sim 2 \times 10^{-2}$ 	<ul style="list-style-type: none"> • Weak Diffusion $j_0/j_{90} \leq 10^{-3}$

realized that other sources existed for the outer zone. Based on the very many fine low-energy composition measurements during the last decade it is obvious that the ionosphere is one source. Recently, it was realized that the outer zone acts as a source for itself through in-situ acceleration processes. During the same convection process that brings particles from the tail, the lower energy, residually trapped ions in the outer zone move in further. Conservation of the first adiabatic invariant μ during earthward motion leads to particle acceleration.

Let us next consider transport. In the early 1970's, $\vec{E} \times \vec{B}$ drift and cross-L diffusion were considered to be the most important transport mechanisms. The cross-L diffusion mechanism was quite successful in explaining the quiet time and the recovery phase non-equilibrium situation for ions above an energy of roughly 100 keV. There had not been measurements, at that time, for ions below 100 keV and above roughly 15-20 keV. Cross-L diffusion has had pitch angle diffusion effects added in order to account for particle loss terms. By 1980, parallel electric fields have provided an obvious transport mechanism that researchers have now worked on for the past several years.

In the early 1970's, adiabatic time variations were identified and were fairly well understood. They had been documented for the high energy ion populations. All other effects were simply labelled non-adiabatic. During the recovery phases of magnetic storms, Coulomb scattering, charge exchange, and wave-particle interactions were considered as primarily responsible for the observed particle losses. Why and how main phase increases occur was unexplained. There were also observed but unexplained non-adiabatic decreases of energetic ions. In 1980

we still recognize the importance of the adiabatic terms but to the known non-adiabatic processes we have to add plasma instabilities and diffusion losses. A quantitative explanation has been given for the main phase increase in the geomagnetic storm, but it is not yet definitive. Only one case has been studied in detail so far. The non-adiabatic flux decreases have now also been explained.

Table 1 shows that the late 1970's brought new information not previously available. In 1970 there were few low altitude ion composition observations, and those were generally > 1 MeV in total energy. These measurements were done by the APL and Aerospace groups. By 1980, the observations had been extended toward lower energies. There is now a large data set both at magnetospheric equatorial altitudes and at low altitudes in the energy ranges less than 20 keV and greater than 600 keV. In 1970, it was recognized that in the outer zone, there was a region of strong pitch angle diffusion where the ratio of the loss cone electron flux to the local 90° pitch angle flux was approximately 1. This strong diffusion region has been studied intensely. The work of Kennel and Petschek¹ considered full loss cone phenomena appropriate to strong diffusion conditions. A weak diffusion region was also observed on L shells inside the plasmopause with a ratio of loss cone to trapped fluxes of roughly a few percent (2×10^{-2}). By 1980, a measurement² was reported showing that perhaps a number of the earlier measurements were either not representative of an equilibrium situation or were bothered by scattering in the detector walls. During a quiet time period, the ratio turns out to be $< 10^{-3}$, which gives a different order of magnitude estimate for the diffusion coefficient. This new limiting number has not yet been worked into pitch angle diffusion calculations for quiet time outer zone conditions. The observational advances made in the last decade include the full differential energy spectrum. It was only in the 1970's that the entire differential energy spectrum has been measured, from a few tens of eV up to energies of several MeV. Full pitch angle distributions have also been measured. We have extended composition measurements and have achieved time resolutions that give several data samples during periods of geomagnetic storms. Satellites with apogees in the vicinity of $5-8 R_E$ have short enough orbital periods. Satellites like ISEE with apogees out to $20 > R_E$ do not, simply because their orbital period is 2 1/2 days. It is very difficult to do any type of systematic study in the radiation zones, with an orbit like that of ISEE. One has to take whatever orbital samples happen to be available at random time periods within storms. It is much better to have the satellite orbits that are tailored to the phenomena being studied by a particular payload.

1. Kennel, C. F., and Petschek, H. E. (1966) Limit on stably trapped particle fluxes, J. Geophys. Res. 71:1.
2. Leinback, H., and Williams, D. J. (1977) Evidence for very weak pitch angle diffusion of outer zone electrons, J. Geophys. Res. 82:5091.

2. ION COMPOSITION

Table 2 summarizes what is currently known about the radiation zone's composition.^{3,4} In the early 1970's most space scientists thought that the positive charge carriers in the ring current were all protons. Today it is not at all clear whether protons are the dominant ring current species from an energy density point of view. The table shows the main elements that have been observed in the radiation belts: hydrogen, helium and oxygen ions at energies less than 20 keV. That identification has been done by direct observation. From ~50 to 100 keV there are essentially no composition measurements. Even inference techniques have not been helpful in that energy range. In the following sequence of figures it is shown that this is the energy range which contains the centrum of the energy density distribution. From 100 keV up to ~ 1 MeV, inference techniques indicate that hydrogen is the primary contributor. Above a total energy of roughly 600 keV, all the species mentioned above plus carbon have been observed experimentally. There is still much work to be done in determining the precise composition of ions in the radiation zones. The elemental ratios vary enormously and depend on time, energy, and spatial location.

Table 2. Ring Current Composition Summary

Energy (keV)	Technique	H	He	C	O	Comments	Source
≤17	Direct Observation	x	x		x	Low Altitude; synoptic surveys; trapped and precipitated; energy, latitude, and time dependence in relative abundances.	Ionosphere
≤30-50	Inference	x	x		x	Equatorial decay rates - charge exchange comparisons; recovery phase; time dependence in relative abundances.	?
50-100						No information; centrum of ring current energy distribution is in 50-100 keV range.	?
100-1000	Inference	x				Equatorial intensity profile - cross L diffusion comparisons; steady state and recovery phase.	?
≥600	Direct Observation	x	x	x	x	High altitude; energy, altitude, and time dependence in relative abundances.	Solar Wind
Depending on energy, altitude, and time of observation, it is possible for any of the ions indicated to dominate the ion distribution.							

3. Williams, D. J. (1980) Ring current composition and sources, in Dynamics of the Magnetosphere, ed. S.I. Akasofu, D. Reidel, Boston, Massachusetts, p 407.
4. Williams, D. J. (1981) Ring current composition and sources, an update, Planet Sp. Sci. (in press).

Figure 1 gives the percentage of the energy density accumulated in the ring current as a function of energy. It shows that during quiet times the centrum of the energy density, i.e., the energy required to accumulate 50 percent of the energy density of the ring current itself, is over 200 keV. During the recovery phase of a magnetic storm, like that of Dec. 17, 1977 which had a minimum D_{st} of -190 gammas, the central energy is reduced to approximately 85 keV. Notice where the composition is known, below 20 keV and above 600 keV. The composition of the whole central energy range of the ions in the trapped regions of the magnetosphere is unknown. For the lower energy ions an ionospheric source is inferred. Similarly, based on the characteristics of the higher energy ions that have been directly measured, the inferred source is the sun, perhaps through the solar wind. So it would seem that a solar wind source populates the top few percent of the energy density curves and an ionospheric source is responsible for the bottom 12 percent of the energy density curve. We do not know either the mix or the primary source for the actual bulk of the ring current. It is also interesting to illustrate this same feature in both the integral form and in a differential form (Figure 2). The data for the curves in Figures 1 and 2 were obtained from one satellite, Explorer 45. They demonstrate that we have a fundamental lack of knowledge of the composition of the central part of the ring current.

3. TIME VARIATIONS OF IONS

We next consider the time variations of ions detected by the Explorer 45 satellite during the December 1971 magnetic storm. Figures 3 and 4 give the phase space densities times twice the mass of a proton at $R = 2.5, 3.5$ and $4.5 R_E$ and at $R = 4.0, 4.5$ and $5.0 R_E$, respectively. The top panel curves are for constant energies (E) and the middle panels for constant first adiabatic invariant ($\mu = E_{\perp}/B$). The point to show here is that one has low energy increases at the time of the main phase storm. As has been recognized since the very early work by Davis and Williamson,⁵ there are high energy decreases at the time of the main phase storm. Previously they were considered to be nonadiabatic decreases. The plots of constant μ show the high energy portions of the phase space densities to be much more steady through the storm indicating that the decreases are not non-adiabatic. Rather they are just adiabatic readjustments of the charged particle population to the new magnetic field established by the low energy particle injection in that region of space.

5. Davis, L. R., and Williamson, J. M. (1963) Low-energy trapped protons, Space Sci. 3:365.

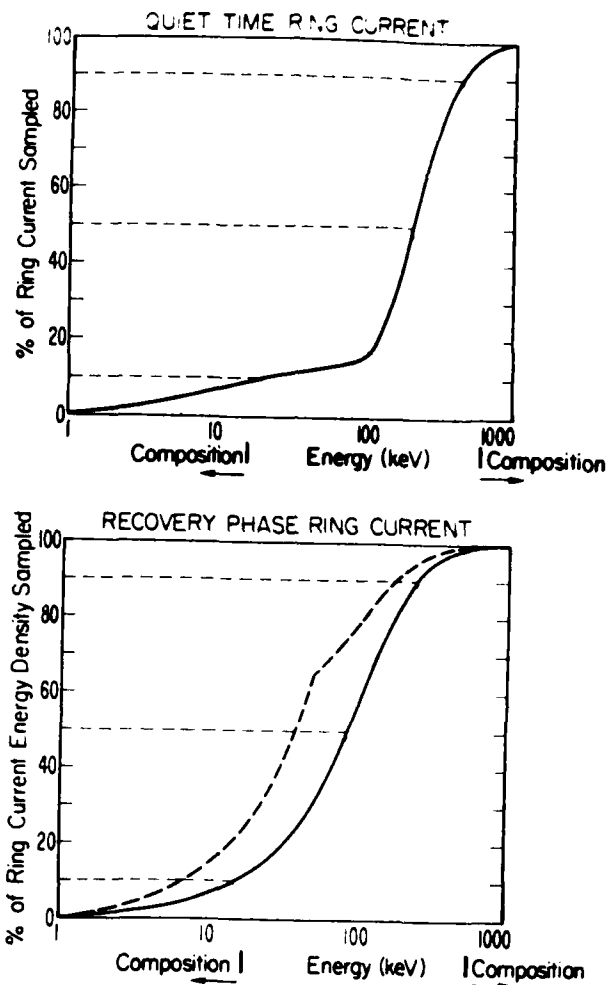


Figure 1. Percent of Ring Current Energy Density Sampled as a Function of Energy for Quiet Time (Top Panel) and Recovery Phase (Bottom Panel) Ring Current. The energy regions of known ion composition are indicated

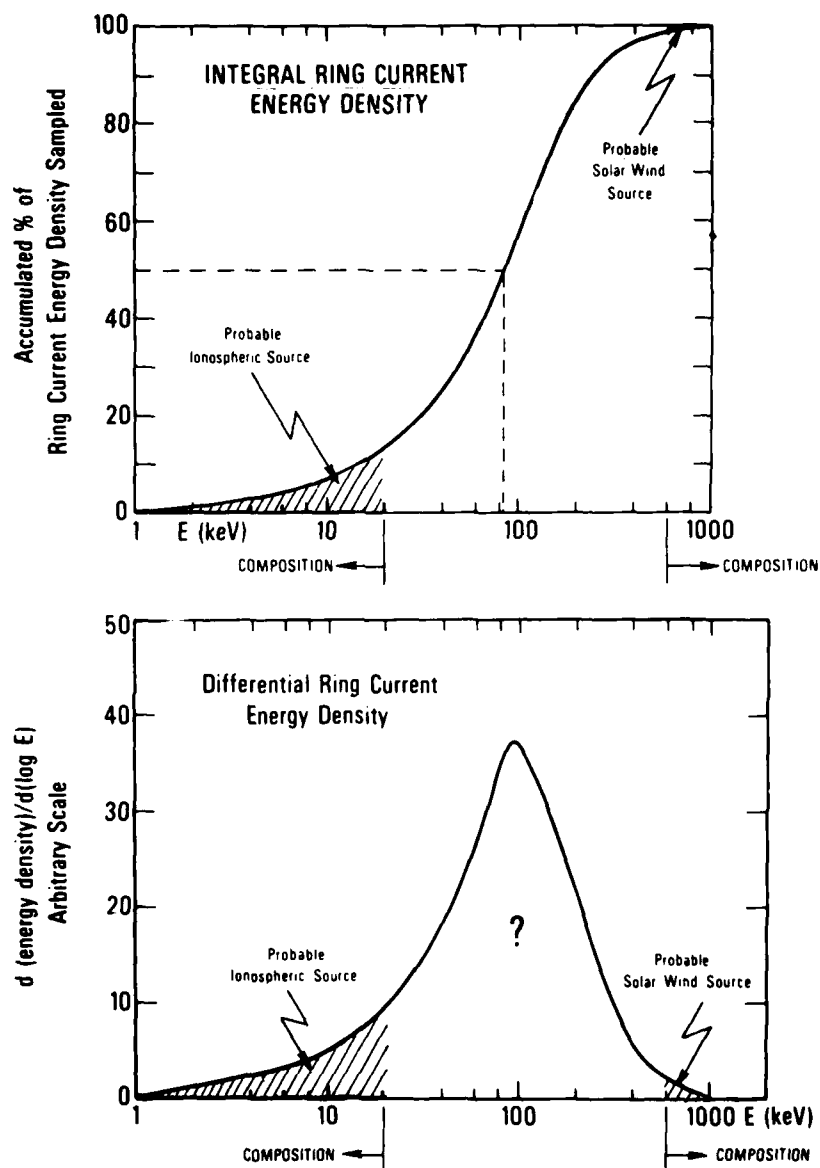


Figure 2. Integral (Top Panel) and Differential (Bottom Panel) Representations of Distribution of Ring Current Energy Density as a Function of Ion Energy

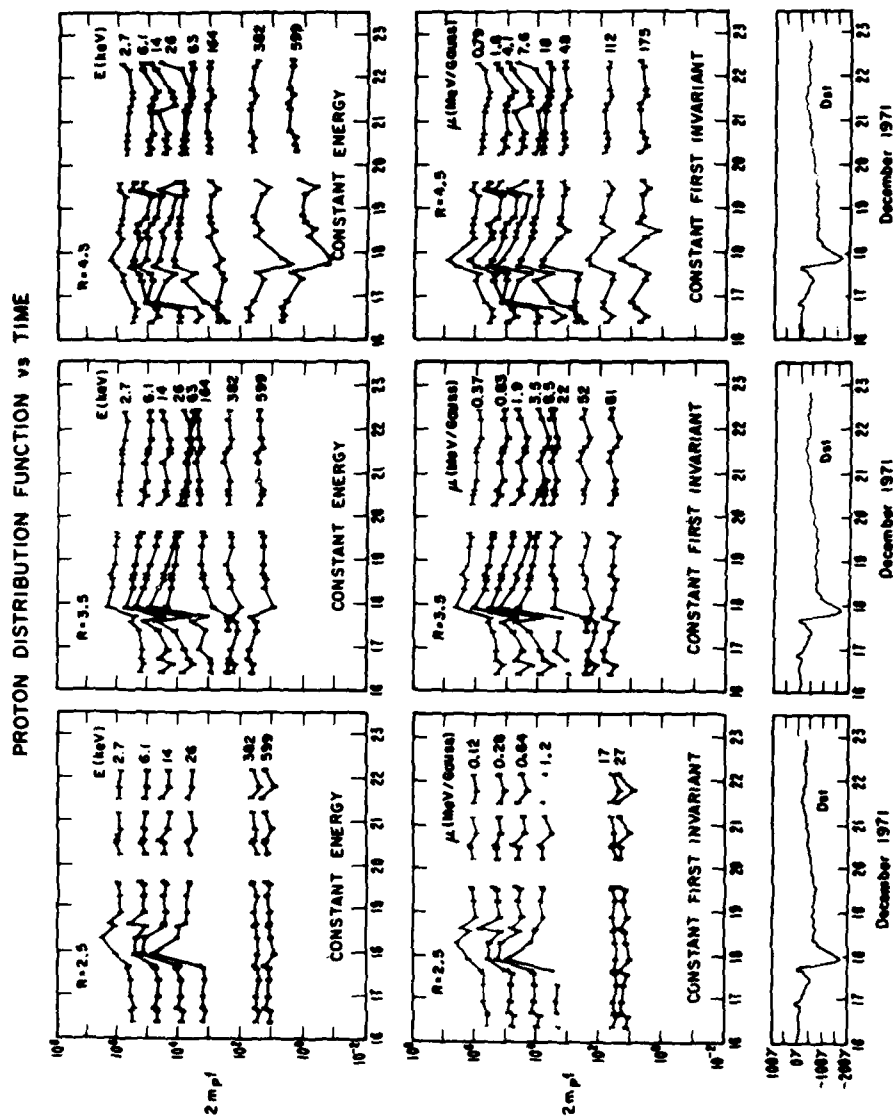


Figure 3. Evaluation of Ring Current Distribution Function Times Twice the Mass of a Proton at $L = 2.5, 3.5$ and 4.5 as a Function of Energy (Top Panel) and the First Adiabatic Invariant (Second Panel) Through Magnetic Storm of December 1971. D_{st} for this storm is provided in the bottom panel

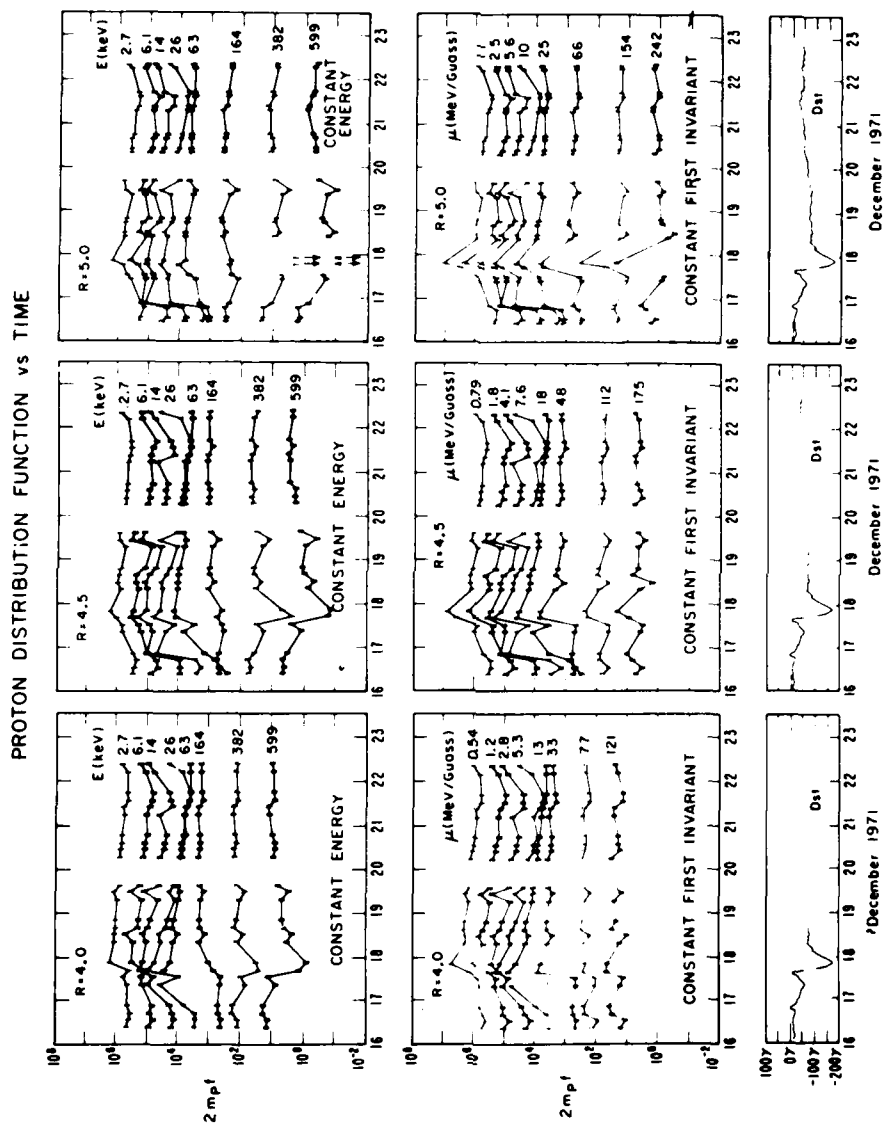


Figure 4. Evaluation of Ring Current Distribution Function Times Twice the Mass of a Proton at $L = 4.0, 4.5$ and 5.0 as a Function of Energy (Top Panel) and the First Adiabatic Invariant (Second Panel) Through Magnetic Storm of December 1971. D_{st} for this storm is provided in the bottom panel

In Figure 5 we examine the evolution of the distribution function plotted as a function of μ throughout the same storm.⁶ This is simply energy adjusted to the magnetic field being measured at the time. The data are given at half R_E intervals from 2.5 to 5.0 R_E . Measurements from the quiet time orbit 97 are provided for reference. Examining the data from the main phase and recovery phases of the storm we see that at high μ values the measurements are relatively constant. The primary change is the injection of low μ (low energy) ions during the main phase of the storm. The same point is illustrated in different ways in Figure 6 where the differential energy density from the pre-storm and main phase periods are plotted. At high energies there is a decrease in energy density whereas the low energy particles show a very large increase in energy density. This result from one satellite, Explorer 45, has been used extensively to justify a general model of energy density within the trapping region.

It is of interest to make a comparison with ISEE data⁷ to see if the same type of variation is discernable. Figure 7 gives the ion energy density in ergs/cm³, plotted as a function of L, for the range of the energetic particle experiment on ISEE, 24 keV to 2 MeV. The dashed line is the post-storm density; the solid line is the pre-storm density, and for the overall energy range, there is an increase in the energy density throughout the regions above $L \approx 3.2$. A large increase in the 24-210 keV channels and a decrease above 210 keV are again apparent; verifying the earlier observation results of Davis and Williamson⁵ that there is indeed a decrease at the high energies.

Figures 8 and 9 give data from a magnetic storm period in November 1978 observed with the ISEE-1 spacecraft. These illustrations show in detail, (every tenth of an R_E), the phase space density plotted versus the first adiabatic invariant. The dashes are distributions obtained prior to the storm and the crosses are distributions obtained in the recovery phase of the storm; the storm main phase could not be observed because of the sampling of the ISEE orbit. Scanning from $L = 8$ to 5.3, we can see that the pre-storm phase space density vs μ plots exhibit a minimum at ~ 1 Mev/G and a clear maximum at an energy of about 24 keV. The plots show, as did the Explorer 45 plots, that the only effect of the storm is to fill up the spectral minimum with low μ value particles which causes the magnetic field to decrease diamagnetically at that point in space. The result of the magnetic field decrease is to readjust the high energy particle population adiabatically. On an energy plot the phase space density decreases at high energies. On a constant μ plot, one can see that the high μ value regions stays constant; nothing happens

6. Lyons, L.R., and Williams, D.J. (1976) Storm associated variations of equatorially mirroring ring current protons, 1-800 keV, at constant first adiabatic invariant, *J. Geophys. Res.* 81:216.
7. Williams, D.J. (1981) Phase space variations of near equatorially mirroring ring current ions. *J. Geophys. Res.* 86:189.

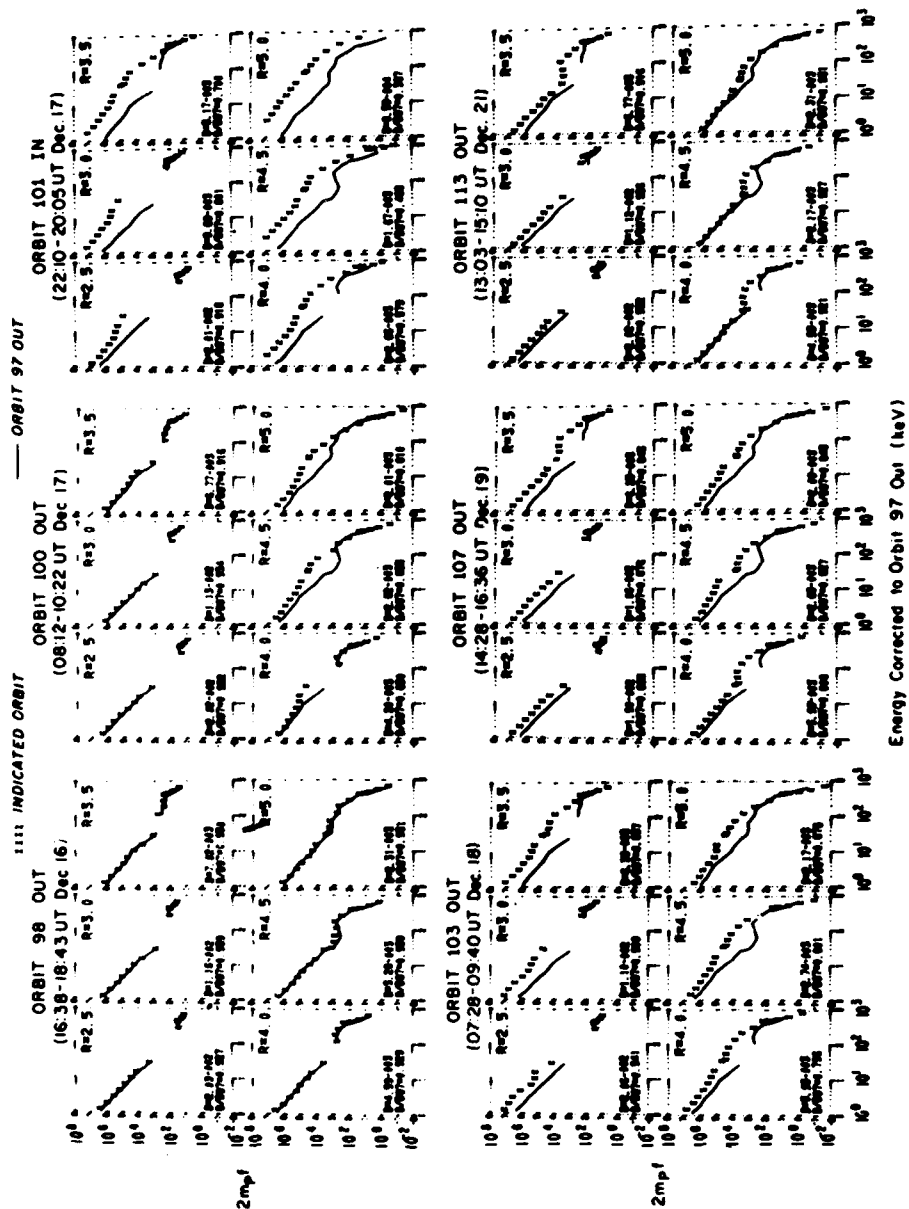


Figure 5. Distribution Functions Times Twice the Mass of Proton as a Function of First Invariant at $1/2 R_E$ Intervals Between 2.5 and $5.0 R_E$ Throughout the December 1971 Storm. The solid line provides quiet time reference distributions. The abscissa is labelled in energy normalized to energy divided by the quiet time magnetic field⁴

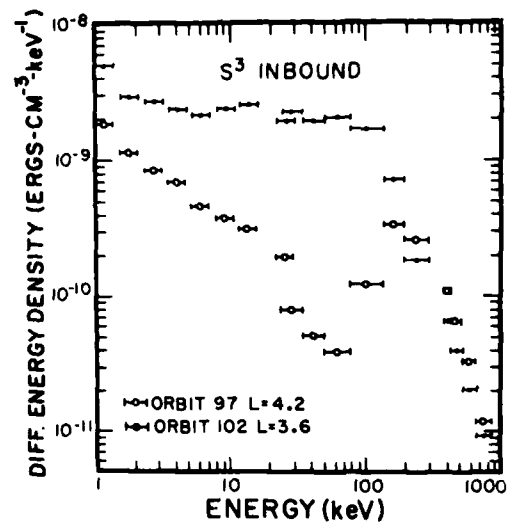


Figure 6. Differential Energy Densities Sampled by Explorer 45 During Prestorm and Main Phase of December 1971 Magnetic Storm

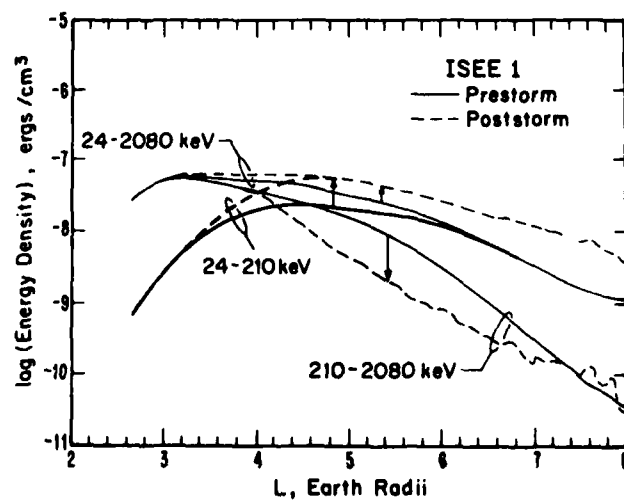


Figure 7. Energy Density of Ring Current as a Function of L Observed by ISEE Prior to and During the Recovery Phase of November 1977 Magnetic Storm

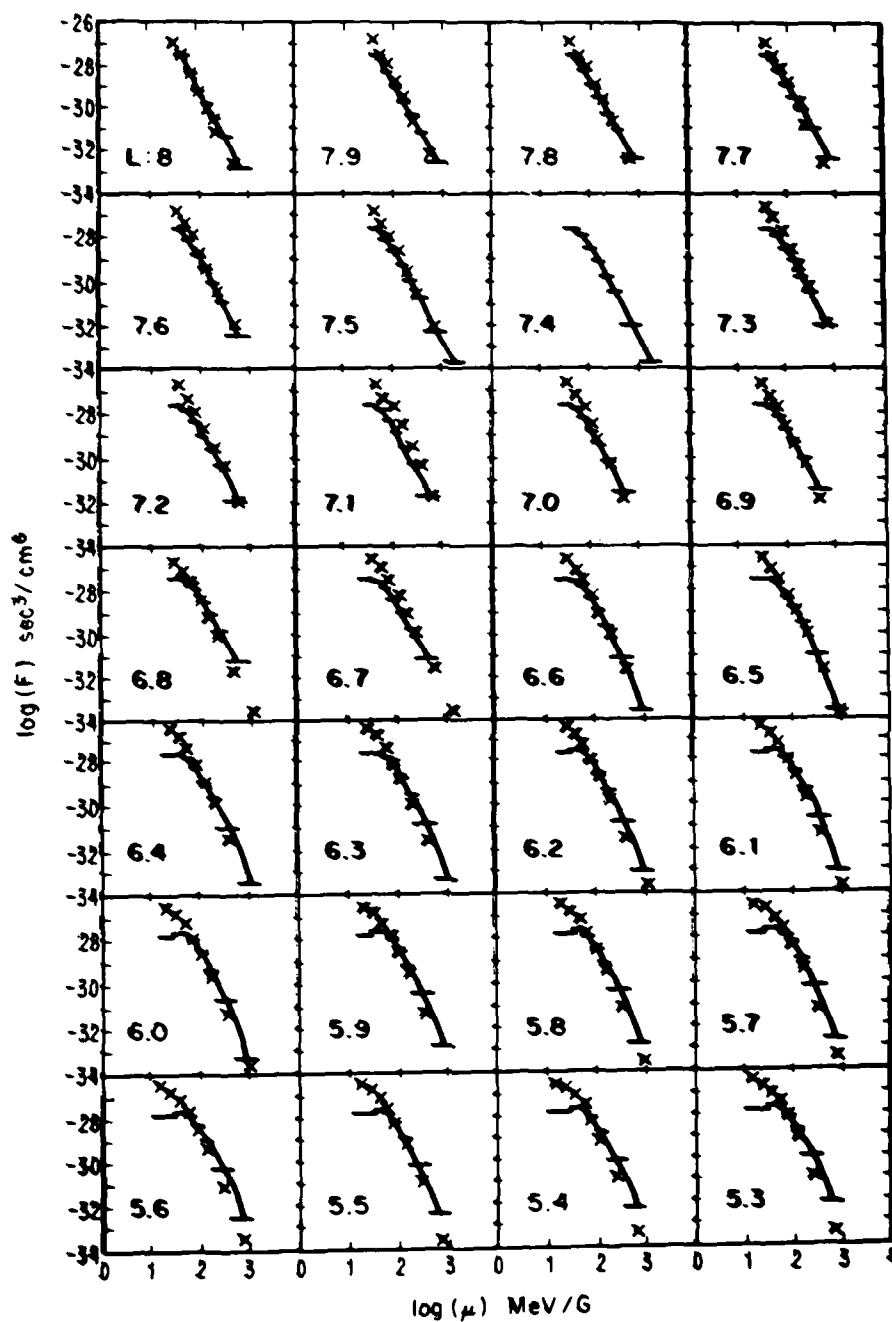


Figure 8. Distribution Functions versus First Invariant Measured by ISEE Prior to and During Recovery Phase of November 1977 Storm from $L = 8$ to 5.3

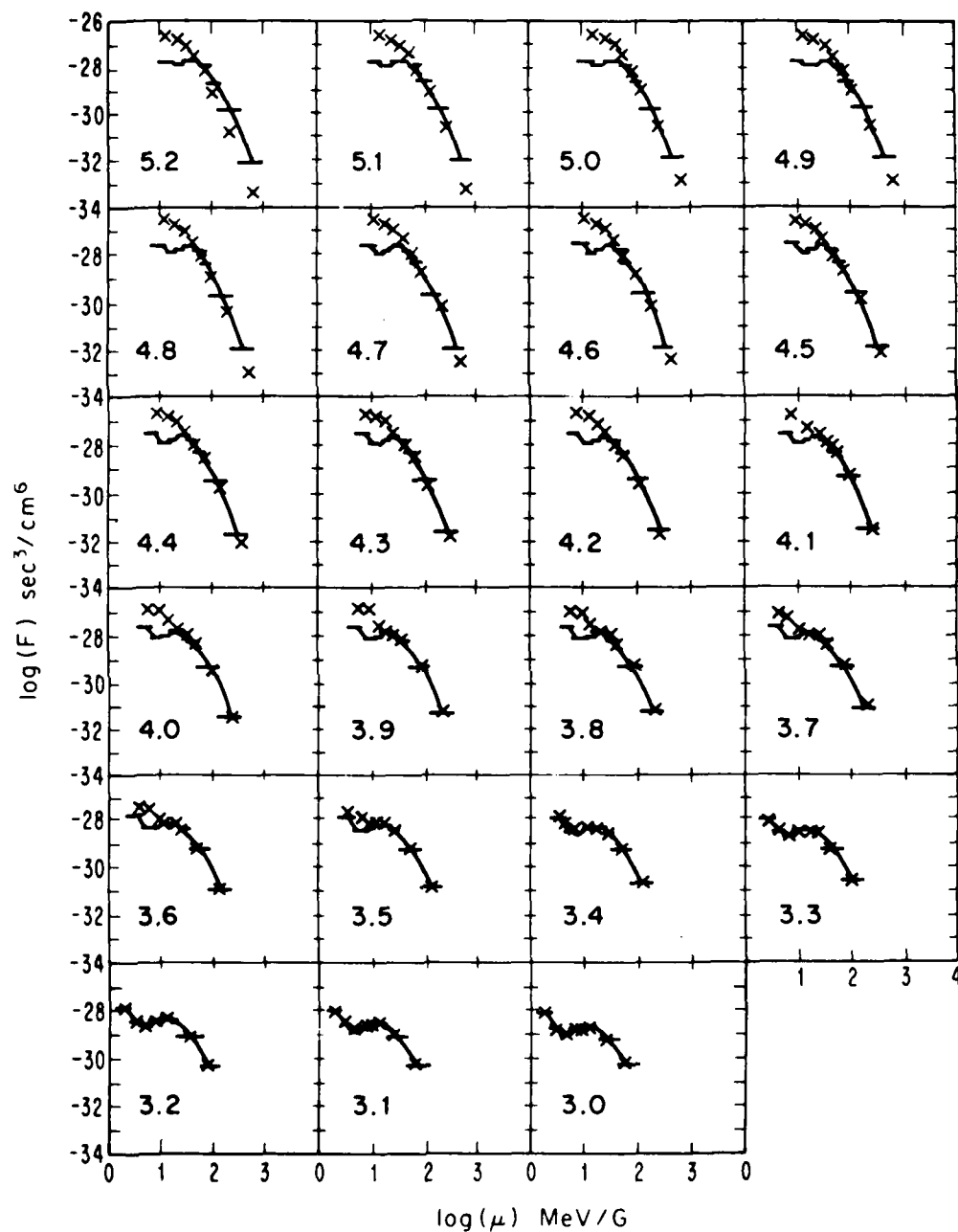


Figure 9. Distribution Functions Versus First Invariant Measured by ISEE Prior To and During Recovery Phase of November 1977 Storm From $L = 5.2$ to 3.0

in phase-space at high μ values during a main phase of a major ($D_{st} \sim -190$) magnetic storm.

Figure 10 shows a comparison of the November 1977 storm with the December 1971 storms. All units are the same as in Figure 3 where twice the mass of a proton times the phase-space density is plotted as a function of time. The plots have been adjusted so that the maximum, main-phase decreases line up on both storms. The connected points are from Explorer 45; the data points represented by open circles are from ISEE. There is remarkable agreement between these observations despite their wide separation in time and the fact that it was not possible to check the main phase magnitudes. Both before the storms and in the recovery phases the agreement is very good. It is worth noting that the ISEE satellite was 180° out of phase around the earth from the position of Explorer 45: The Explorer 45 results were in the dusk quadrant while those of ISEE were in the morning sector. The time separation was 6 years. On the basis of these observations it is reasonable to contend that this type of behavior is a characteristic feature of the trapped ions in the radiation belts. The effect of the storm is solely due to low μ particles being injected by an as yet unknown mechanism. The high energy decreases are nothing more than the adiabatic readjustment of the particles to the new magnetic field established by the low energy injection.

A comparison of differential energy density spectra obtained from Explorer 45 and ISEE-1 is given in Figure 11. The triangular points are from ISEE. We see that, over a 6-year period, during a similar type of magnetic storm, the energy densities, certainly in the energy range above 24 keV, during a quiet time pass, are remarkably similar. Figure 12 shows how the energy densities changed during the November 1977 storm observed by ISEE-1. Open circles represent pre-storm data and the dark points are the after-the-storm data. They look very much like the Explorer 45 curves. Currently, work is in progress incorporating low energy measurements to form the entire energy density curve.

Figure 13 allows an examination of the spatial and temporal evolution of ion phase space densities in the radiation belt as a function of μ . The spatial regime is from $L = 3$ to $8 R_E$. Prior to the storm in the $3 \leq L \leq 6 R_E$ range there are clear minima in the phase space densities. In the recovery phase, for $L > 4$ the minima are filled in. On 29 November (Figure 13c) the minima are beginning to develop again. For high values of μ the distribution functions are unchanged throughout the storm.

In plots of directional differential flux (j) versus energy (Figure 14) it is very difficult to tell what happens physically. It can be seen that there is a low energy injection but there are apparent decreases in the high energy fluxes. In order to understand the recordings of a detector responsive in a fixed energy range, calculations were made for the pass after the storm and the pass before the storm

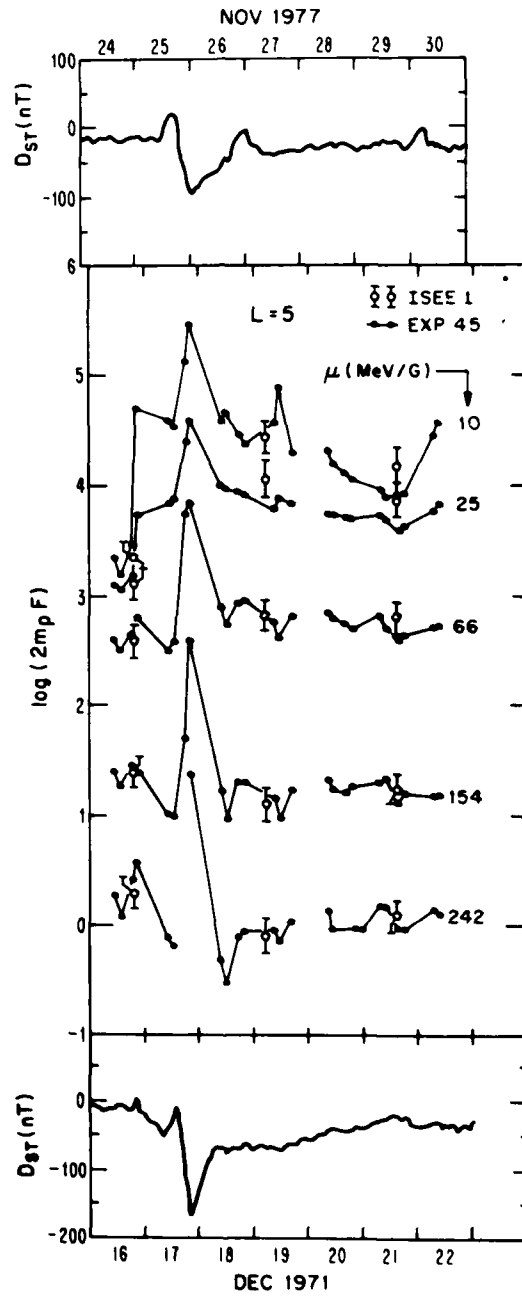


Figure 10. Direct Comparison of ISEE and Explorer 45 Measurements at $L = 5$ during Magnetic Storms of November 1977 and December 1971, respectively. Temporal scales are adjusted so that the maximum main phase excursions of D_{st} coincide

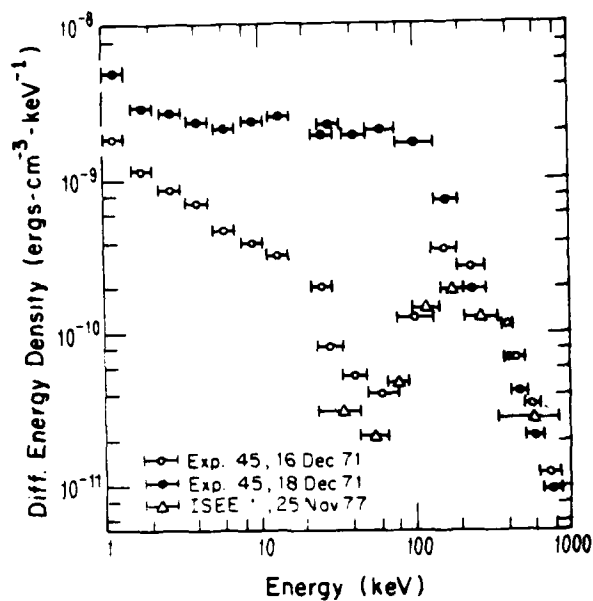


Figure 11. Comparison of ISEE and Explorer 45 Ring Current Differential Energy Densities in Same Format as Figure 6

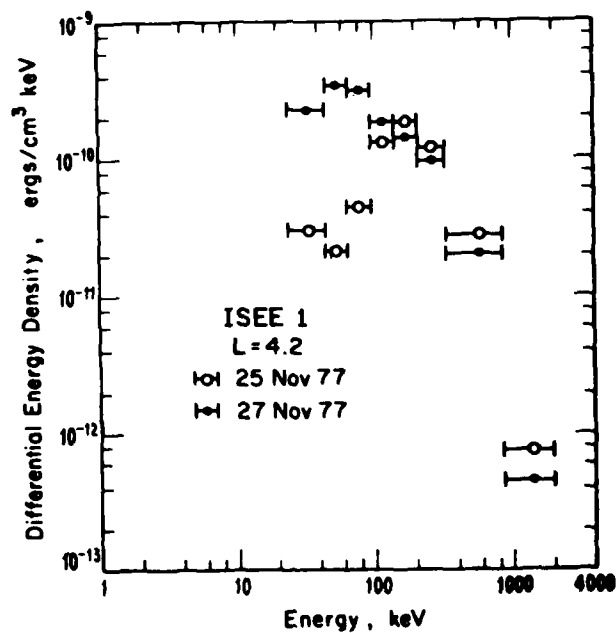


Figure 12. Differential Energy Densities Measured by ISEE Prior To and During Recovery Phase of November 1977 Storm in Same Format as Figure 6

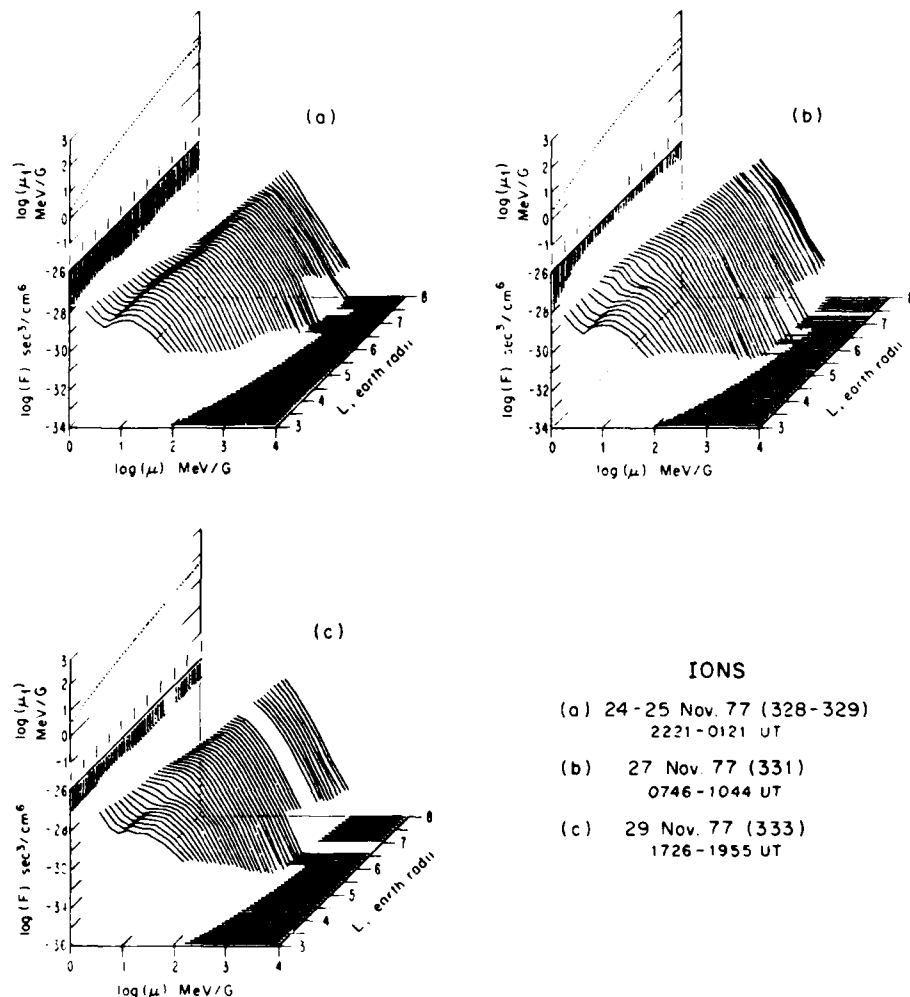


Figure 13. (a) A Perspective View of Phase Space Densities Through the Magnetosphere. $f(\text{s}^3/\text{cm}^6)$ is shown versus μ (MeV/G) for $L = 8$ to $3 R_E$. Variations of the f axis directly show density variations. The plot above the f axis shows the μ variation, μ_1 , of the lowest energy channel as a function of L . The existence of a high μ peak in the phase space densities is clearly seen. (b) Same as Figure 13a but for the poststorm pass of November 27, 1977. Comparison with Figure 6a shows that phase space densities are enhanced below the high μ peak, and remain constant above μ peak. The f axis directly shows the intensity increase at the lowest observed μ values. (c) Same as Figure 13a but for the poststorm pass of November 29, 1977. Comparison with Figures 13a and 13b shows a relaxation toward prestorm values, including the reestablishment of the high μ peak

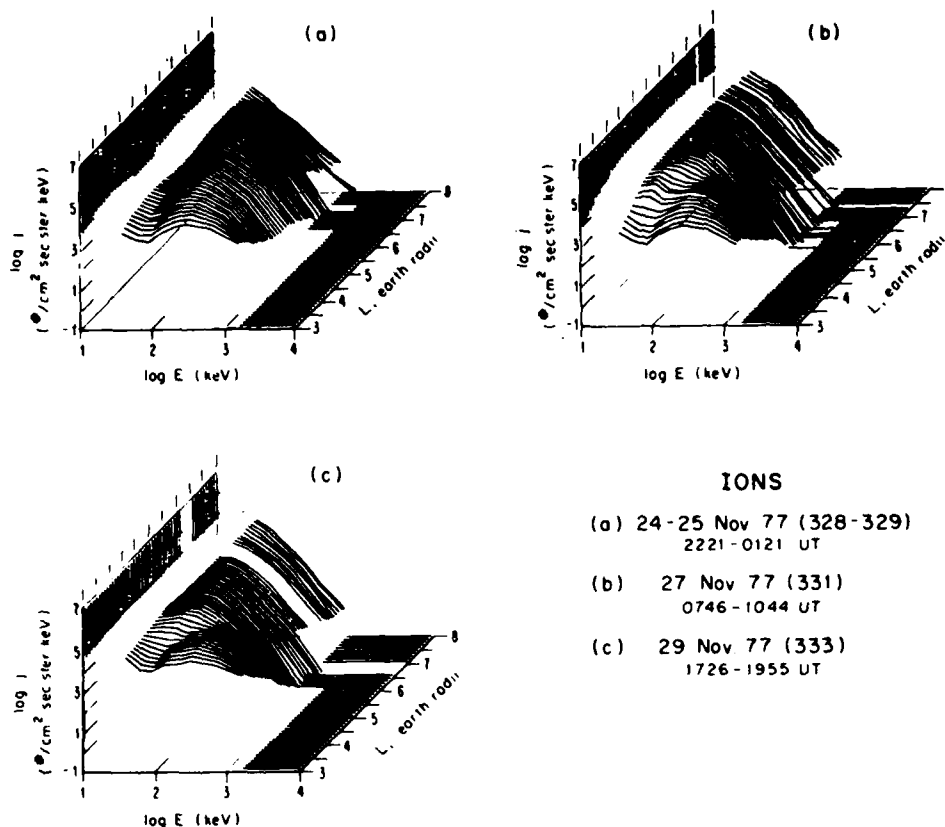


Figure 14. A Perspective View of Directional Differential Flux (j) in Format Similar to Figure 13

giving the fractional increase or decrease in differential particle flux j that occurs as a function of energy (Figure 15). The fractional increase goes from 0 to a factor of 40 or 0 to a factor of -40, plotted as a function of energy. And, of course we see large decreases (dashed lines = decreases) at high energies. As we have seen, those decreases really do not exist when transformed to a μ -space representation. Figure 15b allows us to see the whole radiation zone in one glance; indeed the high energies just adiabatically adjust to what the lower energy particles are doing.

An additional result from some Explorer 45 studies^{8,9} in the radiation belts is that plasma instabilities must be included among ion loss mechanisms. As hot,

8. Williams, D. J., and Lyons, L. R. (1974) The proton ring current and its interaction with the plasmopause: storm recovery phase, *J. Geophys. Res.* 79:4195.
9. Williams, D. J., and Lyons, L. R. (1974) Further aspects of the proton ring current interaction with the plasmopause: main and recovery phases, *J. Geophys. Res.* 79:4791.

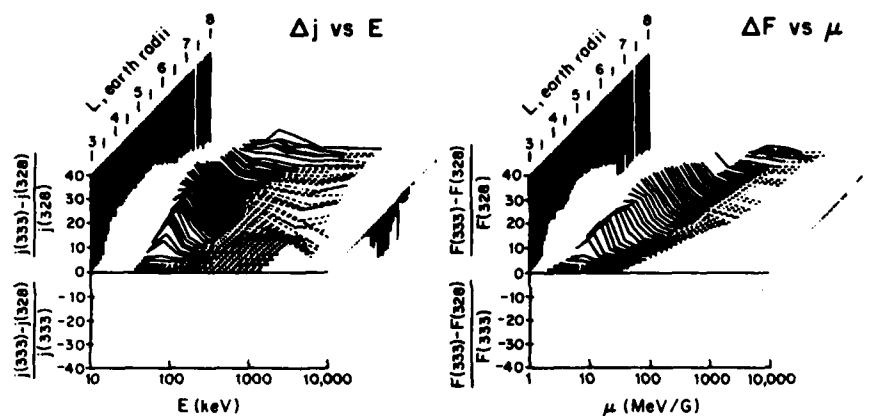


Figure 15. Difference Between $j(E)$ During and Prior to November 1977 Storm as a Function of $E(\mu)$ With Solid Lines Implying Storm Time Increases and Dashed Lines Decreases

injected protons drift into the plasmapause they interact with the dense cold plasma of the outer plasmasphere to drive unstable ion cyclotron waves. The stimulated pitch angle diffusion is weak rather than strong. Figure 16 shows that at some high equatorial altitudes, distributions are isotropic outside empty, atmospheric loss cones. In the interaction region near the plasmapause distributions become rounded when plotted as function of pitch angle. The lower energy particle losses are due to the ion cyclotron instabilities. It is possible to show that the energy of the interaction is sufficient to drive SAR arcs.¹⁰ In fact, structures observed in SAR arc formations are consistent with observed ring current variations.

4. TRANSPORT IN THE RADIATION BELTS

We next consider transport mechanisms. The well established mechanism for ion transport in the radiation belt has been cross-L diffusion by violation of the third adiabatic invariant. Work originally done by Tverskoi,¹¹ Cornwall,¹²

10. Cornwall, J.M., Coroniti, F.V., and Thorne, R.M. (1971) A unified theory of SAR arc formation at the plasmapause, *J. Geophys. Res.* 75:4428.
11. Tverskoi, B.A. (1969) Main mechanisms in the formation of the earth's radiation belts, *Rev. Geophys.* 7:219.
12. Cornwall, J.M. (1972) Radial diffusion of ionized helium and protons: a probe for magnetospheric dynamics, *J. Geophys. Res.* 77:1756.

Schematic Model of Recovery Phase

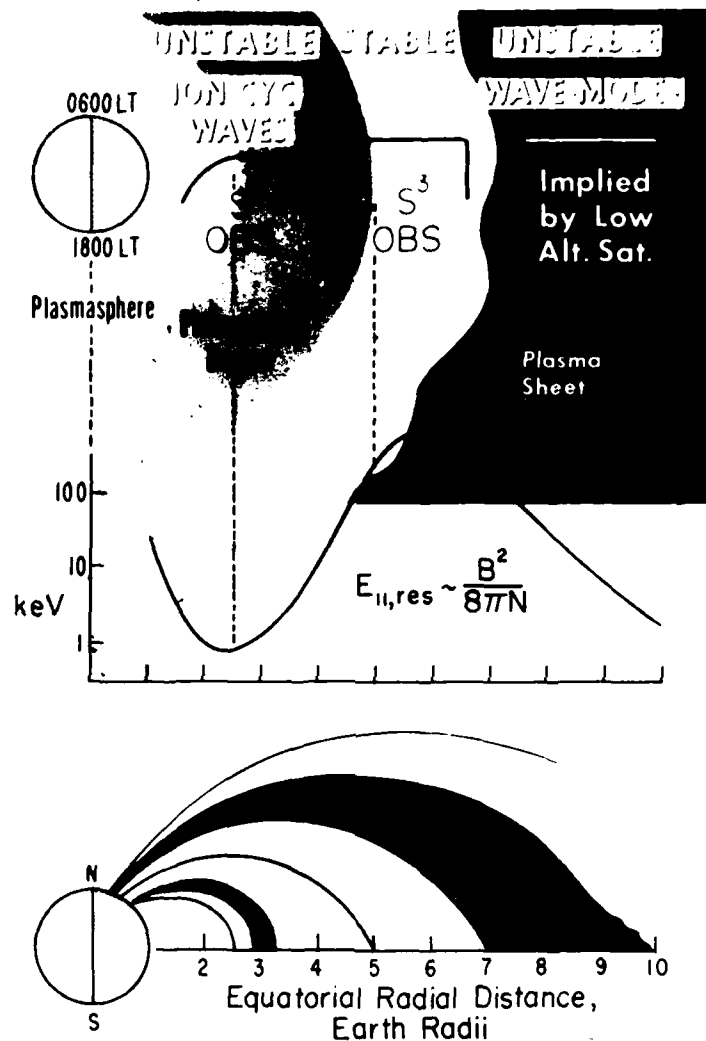


Figure 16. Schematic Picture of Geomagnetic Storm Recovery Phase Showing Hot Ring Current Plasma Behavior in the Geomagnetic Field and Its Interaction With the Cold Plasmaspheric Plasma. A semiquantitative resonant energy versus altitude plot that uses the Explorer 45 results is shown for reference. Moderate pitch angle diffusion occurs for the hot ring current plasma in the plasmopause region owing to amplification of ion cyclotron waves. Each energy of the ring current plasma begins its interaction in the plasmopause region at the appropriate value of $B^2/8\pi N$. Above the plasmopause region the hot ring current plasma is stably trapped with negligible or no losses due to pitch angle scattering. Above this region and above Explorer 45 apogee during the recovery phase the plasma sheet region exhibits strong turbulence and a full loss cone as implied by low-altitude measurements

Nakada and Hess¹³ has been extended by Spjeldvik and Fritz¹⁴ to show how well cross-L diffusion explains many features of ion populations observed in the radiation belts.

Figure 17 gives a sequence of curves where a measured input function, used as a boundary condition at $6.6 R_E$, was obtained from the ATS-6 satellite. That distribution was then used as a "parent" distribution that diffused into the radiation belt.¹⁵ Data from Explorer 45 were used to check the spectral results as particles diffused inward. Above approximately 100 keV theory and observations agree very nicely. In the diffusion calculations, it was assumed that the ions were protons; that is the only assumption that could be made to get the fits looking so good. If it was assumed that another ion was dominant, the spectral distribution fits would not be nearly as good. If it is assumed that the ions are helium ions the disagreement is by orders of magnitude. Figure 18 is a plot of theoretical and observed flux levels for 4 MeV, equatorially mirroring oxygen ions as a function of radial distance. Again the agreement between observations and diffusion theory is quite good. However, from measurements deep within the radiation belts, it is impossible to determine the source of the energetic oxygen ions;¹⁶ by the time they are measured at or below equatorial distances of $\sim 5 R_E$ they have come to equilibrium with a charge state of 4 as the dominant state. This means that all charge state characteristics of the source region are lost.

Finally, the loss terms have to be considered. Figure 19 shows data from a paper by Spjeldvik and Fritz¹⁷ using the helium ion fluxes measured on the Explorer 45 satellite. It shows decay times measured for helium ions in three different energy channels, ranging from 910 keV to 3.15 MeV. The solid curve shows the expected decay time due to diffusion alone. If one injects a group of ions into the radiation belt, the ion flux will diffuse both inward and outward. Outward diffusion across the magnetopause leads to diffusion loss, in terms of intensities of ions at the point in space where one is measuring. In Figure 19 the solid line is the diffusion line; the dashed line shows the charge exchange loss time and the dotted line shows the Coulomb collision loss time. It is apparent that the high

13. Nakada, M. P. and Mead, G. D. (1965) Diffusion of protons in the outer radiation belt, *J. Geophys. Res.* 70:4777.
14. Spjeldvik, W. N. and Fritz, T. A. (1978) Energetic ionized helium in the quiet time radiation belts: theory and comparison with observations, *J. Geophys. Res.* 83:654.
15. Spjeldvik, W. N. (1977), Equilibrium structure of equatorially mirroring radiation belt protons, *J. Geophys. Res.* 82:2801.
16. Spjeldvik, W. N., and Fritz, T. A. (1978) Theory for charge states of energetic oxygen ions in the earth's radiation belts, *J. Geophys. Res.* 83:1583.
17. Spjeldvik, W. N., and Fritz, T. A. (1981) Energetic heavy ions with nuclear charge $Z \geq 4$ in the equatorial radiation belts of the Earth: Magnetic storms, *J. Geophys. Res.* 86:2349.

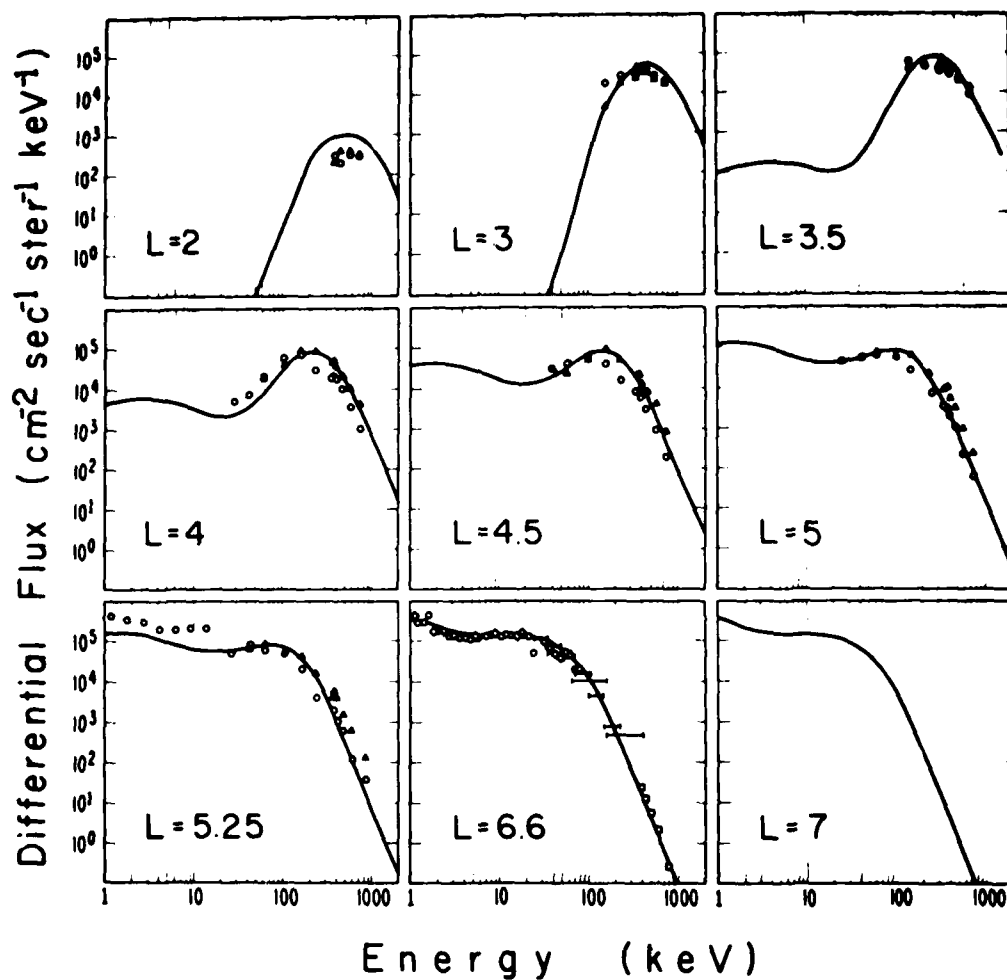


Figure 17. Comparison of Theoretical and Observed Energy Spectra in the keV Energy Range at L Values of 2, 3, 3.5, 4, 4.5, 5, 5.25, 6.6, and 7. The spectrum at L = 7 constitutes the adopted boundary condition on the theoretical calculations. The data at L = 6.6 are taken from a number of experiments on the satellite ATS 6 in geostationary orbit. The data at the lower L values are taken from quiet time observations on board the satellite Explorer 45. Data from orbit 97 are denoted by circles and data from orbit 667 are denoted by triangles

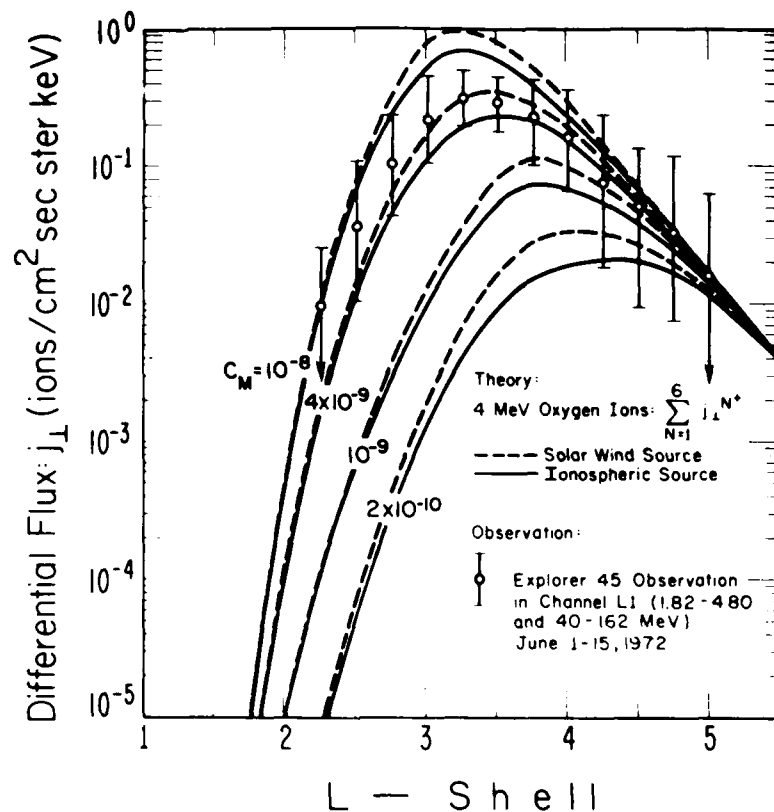


Figure 18. Comparison Between Theory and Observation. The lines indicate computed radial profiles of 4-MeV oxygen ions summed over all charge states in the earth's radiation belts. The solid curves assume an ionospheric source of O^+ and the outer zone boundary and show the profiles for $C_M = 2 \times 10^{-10}$, $C_M = 10^{-9}$, $C_M = 4 \times 10^{-9}$, and $C_M = 10^{-8} R_E^2/\text{day}$. The dashed curves assume a solar wind source of O^{6+} at the outer zone boundary and show the profiles for the same values of C_M . Data on oxygen ions obtained from the L1 channel on the Explorer 45 are also indicated. This channel had two simultaneous energy passbands of 1.82-4.80 and 40-162 MeV per ion for the oxygen ions, and the shown data represent a quiet time average of five quiet days during the period June 1-15, 1972. Standard deviation in the statistical spread is indicated by the vertical error bars

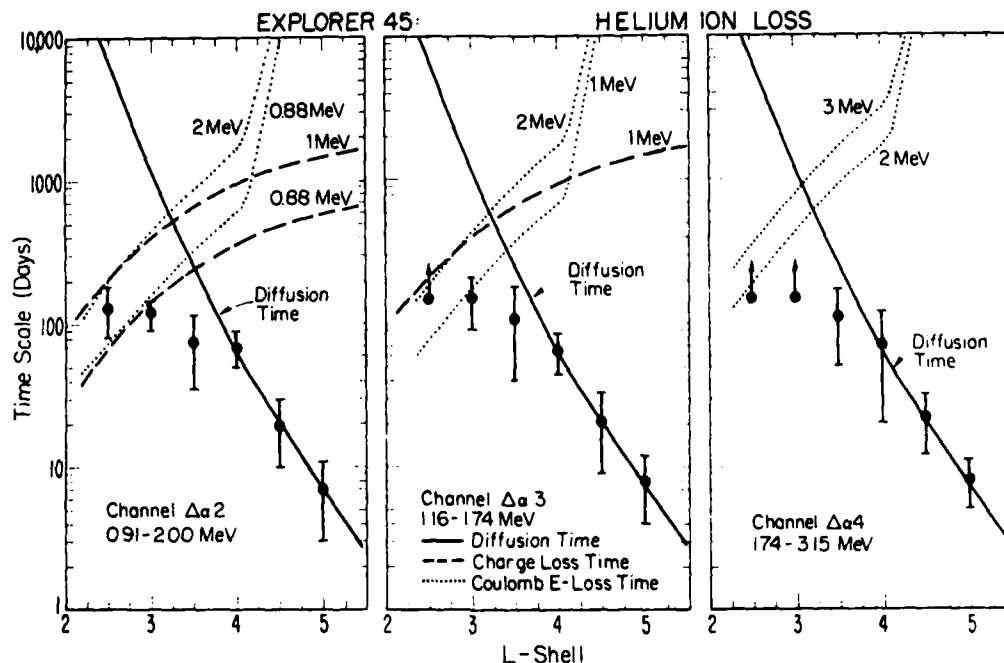


Figure 19. Helium Fluxes Measured by Explorer 45 as a Function of L Compared With Time Scales for Diffusion, Charge Exchange and Coulomb Loss

L shell ions respond to diffusion; they are simply being transported out of the radiation belt trapping region. The normally expected atmospheric loss terms at lower altitudes are dominated by Coulomb collisions and by charge exchange.

5. ELECTRONS

We now turn our attention to radiation belt electrons. Figure 20 is a low altitude profile of 30 keV electron measurements from OGO-6². The symbols 1, 5 and 7 give the counts recorded from locally mirroring, precipitating and backscattered electrons, respectively. The figure shows that the ratio of the precipitated electrons to the locally trapped electrons appears to be approximately 1 percent. Note that at times the records show more backscattered electrons coming up from the atmosphere than going down. However, a study of the spatial and orientation dependences of the satellite with respect to the magnetic field lines on the backscattered flux population, yielded the conclusion that all the particles seen in the upward looking detector, generally were scattered inside the collimator of

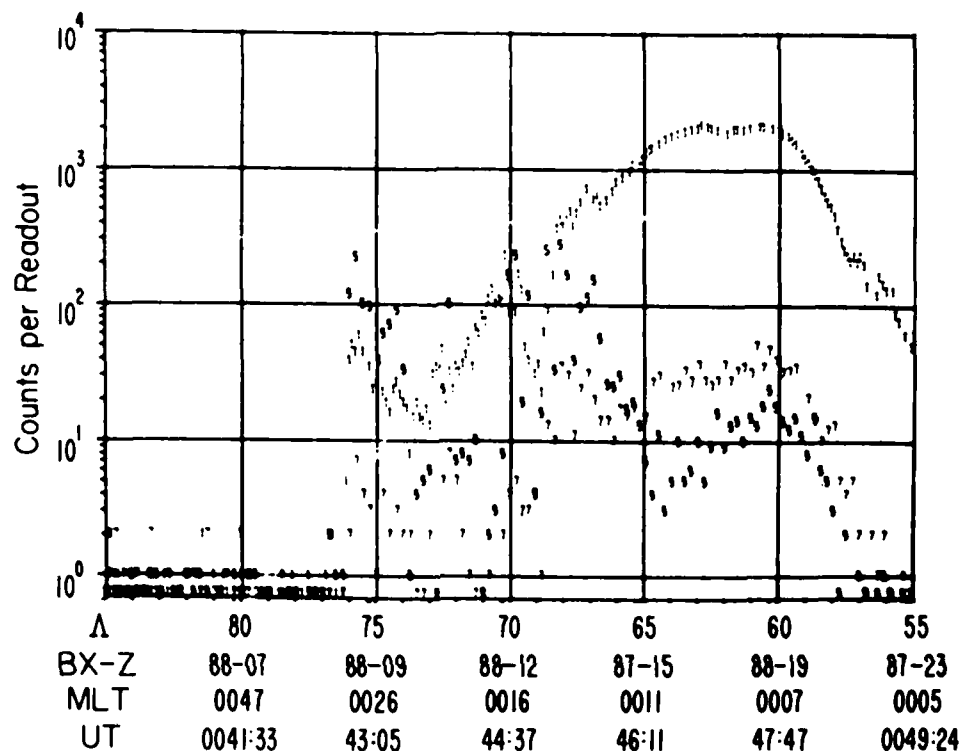


Figure 20. Northern Hemisphere Pass on Orbit 815, August 1, 1969, Showing Different Latitudinal Profiles for the Precipitated and Backscatter Count Rates in the Weak Diffusion Region at Latitudes Less than $\Lambda = 65^\circ$. The precipitated electron count rate (Det 5) represents an upper limit to the true precipitated loss cone flux. The range of altitude and magnetic field strength was from 903 km and 0.381 G at $\Lambda = 80^\circ$ to 1024 km and 0.314 G at $\Lambda = 55^\circ$.

the instrument itself. The measurements were contaminated and thus were not representative of the equilibrium electron precipitation in the outer radiation belt. This may also be the case for other, older measurements. It is possible to do a careful study and find periods where one can expect a minimum contribution from such contamination scattering by picking appropriate orientations with respect to magnetic field lines. From these circumstances ratios that are believable were deduced, and these are somewhat below 10^{-3} . Figure 21 shows comparisons with respect to various calculations,^{2, 18, 19} which include backscatter from the

18. Davidson, G., Walt, M. (1977) Loss cone distributions of radiation belt electrons, *J. Geophys. Res.* 82:48.

19. Spjeldvik, W.N., and Thorne, R.M. (1975) The cause of storm after effects in the middle latitude D region, *J. Atmos. Terr. Phys.* 37:777.

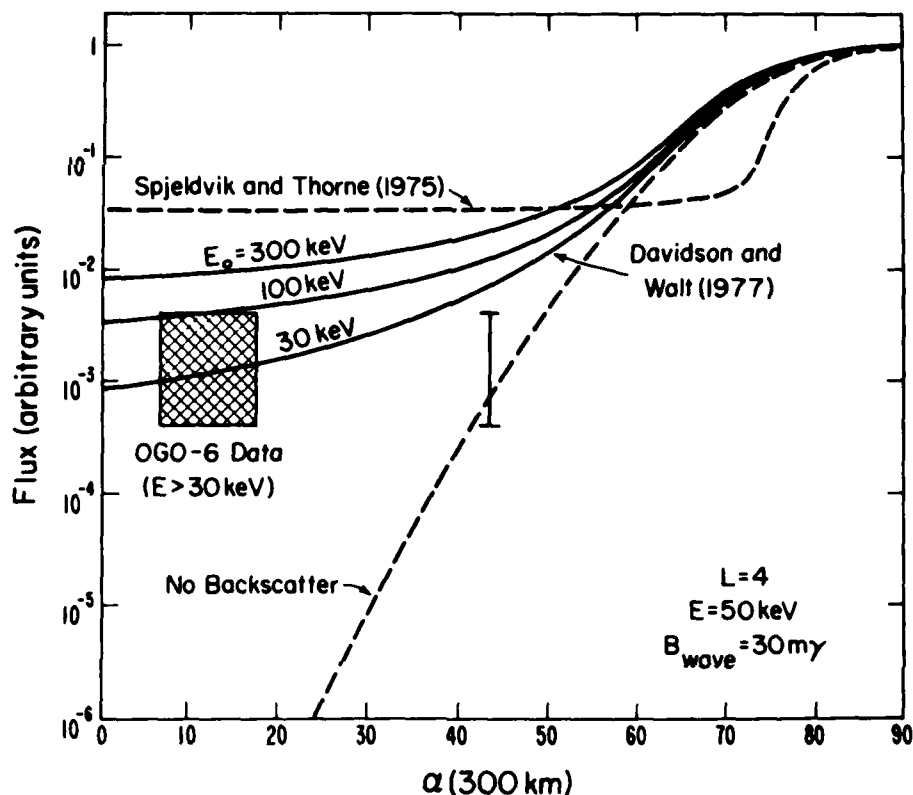


Figure 21. Theoretical Results From the Calculations of Spjeldvik and Thorne¹⁹ and Davidson and Walt,¹⁶ Adapted From Figure 3 of Davidson and Walt. The Davidson and Walt results are shown for three different equatorial omnidirectional energy spectra $j \propto \exp(-E/E_0)$. The curve marked "no backscatter" is based on the diffusion model of Kennel and Petschek.¹ Values of the flux ratio Det 5/(Det 1 \times 3.4) from northern hemisphere data (Figure 8 of Ref. 2) for which Det 7/Det 5 ≥ 2 are bracketed by the box. The single vertical line represents the maximum equivalent pitch angle at 300 km for true loss cone electrons which enter the loss cone detectors

atmosphere. It should be noted these theoretical calculations were made under different physical assumptions that may or may not have been satisfied at the time of the OGO-6 observations.²⁰ The tentative conclusion is that the observed ratio of precipitated to locally trapped electrons is less than 10^{-3} . It is therefore reasonable to suspect that either the previous results were contaminated by backscatter or the results did not pertain to real equilibrium conditions.

20. Spjeldvik, W.N. (1977) Radiation belt electrons: structure of the loss cone, *J. Geophys. Res.* 82:709.

Another quantitative advance of the 1970's was the work done by Lyons and coworkers^{21,22} explaining the structure of the energetic (> 30 keV) electron radiation belt. Figure 22 shows the bounce averaged pitch angle diffusion coefficient obtained by using a model for plasmaspheric hiss, based on the measured wave spectrum in the plasmasphere. The Landau term is represented by the $n = 0$ term of a series of cyclotron resonance harmonics. The other lines represent the contributions from summed cyclotron resonances ($n \geq 1$) terms. We see that by using this type of pitch angle diffusion coefficient, minima develop in the diffusion coefficient. Folding these diffusion coefficients into predictions of pitch angle distributions, yields predictions of distributions which have observable "humps" around 90° . This is because there is fast diffusion at pitch angles away from 90° . The diffusion slows up and then it picks up again at small pitch angles. Figure 23 gives a comparison of the OGO 5 pitch angle distributions for the various energy electrons measured, with the predictions of Lyons and coworkers.²¹ The general features of a "hump" structure around the 90° point is there. The absolute magnitude is not correct. However, the precise magnitude depends on the model of the plasmaspheric hiss, which is somewhat crude and can be changed to match these intensities. The features expected because of pitch angle diffusion from the plasmaspheric hiss spectra are indeed seen in the measured pitch angle distributions.

To carry the electron analysis further one must now introduce cross-L radial diffusion in the same way that was done with ions. This time, instead of having loss terms that are primarily atmospheric, Coulomb and charge exchange, one must include a loss term that represents an approximation to the pitch angle diffusion. When that is done, theory predicts the radial profiles of the electrons presented as dashed lines in Figure 24. There is very good agreement in predicting the two-belt structure separated by a wide slot. It naturally follows from a combination of the source term, cross-L transport, and the loss mechanism. This comparison was done with data from one satellite, OGO-5.

In Figure 25 we continue the electron analysis with data from Explorer 45. This figure shows the pitch angle distributions from the 35 - 70 keV channel, up to the 240 - 560 keV channel. Differential intensities are plotted as functions of pitch angle. From 5 to $2 R_E$ one sees, both in the data and the theory, the evolution of the electron distributions. The quantitative dependence on energy and distance is again matched in the comparison of the theory and the data.

21. Lyons, L.R., Thorne, R.M., and Kennel, C.F. (1972) Pitch-angle diffusion of radiation belt electrons within the plasmasphere, J. Geophys. Res. 77:3455.
22. Lyons, L.R., and Thorne, R.M. (1973) Equilibrium structure of radiation belt electrons, J. Geophys. Res. 78:2142.

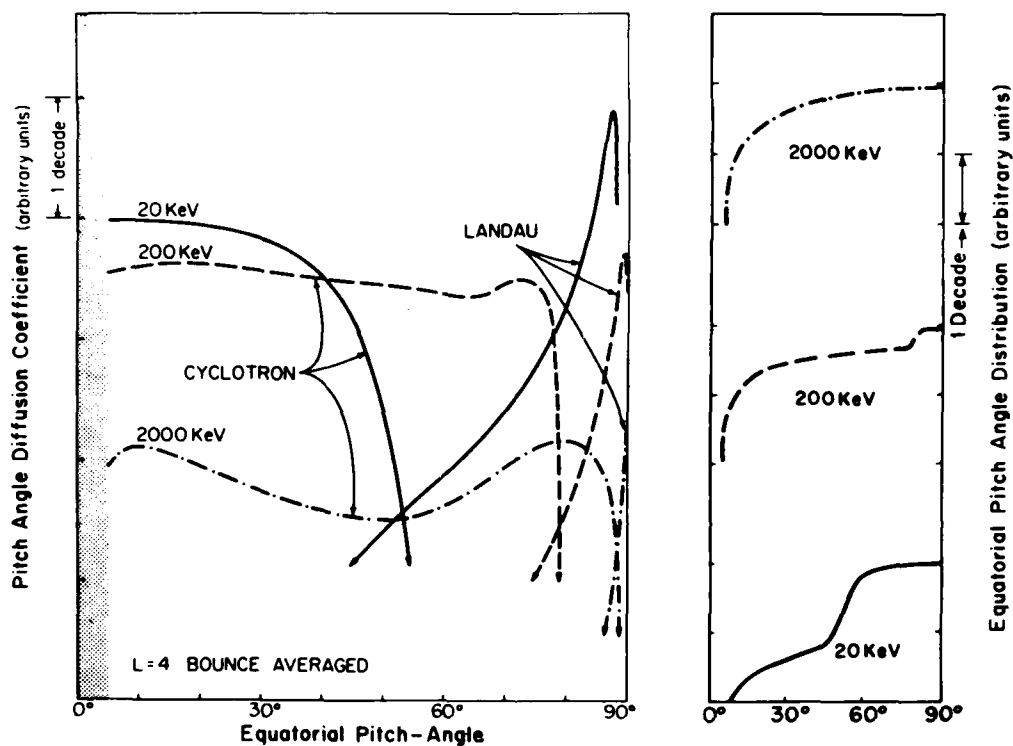


Figure 22. Bounce-orbit Averaged Cyclotron and Landau Resonant Pitch-angle Diffusion Coefficients as a Function of Equatorial Pitch Angle at $L = 4$ for 20-, 200-, and 2000-keV Electrons. At each energy, the line coding used for the Landau resonant diffusion coefficients corresponds to that for the sum of the cyclotron-harmonic resonant diffusion coefficients

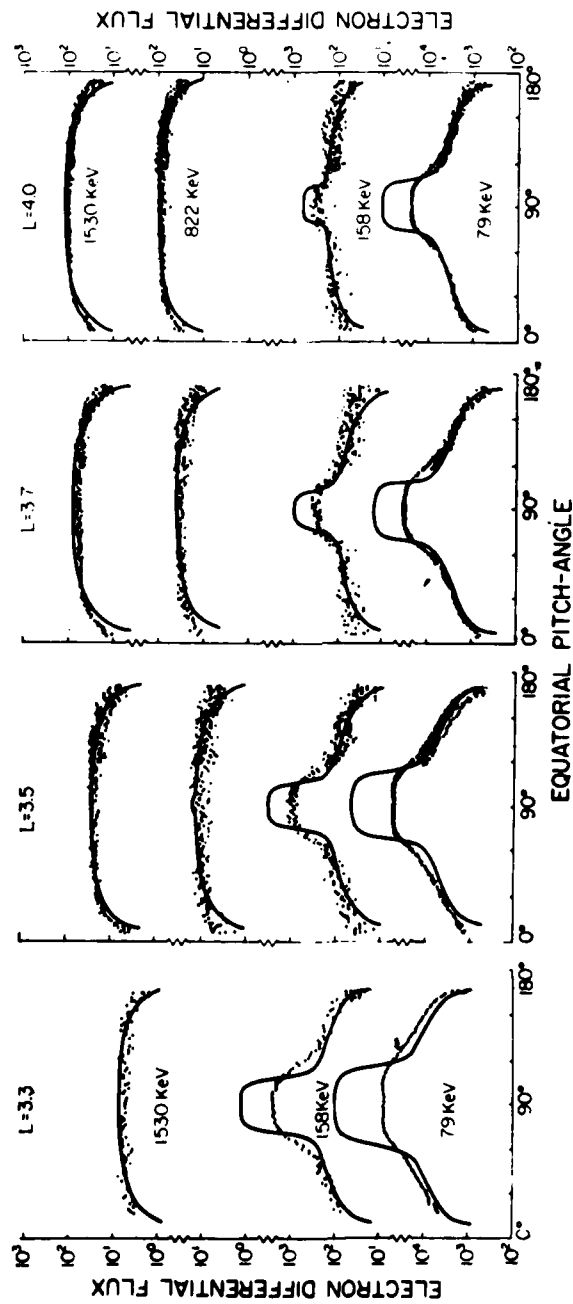


Figure 23. Comparison of Calculated Equatorial Pitch-angle Distributions With Equatorial Distributions Observed Within the Electron Slot During the Decay Phase Following an Injection Event. The data points (electrons/cm²-sec-ster-keV) are plotted as a function of pitch angle at the L values and energies indicated on the figure. The vertical positionings of the corresponding calculated distributions, shown by solid lines, are arbitrary on a logarithmic scale and have therefore been adjusted so as to best fit the data

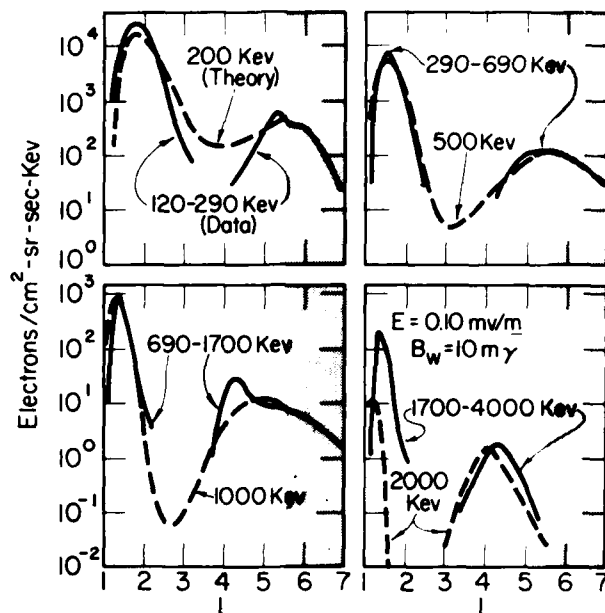


Figure 24. Theoretical Flux Profile for $E = 0.10 \text{ mV/m}$ and $B_w = 10 \text{ m}\gamma$ are Compared With Quiet Time, Solar Minimum Observations

6. TIME VARIATIONS OF ELECTRONS

Magnetic storms profoundly affect radiation belt electrons. The Explorer 45 data from December 16, 1971, given in Figure 26, represent a quiet time period. Differential fluxes as functions of pitch angle are shown for four energy channels. The quiet time equilibrium distributions become greatly distorted due to the storm time energetic electron injection. However, the electron pitch angle distributions very quickly evolve back to shapes that they had during pre-storm equilibrium, as illustrated in this figure. While we do not fully understand the injection process itself, it seems that after the electrons are injected, the same processes that are responsible for the equilibrium pitch angle distribution structure again become dominant. All of the distributions then evolve back towards equilibrium. This also controls the radial profiles (Figure 27). The dashed lines are the quiet time radial profiles; the four energy channels are plots of differential flux as functions of L-shell. The electron study was also done for the December 17, 1971 magnetic storm and the top left panel gives the quiet time radial profiles for comparison with storm time perturbations.

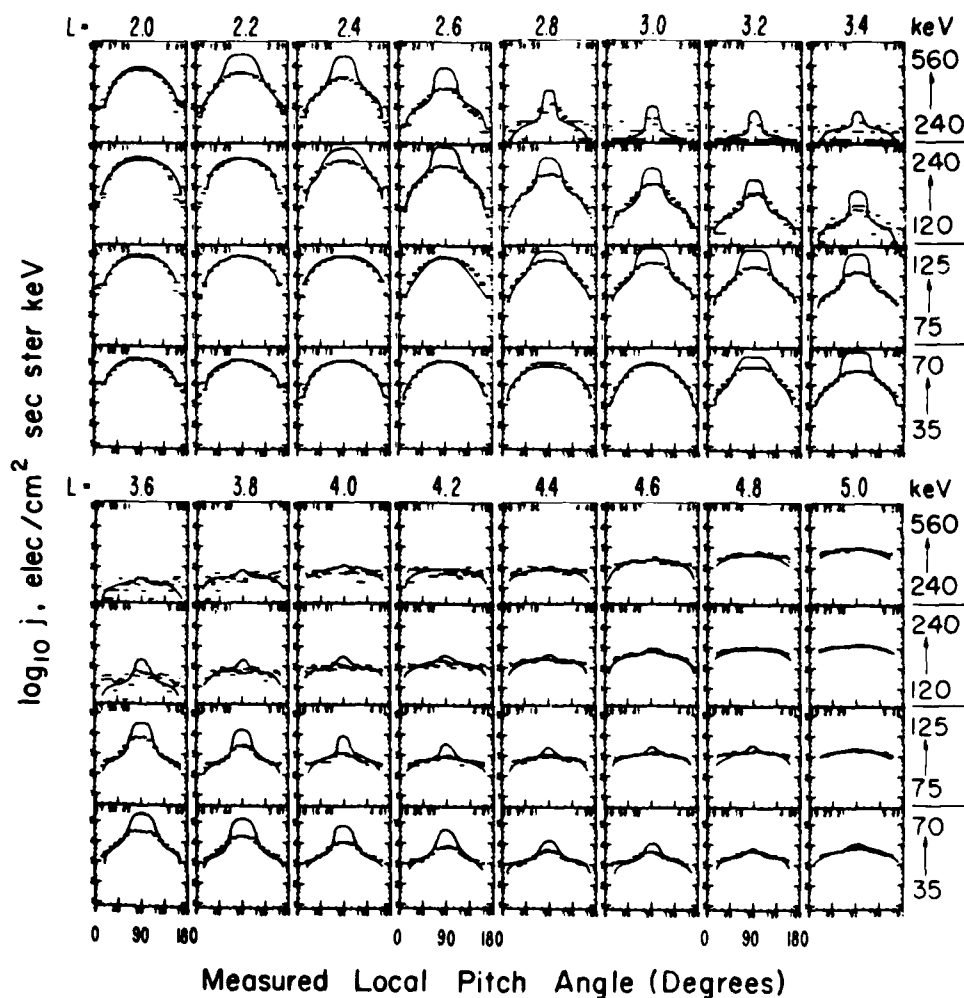


Figure 25. Equatorial Pitch Angle Distributions Observed on December 15, 1971 (Orbit 95), and Those Predicted by Lyons et al²¹ from Resonant Interactions With the Plasmaspheric Whistler Mode Wave Band. Distributions are shown every 0.2 interval in L from L = 2 to L = 5. The four energies are stacked vertically at each L with the lowest energy at the bottom. The dashes give the measured electron flux, their horizontal extent indicating the pitch angle scan for each measurement. The solid curves are the theoretically predicted pitch angle distributions for the geometric mean energy of each energy interval. Diffusion from Coulomb collisions has been added to the theoretical calculations to account for the rounding of the pitch angle distributions within the inner zone. The vertical positioning of the theoretical distributions are arbitrary on a logarithmic scale and have thus been adjusted to illustrate best the comparison with the observations

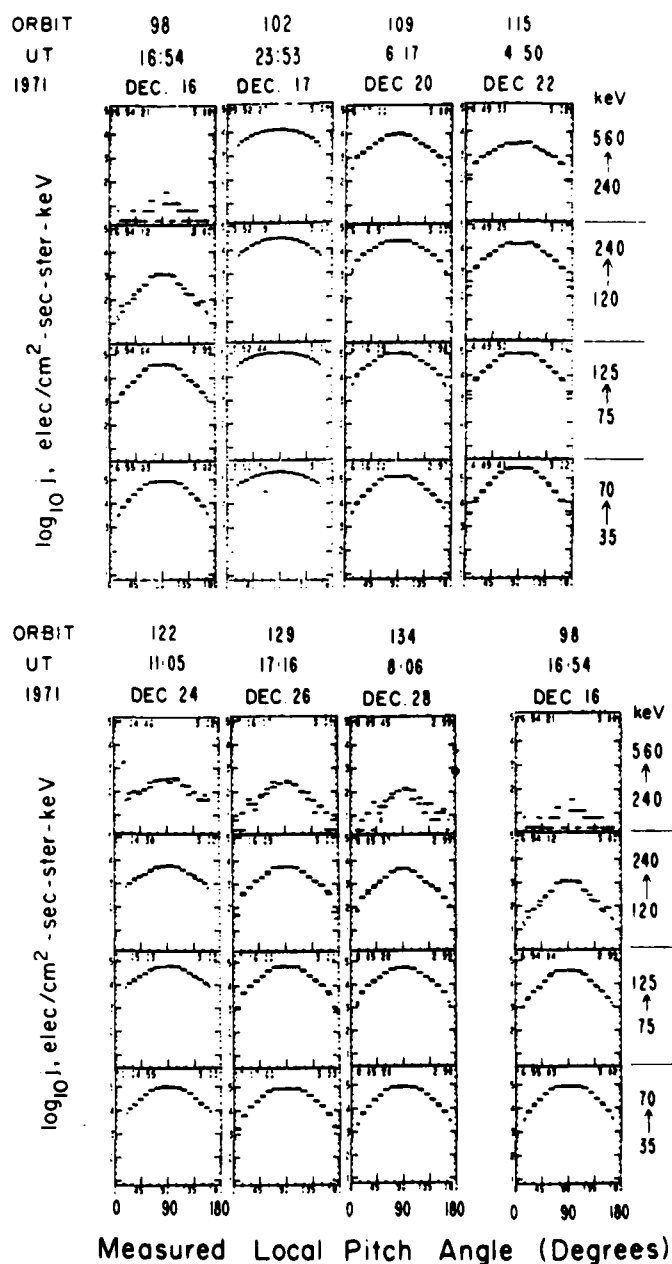


Figure 26. Observed Pitch Angle Distributions at $L = 3$, Approximately Once Per Day, For the Period Following the Storm of December 17, 1971. Pre-storm distributions for December 16, 1971, are also shown. All observations are from the outbound portion of the orbit

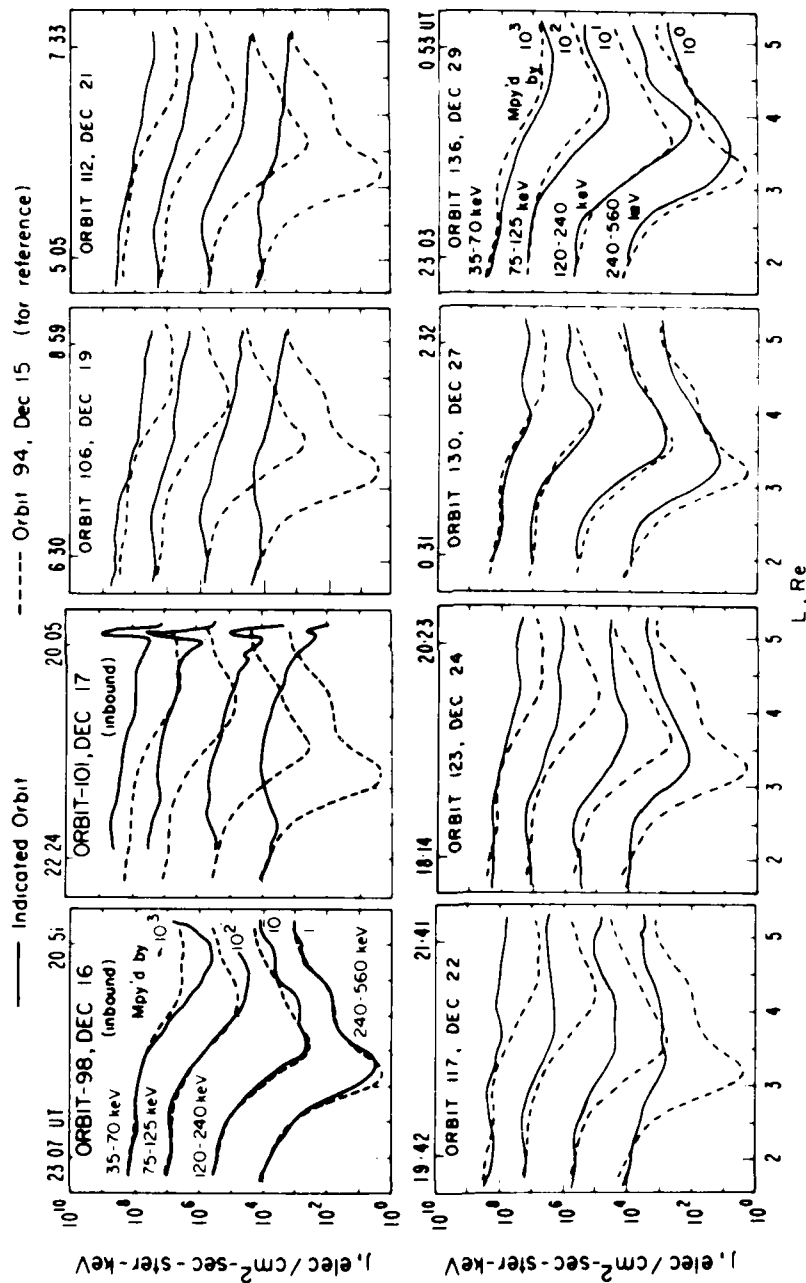


Figure 27. Observed Radial Profiles of the 90° Local Pitch Angle Electron Flux Obtained Near the Geomagnetic Equator for the Periods Just Preceding, During, and Just Following the Storm of December 17, 1971. Solid curves give the profiles from the orbit indicated in each panel, and the dashed curves give the pre-storm profiles from orbit 94 outbound (December 15, 1971) for comparison. To display the data clearly, the 120- to 240-keV, 75- to 125-keV, and 35- to 70-keV fluxes have been multiplied by 10^1 , 10^2 , and 10^3 , respectively. Every available orbit, both outbound and inbound, is shown

7. CONCLUDING REMARKS

Figure 28 presents results of statistical modelling done by the Aerospace group²³ that give the probability of observing a particular flux at geostationary orbit at a variety of energies. These curves are easy to use and from an engineering point of view are very useful. This type of work has been used to show good correlations between the half-year average flux of electrons with $E > 1.5$ MeV at geostationary altitude and the half-year average of the solar wind velocity. Furthermore, attention should also be directed towards specific details, like the fine work by the Los Alamos group²⁴ using electron pitch angle distributions at geostationary altitude as potential precursors to substorms, and deriving inferences on what phenomena are responsible for driving electrons into the loss cone. These are key issues in trying to understand the precise mechanisms operating in the radiation belt zones.

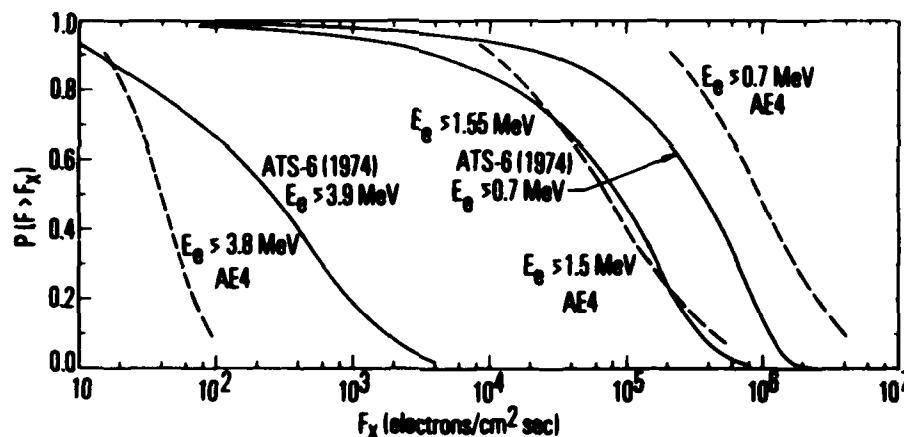


Figure 28. Plots of the Probability $P(F > F_x)$ of Observing a Flux of Electrons Greater than F_x Above Three Integral Thresholds. ATS-6 data (solid curves) and AE4 predictions (dashed curves) are shown. The ATS-6 curves were constructed using 181 days of data obtained between days 165 and 365 of 1974, while ATS-6 was located near 94° W

23. Vampola, A. L., Blake, J. B., and Paulikas, G. A. (1977) A new study of the magnetospheric electron environment, *J. Spacecraft and Rockets* 14:690.
24. Higbie, P. R., Baker, D. N., Hones, E. W., Jr., and Belian, R. D. (1979) Pitch angle distributions of > 30 keV electrons at geostationary altitudes, in *Quantitative Modelling of Magnetospheric Processes*, ed. W. P. Olson, Amer. Geophys. University, Washington, D. C., p. 203.

In summary, the last decade has seen major achievements in radiation belt research. We now understand the principles of radiation belt transport processes and the major loss mechanisms. The years ahead should focus research activity on the precise source mechanisms causing the injection of energetic particles into the radiation belt trapping region.

References

1. Kennel, C.F., and Petschek, H.E. (1966) Limit on stably trapped particle fluxes, J. Geophys. Res. 71:1.
2. Leinback, H., and Williams, D.J. (1977) Evidence for very weak pitch angle diffusion of outer zone electrons, J. Geophys. Res. 82:5091.
3. Williams, D.J. (1980) Ring current composition and sources, in Dynamics of the Magnetosphere, ed. S.I. Akasofu, D. Reidel, Boston, Massachusetts, p 407.
4. Williams, D.J. (1981) Ring current composition and sources, an update, Planet Sp. Sci. (in press).
5. Davis, L.R., and Williamson, J.M. (1963) Low-energy trapped protons, Space Sci. 3:365.
6. Lyons, L.R., and Williams, D.J. (1976) Storm associated variations of equatorially mirroring ring current protons, 1-800 keV, at constant first adiabatic invariant, J. Geophys. Res. 81:216.
7. Williams, D.J. (1981) Phase space variations of near equatorially mirroring ring current ions, J. Geophys. Res. 86:189.
8. Williams, D.J., and Lyons, L.R. (1974) The proton ring current and its interaction with the plasmopause: storm recovery phase, J. Geophys. Res. 79:4195.
9. Williams, D.J., and Lyons, L.R. (1974) Further aspects of the proton ring current interaction with the plasmopause: main and recovery phases, J. Geophys. Res. 79:4791.
10. Cornwall, J.M., Coroniti, F.V., and Thorne, R.M. (1971) A unified theory of SAR arc formation at the plasmopause, J. Geophys. Res. 75:4428.
11. Tverskoi, B.A. (1969) Main mechanisms in the formation of the earth's radiation belts, Rev. Geophys. 7:219.
12. Cornwall, J.M. (1972) Radial diffusion of ionized helium and protons: a probe for magnetospheric dynamics, J. Geophys. Res. 77:1756.
13. Nakada, M.P. and Mead, G.D. (1965) Diffusion of protons in the outer radiation belt, J. Geophys. Res. 70:4777.
14. Spjeldvik, W.N., and Fritz, T.A. (1978) Energetic ionized helium in the quiet time radiation belts: theory and comparison with observations. J. Geophys. Res. 83:654.
15. Spjeldvik, W.N. (1977) Equilibrium structure of equatorially mirroring radiation belt protons, J. Geophys. Res. 82:2801.

16. Spjeldvik, W.N., and Fritz, T.A. (1978) Theory for charge states of energetic oxygen ions in the earth's radiation belts, J. Geophys. Res. 83:1583.
17. Spjeldvik, W.N., and Fritz, T.A. (1981) Energetic heavy ions with nuclear charge $Z \geq 4$ in the equatorial radiation belts of the earth: magnetic storms, J. Geophys. Res. 86:2349.
18. Davidson, G., Walt, M. (1977) Loss cone distributions of radiation belt electrons, J. Geophys. Res. 82:48.
19. Spjeldvik, W.N., and Thorne, R.M. (1975) The cause of storm aftereffects in the middle latitude D region, J. Atmos. Terr. Phys. 37:777.
20. Spjeldvik, W.N. (1977) Radiation belt electrons: structure of the loss cone, J. Geophys. Res. 82:709.
21. Lyons, L.R., Thorne, R.M., and Kennel, C.F. (1972) Pitch-angle diffusion of radiation belt electrons within the plasmasphere, J. Geophys. Res. 77:3455.
22. Lyons, L.R., and Thorne, R.M. (1973) Equilibrium structure of radiation belt electrons, J. Geophys. Res. 78:2142.
23. Vampola, A.L., Blake, J.B., and Paulikas, G.A. (1977) A new study of the magnetospheric electron environment, J. Spacecraft and Rockets 14:690.
24. Higbie, P.R., Baker, D.N., Hones, E.W., Jr., and Belian, R.D. (1979) Pitch angle distributions of > 30 keV electrons at geostationary altitudes, in Quantitative Modelling of Magnetospheric Processes, ed. W.P. Olson, Amer. Geophys. University, Washington, D.C., p.203.

Contents

1. Introduction	47
2. Adiabatic Invariants	48
3. Nonadiabatic Effects	51
4. Saturation	54
5. Radial Diffusion	59
6. Protons (Ions)	63
References	66

2. A Theorist's View of the Earth's Radiation Belts

by

Michael Heinemann
Physics Department
Boston College
Chestnut Hill, Massachusetts 02167

based on a tutorial lecture given by

Michael Schulz
The Aerospace Corporation
El Segundo, California 90009

1. INTRODUCTION

A good understanding of steady-state radiation belt dynamics has emerged over the past 20 years. In the future, the aspects where improved understanding should be sought are the unsteady features of radiation belt dynamics: how the transport coefficients and the boundary conditions themselves vary with solar terrestrial indices and otherwise with time.

From a theoretical point of view, the radiation belts are composed of the high energy portion of the magnetospheric particle population. For kinematical reasons, it is convenient to set a lower bound of 50 to 100 keV on the energy and an upper bound of 50 to 100 MeV. One sees such high energy particles only as ions (protons) in the inner zone; for electrons, there is a practical upper limit of 5 MeV on the actual population. Figure 1 is a contour map of the intensity of 0.5 MeV electrons

46 p. x. 10

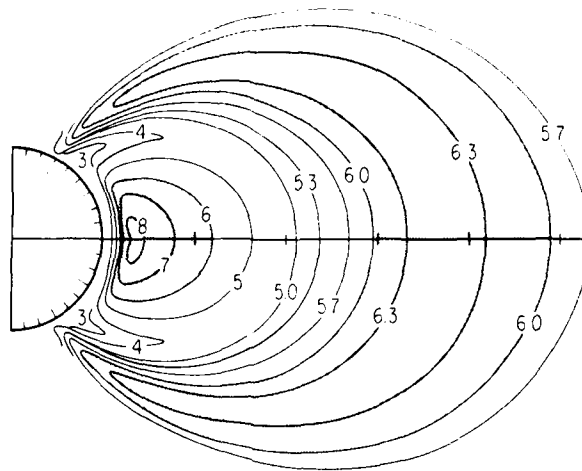


Figure 1. Isoflux Contours of the Earth's Radiation Belt Compiled From Many Spacecraft Observations (Courtesy of Dr. James I. Vette, NASA/Goddard Space Flight Center). The shaded areas show the regions of the equatorial radiation belts where the stably trapped 500 keV electrons have flux intensities exceeding 10^6 electrons/cm²sec. Notice the division into two radiation zones

as compiled by James I. Vette (NASA/Goddard Space Flight Center). The shaded areas are those regions of space where the integral intensity exceeds 10^6 electrons cm⁻²sec⁻¹. There is a nice two-belt structure, the significance of which has emerged over the last 20 years. The radiation belts occupy a portion of the inner part of the magnetosphere, within about $10 R_E$ of the center of the earth, as shown in Figure 2. They reside in a region in which the field lines are closed but do not exhaust that region. There is a so-called quasi-trapping region where, though the field lines are closed, they do not support particle trajectories that form closed drift shells. Rather, particles in that region can drift into the boundary of the magnetosphere, and so for practical purposes one has an outer boundary to the radiation belt region, at which boundary conditions such as particle intensity or phase space density can be imposed.

2. ADIABATIC INVARIANTS

Within the dipolar region of the magnetosphere, or at least within the closed field line region, particles within reasonable energy bounds execute triply periodic

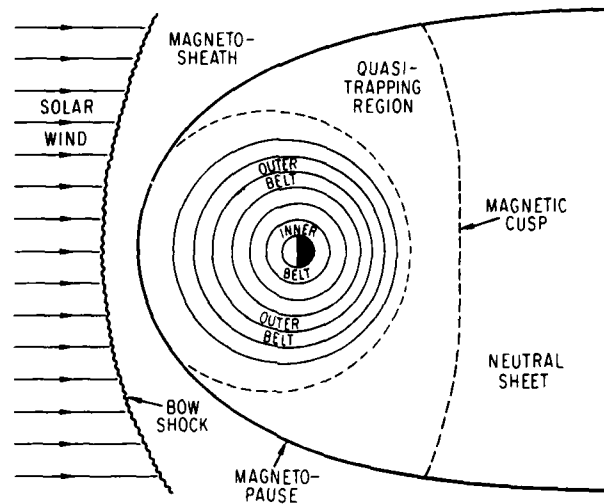


Figure 2. Illustration of Energetic Charged Particle Drift Shells in the Inner Magnetosphere. Notice that some of the drift shells in the outer radiation belt may encounter the magnetopause, the location of which is time variable. The region of the inner magnetosphere where this happens is known as the quasi-trapping region since the particles there are unable to complete their drift motion around the earth

motions. The frequencies of these motions are shown in Figure 3. There is a gyration about a magnetic field line at frequencies ranging from tens to hundreds of Hertz for protons and many kiloHertz for electrons. There is a bounce motion between mirror points along a field line, measured in Hertz for protons and several Hertz for electrons; relativistic corrections enter at higher energies. Finally, there is a drift period measured in tens of minutes, at which particles execute a longitudinal drift around the earth.¹

Associated with these three fundamental periodicities are canonical action integrals which are used kinematically to define the coordinates of particles. The first adiabatic invariant is the integral of the canonical momentum of the particle around the orbit of gyration and is equal to the magnetic moment of the particle divided by the relativistic factor γ , which measures the ratio of relativistic mass to rest mass. The second invariant is the integral of the particle's parallel momentum between mirror points and back. The third invariant emerges from the integral of the canonical momentum around the drift shell; because it involves the

1. Roederer, J.G. (1970) Dynamics of Geomagnetically Trapped Radiation, Springer Verlag, New York.

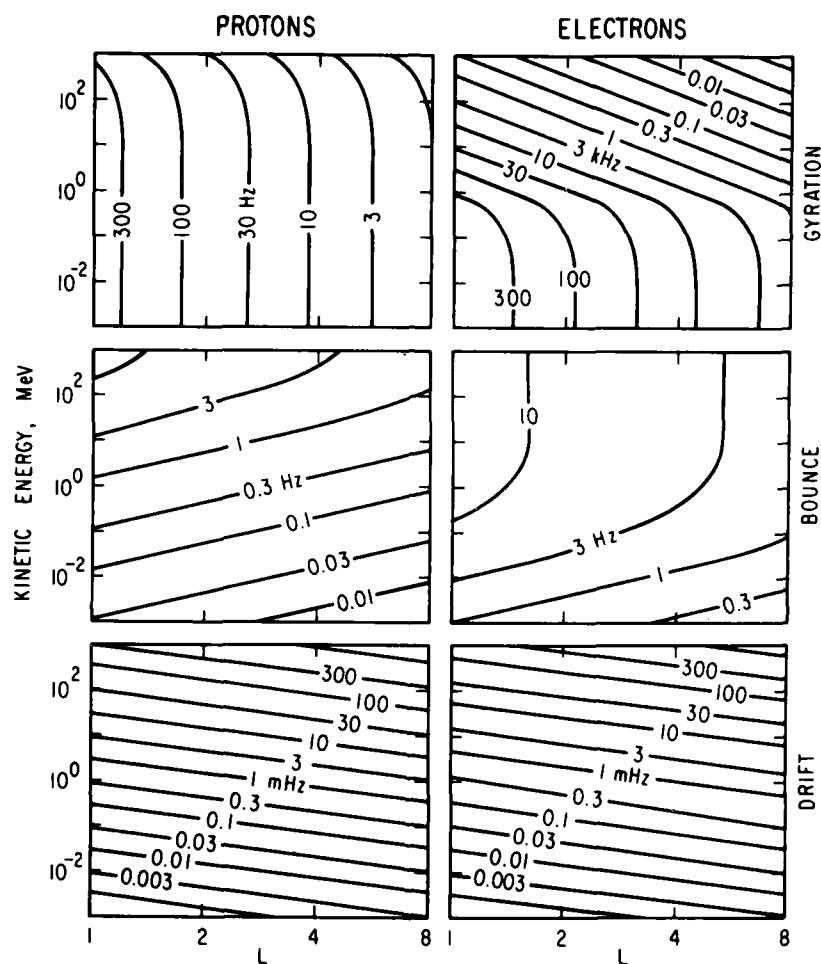


Figure 3. An Overview of the Three Types of Periodic Motion: Gyration Around the Magnetic Lines of Force, Bounce Motion Between the Magnetic Mirror Points and Drift Motion Around the Earth. Values are given for a range of particle kinetic energies for protons and electrons from 10^{-3} MeV (= 1 keV) to 10^3 MeV

vector potential \bar{A} integrated around the closed path, it measures the magnetic flux enclosed by the drift shell and is inversely proportional to the shell parameter, L. For details, see Schulz and Lanzerotti.²

There are certain interesting features of the radiation belts that derive from adiabatic motion alone. The main one is the fact that one must correct for it because detectors are not sensitive to adiabatic invariants but to energies and pitch angles. So one must constantly be aware of the need to transform from what the detector sees to what is kinematically and dynamically significant, namely, the adiabatic invariants, as coordinates. An illustration of this fact, as shown in Figure 4, is the strange pitch angle distribution that one observes particularly in high energies in the outer magnetosphere near midnight, namely that the maximum occurs far away from 90° equatorial pitch angle, whereas at dawn or dusk or on the dayside the maximum occurs for particles mirroring near the equator. This is a consequence of the azimuthal asymmetry of the magnetosphere, which imposes an azimuthal asymmetry on the adiabatic drift shells of charged particles. This imposed asymmetry is the well understood L-shell splitting phenomenon.¹

3. NONADIABATIC EFFECTS

One of the earliest nonadiabatic effects observed was the decay of particle intensities following magnetospheric events such as storms or nuclear detonations. It was found that beyond about $L = 2$, lifetimes could be measured in days to weeks, in contrast with the expectation due to Coulomb collisional effects that would have provided lifetimes of the order of hundreds of years. For electrons, only below $L = 1.25$ can collisional effects totally account for what is seen.^{3,4,5} One must appeal to wave-particle interactions violating the first and second adiabatic invariants of the energetic electrons to account for the anomalously short lifetimes beyond $L = 2$.

What we face in describing the decay of radiation belt electron intensities is a pitch angle diffusion equation which must be formulated in bounce averaged form; that is, one must look at diffusion in terms of violation of the adiabatic invariants

2. Schulz, M., and Lanzerotti, L.J. (1974) Particle Diffusion in the Radiation Belts, Springer Verlag, New York.
3. Walt, M. (1964) The effects of atmospheric collisions on geomagnetically trapped electrons, J. Geophys. Res. 69:3947.
4. Walt, M., and MacDonald, W.M. (1964) The influence of the earth's atmosphere on geomagnetically trapped particles, Reviews of Geophysics and Space Physics 2:543.
5. Wentworth, R.C., MacDonald, W.M., and Singer, S.F. (1959) Lifetimes of trapped radiation belt particles determined by Coulomb scattering, Physics of Fluids 2:499.

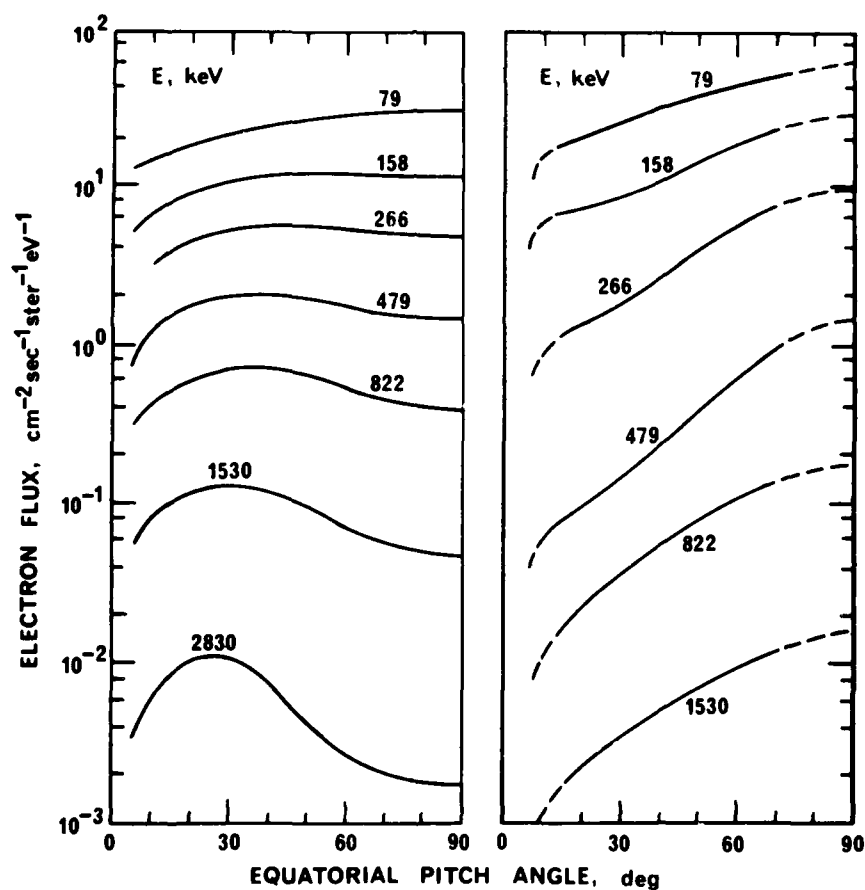


Figure 4. Illustration of the Variation of Energetic (79 keV to 2.83 MeV) Electron Pitch Angle With Geomagnetic Local Time. Left panel shows the pitch angle distributions near local midnight while right panel exemplifies the conditions in the dayside magnetosphere. Notice that the pitch angle distribution peak occurs for off-equatorially mirroring electrons primarily at the higher ($E \geq 250$ keV) energies and is most pronounced in the MeV range

and transform to more convenient quantities such as energy and equatorial pitch angles:

$$\frac{\partial \bar{f}}{\partial t} = \frac{1}{xT(y)} \frac{\partial}{\partial x} \left(xT(y) D_{xx} \frac{\partial \bar{f}}{\partial x} \right) + \bar{S} \quad (1)$$

The coordinates x and y are the sine and cosine of the equatorial pitch angle, f is the phase space density, and S is the particle source. The factor $T(y)$ stems from the Jacobian coordinate transformation matrix. For details see Schulz and Lanzerotti.²

Radial diffusion has not yet been mentioned; that will be added later on. One of the things that a second order differential equation such as Eq. (1) will possess is eigenfunctions; it is relevant in studying charged particle distributions to find the eigenfunctions of the pitch angle diffusion operator. Roberts⁶ showed that for conditions of strong time variability, such as in the early days following a nuclear detonation, that it was appropriate to expand the initial pitch-angle distribution in terms of the first few eigenfunctions. He showed on that basis that one can account for the subsequent evolution of the shape of the pitch angle distribution as the intensity declines owing to pitch angle diffusion into the loss cone. The effect of collisions beyond about $L = 2$ is only to define a loss cone in velocity space so that particles that mirror too far from the equator cannot persist in the radiation belts for more than perhaps a bounce period. The electron lifetimes associated with collisions would be several years at $L = 2$ by this measure; that is not observed. One concludes from that that interactions with waves, instabilities, and plasma turbulence within the magnetosphere are primarily responsible for the loss of particles from the radiation belts, at least for electrons. There is a "zoo" of waves and instabilities in the magnetosphere. There are whistlers, chorus, and emissions from man made radio sources and secondary emissions triggered by them. There is some concern about power line harmonics from electrical utility power lines at the ground and their interaction with radiation belt particles. There are geomagnetic pulsations, which could possibly be interacting with the bounce motions of trapped particles but the role of such low frequency oscillations is far from certain quantitatively. Finally, there is magnetospheric hiss, which will be mentioned later; it is a broad-banded electromagnetic and electrostatic noise that may well be most important of all in terms of the observed pitch angle diffusion.⁷

6. Roberts, C.S. (1969) Pitch angle diffusion of electrons in the magnetosphere, Reviews of Geophysics and Space Physics 7:305.

7. Thorne, R.M., Smith, E.J., Burton, R.K., and Holzer, R.E. (1973) Plasmaspheric hiss, J. Geophys. Res. 78:1581.

Lyons et al⁸ considered particle diffusion in a broad-banded Gaussian wave spectrum representing magnetospheric hiss propagating obliquely to the magnetic field. Both Landau and cyclotron resonances must be averaged over the bounce period to obtain the diffusion coefficient. Thus, pitch angle diffusion in the magnetosphere is non-local from the point of view of one's detector; one is interested not only in waves at the position of the detector, but all along the bounce path of the particle and all around the drift trajectory. For simplicity, Lyons et al⁸ considered the wave energy density to be uniform within the plasmasphere. They tentatively neglected the wave electric field for this purpose; in other words, they considered the scattering to be elastic and looked only for pitch angle diffusion and not for the associated energy loss or gain. They solved for the longest lived eigenfunction of the pitch angle diffusion operator; they found the well-known "bottle neck" (that is, a region of low rate of diffusion in pitch angle space), particularly at low energies, in the diffusion coefficient which translated itself into a shoulder in the lowest eigenfunction, shown in Figure 5. Lyons and Thorne⁹ found eigenvalues corresponding to 1 to 10 days, as shown in Figure 6 which are compatible with observed lifetimes.

4. SATURATION

The lifetime is not itself a constant in time. There is evidence indicating that lifetimes are shorter during storm periods than during the post-storm recovery. This occurs despite the fact that the intensity of the particles builds up during a storm because of enhanced radial diffusion. The rate of pitch angle diffusion into the loss cone appears to be larger during the buildup period and smaller afterwards.

A saturation phenomenon, which is observed in Figure 7 at synchronous altitude is a possible explanation. The term saturation means that the magnetosphere becomes increasingly intolerant of particle fluxes variability as one goes down in energy. The probability of observing an omnidirectional flux $I_{4\pi}$ greater than an arbitrary Q is shown in this figure. There is about a two order of magnitude variability that is tolerated at 2 MeV and less than one order of magnitude at 300 keV; if one extrapolates down to 30 or 40 keV, one sees almost no variation at all. This is evidence that there is something inherent in the magnetosphere that causes radiation belt intensities to be self-limiting. That is the well-known

8. Lyons, L.R., Thorne, R.M., and Kennel, C.F. (1972) Pitch angle diffusion of radiation belt electrons within the plasmasphere, J. Geophys. Res. 77:3455.
9. Lyons, L.R., and Thorne, R.M. (1973) Equilibrium structure of radiation belt electrons, J. Geophys. Res. 78:2142.

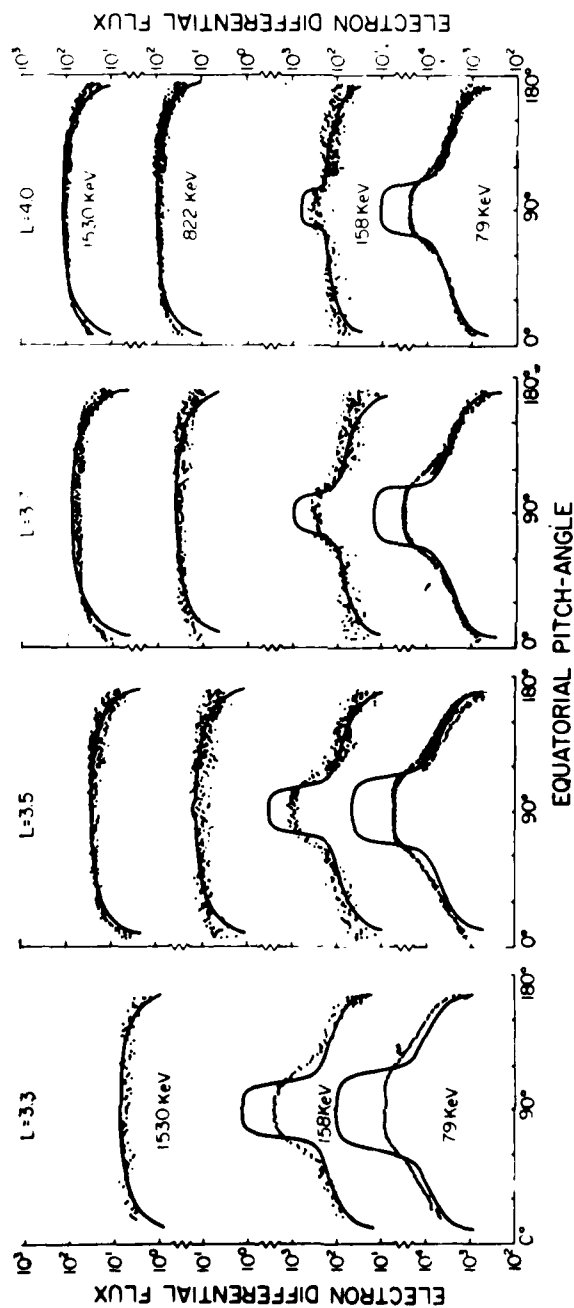


Figure 5. Comparison of Radiation Belt Electron Theoretical Pitch Angle Distributions Calculated From Quasi-linear Whistler Mode Hiss - Energetic Electron Interactions (Solid Lines) and Direct Electron Observations (Dots). The results, which are taken from Lyons et al.⁸ are given for L-shells in the traditional 'slot' - region; here for L-shells $L = 3.3, 3.5, 3.7$ and 4.0 . Notice the characteristic 'bell' shape at the lower energies, primarily below a few hundred keV

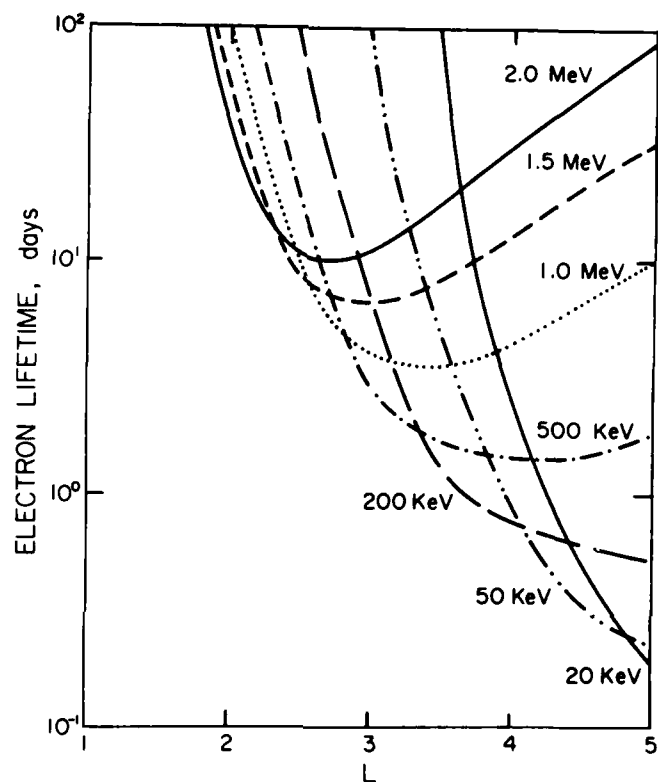


Figure 6. Radiation Belt Electron Precipitation Lifetimes Calculated Based on Quasi-linear Wave-particle Interactions (from Lyons and Thorne⁹). The results are valid only within the plasmasphere; and typical electron lifetimes range from less than one day to hundreds of days, depending on electron energy and location in the radiation belts. Notice that for the higher energies these lifetime profiles for equatorially mirroring electrons exhibit minimum values in the vicinity of $L \sim 3$

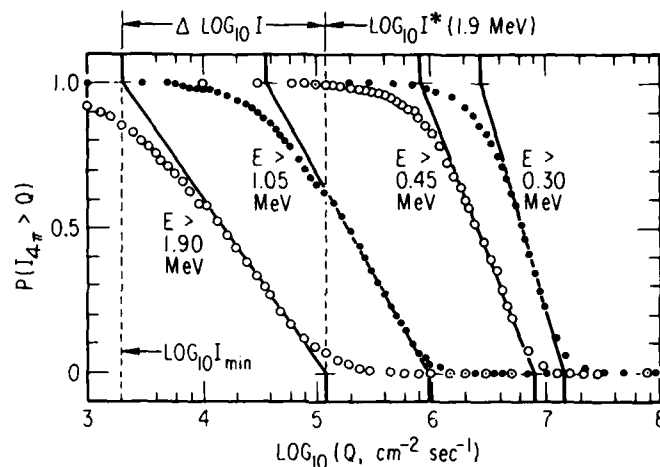


Figure 7. The Probability of Observing Omni-directional Particle Fluxes Above an Arbitrary Value of Q as Function of Q for $E > 1.90, 1.05, 0.45$ and 0.30 MeV Energies

Kennel-Petschek¹⁰ phenomenon whereby the particles, once they get beyond a certain intensity, begin to generate intense waves that scatter the particles into the loss cone.

A simple way of illustrating the saturation phenomenon is by means of prototype equations in which the particle intensity I varies with time through a decay term $-\lambda I$, and λ is proportional to the wave intensity:

$$\frac{dI}{dt} = -\frac{\lambda I}{1 + \lambda \tau} + S \quad (2)$$

$$\frac{1}{\lambda} \frac{d\lambda}{dt} = \frac{2\gamma^*(I/I^*)}{1 + \lambda \tau} + \left| \frac{d\omega}{dk} \right| \frac{\ln R}{La} + \frac{W}{\lambda} \quad (3)$$

$$\gamma^* = (v_g/2La) |\ln R| \quad (4)$$

S is the strength of the particle source and a is the radius of the earth. No matter how intense the waves are, the rate of decay is limited to what is called the strong diffusion lifetime, which is normally a few minutes in the outer radiation belt. This is because the loss cone is only finite in size and the bounce period is likewise finite; so even if the distribution is made completely isotropic by intense

10. Kennel, C. F., and Petschek, H. E. (1966) Limit of stably trapped particle fluxes, J. Geophys. Res. 71:1.

waves, it takes on the average about half a bounce period for an individual particle to reach the atmosphere and thus become unable to complete the bounce motion. Because the loss cone is only a fraction, maybe a hundredth, of the available solid angle, this defines a lifetime of the order of 100 bounce periods for the particle distribution. In model simulations one adopts a source function and models the way the decay rate impacts the particle distribution in terms of a growth rate which is proportional to the intensity of the particles and is proportional in some simple way to the anisotropy of the distribution. That is, one can consider the term $1/(1 + \lambda\tau)$ as a measure of the anisotropy that is inherent in the particle distribution and recognize that for a purely isotropic distribution like a Maxwellian there is no free energy from which to make waves. Likewise, waves do not continue bouncing back and forth indefinitely between the ends of the flux tube. There is only a partial reflection R, whose logarithm enters in this simulation of rate of change of energy within the flux tube. One can, in addition, add a source of waves, W.

These simulated model equations can be solved for a steady state:

$$I = [1 + (WI^*/2\gamma^*S)]^{-1} I^* + \tau S \quad (5)$$

$$= (S/I^*) + (W/2\gamma^*) \quad (6)$$

$$1/(1 + \lambda\tau) \simeq \text{Min}(I^*/I, 1) \text{ for } \tau W/2\gamma^* \ll 1 \quad (7)$$

The result is that the intensity of the particles is given as a function of the source strength of the particles, and the anisotropy of the particles is simulated in terms of intensity. It is found that if the intensity of the particles exceeds the limit I^* , which is known as the Kennel-Petschek limit, then the distribution becomes increasingly isotropic because of the large intensity of waves thereby generated. This can be simulated to obtain the algebraic solutions of the differential equations. These solutions are illustrated in Figure 8. In this figure it is apparent that if there are no waves injected (parasitically) from the outside, that is, if there are only the waves that the particles themselves generated, then the actual particle intensity becomes close to the Kennel-Petschek limit for low source strengths and exceeds the Kennel-Petschek limit only when the source strength is large enough to make the wave intensity grow beyond the level necessary to produce strong diffusion.

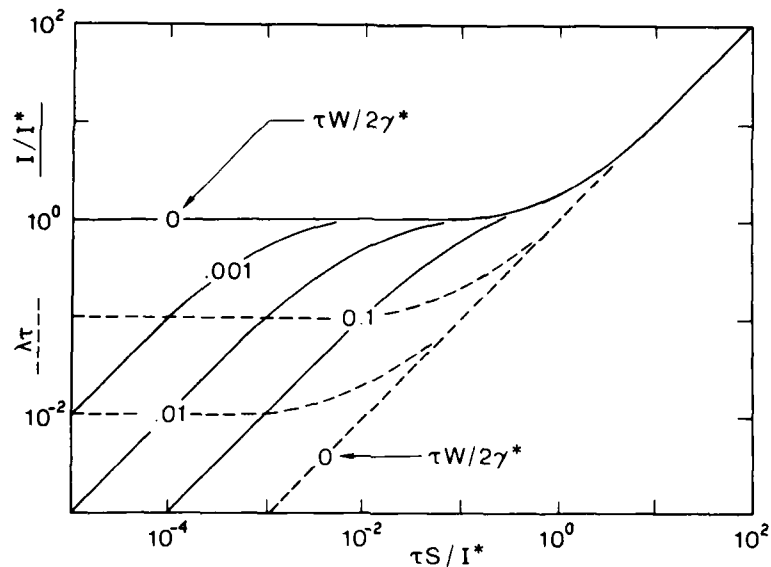


Figure 8. Values of the I/I^* - Ratio and $\lambda\tau$ Versus a Measure for the Particle Source Strength: $\tau S/I^*$; for details, see the text

5. RADIAL DIFFUSION

One of the "gifts" of the nuclear testing program was firm evidence that there was not only pitch angle diffusion in the radiation belts but also radial and energy diffusion. One of the tests injected a very narrow belt which spread in L with time. The broadening was not sufficient to account for the reduction in the peak intensity; about half of the reduction had to be attributed to pitch angle diffusion. So there is evidence that both radial diffusion and pitch angle diffusion are ways of diminishing the intensity of the radiation belts. Normally, radial diffusion causes the radiation belts to be populated naturally through cross- L transport from a source region at some high L -shell.

In fact, what one sees in a storm and its aftermath, viewed as counting rate in a given detector which is bounded as usual by energy and pitch angle, is an inward moving profile, or something that gives that appearance. But energy and pitch angle are not the natural kinematical variables for radiation belt study. What one needs is a presentation in terms of phase space density versus L at fixed first and second adiabatic invariants. When one plots the observations in that manner, as in Figure 9, one sees typically, at least for electrons, a monotonic profile, strong evidence that the particles that we see at L values below 5

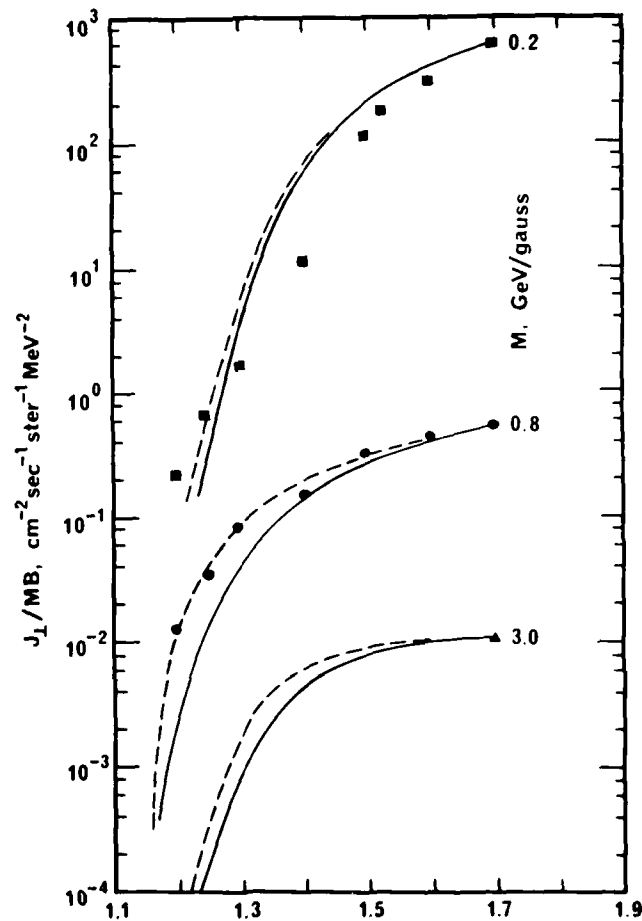


Figure 9. Observed and Computed Values of the Quantity J_l/MB Versus L-shell in the Inner Radiation Zone: J_l is the Flux for Which the Particle Pitch Angle is $\pi/2$, M is the Magnetic Moment in 10^3 MeV/Gauss (with 3 Values Given: 0.2, 0.8 and 3.0) and B is the Magnetic Field Induction

have gotten there by diffusion from larger L values, perhaps from a boundary around $L = 10$.

The canonical form of the radial diffusion operator is given by:

$$\frac{\partial F}{\partial t} = L^2 \frac{\partial}{\partial L} \left(\frac{D}{L^2} \frac{\partial F}{\partial L} \right) - \frac{F}{\tau} \quad (8)$$

Because of the mathematical complexity, we do not try to solve radial diffusion and pitch angle diffusion simultaneously. Instead, we approximate the effects of pitch angle diffusion, energy loss, etc., by means of a simple loss term. The radial diffusion coefficient, D , can arise from various phenomena. It can stem from unsteady solar wind pressure, or an unsteady tail current, resulting in what is called magnetic impulse diffusion. It can also result from unsteady convection such as described theoretically by Richard Wolf and co-workers at Rice University in their storm and substorm models.^{11, 12, 13} The quasi-random unsteadiness in the large-scale geoelectric field can cause electrostatic diffusion. What is to be emphasized here is that there is undoubtedly a time dependence in all of these processes, and hence also in the diffusion coefficient. Presumably, the diffusion coefficient, both the magnetic part and the electric part, will vary in some way with the solar-terrestrial indices.

Lyons and Thorne⁹ have used such an equation to model the formation of the inner electron belt from the outer electron belt. The consideration is that the phase space density, which can be measured as the unidirectional flux divided by the product of the mirror field and the first adiabatic invariant, may well be monotonic when plotted at constant first and second adiabatic invariants. Diffusion may be by both magnetic and electric impulses; the electrostatic impulses may tend to dominate the contributions to the radial diffusion coefficient for first invariants less than 1 keV/Gauss and the magnetic impulses tend to dominate for the higher first invariants, at least for particles mirroring in the immediate vicinity of the equator. Coulomb scattering and energy loss were simulated; wave-particle scattering was simulated through the lowest eigenvalue of the diffusion operator. Lyons and Thorne⁹ solved for the radial profile of particles mirroring at the equator; the result, shown in Figure 10, was a distribution function phase space

11. Harel, M., Wolf, R.A., Reiff, P.H., Spiro, R.W., Burke, W.J., Rich, F.J., and Smiddy, M. (1981) Quantitative simulation of a magnetospheric substorm, 1. Model logic and overview, *J. Geophys. Res.* 86:2217.
12. Harel, M., Wolf, R.A., Spiro, R.W., Reiff, P.H., Chen, C.K., Burke, W.J., Rich, F.J., and Smiddy, M. (1981) Quantitative simulation of a magnetospheric substorm, 2. Comparison with observations, *J. Geophys. Res.* 86:2242.
13. Spiro, R.W., Harel, M., Wolf, R.A., and Reiff, P.H. (1981) Quantitative simulation of a magnetospheric substorm, 3. Plasmaspheric electric fields and evolution of the plasmopause, *J. Geophys. Res.* 86:2261.

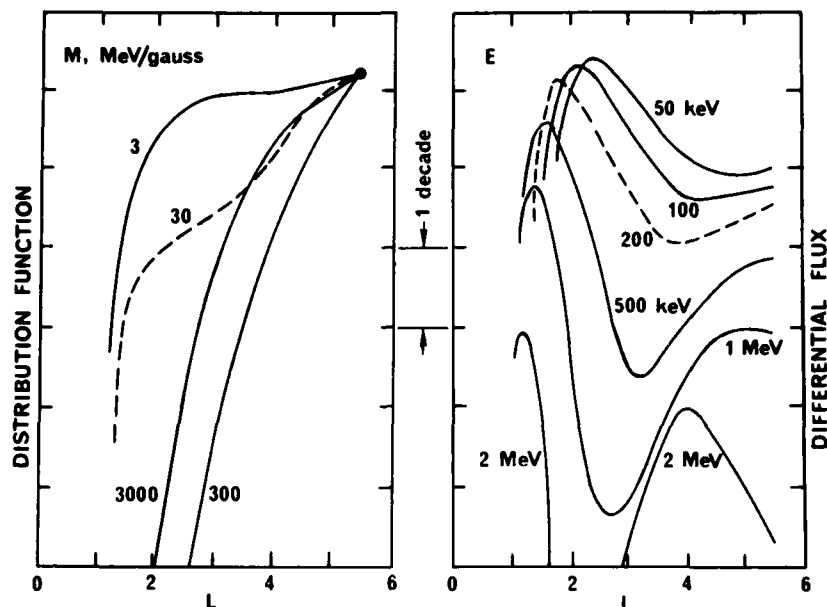


Figure 10. Theoretically Calculated Energetic Electron Distribution Function (Left Panel) for Magnetic Moment Values of 3, 30, 300 and 3000 MeV/Gauss, and Corresponding Values of the Differential Flux. The curves show the L-variation. Notice that while the distribution function is monotonically decreasing with L-shell, the flux profiles show the characteristic 'slot' - structure

density monotonic with L, as one might expect for diffusion from an external source, here placed at $L = 5.5$. But by translating the distribution functions into differential flux at a certain energy, they found the development of two separate zones that a particle detector would see, with an increasingly pronounced slot between the two zones as the energy goes up.

A. Vampola has sponsored a competing interpretation. He emphasizes the fact that during a storm enhanced radial diffusion causes the slot region to fill in, particularly at the lowest energies. Then following a storm, he argues that there is enhanced pitch angle diffusion which causes the slot to form once again and then the pitch angle diffusion coefficient becomes reduced in magnitude so that one goes over into the theory of Lyons and Thorne. This competing theory - it is really complementary - is mentioned because it illustrates the major point of this talk: that over the next decade in interpreting radiation belt phenomena, one must also consider the fact that the transport coefficients and boundary conditions in our diffusion analysis undoubtedly change with time through a dependence on solar-terrestrial conditions.

6. PROTONS (IONS)

Davis and Williamson¹⁴ were the first to notice that the spectral index of an exponential spectrum of their proton observations tended to harden with decreasing L value. Moving, in Figure 11, from L = 6 to L = 2.8, the e-folding energy increases much as the energy of an individual particle would. It is almost as if, in moving from L = 4 to L = 2, all of the particles have their energies multiplied by a factor of eight. It is very probable that that is exactly what happened: the index of an exponential spectrum will transform as the energy of an individual particle. Beyond that, one can even trace from a starting equatorial pitch angle of 90° and find a more efficient energization per unit L than, for example, starting at an equatorial pitch angle of 10°. In other words, the hardening of the spectrum is more efficient the closer the particles are to mirroring at the equator. This is an inherent source of anisotropy for trapped particles. Particles that are energized the most efficiently need not have had as large an energy at the exterior source. So an isotropic distribution at the source will map, just through the energy transformation, into a strongly anisotropic distribution at L = 3 or 4. This is seen not only in protons but also in alpha particles and the other heavy ions that have been looked at.

In the early 1960's Södraas and Davis¹⁵ were the first to recognize the importance of plotting phase space density at first and second invariants for the analysis of where the radiation belts have come from. For protons, they found that in large measure there was a source of particles outside the magnetosphere which populated the interior by radial diffusion. But the distribution profiles turned out to be non-monotonic. There are two possible explanations. There may have been an interior source, to be mentioned later. There may also have been a change in the boundary conditions; temporal changes in the boundary conditions could quite possibly lead to a peak inside the trapping region rather than at the boundary. This is likewise something that will have to be kept in mind in future analyses. Not only the transport coefficients may vary with time or with solar-terrestrial conditions, but also the boundary conditions may change according to the number of particles impinging on the magnetosphere from the outside or being injected into the trapping region from the ionosphere, perhaps prior to being processed in the plasma sheet.

Certain additional considerations enter for inner zone protons. These are the very high energy, perhaps 10 to 100 MeV, particles that reside on L-shells below

14. Davis, L. R., and Williamson, J. M. (1963) Low energy trapped protons, Space Science 3:365.
15. Södraas, F., and Davis, L. R. (1968) Temporal Variations of the 100 keV to 1700 keV Trapped Protons Observed on Satellite Explorer 26 During the First Half of 1965, Report X-612-68-328, NASA/Goddard Space Flight Center, MD.

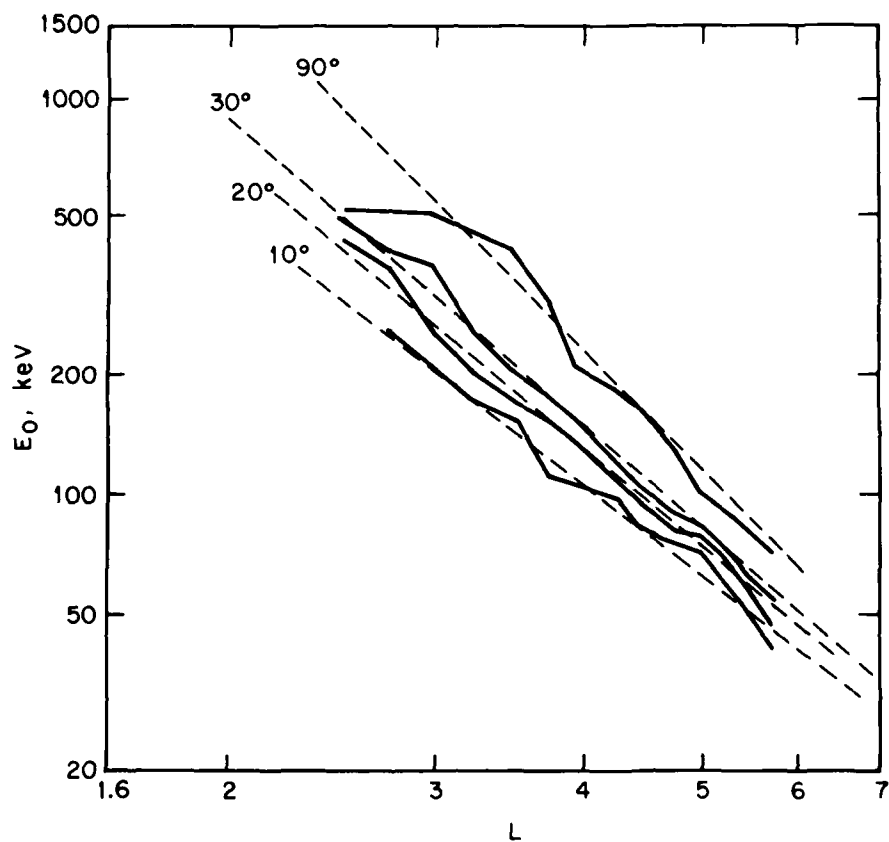


Figure 11. Dependence of the Spectral Index E_0 in the Exponential Spectrum From $J = J_0 (\exp -E/E_0)$ vs L-shell. The dashed lines indicate theoretical expectations based on conservation of the first and second adiabatic invariants and the solid lines show actual data for energetic radiation belt ions (usually labeled protons)

$L = 2$. We consider radial diffusion and Coulomb loss, which acts as a frictional drag as energetic particles cause ionization when encountering the ambient atmosphere. For higher energy particles, one must also consider nuclear collisions. One must also consider the Cosmic Ray Albedo Neutron Decay (CRAND) source, the decay of neutrons that have been ejected from the atmosphere by incident cosmic rays. Because of the long lifetimes of the trapped particles at these high energies, one must consider the fact that the earth's magnetic moment is not constant in time. The electric field induced by the secular decrease of the earth's magnetic moment creates an inward convection of particles; it also energizes them and this makes a minor but nevertheless significant difference in the predicted intensities of inner belt protons. Without radial diffusion, one can conduct an analysis just balancing off the CRAND source^{16, 17} against Coulomb loss. And one finds very little agreement between the predictions—the dashed curves in Figure 12—and the observations—the dashed points. However, Farley and Walt¹⁸ showed that by considering radial diffusion, much better agreement was achieved—the solid curves. And in collaboration with M.G. Kivelson¹⁹ they showed that adding the geomagnetic secular variation improved things even more.

We found in a subsequent study of inner zone protons that the spectrum tended to develop a maximum, that is, it was no longer monatomic. In an earlier paper, Blanchard and Hess²⁰ showed exactly the same thing, but their result was not obtained by a steady state analysis but rather by taking account of the variations of the atmospheric density and the CRAND source with time. By integrating over the solar cycle, they found this same feature which we had noted at low altitudes. Since this was done without radial diffusion, this tells us that there is more work to be done in the area, namely, that one must consider looking at the inner proton belt as a time varying phenomenon, at least over the solar cycle, in addition to taking account of the secular contraction of drift shells caused by the diminution of the dipole moment of the earth.

16. Hess, W.N., and Killeen, J. (1966) Spatial distribution of protons from neutron decay trapped by the geomagnetic field, J. Geophys. Res. 71:2799.
17. Chupp, E.L., Hess, W.N., and Curry, C. (1967) The neutron flux in space after the November 15, 1960 polar cap neutron events, J. Geophys. Res. 72:3809.
18. Farley, T.A., and Walt, M. (1971) Source and loss processes of protons of the inner radiation belt, J. Geophys. Res. 76:8223.
19. Farley, T.A., Kivelson, M.G., and Walt, M. (1972) Effects of the secular magnetic variation on the distribution function of inner zone protons, J. Geophys. Res. 77:6087.
20. Blanchard, R.C., and Hess, W.N. (1964) Solar cycle changes in the inner-zone protons, J. Geophys. Res. 69:3927.

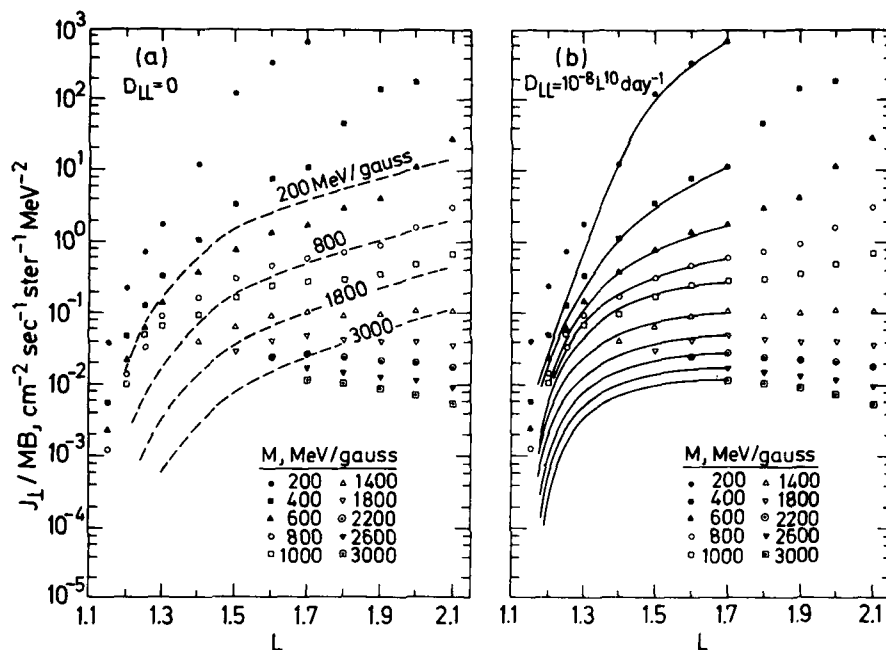


Figure 12. Comparison of Expected Ion (Proton) Radial Profiles Assuming a Coulomb Collision Energy degradation Process Only (Left Panel) and a Combination of Coulomb Collisions and Radial Diffusion (Right Panel; from Farley and Walt¹⁸). Notice the vast improvement in the comparison of the theory with data when the radial diffusion process is included. Further detailed improvement was achieved when secular B-field variations were included

To conclude, it is to be emphasized that we have achieved over the past 20 years a good understanding of steady state radiation belt dynamics. In the future, what we must try to understand are the unsteady aspects, namely, how do the boundary conditions and transport coefficients vary with solar-terrestrial indices?

References

1. Roederer, J.G. (1970) Dynamics of Geomagnetically Trapped Radiation, Springer Verlag, New York.
2. Schulz, M., and Lanzerotti, L.J. (1974) Particle Diffusion in the Radiation Belts, Springer Verlag, New York.
3. Walt, M. (1964) The effects of atmospheric collisions on geomagnetically trapped electrons, J. Geophys. Res. 69:3947.

4. Walt, M., and MacDonald, W.M. (1964) The influence of the earth's atmosphere on geomagnetically trapped particles, Reviews of Geophysics and Space Physics 2:543.
5. Wentworth, R.C., MacDonald, W.M. and Singer, S.F. (1959) Lifetimes of trapped radiation belt particles determined by Coulomb scattering, Physics of Fluids 2:499.
6. Roberts, C.S. (1969) Pitch angle diffusion of electrons in the magnetosphere, Reviews of Geophysics and Space Physics 7:305.
7. Thorne, R.M., Smith, E.J., Burton, R.K., and Holzer, R.E. (1973) Plasmaspheric hiss, J. Geophys. Res. 78:1581.
8. Lyons, L.R., Thorne, R.M., and Kennel, C.F. (1972) Pitch angle diffusion of radiation belt electrons within the plasmasphere, J. Geophys. Res. 77:3455.
9. Lyons, L.R., and Thorne, R.M. (1973) Equilibrium structure of radiation belt electrons, J. Geophys. Res. 78:2142.
10. Kennel, C.F., and Petschek, H.E. (1966) Limit of stably trapped particle fluxes, J. Geophys. Res. 71:1.
11. Harel, M., Wolf, R.A., Reiff, P.H., Spiro, R.W., Burke, W.J., Rich, F.J., and Smiddy, M. (1981) Quantitative simulation of a magnetospheric substorm, 1. Model logic and overview, J. Geophys. Res. 86:2217.
12. Harel, M., Wolf, R.A., Spiro, R.W., Reiff, P.H., Chen, C.K., Burke, W.J., Rich, F.J., and Smiddy, M. (1981) Quantitative simulation of a magnetospheric substorm, 2. Comparison with observations, J. Geophys. Res. 86:2242.
13. Spiro, R.W., Harel, M., Wolf, R.A., and Reiff, P.H. (1981) Quantitative simulation of a magnetospheric substorm, 3. Plasmaspheric electric fields and evolution of the plasmopause, J. Geophys. Res. 86:2261.
14. Davis, L.R., and Williamson, J.M. (1963) Low energy trapped protons, Space Science 3:365.
15. Söraas, F., and Davis, L.R. (1968) Temporal Variations of the 100 keV to 1700 keV Trapped Protons Observed on Satellite Explorer 26 during the First Half of 1965, Report X-612-68-328, NASA/Goddard Space Flight Center, Maryland.
16. Hess, W.N., and Killeen, J. (1966) Spatial distribution of protons from neutron decay trapped by the geomagnetic field, J. Geophys. Res. 71:2799.
17. Chupp, E.L., Hess, W.N., and Curry, C. (1967) The neutron flux in space after the November 15, 1960 polar cap neutron events, J. Geophys. Res. 72:3809.
18. Farley, T.A., and Walt, M. (1971) Source and loss processes of protons of the inner radiation belt, J. Geophys. Res. 76:8223.
19. Farley, T.A., Kivelson, M.G., and Walt, M. (1972) Effects of the secular magnetic variation on the distribution function of inner zone protons, J. Geophys. Res. 77:6087.
20. Blanchard, R.C., and Hess, W.N. (1964) Solar cycle changes in the inner-zone protons, J. Geophys. Res. 69:3927.

Contents

1. Introduction	69
2. Theory	76
3. Observation	81
4. Simulations	84
5. Discussion	94
6. References	96

3. The Role of Waves and Cold Plasma in the Dynamics of the Earth's Radiation Belts

by

Delia E. Donatelli
Physics Dept. Boston College
Chestnut Hill, Mass. 02167

based on a tutorial lecture given by

Maha Ashour-Abdalla*
University of California
Los Angeles, California 90024

1. INTRODUCTION

Modern spacecraft detectors are capable of measuring virtually the whole range of plasma waves of interest to theory, from well below the ion cyclotron frequency to above the electron plasma frequency, both electromagnetic and electrostatic. They are sensitive enough to detect thermal fluctuations in many regions of space. Three-dimensional ion and electron velocity distributions can be measured, with a resolution rarely matched in the laboratory, at the same time as the plasma wave spectra. Such exquisite diagnosis disturbs space plasma much less than laboratory plasmas. Of course, space plasma physicists pay a price for

*Much of this talk was based on "Electrostatic waves and the strong diffusion of magnetospheric electrons" by C. F. Kennell and M. Ashour-Abdalla in Magnetospheric Plasma Physics ed. by A. Nishida, Center for Academic Publications, Tokyo, 1981.

these advantages. It is difficult to measure wavelengths. The magnetosphere's global structure, hard to deduce from a few point measurements, is always changing uncontrollably. But even the price contains a hidden benefit, for this variability creates a rich plasma wave phenomenology.

Figure 1, a theoretician's cartoon of the magnetosphere, lists some plasma waves discussed in the magnetospheric literature and indicates where they occur. It is an extraordinarily diverse list. The plasma waves range in scale from the strong hydrodynamic turbulence in the magnetosheath, with wavelengths a good fraction of an earth radius, to the Debye length scale cavitons that perhaps form on auroral arc field lines and in the solar wind. Some instabilities, such as those associated with reconnection at the magnetopause and in the geomagnetic tail, may regulate the magnetosphere's time-dependent behavior. Others are associated with the energetic electron beams responsible for auroral arcs, and may also populate the magnetosphere with ionospheric ions. Still others regulate the heat flux escaping upstream from the earth's bow shock along magnetic field lines.

Virtually all the waves and instabilities in the plasma literature, except those dependent upon machine geometry, can be found in magnetospheric research. In this report attention is focused on pitch angle scattering by plasma waves, the oldest microscopic turbulence problem in plasma physics. The first experiments in laboratory mirror devices and observations in the earth's radiation belts took place at about the same time. Remarkably similar explanations for the anomalous losses of their ostensibly trapped particles emerged almost simultaneously in the mid-sixties.^{1,2}

Figure 2 illustrates the most important difference between laboratory mirrors and the geomagnetic mirror. Laboratory devices have a small mirror ratio M , the ratio of maximum to minimum magnetic field on a flux tube, whereas the geomagnetic mirror ratio is huge. M is about 2 for laboratory machines, and $2L^3$ for the geomagnetic dipole field, where L is the geocentric distance in units of earth radii at which the field line crosses the geomagnetic equator. Particles are lost if they penetrate to the maximum magnetic field point, which is at the end plates in the laboratory and in the atmosphere at the earth.

In the absence of fluctuations near their cyclotron frequencies, particles conserve their energy E and their magnetic moment μ ($= mv_{\perp}^2/2B$). In terms of the local pitch angle α , $\mu = E \sin^2 \alpha / B$. Their orbits can be classified by their pitch angle α_0 at the minimum magnetic field point, and by the adiabatic constant of the

1. Rosenbluth, M.N., and Post, R.F. (1965) High-frequency electrostatic plasma instability inherent to "loss-cone" particle distribution, Phys. Fluids 8:547.
2. Kennel, C.F., and Petscheck, H.E. (1966) Limit on stably trapped particle fluxes, J. Geophys. Res. 71:1.

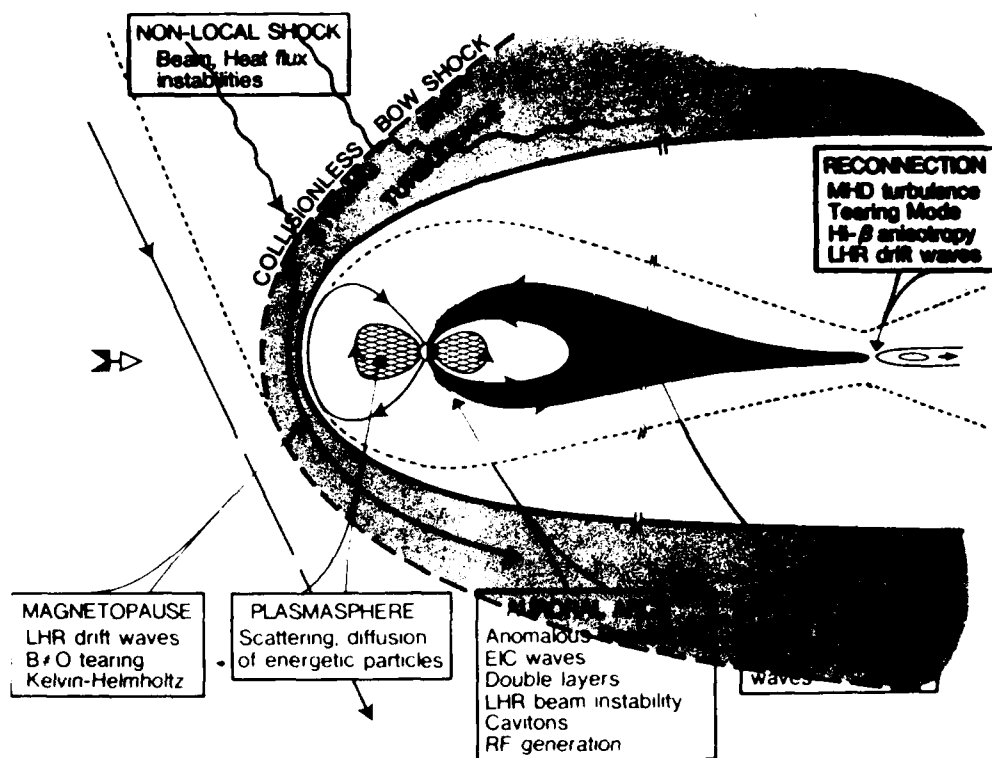


Figure 1. Theoretician's Magnetosphere: A Schematic of the Earth's Magnetosphere. The view is of a magnetic meridian plane from the local geomagnetic dusk direction. The solar wind streams from the left; its interaction with the geomagnetic field creates a standing collisionless fast shock. The magnetopause (dark line) separates shocked solar wind in the plasma sheet from magnetosphere. The transport of momentum and energy across the magnetopause sets magnetospheric plasma and field lines in motion. The boxes list various plasma instabilities and the arrows indicate where they are thought to occur

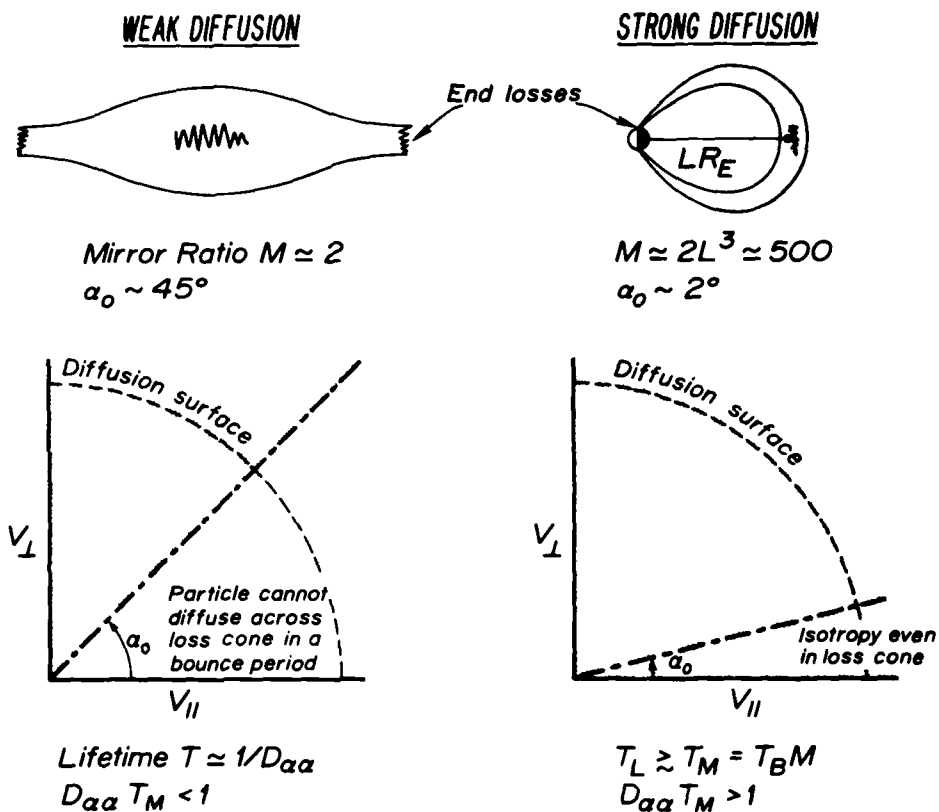


Figure 2. Weak and Strong Velocity Space Diffusion: At the Top Left and Right, Respectively, are Schematics of a Typical Laboratory Mirror and the Geomagnetic Mirror. They have very different mirror relations M . When waves (indicated by wavy lines) are present, this leads to significant differences in how the plasma diffuses in velocity space. The bottom left and right contain schematics of a (v_\perp, v_\parallel) space, where v_\perp and v_\parallel are the particle velocities perpendicular and parallel to the magnetic field respectively. The loss cone, large in the laboratory and small in space, is indicated by the dot-dash line. Typical diffusion surfaces, assuming for simplicity that particles scatter only in pitch angle, are shown by dashed lines

motion μ . Trapped particles, which satisfy $\sin \alpha_0 > M^{-1/2}$ mirror before reaching the end plates or atmosphere. Particles with $\sin \alpha_0 < M^{-1/2}$ are lost. $\alpha_0 = \sin^{-1}(M^{-1/2})$ defines the opening angle of the loss cone in velocity space.

α_0 is about 45° in laboratory devices, and about 3° at $L = 6$ in the geomagnetic field. This leads to crucial differences in behavior when plasma turbulence that diffuses particles in pitch angle is present. Suppose the pitch angle diffusion coefficient is $D_{\alpha\alpha}$. Particles in mirror machines would diffuse to the loss cone and be lost on the next bounce. Their "precipitation" lifetime would be $D_{\alpha\alpha}^{-1}$, and the loss cone would be virtually empty. On the other hand, even a modest $D_{\alpha\alpha}$ can diffuse particles into, and back out of, the small geomagnetic loss cone in a quarter bounce time T_B , the time it takes them to reach the atmosphere. In this limit, the pitch angle distribution, even within the loss cone, is nearly isotropic. The distribution function becomes independent of position along the field line at all energies where the pitch angle distribution is kept isotropic. The trapping lifetime T_L approaches a lower limit $T_M = T_B M$. Space physicists have therefore introduced a distinction between the weak ($D_{\alpha\alpha} T_M < 1$) and strong ($D_{\alpha\alpha} T_M > 1$) pitch angle diffusion.^{2,3}

Figure 3 demonstrates the occurrence of strong diffusion on auroral field lines.⁴ DMSP-32 is a low-altitude polar-orbiting spacecraft, and ATS-6 a geostationary orbiter ($L = 6.6$) in the geomagnetic equatorial plane. Detailed magnetic field models determine when DMSP-32 and ATS-6 are on the same field line. Figure 3 shows simultaneously measured energy distribution functions for precipitating electrons at DMSP-32 and those with $-18^\circ < \alpha_0 < +16^\circ$ at ATS-6. The two are virtually identical between 200 eV and 10 keV. The factor of 2 difference between them may stem in part from the fact that the two detectors were not intercalibrated before launch. Meng et al.⁴ even used particle data to detect inaccuracies in the magnetic field model. The most nearly identical particle distributions were encountered about one degree equatorward of the calculated geomagnetic latitude of the ATS-6 field line.

Strong pitch angle diffusion is a subtle plasma physical problem. The empty mirror-machine loss cone is clearly a free energy source for instability. By contrast, the free energy sources of space plasmas in strong diffusion are not obvious and may be difficult to resolve experimentally. That there is little structure in the energy as well as the pitch angle distribution only compounds the problem of understanding events such as that of Figure 3. Yet there the electrons between

3. Kennel, C.F. (1969) Consequences of a magnetospheric plasma, Revs. Geophys. 7:379.

4. Meng, C.I., Mauk, B., and McIlwain, C.E. (1979) Electron precipitation of evening diffuse aurora and its conjugate electron fluxes near the magnetospheric equator, J. Geophys. Res. 84:2545.

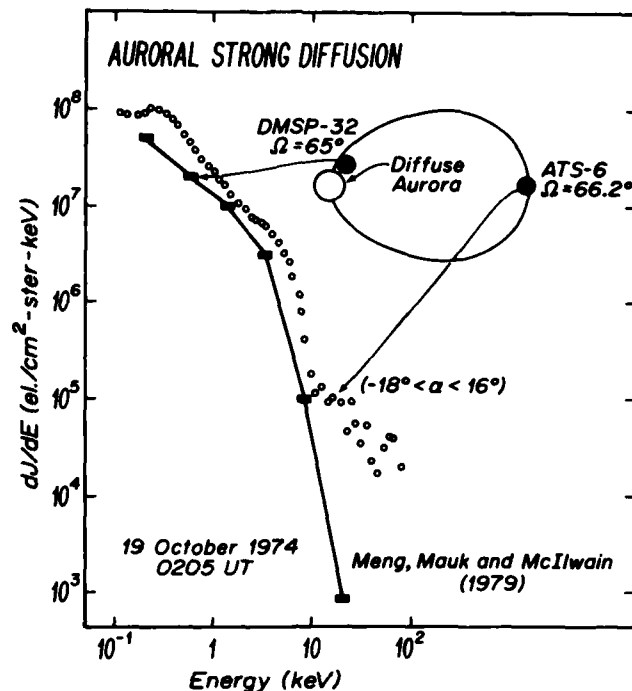


Figure 3. Auroral Strong Diffusion: This Figure Has Been Adapted from Ref. 4. The distribution functions were measured near the geomagnetic equator by ATS-6 (open dots) and near the atmosphere on the same flux tube by DMSP-32 (solid line). The two differ by no more than a factor of 2 between 100 eV and 10 keV energy. Thus the pitch angle distributions are maintained nearly isotropic in this energy range

200 eV and 10 keV were precipitating near their maximum possible rates. Evidently, the waves responsible for their pitch angle scattering must have been destabilized by small features in their distribution function.

Since magnetospheric particle precipitation is often quasi-steady, a complete understanding demands specification of particle sources as well as sinks. Although in situ acceleration of particles to high energies is often invoked, the greatest successes thus far have come from saying that the particles precipitated at one place come from somewhere else. We will therefore be concerned with the coupling of spatial transport to mirror losses.

Figure 4 sketches the two problems of coupled spatial transport and pitch angle diffusion that we will review. Auroral substorms and magnetic storms inject energetic (> 40 keV) electrons into the inner magnetosphere. Following

COUPLING OF CROSS-FIELD TRANSPORT TO MIRROR LOSSES

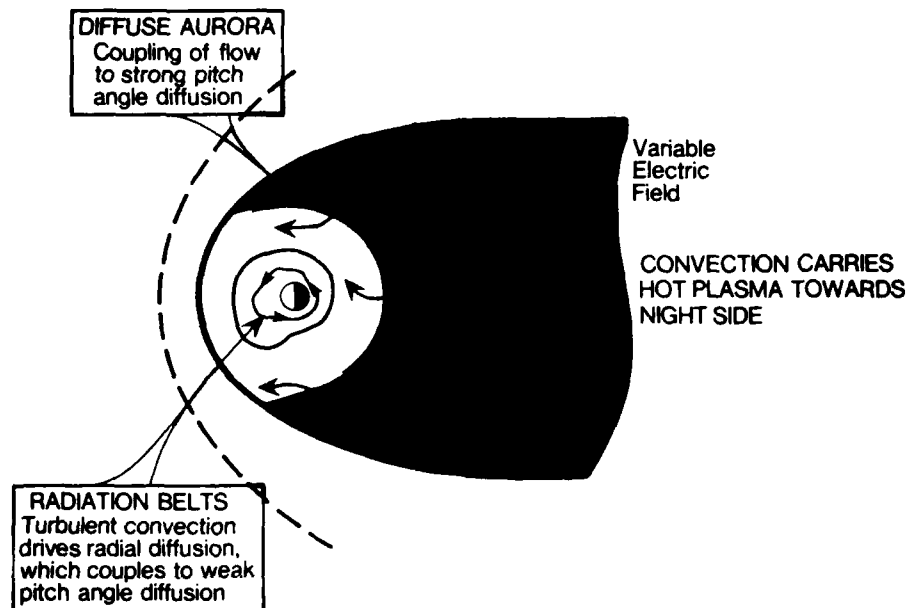


Figure 4. Coupling of Radial Transport to Mirror Losses: Shown Here is a Cut of the Magnetosphere in the Equatorial Plane Looking Down from the North. The dashed line symbolizes the time-variable convection electric field imposed upon the magnetosphere by its dissipative interaction with the solar wind

injection, they are diffused across the plasmopause by fluctuations in the geomagnetic convection electric field. Once inside the plasmasphere, they interact with a steady band of ELF whistler mode hiss which puts them in weak pitch angle diffusion. Radial and pitch angle diffusion combine to produce the quasi-steady structure of the decaying electron radiation belts.⁵ Our second problem involves thermal (1-10 keV) plasma sheet electrons that convect from the geomagnetic tail towards the night-side under the action of the steady component of the convection electric field. When they reach auroral field lines ($L = 6-10$) they are lost to the atmosphere by strong pitch angle scattering. Their precipitation creates the diffuse aurora.

5. Coroniti, F.V., and Thorne, R.M. (1973) Magnetospheric electrons, Ann. Rev. of Earth and Planetary Sci. 1:107.

2. THEORY

Our understanding of radial diffusion and weak pitch angle scattering by ELF whistler hiss of energetic electrons within the plasmasphere sets a standard for our future comprehension of the strong pitch angle diffusion of plasma sheet diffuse auroral electrons by electrostatic cyclotron waves. The morphology of the diffuse aurora has been understood for ten years in terms of the balance between convection of plasma sheet electrons into the inner magnetosphere and precipitation governed by the minimum lifetime. Our present, more subtle difficulties relate to how convection maintains free energy for wave growth in the presence of strong diffusion; which electron cyclotron waves are unstable; whether and how they propagate and, consequently what their spatial distribution is; how they saturate nonlinearly; and (surprisingly) what role cold electrons of ionospheric origin play in these processes.

An important methodological difference between theoretical laboratory and space plasma physics is that in the laboratory, one studies the time evolution to nonlinear saturation of an instability, whereas in space one must address the delicate balances between sources and sinks of particles and waves that maintain the observed steady turbulent state.

It is of interest to study the waves responsible for the pitch angle diffusion of energetic electrons. The cold plasma dispersion relation for right hand (RH) circularly polarized whistler waves propagating parallel to a uniform magnetic field is

$$\frac{\omega^2}{k^2} = C_a^2 \frac{\omega}{\Omega} \left[1 - \frac{\omega}{\Omega} \right] \quad (1)$$

where ω is the wave frequency, k the wave number, Ω the electron cyclotron frequency $\frac{eB}{m_e}$, and C_a the Alfvén speed based upon the electron mass m :

$$C_a^2 = B^2 / 4\pi N m \quad (2)$$

where N is the electron number density.

A resonant particle sees a constant whistler electric field when its parallel velocity Doppler-shifts the frequency to its cyclotron frequency. The condition for resonance, $v_{\parallel} = v_R = \frac{\omega - \Omega}{k_{\parallel}}$, combined with the dispersion relation, defines the resonant energy E_R

$$E_R = 1/2 m v_R^2 = \frac{B^2}{8\pi N} \frac{\omega}{\Omega} \left(1 - \frac{\omega}{\Omega}\right)^2 \quad (3)$$

which is the minimum total energy for resonance, since resonant electrons can have arbitrary perpendicular energy. E_R is seen to be dependent on the thermal plasma number density N .

The parallel whistler mode growth rate γ is

$$\gamma = \pi \Omega \left(1 - \frac{\omega}{\Omega}\right)^3 \eta(v_R) \left[\bar{A}(v_R) - \frac{1}{\frac{\omega}{\Omega} - 1} \right] \quad (4)$$

where \bar{A} , the anisotropy,

$$\bar{A}(v_R) = \frac{\int_0^\infty \frac{v_\perp^2}{v_\parallel} dv_\perp \left[v_\parallel \frac{\partial F_H}{\partial v_\perp} - v_\perp \frac{\partial F_H}{\partial v_\parallel} \right]}{2 \int_0^\infty v_\perp dv_\perp F_H} \bigg|_{v_\parallel = v_R} \quad (5)$$

reduces to $\bar{A} = (T_\perp - T_\parallel)/T_\parallel$, when the hot electron distribution function F_H is an anisotropic bi-Maxwellian. \bar{A} must be positive for instability. $\eta(v_R)$, measures the number of electrons near cyclotron resonance, and is defined by

$$\eta(v_R) = 2\pi |v_R| \int_0^\infty v_\perp dv_\perp |F_H| \bigg|_{v_\parallel = v_R} \quad (6)$$

which should increase with increasing ω/Ω , since E_R decreases. γ consequently increases with increasing ω/Ω , maximizes, and drops to zero at $\omega/\Omega = \bar{A}/(1+\bar{A})$. Thus, unstable whistlers resonate with electrons whose parallel energy exceeds $B^2/8\pi N\bar{A}(1+\bar{A})$. These are ordinarily in the tail of the energy distribution, unless the ratio of the electron pressure to magnetic pressure β is of order unity. Therefore, hot electrons determine the growth rate without affecting the whistler phase and group velocities, which depend upon the cold electron density.

E_R is lowest in the equatorial plane, because it depends strongly on B . Since the observed electron fluxes decrease with increasing energy, the most resonant electrons, and therefore the largest local whistler growth rate, will be at the equator. The equatorial cold electron density therefore determines which electrons

resonate with whistlers. Electrons with energies of a few tens of thousands of electron-Volts only resonate with whistlers just inside the plasmopause and possibly in the diffuse auroral region beyond $L = 6$. Between the plasmopause and $L = 6$, and well within the plasmasphere, $B^2/8\pi N$ is too large for resonance.

If $\gamma l/V_G > 10$, where l is an amplification scale length and V_G is the group velocity, the whistler amplitude will e-fold 10 times as the wave passes through the geomagnetic equator, a rough criterion for the onset of significant quasi-linear diffusion. Because the whistler wave magnetic field exceeds its electric field, resonant electrons diffuse in pitch angle with little change in energy. Kennel and Engelmann⁶ have shown the quasi-linear energy diffusion is much slower than pitch angle diffusion when $\frac{\omega}{\Omega} \ll 1$. Since pitch angle diffusion leads to mirror losses, whistler instability places an upper limit on the energetic electron fluxes that can be stably trapped. Kennel and Petschek² showed that the observed fluxes of electrons with a few tens of thousands of electron-Volts energy rarely exceed the limit computed using these dimensional arguments.

Pitch angle diffusion and consequent loss of the more energetic electrons within the plasmasphere do not conform to the above picture. Except near the plasmopause, $B^2/8\pi N$ and the corresponding resonant energies are so large that the observed electron fluxes are below the stably trapped limit. Only a more detailed analysis can explain the losses of plasmaspheric electrons. For example, a 500 Hz wave, initially amplified in the equatorial plane near the plasmopause, propagates away more or less along field lines and reflects when its frequency equals the local lower hybrid frequency ω_{LHR} .⁷ If its propagation vector is canted towards the plasmopause, it will move outward; otherwise it will travel towards the earth. Since outward moving waves reflect at the plasmopause, all waves eventually move inward and reach a point where their frequency is less than the equatorial lower hybrid frequency. When $\omega > \omega_{LHR}$ their group velocities are confined to within 20° of the magnetic field direction, but when $\omega < \omega_{LHR}$ they may make any angle to the magnetic field. Similarly, \vec{k} can make a large angle to \vec{B} , when $\omega < \omega_{LHR}$. Since whistlers are confined by reflections at the plasmopause and ionosphere, a locally unstable region can fill the entire plasmopause with obliquely propagating whistlers. The whistler mode ELF hiss observed throughout the plasmasphere fits this picture, because it has nearly constant amplitude and frequency. Its few hundred Hertz frequency is consistent with unstable amplification by 10-100 keV electrons near the plasmopause.

6. Kennel, C. F., and Engelmann, F. (1966) Velocity space diffusion from plasma turbulence in a magnetic field, *Phys. Fluids* 9:2377.

7. Thorne, R. M., and Kennel, C. F. (1967) Quasi-trapped VLF propagation in the outer magnetosphere, *J. Geophys. Res.* 72:357.

In contrast to parallel whistlers, oblique whistlers have many wave particle resonances defined by $k_{\parallel} v_{\parallel} = \omega - n\Omega$, where n is any integer. Higher cyclotron resonances $|n| > 1$ couple to electrons whose parallel energies are of order n^2 larger than for $n = 1$ resonance. These interactions scatter electrons in pitch angle. The $n = 0$ Landau resonant electrons have low parallel energies, of order $(\omega/\Omega) \frac{B^2}{8\pi N}$. Landau interactions scatter particles in v_{\parallel} . Because $B^2/8\pi N$ increases away from the equator, high energy electrons have an $n = 1$ resonance at high geomagnetic latitudes, $n = 2$ at intermediate, and high order resonances at the equator. Moreover, the electrons all pass through $n = 0$ Landau resonance near their mirror points, where their pitch angles are near 90° , so that this interaction amounts to pitch angle scattering as well.

Detailed computations of the pitch angle diffusion coefficient bounce-average the contributions of all wave-particle resonances near and far from the equator. Lyons et al.^{8,9} modeled the whistler hiss by a Gaussian frequency distribution centered at 600 Hz with a 300 Hz e-folding width and a relatively isotropic distribution of wave energy in k -space. This spectrum was independent of geomagnetic latitude and L -shell. The overall diffusion coefficient sums these contributions. A notable feature is a "hole" in the summed diffusion coefficients between the cyclotron and Landau regions for lower energy electrons.

The pitch angle diffusion coefficients can be incorporated into the quasilinear diffusion equation to solve for the electron pitch angle distribution and the precipitation lifetime. A comparison between theoretical pitch angle distributions and those measured on OGO-5 by West et al.¹⁰ is shown in Figure 5. The low energy flux enhancements observed near 90° result from the slow diffusion predicted in the region between strong cyclotron and Landau interactions. At higher energies, no 90° enhancements are expected and none are observed. The calculated lifetimes are in rough accord with observation.

The precipitation lifetime can be inserted into the radial diffusion equation to solve for the radial profile of plasmaspheric electrons as a function of energy. Theory and observation¹¹ are compared in Figure 6. Despite the simplifications made in computing the radial profile, the agreement is excellent. In particular,

8. Lyons, L.R., Thorne, R.M., and Kennel, C.F. (1971) Electron pitch angle diffusion driven by oblique whistler mode turbulence, J. Plasma Phys. 6:589.
9. Lyons, L.R., Thorne, R.M., and Kennel, C.F. (1972) Pitch angle diffusion of radiation belt electrons within the plasmasphere, J. Geophys. Res. 77:3455.
10. West, H.I., Jr., Buck, R.M., and Walton, J.R. (1972) Electron pitch angle distributions throughout the magnetosphere as observed on OGO-5, J. Geophys. Res. 78:1064.
11. Lyons, L.R., and Thorne, R.M. (1973) Equilibrium structure of radiation belt electrons, J. Geophys. Res. 78:2142.

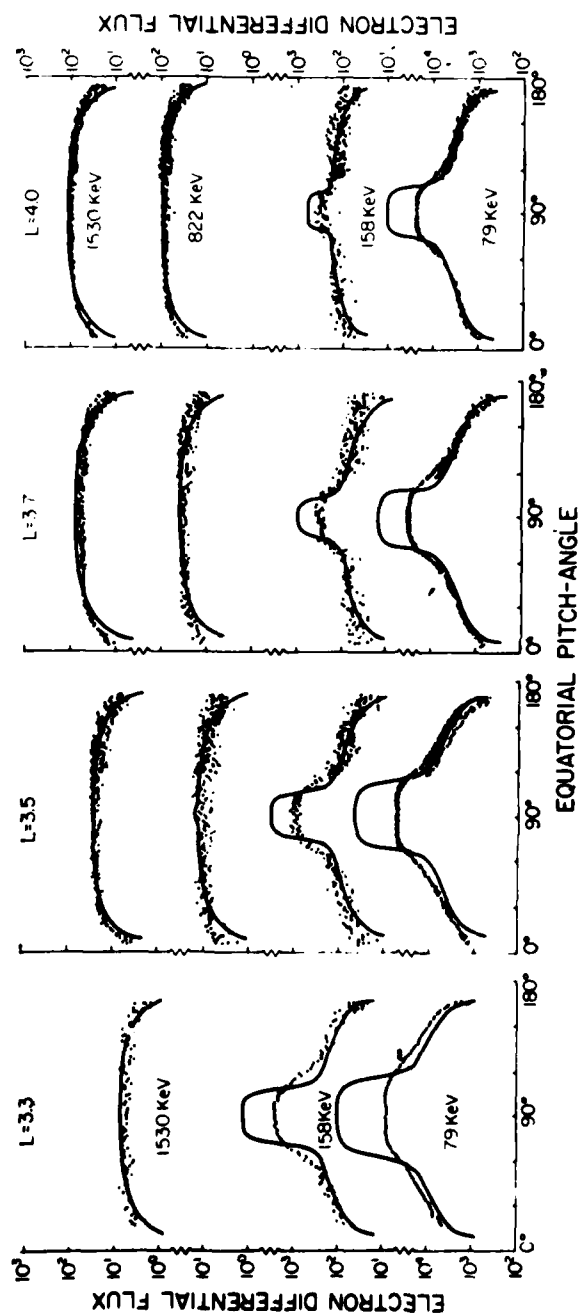


Figure 5. Theoretical and Experimental Pitch Angle Distributions: The Pitch Angle Diffusion Equation can be Solved for the Steady State Pitch Angle Distribution. Theoretical calculations (solid line) are compared with experimental results (dots) for several electron energies at several L-shells⁹

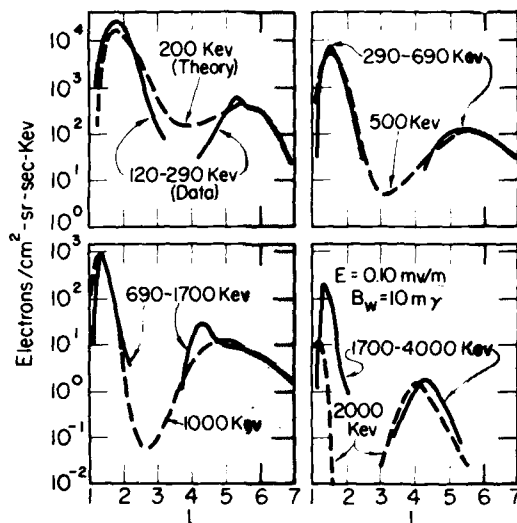


Figure 6. Equilibrium Energetic Electron Radial Profiles Within the Plasmasphere: Given the Precipitation Lifetimes Due to Whistler Mode Induced Energetic Electron Scattering, Calculated Using the Result of Ref. 9 at Large L and Classical Coulomb Scattering at Small L, the Radial Diffusion Equation was Solved for the Radial Profile of Energetic Electron Fluxes for a Given Steady Injection Source At and Beyond the Plasma-pause (Shaded Region)

the high energy electron "slot" near $L = 3$ emerges naturally from the way whistler and Coulomb scattering combine with radial diffusion. No further plasma physics is needed to understand it.

3. OBSERVATION

The spatial morphology of terrestrial electrostatic emissions can be interpreted in terms of what is generally known about the distribution of hot and cold electron densities in the magnetosphere. For example, both theory and observation agree that electrostatic cyclotron harmonic waves should not survive well within the plasmasphere. Moreover, intense upper hybrid emissions occur near but beyond the plasmapause because they require $n_c \gg n_H$. Since the density of cold electrons of ionospheric origin is larger on the dayside than on the nightside, multiharmonic emissions, which require the cold upper hybrid frequency to exceed

twice the cyclotron frequency, ought to be more frequent on the dayside. Finally, if cold electrons stream outward from the ionosphere with little pitch angle scattering, their density would be proportional to the magnetic field strength; then the ratio of the cold upper hybrid frequency to the local electron cyclotron frequency would decrease away from the geomagnetic equator along a field line, potentially explaining the predominance of $f = f_c$ over $3/2$ emissions at geomagnetic latitudes above 20° .

Figure 7 shows an ISEE-1 Swept-frequency-receiver spectrogram of plasma wave data recorded on the November 5, 1977 inbound pass.^{12, 13} On this day, ISEE-1 penetrated the plasmopause at 1720 UT near local noon at about 20° N geomagnetic latitude. Sporadic bursts of $3/2$ and multiharmonic emissions were observed to occur until 1900 UT, at which time the intensity of electrons with energies exceeding 230 eV measured by the LEPDEA instrument decreased abruptly, and the emissions ceased. A period of sustained $3/2$ activity, with amplitudes of 0.1 - 1 mV/m occurred from 1825-1837 UT. Low intensity diffuse bands were observed between 1900 and 2030 UT. An intense upper hybrid emission dominated the wave activity from 2030 UT until ISEE-1 crossed the plasmopause at 2125 UT. A burst with peak amplitude of 7 mV/m occurred between 2108 and 2118 UT.¹³ A similar upper hybrid event recorded by ISEE-1 on December 9, 1977, has been studied by Kurth et al.¹⁴ Figure 8 shows the three dimensional velocity distribution measured during the upper hybrid emission. A small loss cone feature appears only when the hybrid emission was present; in addition the detector happened to be sampling 90° pitch angles when the waves intensified. The distribution shows a well organized relative maximum near 7.2×10^9 cm/sec, which extends to nearly the full range of pitch angles including the especially important pitch angle near 90° . This relative maximum at large pitch angles necessarily implies a positive slope with respect to v_\perp at slightly lower velocities. A positive slope in the perpendicular velocity distribution provides a free energy source to generate the electrostatic waves. In this particular case, we were able to identify the free energy source. In other cases the free energy source was so small that it was difficult to detect.

12. Gurnett, D.A., Scarf, F.L., Fredricks, R.W., and Smith, E.J. (1978) ISEE-2 plasma wave investigation, IEEE Trans. Geoscience Electronics GE-16:225.
13. Gurnett, D.A., Anderson, R.R., Scarf, F.L., Fredricks, R.W., and Smith, E.J. (1979) Initial results from the ISEE-1 and -2 plasma wave investigation, Space Sci. Rev. 23:103.
14. Kurth, W.S., Craven, J.D., Frank, L.A., and Gurnett, D.A. (1979) Intense electrostatic waves near the upper hybrid resonance frequency, J. Geophys. Res. 84:4145.

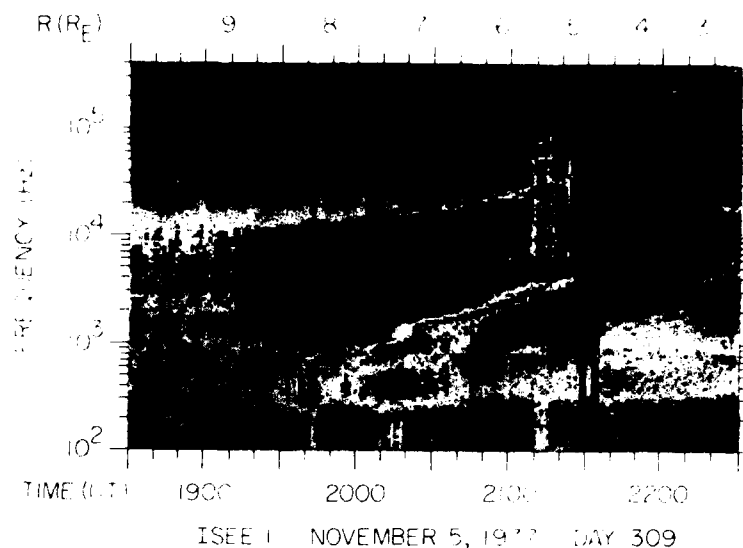


Figure 7. A Survey of the Plasma Waves Observed by ISEE-1 on November 5, 1977: ISEE-1 Encountered the Bowshock at About 1320 UT, and the Magnetopause near 1715 UT on an In-bound Pass on November 5, 1977. These features may be discerned by sharp changes in the frequency-time display produced by the swept frequency receiver. The local electron plasma frequency is discernible as a line at the lower frequency boundary of the continuum radiation. The local plasma frequency increases sharply during the plasmopause entry between 2115 and 2130 UT

Detailed comparisons of measured wave and electron distributions with theory are still in their infancy. Electron measurements are hampered by a time and velocity space resolution that is often barely adequate to detect the weak free energy sources thought responsible for cyclotron harmonic waves, as well as inadequate definition of cold electron properties. Nonetheless, a promising beginning has been made for intense upper hybrid emissions. The next task is to extend these efforts to other emission classes, and particularly to nightside $3/2 \Omega$ diffuse auroral emissions. Moreover, the types of free energy sources that destabilize magnetospheric cyclotron harmonic waves need to be classified observationally. On the theoretical side, parametric studies of nonlinear saturation that are similar in scope to those for linear theory are needed.

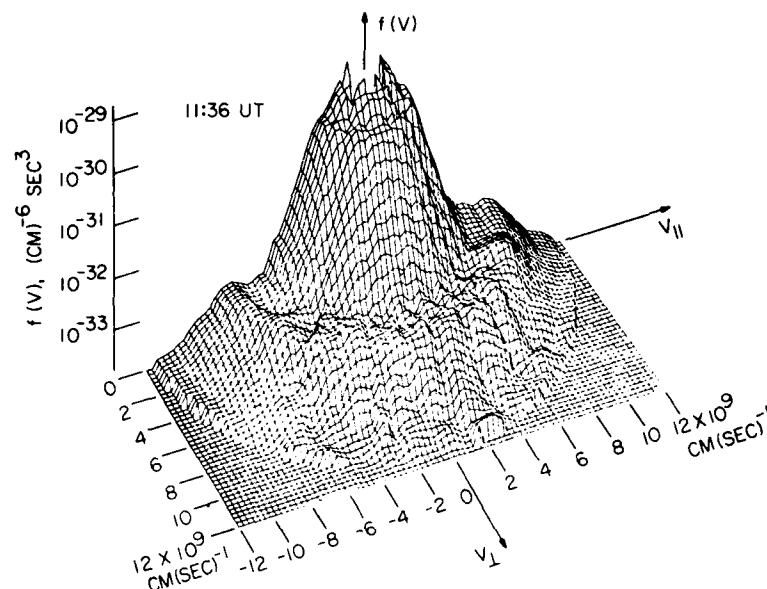


Figure 8. Three Dimensional Velocity Distribution during an ISEE-1 Upper Hybrid Event on December 9, 1977: In This Case, the Free Energy Source was Probably Detected. Note the relative maximum at $7.2 \times 10^9 \text{ cm sec}^{-1}$

4. SIMULATIONS

A laboratory experimentalist attempts to create the same initial state each time he runs his experiment. If he is studying the nonlinear saturation of an instability, he will inject the same unstable particle distribution into the same background plasma over and over again until he has measured the parameters necessary to understand the behavior he observes. The facts that laboratory experiments are repeatable and may be relatively completely diagnosed motivate laboratory theoreticians to specialize their analyses to a narrow range of parameters. Space physicists, on the other hand, do not create the plasma they work with. They can not even observe all of it. They must cope with observations made at a single point, knowing that the phenomena they detect are affected by things they do not measure that occur elsewhere in the immensity of the magnetosphere. When their spacecraft returns to the same point in space, the magnetosphere will have changed. The spacecraft encounters along its orbit a variety of plasma environments equivalent to many laboratory experiments. The goal of the theoretician studying plasma waves in space differs therefore from those of his laboratory colleagues. He must arrive at a general understanding of whole classes of related instabilities

before he can comprehend space observations. Nowhere is this goal more challenging than with the instabilities contained in the Harris¹⁵ dispersion relation, because of the many ways plasmas can produce waves in essentially the same frequency bands. Systematic instability studies are only the first step in the space theoretician's program. Since waves in space are observed in saturated states, he must also study how the instabilities saturate in different parameter regions.

The loss cone is the one distribution for which there have been extensive instability studies exploring parameters that are plausibly realistic for the magnetosphere.¹⁶⁻²³ These studies have concentrated on two issues. First, can relatively gentle loss cone distributions produce an instability that can persist in strong diffusion conditions? And second, what is the role of cold electrons? The problem of cold electrons underlines the need for a parametric study. We know that a small admixture of cold electrons $n_c/n_H < 1$, profoundly affects Harris¹⁵ loss cone instabilities. Yet it is just when n_c/n_H is small that the cold electrons are difficult to measure, so that we must investigate the range of situations permitted by our ignorance of their properties. When we can measure the cold electrons, we find that their density varies considerably from the dayside to the nightside of the magnetosphere and from inside to outside the plasmopause. In this case, parametric studies help us understand why the various cyclotron harmonic waves occur where they do. Finally, the distributions we observe in space have already been smoothed by interactions with waves whose instabilities we are studying. We can estimate the effects of wave-particle interactions on the growth

15. Harris, E.G. (1959) Unstable plasma oscillations in a magnetic field, Phys. Rev. Lett. 2:34.
16. Young, T.S.T., Callen, J.D., and McCune, J.E. (1973) High frequency electrostatic waves in the magnetosphere, J. Geophys. Res. 78:1082.
17. Young, T.S.T. (1974) Electrostatic waves at half electron gyrofrequency, J. Geophys. Res. 79:1985.
18. Ashour-Abdalla, M., and Kennel, C.F. (1976) Convective cold upper hybrid instabilities, in Magnetospheric Particles and Fields, ed. B.M. McCormac p. 181, D. Reidel, Dordrecht, Holland.
19. Ashour-Abdalla, M., and Kennel, C.F. (1978) Nonconvective and convective electron cyclotron harmonic instabilities, J. Geophys. Res. 83:1531.
20. Ashour-Abdalla, M., and Kennel, C.F. (1979) Multiharmonic electron cyclotron instabilities, Geophys. Res. Lett. 5:711.
21. Hubbard, R.F., and Birmingham, T.J. (1978) Electrostatic emissions between electron gyroharmonics in the outer magnetosphere, J. Geophys. Res. 83:4837.
22. Ashour-Abdalla, M., Kennel, C.F., and Sentman, D.D. (1979) Magnetospheric multiharmonic instabilities, in Astrophysics and Space Sciences Book Series, ed. P.J. Palmadesso, D. Reidel, Dordrecht, Holland.
23. Ashour-Abdalla, M., Kennel, C.F., and Livesey, W. (1976) A parametric study of electron multiharmonic instabilities in the magnetosphere, J. Geophys. Res. 84:6540.

rates by varying parameters in the general directions expected from quasilinear theory.

Figure 9 shows a three dimensional representation of a gentle distribution that still leads to strong instability. This situation is discussed in detail in Reference 24. If we choose the ratio X_{UHC} of the cold upper hybrid frequency to the electron cyclotron frequency to be 1.5 (and with $n_c/n_H = 0.2$, the total X_{UHC} to be 3.8), we may then solve the Harris¹⁵ dispersion relation numerically and display the results for the first harmonic as in Figure 9. The real part of the frequency, ω_R , is shown as a function of $k_\perp \rho_H$ and $k_\parallel \rho_H$ at the top and $k_\perp \rho_H$, the imaginary part of the spatial growth rate normalized to the hot electron cyclotron radius ρ_H , at the bottom.

The dependence of ω_R upon k_\perp and k_\parallel contains the answer to the question: "how can a gentle loss cone distribution create persistent cyclotron harmonic instabilities?" For a given $k_\parallel \rho_H$, $\omega_R(k_\perp)$ contains the local maximum that one expects from the Bessel function structure of the Harris¹⁵ dispersion relation. It requires no numerical solution to assert that there can be regions where the perpendicular group velocity $\partial\omega/\partial k_\perp$ is zero. However, the numerical solution reveals that the dispersion relation has a saddle shape. In particular there are two points where $\partial\omega/\partial k_\parallel$ and $\partial\omega/\partial k_\perp$ are zero simultaneously. Here we expect nonconvective instability. Moreover, $\partial\omega/\partial k_\parallel$ is much smaller than A_H , the hot electron anisotropy (see Equ. 5), at other points near the top of the saddle. Therefore, our gentle distribution function produced small temporal growth rates, but large spatial growth rates. This suggests that the even more gentle distributions in the magnetosphere could be strongly unstable.

To determine the generality of the conclusions we drew above, we solve the Harris¹⁵ dispersion relation for all unstable k_\perp and k_\parallel to find the maximum spatial growth rates, or point(s) of nonconvective instability, for a given n_c/n_H and T_c/T_H . We then repeat this procedure for many n_c/n_H and T_c/T_H . Figure 10 presents a complete parameter search of the first and second harmonic bands for $X_{UHC} = 3$ and a partially filled loss cone width of $\Delta = 0.2$. We have shaded the regions of nonconvective instability in a $(n_c/n_H, T_c/T_H)$ parameter space of nonconvective instability; outside of them, we have contoured the spatial growth rates (solid lines) and frequencies (dotted lines) of the maximally growing modes. Nonconvective instability occurs for a finite range of n_c/n_H , between 0.1 and 2 in this case. Moreover, both harmonic bands turn convective at the same $T_c/T_H = 0.5$, when $n_c/n_H < 1$. This third harmonic band was convective throughout.

24. Ashour-Abdalla, M., Leboeuf, J.M., Dawson, J.M., and Kennel, C.F. (1980) A simulation study of cold electron heating by loss-cone instabilities, Geophys. Res. Lett. 7:889.

ROLE OF COLD ELECTRONS

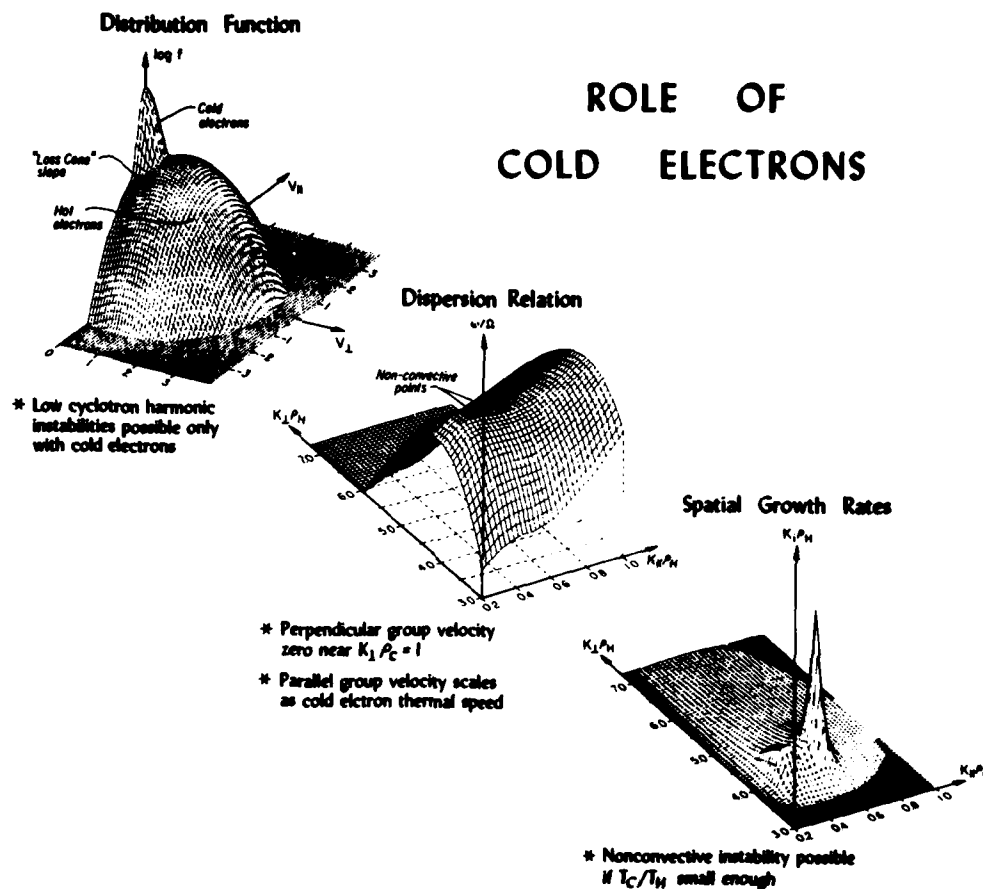


Figure 9. Role of Cold Electrons: At the Top Left is a Representation of a "Gentle" Loss Cone Distribution, with $n_C/n_H = 0.2$, $T_C/T_H = 10^{-2}$ and $\Delta = 0.2$, that Leads to Strong Spatial Growth. In the center is a three dimensional representation of the first harmonic dispersion relation. Note the two points where the group velocity is zero. At these points, the spatial growth rate (lower right) maximizes. For further details, see Ref. 24

SURVEY OF $\frac{T_C}{T_H}$ DEPENDENCE VERSUS $\frac{n_C}{n_H}$

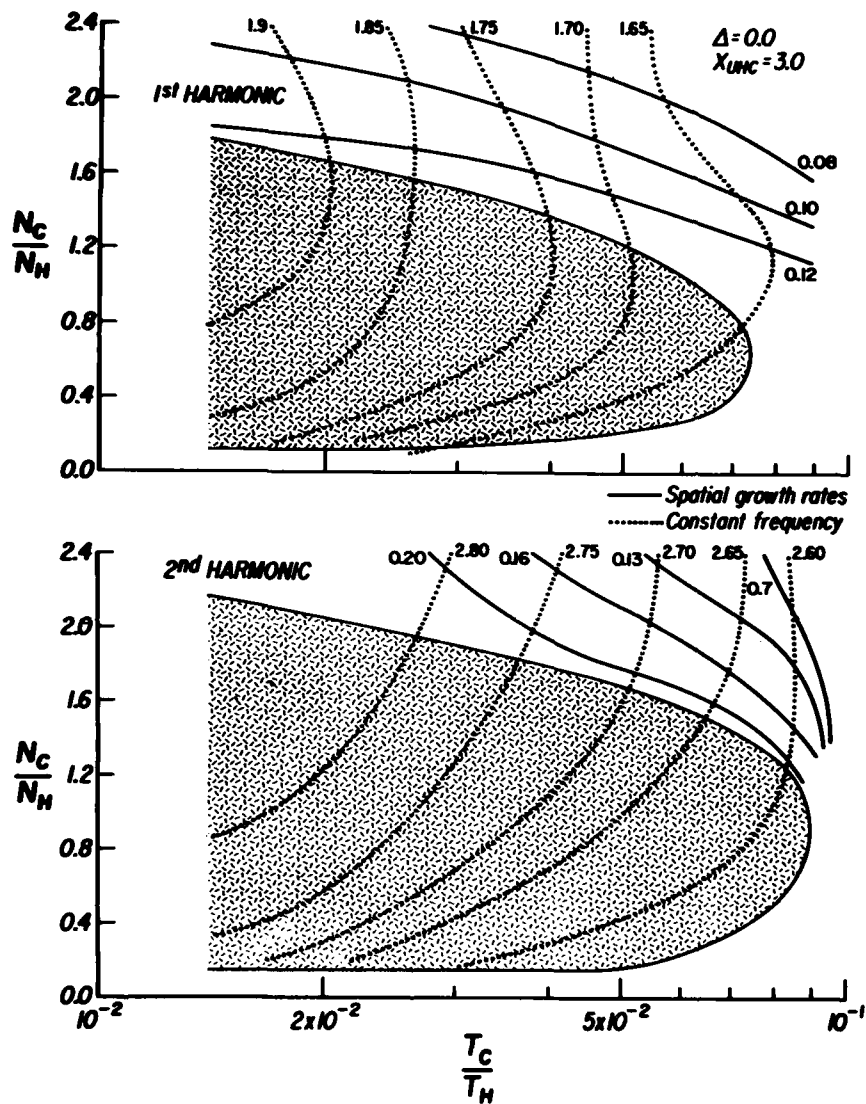


Figure 10. Survey of T_C/T_H Dependence versus n_C/n_H : Shown Here are the Results of a Complete Parameter Search. Keeping X_{UNC} and $\Delta = 0$, the entire unstable region was calculated for each n_C/n_H and T_C/T_H , and the nonconvective or fastest spatially growing modes were identified. The nonconvective zones are shaded. Outside, the solid lines are contours of constant maximum $k_{\perp} \rho_H$. The dotted lines show the frequencies of the fastest growing or nonconvective modes

When n_c/n_H is sufficiently large, we expect nonconvective instability only in the harmonic band containing the cold upper hybrid frequency. In this limit, the cold electrons dominate the real part of the dispersion relation everywhere, and the hot electrons only affect the growth rate.

Parameter searches reveal physical trends that can guide the qualitative interpretation of magnetospheric observations. However, specific numerical predictions, such as the T_c/T_H for convective-nonconvective transition, may not be applicable to given observation. Only use of measured hot and cold electron distributions tests the theory reliably. Nonetheless, these trends help to sort out the phenomenology of the waves observed in the magnetosphere. For example, cyclotron harmonic waves should not occur inside the plasmasphere because n_c/n_H is much too large; but just beyond the plasmapause, we expect upper hybrid emissions because n_c/n_H is moderately large. We expect first harmonic emissions on nightside diffuse auroral lines of force because n_c/n_H should be small and X_{UHC} not too large. Moreover, emissions observed at high latitudes where X_{UHC} can be near unity should be nearer the cyclotron frequency than those at the geomagnetic equator where X_{UHC} probably is largest on the given flux tube.

The OGO-5 electric field experiment detected a number of electrostatic plasma waves with frequencies ω exceeding the local electron cyclotron frequency.²⁵ The dominant class of these waves had frequencies between multiples of the electron gyrofrequency and has thus come to be known as "odd half-harmonic" emissions since $\omega \approx (n + 1/2)\Omega$. More recently both the ISEE¹² and GEOS²⁶ spacecraft which have experiments with much improved sensitivity, have detected these waves over a much broader region of latitude than that of earlier observations.²⁷

Ashour-Abdalla et al²² have presented results of a simulation study of such electron cyclotron harmonic waves. The goals were two-fold; first, to determine the nonlinear saturation mechanism, and second, to see if the cold electrons could be heated and if so, by what mechanism. The results show clearly that the onset of nonlinear cyclotron resonance plays the key role in these phenomena for the situation considered. A 2-1/2 D (2 space and field and three velocity dimensions) electrostatic finite size particle simulation code was used. Details

25. Kennel, C.F., Scarf, F.L., Fredericks, R.W., McOedee, J.G., and Coroniti, F.V. (1970) VLF electric field observations in the magnetosphere, *J. Geophys. Res.* 75:6136.

26. Ronmark, K., Borg, H., Christiansen, P.J., Gough, M.P., and Jones, D. (1978) Banded electron cyclotron harmonic instability - a first comparison of theory and experiment, *Space Sci. Rev.* 22:401.

27. Fredericks, R.W. (1971) Plasma instability at $(n + 1/2)f_c$ and its relationship to some satellite observations, *J. Geophys. Res.* 76:5344.

concerning the numerics can be found in Dawson *et al.*²⁸ The spatial variations are in the x and y directions. The system is $L_x \times L_y = 64\lambda_{De} \times 64\lambda_{De}$ where λ_{De} is the Debye length of the electron at $t = 0$. We have used 8 electrons per unit cell loaded uniformly on the periodic spatial grid in each of the x and y directions. The ions are immobile and constitute a uniform, charge-neutralizing background. The electron spatial distribution has a Gaussian shape and is of a size $a = 1\lambda_{De}$. The simulation was started with a particle distribution function which is known to be unstable to the growth of electron cyclotron harmonic waves. The model magnetospheric population is composed of two components: a hot free energy source presumably of plasma sheet origin, and a cold ionospheric component. The hot plasma has a temperature T_H and particle density n_H and the cold particles a temperature T_C and density n_C . In the particular results shown here the free energy source consists of a ring in velocity space in the direction perpendicular to the static magnetic field of strength such that $\Omega_{ce} = 0.3\omega_{pe}$ with $v_b = 5v_{te}$ (where v_b is the velocity of the ring and v_{te} is the thermal velocity of the hot component).

The cooler component has a fractional density $n_C/n_H = 0.25$ and temperature $T_C/T_H = 10^{-2}$. Just as predicted by linear theory¹⁶ and shown by 1-D simulation^{29, 30} the presence of this cooler plasma allows less extreme free energy sources to be unstable to wave growth.

In Figure 11, the time development of the distribution function is presented. In this plot the particles are represented by points in the $v_z - v_y$ space. The upper panel shows the initial distribution of particles, the thermal velocity being 10 times smaller than that of the hot particles. The ring of hot particles is apparent around $v_o = 5.0$. This gives the $\partial f/\partial v_{\perp}$ which is necessary for the growth of electron cyclotron harmonic waves. At $t = 50\omega_{pe}^{-1}$ the particles are present. The time development of these phase-space plots shows that the time scale for affecting the cold particles distribution is much faster than the hot particle one. Using quasi-linear theory, Ashour-Abdalla and Kennel^{19, 20} relate these two time scales as follows

$$\frac{\tau_c}{\tau_H} = \frac{\Omega_{ce}}{\gamma} \frac{T_c}{T_H}$$

28. Dawson, J.M., Okuda, H., and Rosen, B. (1976) Collective Transport in Plasmas, Methods of Computational Physics, ed. B. Adler et al, Vol. 16, p. 281.
29. Byers, J. and Greural, M. (1970) Perpendicularly propagating plasma cyclotron instabilities simulated with a one dimensional computer model, Phys. Fluids 13:1819.
30. Lee, J.K. and Birdsall, C.K. (1979) Velocity space ring plasma instability, magnetized, Phys. Fluids 22:1306 and 1315.

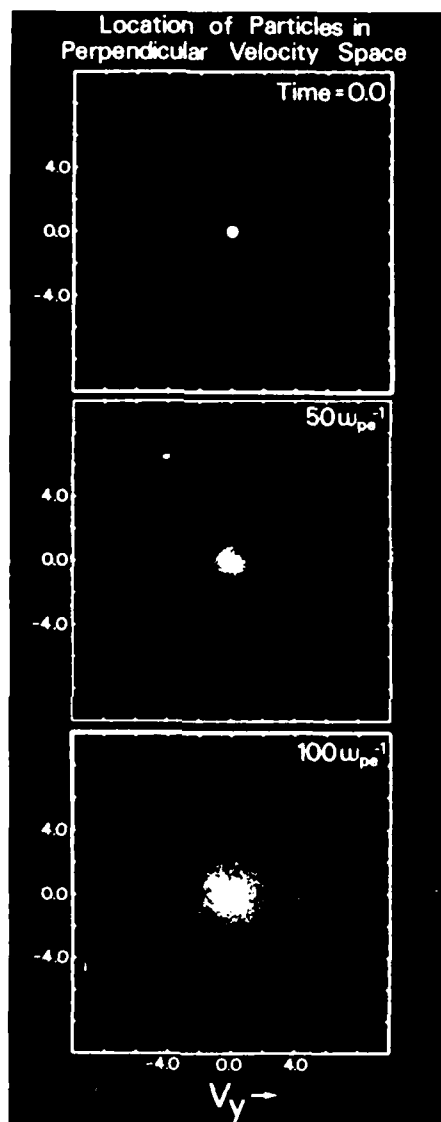


Figure 11. Cold Electron Heating Observed in a Numerical Simulation of 3/2 Instabilities: Perpendicular Velocity Distribution of the Cold and Hot Particles: Their $v_z - v_y$ Phase Space at time a) $t = 10 \omega_{pe}^{-1}$, b) $t = 50 \omega_{pe}^{-1}$ and c) $t = 100 \omega_{pe}^{-1}$

where τ_c and τ_H are the respective time scales for the evolution of the cold and hot distributions. The growth rate is $\gamma \sim 0.1 \Omega_{ce}$, so that $\tau_c/\tau_H \approx 0.1$ and this equation predicts that the distribution of the cold particles will evolve ten times faster than that of the hot particles, in qualitative agreement with the simulation results. In Figure 12 we show the time evolution of the electrostatic wave energy, kinetic energy of the hot particles, and the cold electron temperature in directions perpendicular and parallel to the magnetic field. The wave energy grows from a loss of kinetic energy of the hot particles, saturates at about $t = 50 \omega_{pe}^{-1}$ and then decays to a level slightly higher than the original thermal level. The global growth rate of the electric field amplitude is measured as $\gamma = 0.025 \omega_{pe}$. In the lower panel we note the preferential gain in perpendicular cold electron temperature. The energy is gained from the hot particles with the unstable waves acting as a heat exchanger. After saturation, there is still energy exchange between the hot and cold particles. At time $t = 100 \omega_{pe}^{-1}$, the cold electron temperature still increases but at a much slower rate. By that time, the wave activity has subsided. The temperature of the hot particles (not shown) shows decrease in the perpendicular direction and slight increase in the parallel direction consistent with a tendency toward isotropy of the hot electron distribution.

The wave growth in the upper panel of Figure 12 is caused by the growth of only two modes. These two modes are $(k_{\parallel}, k_{\perp}) = (2\pi/64 \times 1, 2\pi/64 \times 2)$ and $(2\pi/64 \times 1, 2\pi/64 \times 3)$ with the latter attaining a higher level. The power spectra of modes (1,2) and (1,3) are plotted in Figure 13. They peak at around $\omega \sim 0.45 \omega_{pe}$, which corresponds to $\omega \sim 1.5 \Omega_{ce}$, in agreement with linear theory. Thus odd half harmonics emissions are excited. From Figure 13 the angle for maximum growth is given by $\Theta = \tan^{-1}(3) = 71^\circ$ and the maximum growth rate of the electric field amplitude is measured as $\gamma \sim 0.04 \omega_{pe}$, in reasonable agreement with linear theory prediction of $0.03 \omega_{pe}$ and $\Theta \sim 80^\circ$. Note the angle is limited in the simulation by the discreteness of the wave number parallel to the magnetic field, that is, $k_{\min} = 2\pi/64 \times 1 \lambda_{De}$. Heating of the particles can only take place if the particles resonate with the waves. Initially, the cold electrons have a thermal velocity $v_{tc} = 0.1 v_{te}$, and the smallest resonant velocity (the cyclotron one) with the waves is $v_{\parallel} = (\omega_0 - \Omega_{ce})/k_{\parallel} = (1.5 v_{te})$, then the cold electron temperature increases in the direction perpendicular to the magnetic field. The hot electrons do not participate in the interaction (their perpendicular temperature actually decreases) because the effect of the waves is averaged out over their larger Larmor radius, that is, $\rho_H = 15 \lambda_{De} > \text{most unstable perpendicular wavelength} \sim 10 \lambda_{De}$. The above scenario is not inconsistent with the lower panel of Figure 12 where the cold electron temperature increases from the beginning of the run.

The candidate for saturation is cyclotron resonance damping by the cold electrons. From the agreement between the measured electric field at saturation (0.6)

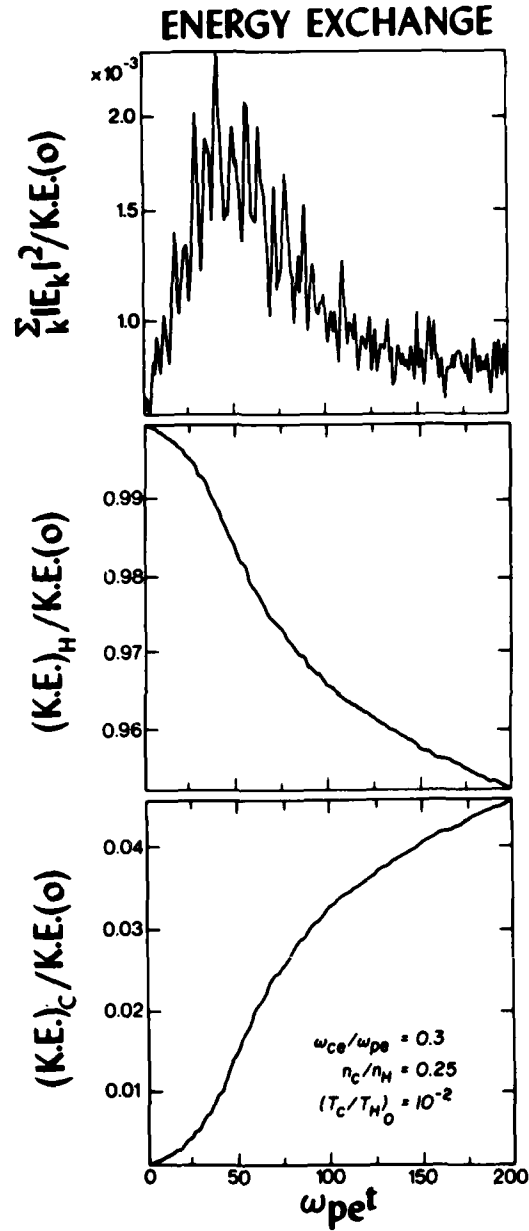


Figure 12. Energy Exchange: Time Evolution of: a) The Electric Field Energy, b) The Kinetic Energy of the Hot Electrons, and c) The Perpendicular and Parallel Temperature of the Cold Electrons. $K.E.(0)$ is the kinetic energy of the hot particles at time $t = 0$. For details see Ref. 24

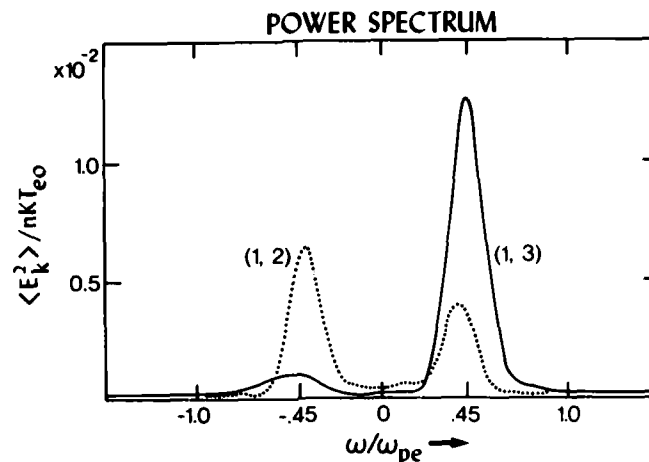


Figure 13. Power Spectra of the Two Most Unstable Modes. The dashed curve refers to mode (1, 2) the solid one to mode (1, 3)

and the calculated electric field for cyclotron resonance to take place (0.7), it is certainly plausible. Cyclotron damping is further confirmed by a comparison of the global damping rate of wave energy and the rate of increase of perpendicular temperature, measured from $70 \omega_{pe}^{-1}$ to $125 \omega_{pe}^{-1}$ in Figure 12. The wave energy (W_E) yields $\gamma_D = 0.016 \omega_{pe}$ whereas the perpendicular temperature in the y-direction gives $\gamma_y = 9.25 \times 10^{-3}$ and $\gamma_t = 2 \times \gamma_y$, so that $\frac{dT_{\perp}}{dt} \cong \frac{-dW_E}{dt}$. We conclude that the onset of cyclotron resonance is the cause of the saturation of the unstable electron cyclotron harmonic waves and use of the heating of the cold particles.

5. DISCUSSION

The real question is not whether the cold electrons have been heated in the simulation but whether they will be heated in a realistic magnetosphere. For no matter how large the magnetosphere may seem to both theoretician and a spacecraft it is neither infinite nor homogeneous. Into the local spatial region which is generating the unstable wave turbulence, convection and ionospheric flows continuously inject new sources of free energy and remove partially dissipated free energy. The challenge is to understand the delicate nonlinear balance between plasma and wave sources and sinks by which a quasi-steady strong diffusion state is maintained. Although magnetospheric particle interactions are spatially localized, representing the magnetospheric system as a simulation box (Figure 14) will

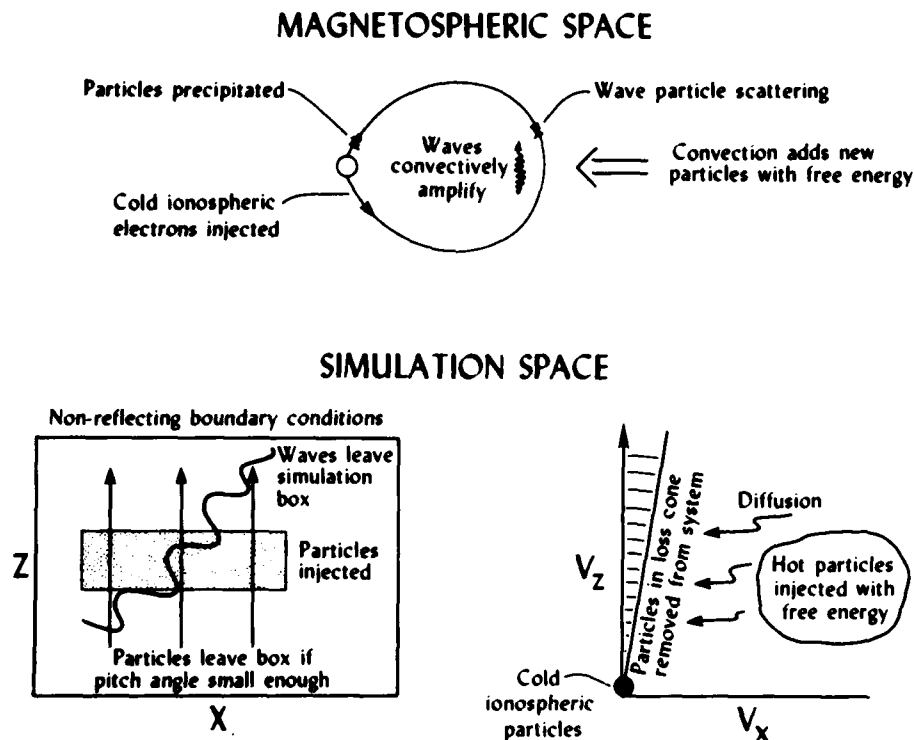


Figure 14. The Magnetosphere as a Simulation Box: The Magnetospheric System (Top Figure) is Simulated as Shown in Bottom Figures

be valid only if the simulation boundary conditions are sufficiently flexible to model the influence of the macrophysics on the microinstabilities. Simulations should allow for the precipitation loss of particles and the continuous injection of new particles. Efforts should be made to model the effect of wave propagation in the inhomogeneous geomagnetic field. Despite their difficulty, simulations hold the promise of placing the conceptual framework of the diffuse aurora on a sound quantitative foundation from which precise comparisons with satellite observations can be made.

In virtually every important plasma physical aspect, the diffuse aurora and the radiation belts are at opposite extremes. ELF whistlers propagate throughout the plasmasphere, whereas electrostatic electron waves propagate short distances at best. The smooth ELF spectrum satisfies the constraints of quasilinear theory, and it is easy to construct bounce averaged diffusion coefficients. Yet these complications make strong diffusion much more interesting. We will have to plumb the depths of modern plasma turbulence theory to understand it. In the meantime, we

can be satisfied that our experimental and theoretical work on magnetospheric strong diffusion is comparable in scope and depth to that on laboratory mirror trapping, and that both are paradigm problems that lead the development of contemporary plasma physics.

Let us now propose a research strategy that may help resolve our present uncertainties. On the experimental side, high time resolution wave measurements and better measurements of cold electrons are needed. On the theoretical side, further studies of nonlinear saturation and propagation that explore the parameters encountered in the Earth's and Jupiter's magnetospheres are called for. While numerical simulations have provided much insight into nonlinear plasma physics, they must be carefully tailored to suit magnetospheric problems. They should model not only the temporal growth to saturation of a strong instability, but also attempt to simulate the magnetosphere's delicate web of quasi-steady processes — the balance of particle injection and loss that leads to smooth distributions and relatively low average amplitudes. Because of the magnetosphere's great size, propagation studies have proven invaluable in interpreting space measurements, more than in the laboratory. Moreover, theoreticians need to know whether a few or many modes are excited. Because wavelength measurements are difficult and because linear theory tells us that many modes with different wave vectors are crowded into the same frequency range, this question may not be answerable by observation. Propagation studies can tell us how rich the wave-number spectrum of amplified waves can be.

References

1. Rosenbluth, M.N., and Post, R.F. (1965) High-frequency electrostatic plasma instability inherent to "loss-cone" particle distribution, Phys. Fluids 8:547.
2. Kennel, C.F., and Petscheck, H.E. (1966) Limit on stably trapped particle fluxes, J. Geophys. Res. 71:1.
3. Kennel, C.F. (1969) Consequences of a magnetospheric plasma, Revs. Geophys. 7:379.
4. Meng, C.I., Mauk, B., and McIlwain, C.E. (1979) Electron precipitation of evening diffusion aurora and its conjugate electron fluxes near the magnetospheric equator, J. Geophys. Res. 84:2545.
5. Coroniti, F.V., and Thorne, R.M. (1973) Magnetospheric electrons, Ann. Rev. of Earth and Planetary Sci. 1:107.
6. Kennel, C.F., and Engelmann, F. (1966) Velocity space diffusion from plasma turbulence in a magnetic field, Phys. Fluids 9:2377.
7. Thorne, R.M., and Kennel, C.F. (1967) Quasi-trapped VLF propagation in the outer magnetosphere, J. Geophys. Res. 72:357.

8. Lyons, L.R., Thorne, R.M., and Kennel, C.F. (1971) Electron pitch angle diffusion driven by oblique whistler mode turbulence, J. Plasma Phys. 6:589.
9. Lyons, L.R., Thorne, R.M., and Kennel, C.F. (1972) Pitch angle diffusion of radiation belt electrons within the plasmasphere, J. Geophys. Res. 77:3455.
10. West, H.I., Jr., Buck, R.M., and Walton, J.R. (1972) Electron pitch angle distributions throughout the magnetosphere as observed on OGO-5, J. Geophys. Res. 78:1064.
11. Lyons, L.R., and Thorne, R.M. (1973) Equilibrium structure of radiation belt electrons, J. Geophys. Res. 78:2142.
12. Gurnett, D.A., Scarf, F.L., Fredricks, R.W., and Smith, E.J. (1978) ISEE-2 plasma wave investigation, IEEE Trans. Geoscience Electronics GE-16:225.
13. Gurnett, D.A., Anderson, R.R., Scarf, F.L., Fredricks, R.W., and Smith, E.J. (1979) Initial results from the ISEE-1 and -2 plasma wave investigation, Space Sci. Rev. 23:103.
14. Kurth, W.S., Craven, J.D., Frank, L.A., and Gurnett, D.A. (1979) Intense electrostatic waves near the upper hybrid resonance frequency, J. Geophys. Res. 84:4145.
15. Harris, E.G. (1959) Unstable plasma oscillations in a magnetic field, Phys. Rev. Lett. 2:34.
16. Young, T.S.T., Callen, J.D., and McCune, J.E. (1973) High frequency electrostatic waves in the magnetosphere, J. Geophys. Res. 78:1082.
17. Young, T.S.T. (1974) Electrostatic waves at half electron gyrofrequency, J. Geophys. Res. 79:1985.
18. Ashour-Abdalla, M., and Kennel, C.F. (1976) Convective cold upper hybrid instabilities, in Magnetospheric Particles and Fields, ed. B.M. McCormac p. 181, D. Reidel, Dordrecht, Holland.
19. Ashour-Abdalla, M., and Kennel, C.F. (1978) Nonconvective and convective electron cyclotron harmonic instabilities, J. Geophys. Res. 83:1531.
20. Ashour-Abdalla, M., and Kennel, C.F. (1979) Multiharmonic electron cyclotron instabilities, Geophys. Res. Lett. 5:711.
21. Hubbard, R.F., and Birmingham, T.J. (1978) Electrostatic emissions between electron gyroharmonics in the outer magnetosphere, J. Geophys. Res. 83:4837.
22. Ashour-Abdalla, M., Kennel, C.F., and Sentman, D.D. (1979) Magnetospheric multiharmonic instabilities, in Astrophysics and Space Sciences Book Series, ed. P.J. Palmadesso, D. Reidel, Dordrecht, Holland.
23. Ashour-Abdalla, M., Kennel, C.F., and Livesey, W. (1976) A parametric study of electron multiharmonic instabilities in the magnetosphere, J. Geophys. Res. 84:6540.
24. Ashour-Abdalla, M., Leboeuf, J.M., Dawson, J.M., and Kennel, C.F. (1980) A simulation study of cold electron heating by loss-cone instabilities, Geophys. Res. Lett. 7:889.
25. Kennel, C.F., Scarf, F.L., Fredericks, R.W., McOedee, J.G., and Coroniti, F.V. (1970) VLF electric field observations in the magnetosphere, J. Geophys. Res. 75:6136.
26. Ronmark, K., Borg, H., Christiansen, P.J., Gough, M.P., and Jones, D. (1978) Banded electron cyclotron harmonic instability - a first comparison of theory and experiment, Space Sci. Rev. 22:401.

27. Fredricks, R.W. (1971) Plasma instability at $(n + 1/2)f_c$ and its relationship to some satellite observations, J. Geophys. Res. 76:5344.
28. Dawson, J.M., Okuda, H., and Rosen, B. (1976) Collective transport in plasmas, in Methods of Computational Physics, ed. B. Adler et al, Vol. 16, p. 281.
29. Byers, J., and Greural, M. (1970) Perpendicularly propagating plasma cyclotron instabilities simulated with a one dimensional computer model, Phys. Fluids 13:1819.
30. Lee, J.K., and Birdsall, C.K. (1979) Velocity space ring plasma instability, magnetized, Phys. Fluids 22:1306 and 1315.

AD-A113 959

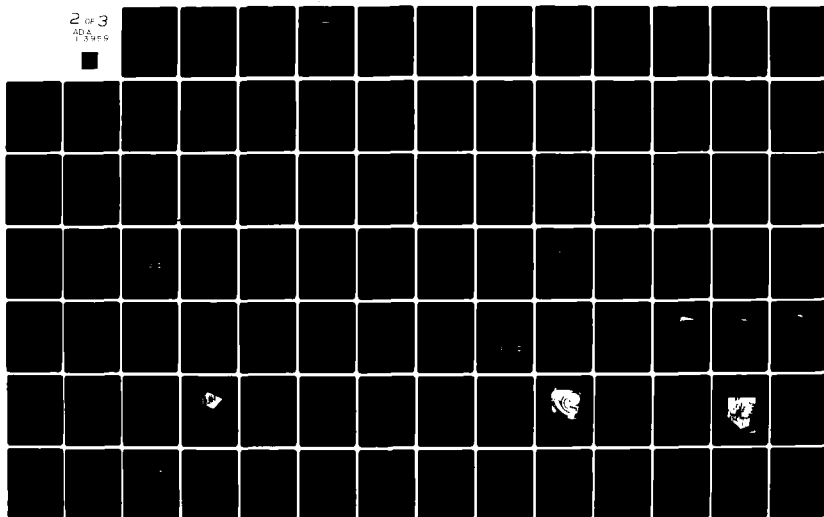
AIR FORCE GEOPHYSICS LAB HANSCOM AFB MA
PROCEEDINGS OF THE AIR FORCE GEOPHYSICS LABORATORY WORKSHOP ON --ETC(U)
OCT 81 R C SABALYN, W N SPJELDVIK, W J BURKE
AFGL-TR-81-0311

F/G 4/1

UNCLASSIFIED

NL

2 of 3
ADA
1.3496



Contents

1. Introduction	99
2. Soft Errors	100
3. Mechanisms for Bit Upsets	101
4. Laboratory Simulations of Soft Errors	107
5. Dose and Dose Rate Sensitivity	114
6. Accelerated Testing	116
7. Dielectric Charging on Spacecraft	117
8. Radiation Environment in Space	119
9. Future Studies and Needs	119
References	122

4. Radiation Effects on Electronic Systems

by

Peter J. McNulty
Physics Department
Clarkson College of Technology
Potsdam, New York 13676

based on a tutorial lecture given by

J. Bernard Blake
The Aerospace Corporation
El Segundo, California 90009

and contributed presentations by

Dr. Vitaly Danchenko (NASA/GSFC)
Dr. Peter J. McNulty (Clarkson College)
Dr. Ed Peterson (Naval Research Laboratory)
Dr. William E. Price (Jet Propulsion Laboratory)
Dr. Jason Wilkenfeld (Instrumentation/Research/Technology)

I. INTRODUCTION

The problem of electronic systems flown in space being vulnerable to ionizing radiation is of growing importance and complexity. Dielectric charging by energetic particles and single-particle effects have been added to the ongoing concerns of total dose and dose-rate vulnerability of circuit components. The dielectric charging phenomena are the result of exposure to large fluxes of energetic electrons.

The single-particle effects occur when individual energetic charged particles (cosmic-ray nuclei) traverse, or initiate a nuclear reaction within, digital circuit elements or sensing devices.

The single-particle effects may introduce both soft and hard errors. The soft errors include anomalous signals, bit upsets (changes in information stored in memory), and incorrect logic execution. While the circuit continues to function as designed after a soft error, it processes false information. Hard errors, on the other hand, are permanent effects such as "latch up". The "latch up" phenomenon is particularly serious because it can produce catastrophic results. Some "latch ups" lead to strong surges of instrument currents. If the circuit was improperly designed, and is not able to withstand the enhanced current, it simply burns up. Although at present the cross section for "latch ups" is substantially smaller than that for soft errors, this may change as the size of circuit elements decreases.

Systems designers have to take both hard and soft errors into account when designing for space. Predicting effects and the rates of occurrence in space requires improved knowledge of certain components of the radiation environment, a better understanding of the mechanisms for both hard and soft errors, and considerable accelerated testing on the ground. Even then, arguments can be made that new integrated circuit technologies should be flown first in "test packages" before being incorporated as essential components of satellite systems. The following sections contain brief reviews of the physical mechanisms causing these new concerns in radiation effects, some discussion of the current issues of accelerated testing, and a brief attempt to address the question of what information is needed before new VLSI (very large scale integrated) and VHSIC (very high speed integrated circuits) circuits are incorporated into DOD satellite systems.

2. SOFT ERRORS

The early reports of soft-error phenomena were of anomalous "toggles" of circumvention detectors on classified satellites. With the introduction of large-scale-integrated (LSI) devices on satellites the problem has grown in significance.^{1,2}

A circumvention detector looks for prompt radiation (gamma rays) from a detonating nuclear weapon. Upon triggering it closes down many of the spacecraft control systems such as the attitude adjustment system. This prevents the

1. Binder, D., Smith, E.E., and Holman, A.B. (1975) Satellite anomalies from cosmic rays, IEEE Trans. Nucl. Sci. NS-22:2675.
2. Pickele, J. C., and Blandford, J. T. (1978) Cosmic ray induced errors in MOS memory celis, IEEE Trans. Nucl. Sci. NS-25:1166.

spacecraft steering jets from going out of control. Intervention from the ground control is required to turn the attitude and other control systems back on again. It has been shown that cosmic ray particles, such as iron nuclei, also occasionally trigger the diode in the detector device. A dual (or multiple) detector device requiring simultaneous triggering might solve the problem of spurious spacecraft shutdowns.

There have been reports of bit upsets in memory devices on a number of satellites, among them, Intelsat IV, SDS, and Pioneer Venus. The characteristics of spacecraft memory errors may be summarized as follows: They occur at random, nonrepeating locations in memory; they are predominantly single-bit errors with the possibility of rare two-bit errors; no obvious dependence on orbit location and parameters has been observed. Anomalous signals have also occurred in the form of "blips" on photographs from DMSP³ and Landsat satellites.⁴ The "light-flashes" experienced by Apollo and Skylab astronauts are also believed to be the result of single-particle interactions in sensitive elements at or near the astronaut's retina.⁵

3. MECHANISMS FOR BIT UPSETS

A number of mechanisms have been proposed to explain the soft errors in memory devices flown in space.^{1, 2, 6-14} All involve the generation of free charges in the form of electron-hole pairs along the trajectories of the energetic particles that make up the primary radiation and any energetic secondaries produced. Figure 1 is a schematic representation of a cosmic-ray particle traversing a sensitive volume element on a circuit device. If a sufficient amount of charge is generated within the sensitive volume element, the electrical and hence the logic state of the element can be altered.^{1, 2, 10, 12, 13} The models assume that if one knows the effective sizes of all the sensitive volume elements, the critical charges necessary to change the logic states, and the energy-deposition characteristics of the radiation to which the device is exposed, one can predict the soft-error rates for the device. Since the number of charges generated along the trajectories of energetic charged particles is proportional to the stopping power, or rate of energy loss of the particle, the contribution from a given particle's trajectory through the sensitive volume element depends upon the particle's atomic number Z , kinetic energy E , and path length through the sensitive region.

Figure 2 plots the energy deposition along a $10\text{ }\mu\text{m}$ long trajectory through silicon versus kinetic energy for various heavy ions.¹¹ If the threshold for soft errors

Because of the large number of references cited above, they will not be listed here. See References, pages 122, 123.

Schematic Representation of Sensitive Region in a Single Memory Cell

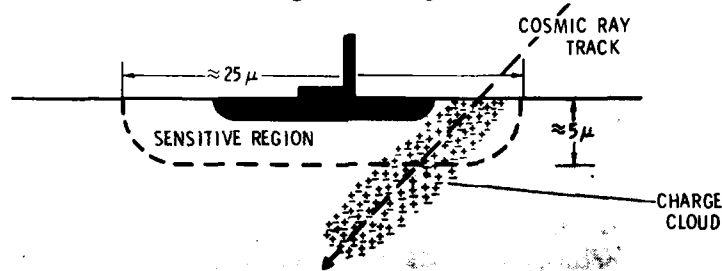


Figure 1. Electron-Hole Pairs Resulting from the Traversal of Memory Cell by a Cosmic-Ray Nucleus. (Courtesy of J. B. Blake)

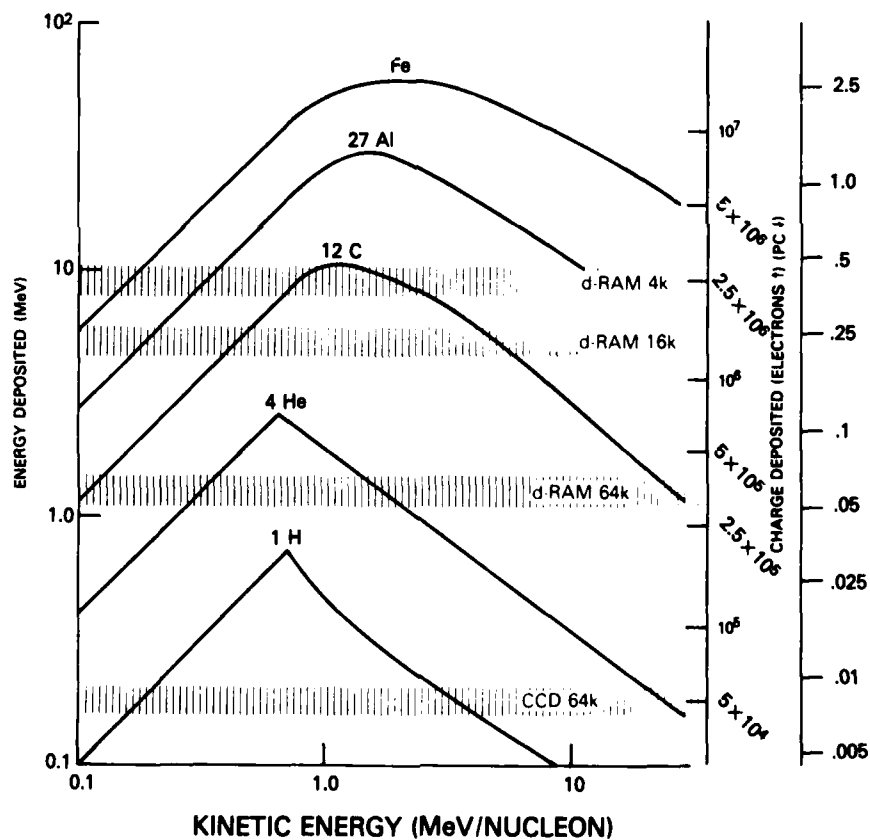


Figure 2. Energy Deposited in $10 \mu\text{m}$ of Silicon by Various Ions. The scale on the right shows the number of electrons deposited. The straight part of the curves at low energies occurs when the ion range is less than $10 \mu\text{m}$ and it deposits all of its energy. (Petersen¹¹)

in a device with sensitive elements $10\text{ }\mu\text{m}$ thick corresponds to the deposition of no more than 2-4 MeV, the device will be sensitive to individual alpha particles emitted from the packaging material surrounding the device as well as to stopping alphas emitted from nuclear interactions outside the sensitive volume. If more than 6 MeV must be deposited, then an energetic cosmic-ray particle must have a relatively high value of Z (HZE particle) to induce an upset through simple traversal. Cosmic ray particles with lower Z values can only deposit energies above threshold near the end of their range ($E \leq 10\text{ MeV/nucleon}$). The intensity of the heavy cosmic rays as a function of Z shows a pronounced peak around iron ($Z = 26$), and it abruptly decreases by two orders of magnitude for higher Z values. The intensity of iron nuclei in space as measured by Simpson's group is plotted in Figure 3 as a function of energy.¹³ While the large solar component of the iron flux in Figure 3 represents the September 1977 solar flare and such flares may be quite rare and of short duration, the possibility of their occurrence is an important consideration.

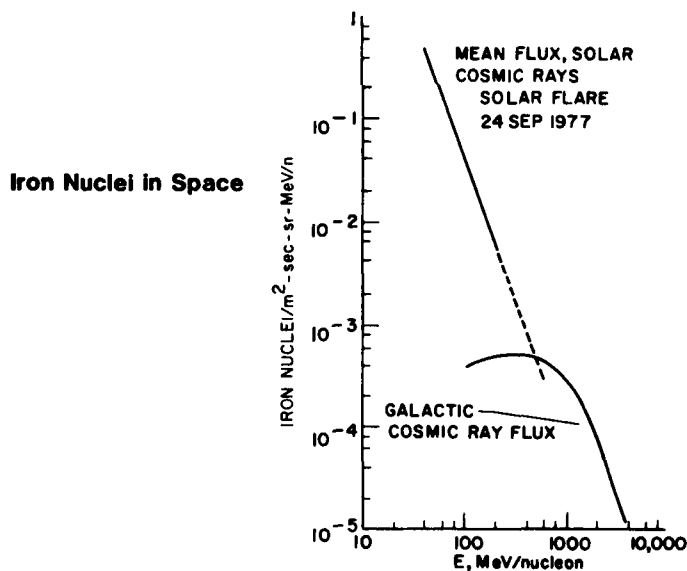


Figure 3. Spectra of Galactic and Solar Cosmic-Ray Iron Nuclei. (Kolasinski et al¹³)

Nuclear reactions provide a second mechanism for depositing considerable energy in a microscopic volume element.^{5-9, 11} Figure 4 shows a schematic representation of a nuclear interaction occurring within a sensitive volume element. The charge collected is proportional to the total energy deposited in the volume element along the trajectories of the primary and all the secondary charged particles, including the nuclear recoil. An analysis of the interaction of a 30 MeV proton with a Si nucleus is outlined in Figure 5. The interaction leads to the formation of a compound nucleus and the subsequent emission of secondary particles – shown as a proton and an alpha particle in this figure. Such a reaction could result in energy deposition in a $(10 \times 20 \times 20\text{-}\mu\text{m})$ volume element of as much as 7.3 MeV. The upset rate to be expected for a system of 6.4×10^7 bits exposed to a flux of 40 MeV protons of 10^6 protons/cm²-day is plotted in Figure 6 versus the critical number of charges needed to be collected. Again, processes of the type described in Figure 5 deposit less than 8 MeV, but rare fission events may result in as much as 20 MeV (or 5×10^6 electronic charges).

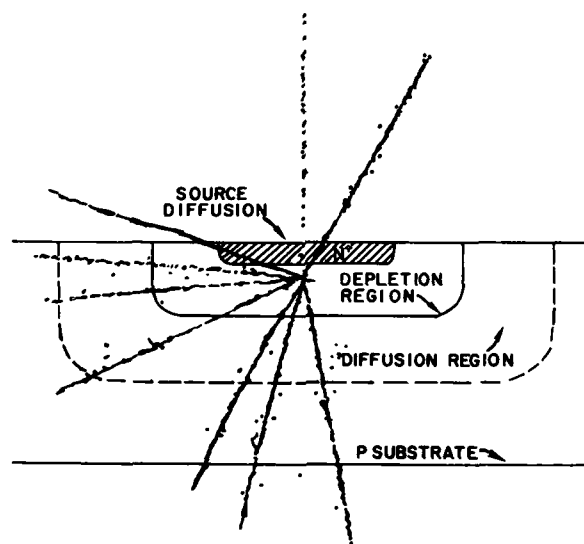
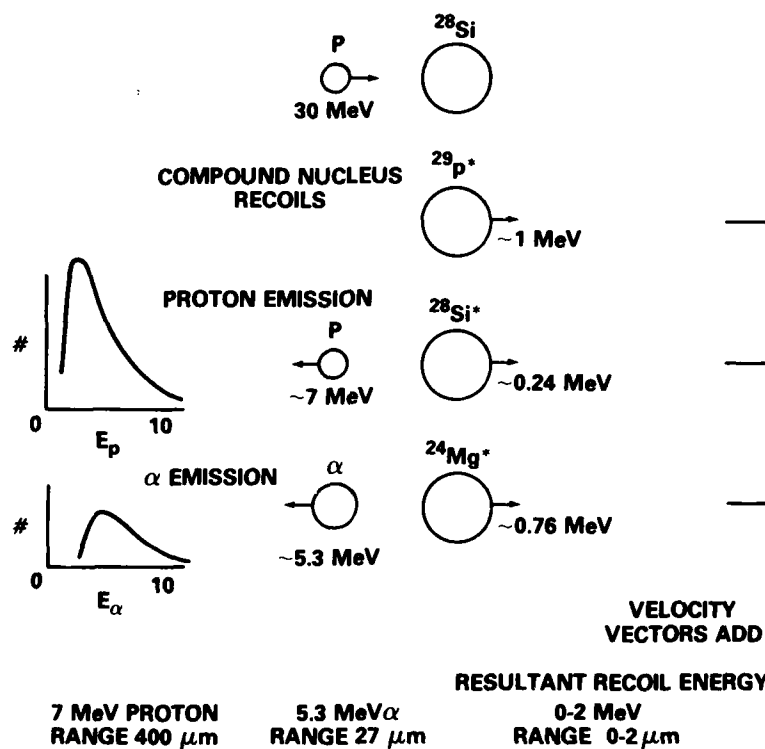


Figure 4. Schematic Drawing of a Nuclear Interaction in a Sensitive Volume Element. (McNulty et al¹⁵)

15. McNulty, P.J., Wyatt, R.C., Farrell, G.E., Filz, R.C., and Rothwell, P.L., (1980) Proton upsets in LSI memories in space, in Space Systems and Their Interactions with Earth's Space Environment, Eds. H.B. Garrett and C.P. Pike, American Institute of Astronautics and Aeronautics, New York, p 413.

NUCLEAR REACTIONS IN SILICON

EXAMPLE $^{28}\text{Si} (P, P\alpha) ^{24}\text{Mg}$ $Q = -10 \text{ MeV}$



THIS REACTION COULD DEPOSIT ~7.3 MeV
IN A $(10 \times 20 \times 20) \mu\text{m}^3$ VOLUME

Figure 5. The Energetics of a Particular Nuclear Interaction Demonstrates How Large Amounts of Energy can be Deposited in a Small Sensitive Volume. (Courtesy of E. Petersen)

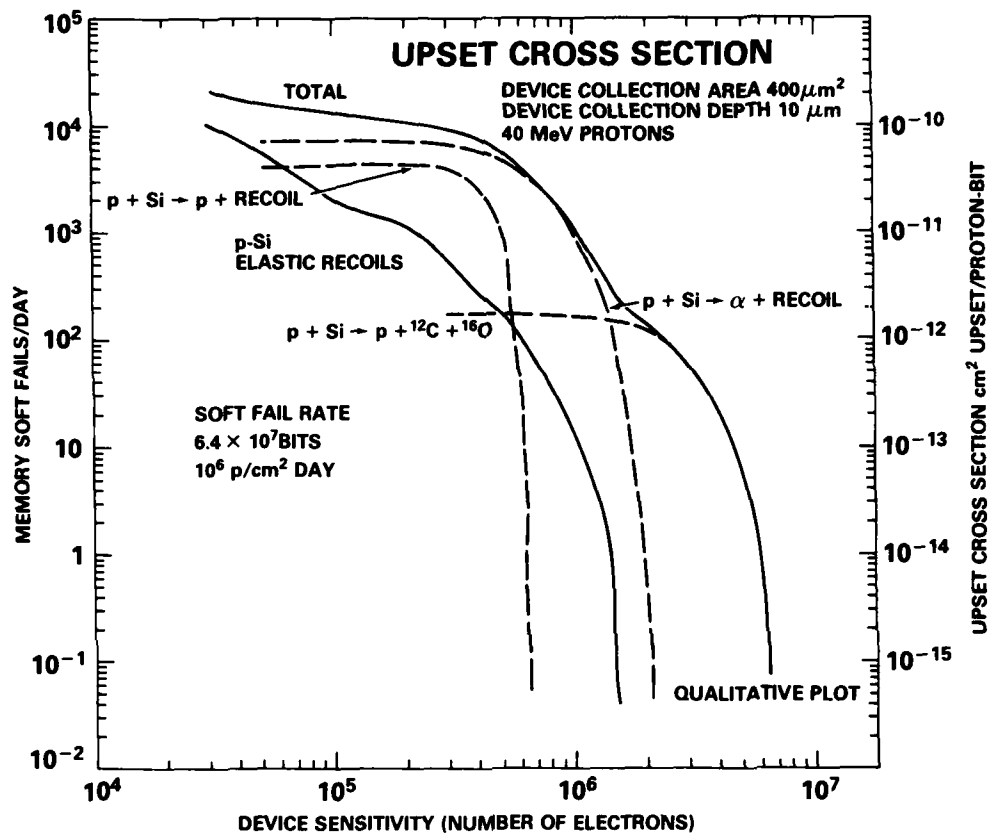


Figure 6. Probability of Soft Upsets as a Function of Critical Charge for a Particular Device Size. The scale on the left shows the fail rate for a given size of memory and proton fluence. (Courtesy of E. Petersen)

One should also point out that at higher incident proton energies the nuclear recoils are more energetic, resulting in a larger local deposition of energy. Figure 7 shows model calculations of proton integral fluxes for protons having kinetic energies greater than 30 MeV as a function of spacecraft altitude for earth orbits of various inclinations.

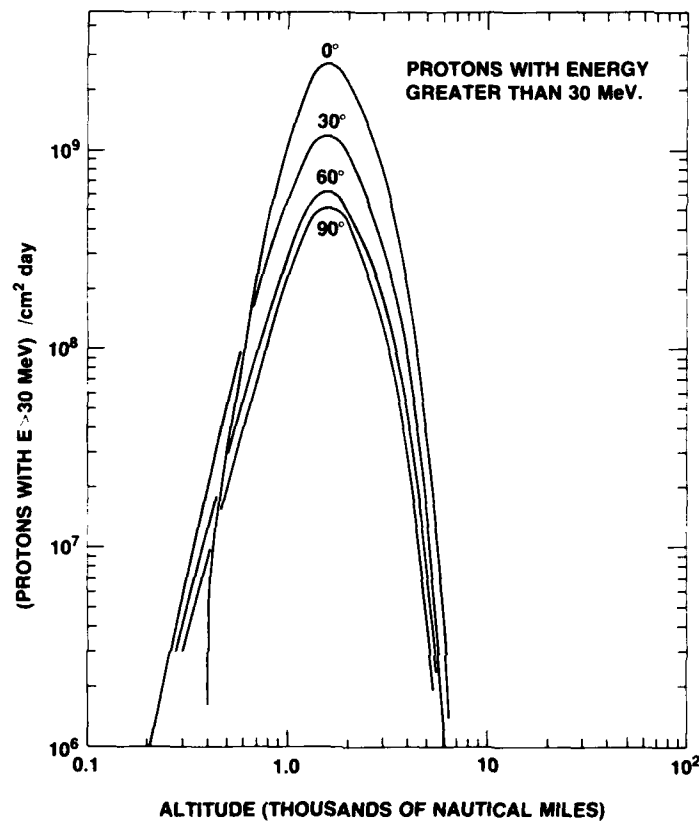


Figure 7. Time-Integrated Fluxes (Fluences) of High Energy Protons for Various Circular Orbits as a Function of Altitude. (Courtesy of E. Petersen)

4. LABORATORY SIMULATIONS OF SOFT ERRORS

A number of laboratories have been actively simulating the soft-error phenomena using accelerator facilities. Figure 8 is a schematic of the heavy-ion exposure facility set up at the Lawrence Berkeley Laboratory which has been used for testing by the Aerospace, Jet Propulsion Laboratory, Hughes Aircraft, and Rockwell groups.^{13, 16} The heavy ions from the cyclotron pass under vacuum through a brass collimator and a thin scintillation foil before striking the circuit device.

16. Brucker, G. J., Chater, W., and Kolasinski, W. A. (1980) Simulation of Cosmic-ray-induced soft errors in CMOS/SOS memories, IEEE Trans. Nucl. Sci. NS-27:1490.

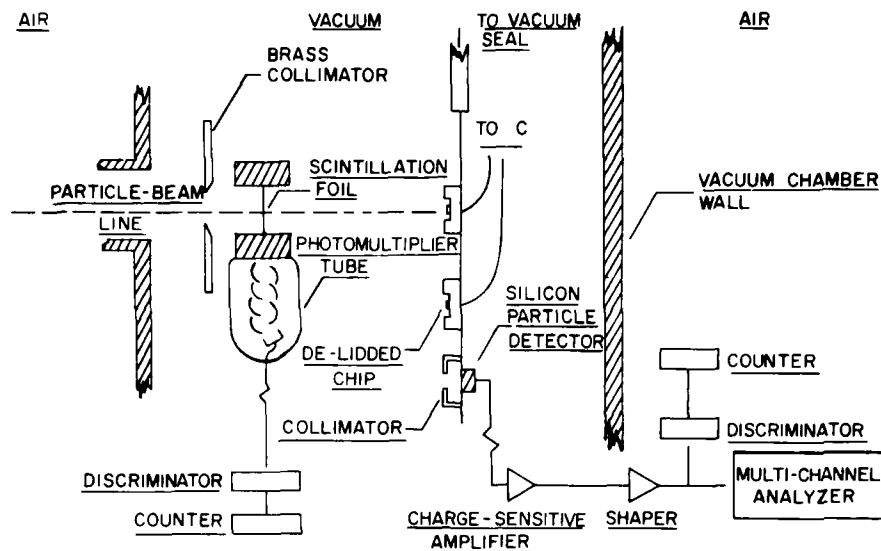


Figure 8. Schematic Representation of Test-Sample Hardware and Beam Monitoring System Used For Device Testing at the LBL 88 Inch Cyclotron. (Kolasinski et al¹³)

The angle of incidence can be varied and a silicon particle detector can be moved into the beam to determine the exposure rate. The Aerospace tests using this device are summarized in Table 1. Table 2 presents an example of test results for a particular device. A number of proton facilities have also been used for device testing: the RARAF Van de Graaf facility at Brookhaven National Laboratory has been used for studies by McNulty et al⁶ for protons below 4 MeV; the Naval Research Laboratory 75 MeV cyclotron has been used by Guenzer et al^{7, 17} and Price et al¹⁸ to test devices exposed to 32 MeV protons and 6-14 MeV neutrons; and the Harvard Cyclotron has been used by McNulty et al^{15, 18, 19} for proton energies between 32 and 130 MeV. Figure 9 illustrates the experimentally determined soft-error cross section versus proton energy for 4K dynamic and static

17. Guenzer, C.S., Allas, R.G., and Campbell, A.B., Kidd, J.M., Petersen, E.L., Seeman, M., and Wolicki, E.A. (1980) Single event upsets in RAMs induced by protons at 4.2 GeV and protons and neutrons below 100 MeV, IEEE Trans. Nucl. Sci. NS-27:1485.
18. Price, W.E., Nichols, D.K., and Soliman, K.A. (1980) A study of single event upsets in static RAMs, IEEE Trans. Nucl. Sci. NS-27:1506.
19. McNulty, P.J., Farrell, G.E., Wyatt, R.C., Rothwell, P.L., and Filz, R.C. (1980) Upset phenomena induced by energetic protons and electrons, IEEE Trans. Nucl. Sci. NS-27:1516.

Table 1. History of USAF Space Division and the Aerospace Corporation Involvement in Heavy Ion Tests

DATE	TEST FACILITY	OTHER PARTICIPANTS	PARTICLE SPECIES	EFFECT OBSERVED
JUN 78	LBL BEVALAC	HUGHES	Fe	BIT ERRORS
SEP 78	LBL 88" CYCLOTRON	ROCKWELL	Ar	BIT ERRORS
JAN 79	LBL 88" CYCLOTRON	HUGHES, JPL	Ar, Kr	BIT ERRORS, LATCHUP
FEB 79	LBL 88" CYCLOTRON	HUGHES, JPL	Ar, Kr	BIT ERRORS, LATCHUP
APR 79	LBL 88" CYCLOTRON	ROCKWELL	Ar, Kr	BIT ERRORS
JUN 79	LBL 88" CYCLOTRON	LOCKHEED	Kr	BIT ERRORS, LATCHUP
AUG 79	LBL 88" CYCLOTRON	LOCKHEED, SANDIA	Kr, Ar, Ne	BIT ERRORS, LATCHUP
JAN 80	LBL 88" CYCLOTRON	LOCKHEED, SANDIA, RCA	Kr	BIT ERRORS, LATCHUP
MAY 80	LBL 88" CYCLOTRON	LOCKHEED, RCA	Kr, Ar, Ne, O, C	BIT ERRORS, LATCHUP
JUN 80	LBL 88" CYCLOTRON	ROCKWELL, NASA	Kr, A	BIT ERRORS, LATCHUP
AUG 80	LBL 88" CYCLOTRON	NONE	Kr	BIT ERRORS
DEC 80	LBL 88" CYCLOTRON	JPL, NASA, ROCKWELL	Kr, Ar, O	BIT ERRORS, LATCHUP

Table 2. Example of Test Results
HM6508 RAM - 150 MeV ⁸⁴Kr Ions

PART SOURCE AND ID	LATCH-UP CROSS SECTION	BIT-FLIP CROSS SECTION	ANGLE OF INCIDENCE
SP-8 A	$4.1 \times 10^{-5} \text{ cm}^2$	$1.1 \times 10^{-2} \text{ cm}^2$	0°
SP-8 B	7.0×10^{-5}	1.1×10^{-2}	0°
SP-8 C	5.9×10^{-5}	1.1×10^{-2}	0°
SP-8 D	9.3×10^{-5}	1.1×10^{-2}	0°
SP-8 E	6.4×10^{-5}	1.1×10^{-2}	0°
SP-8 F	7.3×10^{-5}	1.1×10^{-2}	0°
GPS A'	0	0.2×10^{-3}	30°
GPS B'	0	0.5×10^{-3}	30°
GPS C'	0	0.2×10^{-3}	30°
GPS D'	0	0.2×10^{-3}	30°
GPS A'	0	3.8×10^{-3}	60°
GPS B'	0	3.2×10^{-3}	60°
GPS C'	0	2.7×10^{-3}	60°
GPS D'	0	1.4×10^{-3}	60°

ESTIMATES OF INFLIGHT ANOMALY RATE		
HM6508 SP-8	6 LATCHUPS PER 1000 YEARS PER CHIP	
	3 BIT ERRORS PER YER PER CHIP	
HM6508 GPS	NO LATCHUP SUSCEPTIBILITY	
	1 BIT ERROR PER 25 YEARS PER CHIP	

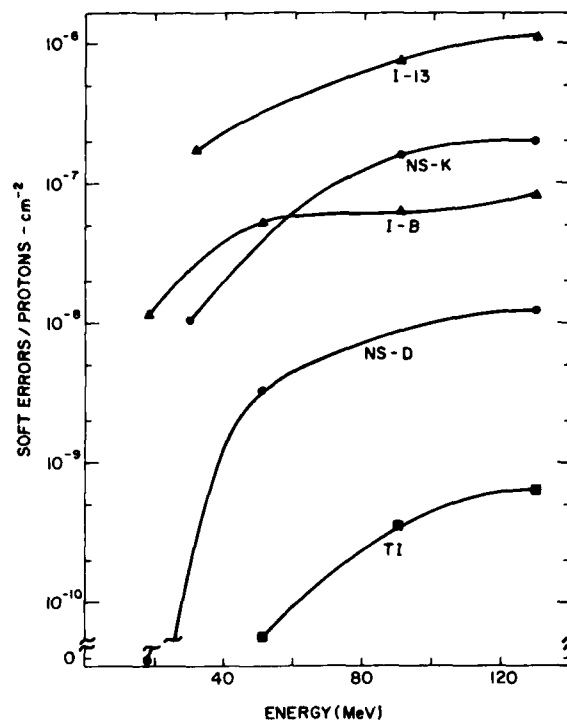


Figure 9. Soft-Error Cross Section Versus Proton Beam Energy. (McNulty et al¹⁹)

RAMs. Although the trend is the same for all devices, there is considerable variation among devices of the same type. All soft-error cross sections increase with proton energies from 32 to 130 MeV.

It is of interest to consider the results of a simulation study in which surface-barrier detectors were used to represent the sensitive volume element. The detectors range in thickness from 2 to 200 μm . Figure 10 is a schematic drawing of a nuclear interaction occurring in a thin surface-barrier detector. Figure 11 shows the experimental configuration used at the Harvard Cyclotron to test such devices. The integral event rate (that is, events in which energy $\geq E$ is deposited) is plotted in Figure 12 versus particle energy for detectors 2.5, 4.0, 24.1, 100 and 200 μm thick. The rate of events in which at least a threshold amount of energy is deposited in a 4 μm thick detector is plotted versus incident proton energy in Figure 13 for different threshold values. It was found that the detector data in this figure exhibit a dependence on proton energy similar to that exhibited for 4K RAM devices in Figure 9.

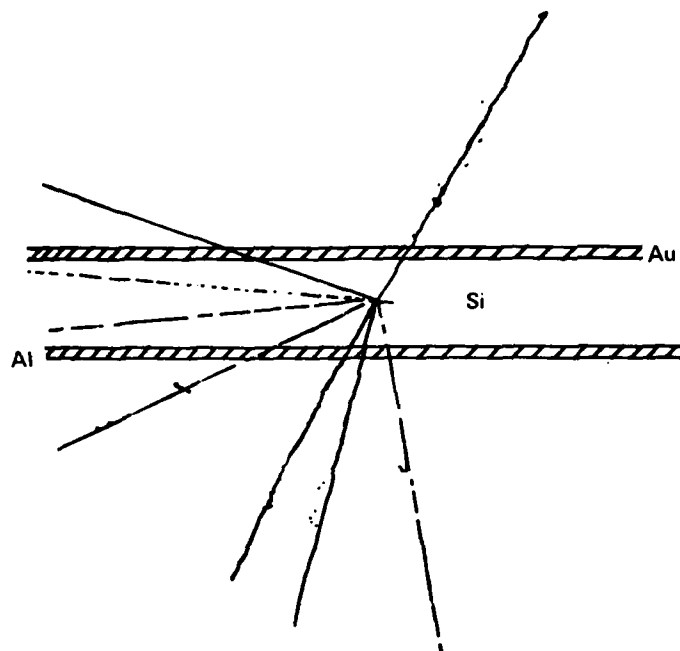


Figure 10. Proton-Induced Nuclear Interaction in a Silicon Surface-Barrier Detector. (McNulty et al¹⁹)

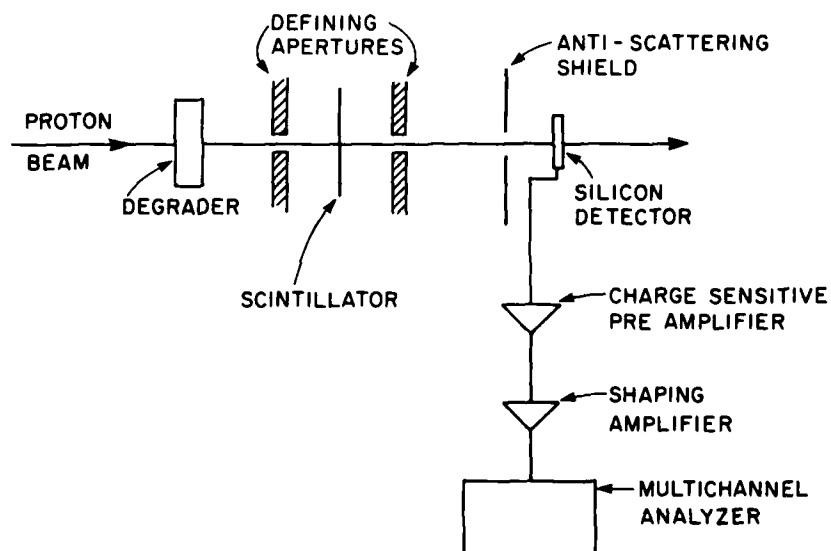


Figure 11. Experimental Configuration for the Surface-Barrier Detector Exposures to Protons at the Harvard Cyclotron (McNulty et al¹⁹)

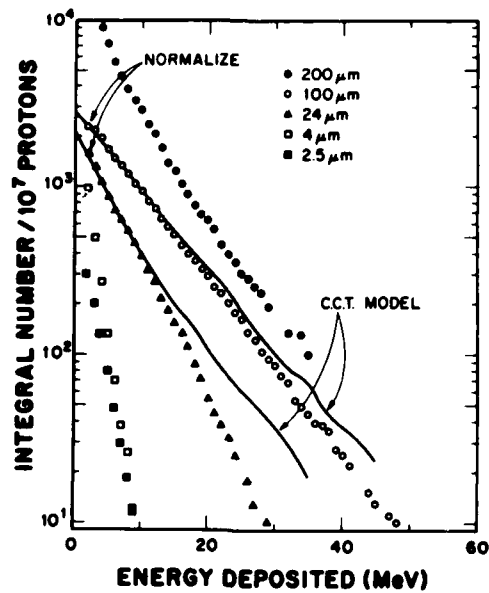


Figure 12. Event Rate for Depositing $\geq E$ versus E for Detectors 4, 24, 100, and 200 μm Thick

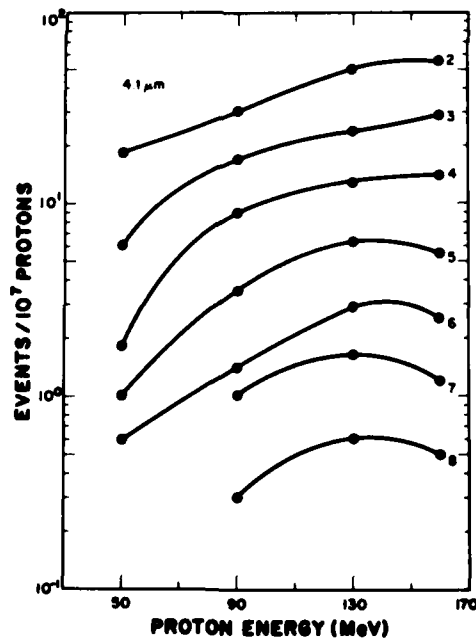


Figure 13. Event Rate versus Proton Energy for Various Values of E in a 4 μm Thick Detector

5. DOSE AND DOSE RATE SENSITIVITY

Different devices have different degrees of total dose vulnerability. Table 3 summarizes the hardness levels attainable in various IC technologies. Notice that one type of component is vulnerable at only 700 rad (SI), and thus is only slightly more radiation resistant than the human body. Figure 14 plots the predicted yearly dose for devices on GPS satellites versus the thickness of shielding. The data in Figure 15 illustrate how the dose periodicity measured by a dosimeter on a GPS satellite varies with solar rotation phase. Notice that order-of-magnitude changes in radiation doses can be experienced from one day to the next. Solar events also increase the dosage by large amounts during short periods.

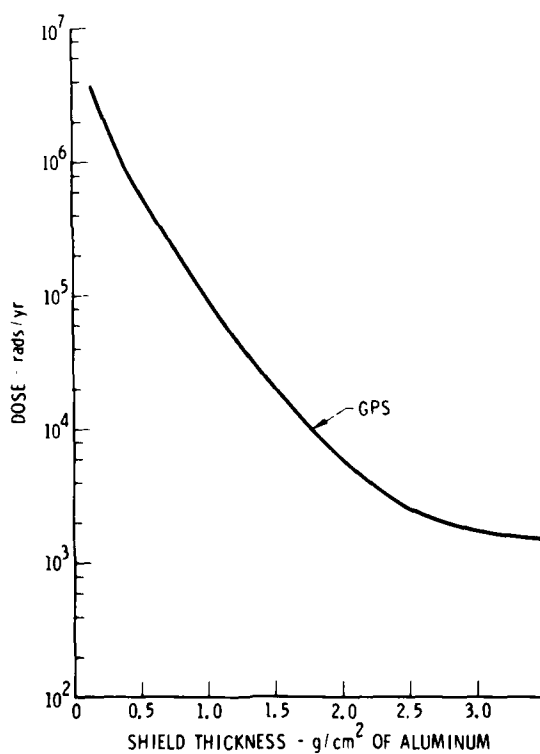


Figure 14. Annual Dose on GPS Satellites Versus Shielding Thickness. (Courtesy of J. B. Blake)

Table 3. State-of-the-Art Hardness Levels in Digital IC Technologies
D.M. Long (IEEE NS-27, 1974)

DIGITAL IC TECHNOLOGY	NEUTRON HARDNESS n/cm^2 (1 MEV)	TOTAL DOSE HARDNESS		SHORT PULSE TRANSIENT UPSET HARDNESS (RAD (SI)/SEC)
		COMMERCIAL (RAD(SI))	HARDENED (RAD(SI))	
BIPOLAR:				
TTL:				
LSI PRODUCTS	1×10^{14}	1×10^6	1×10^6	5×10^7
ECL:				
100K SERIES	1×10^{15}	1×10^7	1×10^7	3×10^8
IL:				
9900 SERIES	3×10^{13}	3×10^6	3×10^6	3×10^9
ISL	5×10^{14}	5×10^6	5×10^6	2×10^7
MOS:				
NMOS:				
LSI PRODUCTS	1×10^{15}	7×10^2	1×10^4	3×10^5
CMOS:				
LSI PRODUCTS	1×10^{15}	1×10^3	5×10^4	3×10^7
4000 SERIES	1×10^{15}	5×10^3	1×10^5	3×10^7
CMOS/SOS:	1×10^{15}	1×10^3	1×10^6	5×10^9

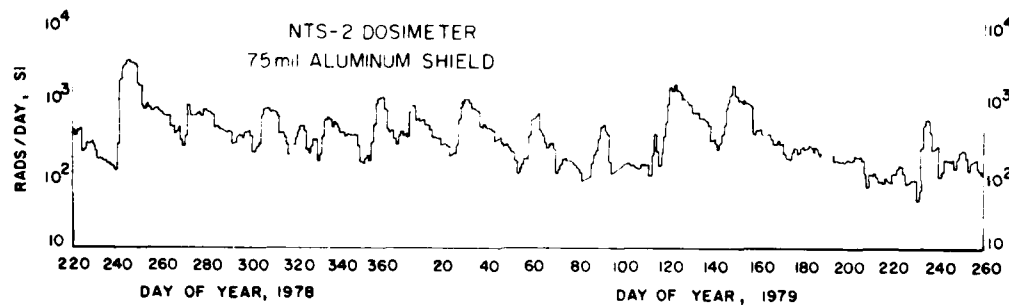


Figure 15. Fluctuations in Daily Dose on a GPS Satellite. (Courtesy of J. B. Blake)

6. ACCELERATED TESTING

A common way to measure the effects of radiation exposure is to place the device to be studied in front of a source or into an accelerator beam, in a few minutes simulating the total dose expected over several years in space. While necessary, this accelerated testing has some potential for misleading results. Some devices may be subject to the "reciprocity error" analogous to photographic emulsions exposed to light, that is, the response is different for a high-level exposure over a short duration than for low level exposure over a long period. There is some reason to believe that recent data from the GEOS-2 satellite suffers from this error source. However, there does seem to be a consensus in the radiation-effects community that adequate laboratory procedures have been developed which, if followed, provide the data necessary to screen parts for total dose and dose-rate failures.

The single-particle effects, on the other hand, represent a new type of problem in dosimetry and developing screening procedures may prove more difficult. The terms dose and dose rate are less useful; there is no threshold dose for effects that can be caused by a single particle, only a probability of a critical or threshold amount of energy being deposited within one of the microscopic sensitive-volume elements. Different radiation types can have far different efficiencies for inducing soft errors or latch up, perhaps requiring the introduction of terms analogous to the Relative Biological Effectiveness (RBE) used by radiation biologists. These relative efficiencies may change dramatically if one of the microscopic dimensions of the sensitive element and/or its bias are changed.

One difficulty in developing accelerated testing procedures for sensitivity to single-particle effects is the fact that no single facility is adequate to represent the radiation environment of space which includes many components, each of which has a wide range of incident energies. Currently, testing must be done at more

than one cyclotron and even then there are potentially significant gaps. Exposures must be carried out at reduced intensities to ensure that the observed effects are induced by individual particles.

There is every reason to believe that adequate testing procedures for single-particle effects will eventually be developed. Perhaps what is most needed is a way to confirm the adequacy of the procedures developed. A possible scenario is for a panel of "experts" to agree on a test procedure and algorithms for using the data to predict error rates in space. The procedures would be tried on a variety of device technologies and the results compared with at least one space trial. The devices compared should cover a wide range of sensitivities and different sensitive microelement geometries and sizes in order to validate the procedures' predictive power.

Any space trial of circuits should include microdosimetry that is relevant to single-particle effects. This should include simultaneous measurements of energies and directions of the incident particles and the energy-deposition spectra for typical microelement geometries.

7. DIELECTRIC CHARGING ON SPACECRAFT

An important disruptive process for spacecraft electronic systems is dielectric charging by energetic particles. Particles of keV and MeV energies incident upon a dielectric, such as the insulator of a connector cable, will penetrate below the material surface and can remain there, imbedded in the good insulator. If a large number of such particles build up a substantial space charge, breakdown of the dielectric medium in a discharge process takes place. This not only causes physical damage to the insulator itself, it also causes fast electronic pulses in the devices connected to the cable. These events are known as cable charging and discharging phenomena. Also, prior to the discharge, the space charge within the dielectric causes image charges on nearby conductors, the electrical state of which is thus altered.

Another well-known charging phenomenon is spacecraft surface charging. This process is thought responsible for "arcing" in the vicinity of sharp edges and irregularities on the spacecraft body. This is primarily a conducting surface effect caused by lower energy ambient plasma electrons in the immediate spacecraft environment, perhaps energies in the tens of thousands electron-Volt range. These electrons are plentiful in the outer radiation zone where they contribute to the extraterrestrial ring current. The SCATHA spacecraft research program is used for studying cable effects and surface-charging effects in space. The results of 377 days of data from the SCATHA Pulse Analyzer experiment are summarized in Figure 16. Here a significant number of substantial charging currents are illustrated

SCATHA Pulse Analyzer Results

377 DAYS OF DATA

- 3911 TOTAL PULSES

- 2492 VEHICLE COMMANDS OR S-TONES

- 1400 BEAM OPERATIONS

- 15 SURFACE CHARGING EVENTS

- 4 CABLE CHARGING EVENTS

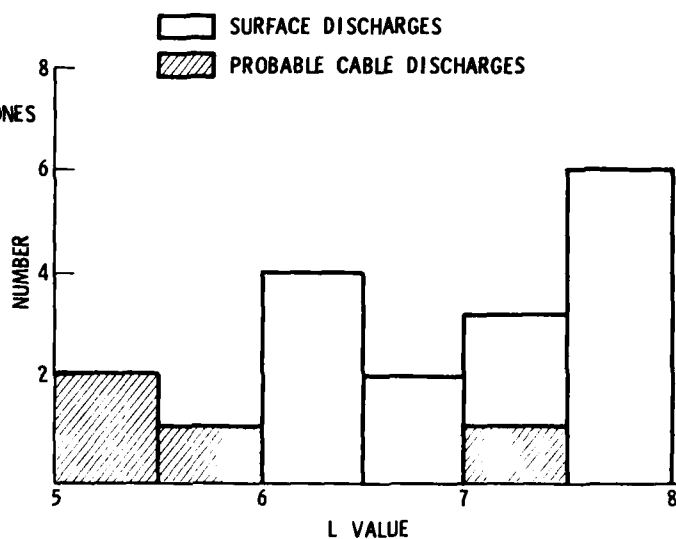


Figure 16. Summary of SCATHA Pulse Analyzer Results. (Courtesy of J. B. Blake)

GPS Clock Anomaly

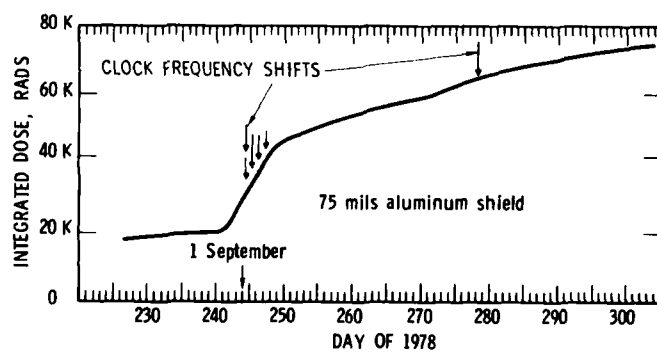


Figure 17. Integrated Dose as a Function of Time. The arrows represent anomalous clock events. (Courtesy of J. B. Blake)

as function of L-Shell where they occurred. Onboard anomalous clock frequency shifts on GPS appeared to correlate with changes in dose as illustrated in Figure 17. Improved data on fluctuations in the flux of energetic (> 100 keV) particles are clearly desirable if we are to understand fully this type of environment-spacecraft interaction.

8. RADIATION ENVIRONMENT IN SPACE

A precise understanding of the various radiation environments for different locations of interest in space, including low orbits which go through the South Atlantic Anomaly, medium orbits in the radiation belts, geosynchronous orbits with time-varying dose rates, trajectories through the Jovian belts, and the universally encountered cosmic rays of deep space is necessary in order to achieve optimum spacecraft instrument design. A knowledge of the types of particles and their energies is particularly important for predicting single-particle effects. Calculations would involve combining the measured spectra with soft-error and latch-up cross sections measured in the laboratory.

A microdosimetry study of the radiation environment of space has never been carried out. It is important to initiate such studies because single-particle effects result from energy deposition in microscopic volume elements. It will be essential to ensure that the energy-deposition spectra measured for characteristic microvolumes in space are being adequately simulated in accelerated testing studies.

9. FUTURE STUDIES AND NEEDS

A number of new testing procedures must be developed to meet current and future needs. Tests are currently being developed for flip flops, microprocessors, and other charge-storage devices. In addition to device modeling, one needs improved and simplified definitions of the heavy-ion environment in space. A new testing experiment entitled "Component Radiation Effects Measurement" (CREM) which is designed to measure the effects of radiation on devices and integrated circuits in space and on the ground, has now been proposed. It is a general finding that the soft-error problem becomes increasingly difficult as devices get smaller. The two solid curves in Figure 18 show Kirkpatrick's calculations of how the charge collection resulting from the traversal of an alpha particle changes as the dimensions of a circuit element are reduced.²⁰

20. Kirkpatrick, S. (1979) Modeling diffusion and collection of charge from ionizing radiation in silicon devices, IEEE Trans. Elect. Devices ED-26:1742.

SOFT UPSETS AND DEVICE SCALING

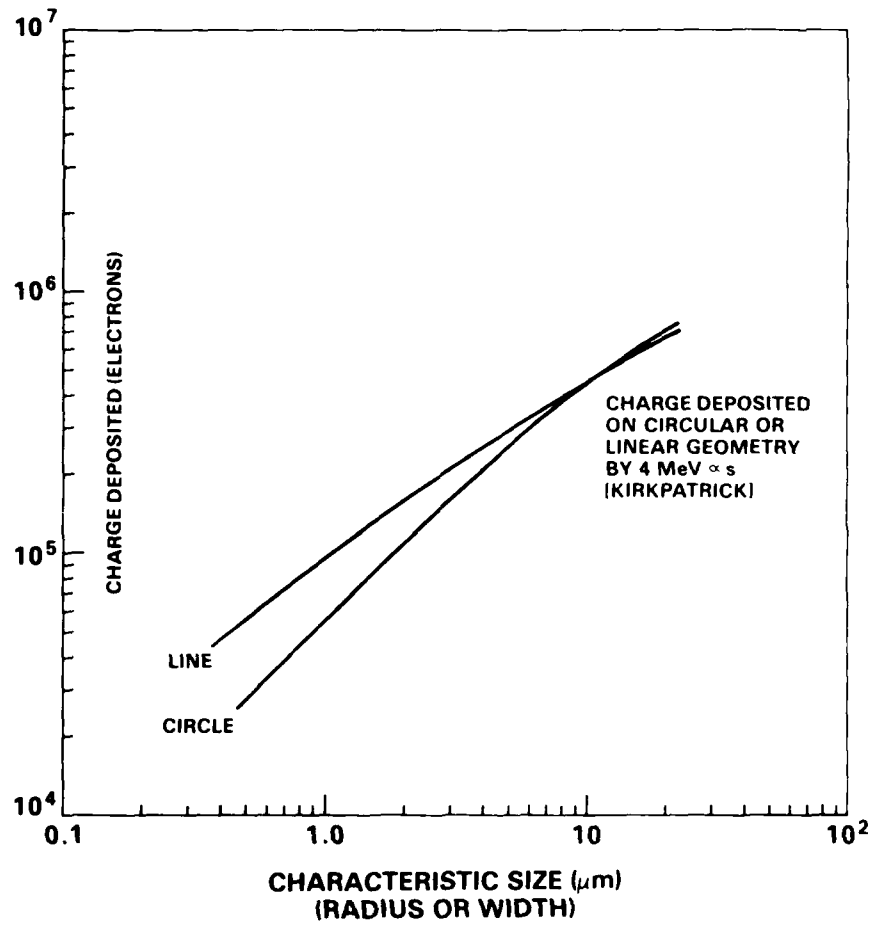


Figure 18. Charge Collection as a Function of Device Dimension. Solid curves represent Kirkpatrick's calculations²⁰ of the charge collection as characteristic dimensions are reduced

The problem of estimating soft-fail rates for LSI or VLSI devices to be flown in space requires accurate microdosimetric models of the type described by Bradford^{9,21,22} for the deposition of energy in volume elements having dimensions of a few microns or less, as well as good definition of the physical and electrical parameters of the sensitive elements. To apply such models it will be necessary to have improved measurements and/or precise models of the energetic protons and heavy ions in the radiation belts.

In summary, further miniaturization and increase in complexity of onboard microprocessor electronics will result in increased vulnerability of these circuits to radiation. It is imperative that future work on "hard" electronics components, error correcting circuitry, and redundancy design in critical areas be carried out. It is also vital to know precisely the radiation environment in which these devices operate.

-
21. Bradford, J.N. (1980) Geometric analyses of soft errors and oxide damage produced by heavy cosmic rays and alpha particles, IEEE Trans. Nucl. Sci. NS-27:942.
 22. Bradford, J.N. (1980) Single event error generation by 14 MeV neutron reactions in silicon, IEEE Trans. Nucl. Sci. NS-27:1480.

References

1. Binder, D., Smith, E.E., and Holman, A.B. (1975) Satellite anomalies from cosmic rays, IEEE Trans. Nucl. Sci. NS-22:2675.
2. Pickele, J.C., and Blandford, J.T. (1978) Cosmic ray induced errors in MOS memory cells, IEEE Trans. Nucl. Sci. NS-25:1166.
3. Filz, R.C., and Katz, L. (1974) An Analysis of Imperfections in DMSP Photographs Caused by High Energy Solar and Trapped Protons, Air Force Report AFCRL-TR-74-0469, AD A007 679.
4. Croft, T.A. (1977) Nocturnal Images of the Earth From Space, Stanford Research Institute Report No. 68197.
5. McNulty, P.J., Pease, V.P., Bond, V.P., Filz, R.C., and Rothwell, P.L. (1977) Particle induced visual phenomena in space, Radiation Effects 34:153.
6. Wyatt, R.C., McNulty, P.J., Toumbas, P., Rothwell, P.L., and Filz, R.C. (1979) Soft errors induced by energetic protons, IEEE Trans. Nucl. Sci. NS-26:4905.
7. Guenzer, C.S., Wolicki, E.A., and Allas, R.G. (1979) Single event upset of dynamic RAMs by neutrons and protons, IEEE Trans. Nucl. Sci. NS-26:5048.
8. Ziegler, J.F., and Lanford, W.A. (1979) Effect of cosmic rays on computer memories, Science 206:776.
9. Bradford, J.N. (1980) Cosmic ray effects in VLSI, in Space Systems and Their Interactions with Earth's Space Environment, Eds. H.B. Garrett and C.P. Pike, American Institute of Aeronautics and Astronautics, New York.
10. Sivo, L.L., Andrews, J.L., and Mathers, H.W. (1979) Upset testing of LSI devices, IEEE Trans. Nucl. Sci. NS-26:4778.
11. Petersen, E.L. (1980) Nuclear reactions in silicon, IEEE Trans. Nucl. Sci. NS-27:1494.

12. Sivo, L.L., Peden, J.C., Brettschneider, M., Price, W., and Pentecost, P. (1979) Cosmic-ray-induced soft errors in static MOS memory cells, IEEE Trans. Nucl. Sci. NS-26:5042.
13. Kolasinski, W.A., Blake, J.B., Anthony, J.K., Price, W.E., and Smith, E.C. (1979) Simulation of cosmic-ray-induced soft errors and latchup in integrated-circuit computer memories, IEEE Trans. Nucl. Sci. NS-26:5087.
14. Hamm, R.M., Turner, J.B., Wright, H.A., and Ritchie, R.H. (1979) Heavy ion track structure in silicon, IEEE Trans. Nucl. Sci. NS-26:4892.
15. McNulty, P.J., Wyatt, R.C., Farrell, G.E., Filz, R.C., and Rothwell, P.L. (1980) Proton upsets in LSI memories in space, in Space Systems and Their Interactions with Earth's Space Environment, Eds. H.B. Garrett and C.P. Pike, American Institute of Astronautics and Aeronautics, New York p 413.
16. Brucker, G.J., Chater, W., and Kolasinski, W.A. (1980) Simulation of cosmic-ray-induced soft errors in CMOS/SOS memories, IEEE Trans. Nucl. Sci. NS-27:1490.
17. Guenzer, C.S., Allas, R.G., and Campbell, A.B., Kidd, J.M., Petersen, E.L., Seeman, M., and Wolicki, E.A. (1980) Single event upsets in RAMs induced by protons at 4.2 GeV and protons and neutrons below 100 MeV, IEEE Trans. Nucl. Sci. NS-27:1485.
18. Price, W.E., Nichols, D.K., and Soliman, K.A. (1980) A study of single event upsets in static RAMs, IEEE Trans. Nucl. Sci. NS-27:1506.
19. McNulty, P.J., Farrell, G.E., Wyatt, R.C., Rothwell, P.L., and Filz, R.C. (1980) Upset phenomena induced by energetic protons and electrons, IEEE Trans. Nucl. Sci. NS-27:1516.
20. Kirkpatrick, S. (1979) Modeling diffusion and collection of charge from ionizing radiation in silicon devices, IEEE Trans. Elect. Devices, ED 26:1742.
21. Bradford, J.N. (1980) Geometric analyses of soft errors and oxide damage produced by heavy cosmic rays and alpha particles, IEEE Trans. Nucl. Sci. NS-27:942.
22. Bradford, J.N. (1980) Single event error generation by 14 MeV neutron reactions in silicon, IEEE Trans. Nucl. Sci. NS-27:1480.

Contents

1. Introduction	126
2. The Radiation Environment: Empirical Data	127
3. Requirements for Radiation Belt Measurements	131
4. Energetic Ion (Proton) Detectors: Bulk Measurements	134
5. Low Energy Ion Composition Measurements	148
6. Energetic Ion Composition Measure- ments	154
7. Low Energy Electron and Bulk Ion Measurements	175
8. Energetic Electron Measurements	187
9. Other Types of Measurements	197
9.1 X-ray Cameras	197
9.2 High Energy Dose and Flux Meters	202
9.3 Nuclear Track Techniques	204
10. Summary	205
References	205

5. State of the Art of Energetic Particle Measurements in the Earth's Magnetosphere

by

Walther N. Spjeldvik
Nordmann Research Ltd.
Boulder, Colorado 80303
and

Cooperative Institute for Research in
Environmental Sciences
University of Colorado
Boulder, Colorado 80309

based on presentations given by

Daniel N. Baker (Los Alamos Scientific Laboratories)
Richard G. Johnson (Lockheed Palo Alto Research Laboratories)
Berend Wilken (Max Planck Institute for Aeronomy)
R.W. McEntire (Applied Physics Laboratory)
David A. Hardy (Air Force Geophysics Laboratory)
Joseph Reagan (Lockheed Palo Alto Research Laboratories)
R.C. Filz (Air Force Geophysics Laboratory)
George Parks (University of Washington)

I. INTRODUCTION

More than two decades have passed since the discovery of the earth's radiation belts.^{1,2,3} This period has been one of rapid development of space technology in general and of instrumentation for measurements of charged particle populations in particular. Early measurements used recoverable nuclear emulsions on rockets and satellites, and other types of instruments including Geiger tubes with different kinds of shielding material, NaI scintillation crystals, CsI detectors, plastic scintillators and various fluorescent screens mounted on photomultiplier tubes.⁴ Later, solid state detectors came into use and increasingly sophisticated onboard data discrimination and processing electronics were developed. For a review of energetic particle space instrumentation used or designed prior to 1970, see Ögelman and Wayland⁵ and for a detailed treatment of semiconductor detectors, see Brown et al.⁶

This paper emphasizes the later developments in instrument technology and is organized into a section on empirical data for the radiation environment showing the great dynamical range of the particle fluxes, and a section on ideal requirements for radiation belt measurements. This is followed by description of existing and currently developed instrumentation to meet these requirements. There is a section on bulk measurements of energetic ions, a section on low energy ion composition measurements, a section on energetic ion composition measurements, a section on low energy electron and ion bulk measurements, and a section on energetic electron measurements. Other types of measurement techniques are also briefly mentioned and the summary section gives an overview of the status of the

1. Van Allen, J.A. (1957) Direct detection of auroral radiation with rocket equipment, Proc. National Academy Sci. 43:57.
2. Van Allen, J.A., Ludwig, G.H., Ray, E.C., and McIlwain, C.E. (1958) Observation of high intensity radiation by satellites 1958 Alpha and Gamma, Jet Propulsion, 28:588.
3. Van Allen, J.A. (1959) The geomagnetically-trapped corpuscular radiation, J. Geophys. Res. 64:1683.
4. Van Allen, J.A. (1962) Dynamics, composition and origin of the geomagnetically-trapped corpuscular radiation, Trans. International Astronomical Union, XIB:99.
5. Ögelman, H. and Wayland, R.H. (1970) Introduction to Experimental Techniques of High Energy Astrophysics, NASA/Goddard Space Flight Center, Washington, D.C.
6. Brown, W.L., Higginbotham, W.A., Miller, G.L., and Chase, R.L. (editors) (1969) Semiconductor Nuclear-Particle Detectors and Circuits, National Academy of Sciences, Publication 1594, Washington, D.C.

space instrumentation for magnetospheric particle measurements over energies ranging from ~ 10 eV to hundreds of MeV. No claim of completeness in description of all types of instruments for magnetospheric particle measurements is made; in particular instrument designs of Soviet origin are not included.

The paper is generated based on topical presentations given at the Air Force Geophysics Laboratory Radiation Belt Workshop, 26-27 January 1981, by Drs. Daniel N. Baker of Los Alamos Scientific Laboratories, Richard G. Johnson of Lockheed Palo Alto Research Laboratories, Berend Wilken of Max-Planck Institut für Aeronomie, R. W. McEntire of Applied Physics Laboratory, Johns Hopkins University, David A. Hardy of Air Force Geophysics Laboratory and Joseph Reagan of Lockheed Palo Alto Research Laboratories, and also on brief presentations given by R. C. Filz of Air Force Geophysics Laboratory, George Parks of University of Washington and other participants in the workshop who helped clarify specific points. The aim of the instrumentation session was not to review all possible detector designs but rather to give a representative overview of existing and proposed quality instrumentation for radiation belt particle measurements. The material presented in this paper is based on contributions from a number of institutions. Significant progress in energetic ion spectroscopy resulted from development work in many laboratories, among them the Aerospace Corporation, APL-Johns Hopkins University, NOAA/ERL-SEL, University of Maryland and the Max-Planck Institut in West Germany. Advances in low energy particle analyzers were made by UCSD, Lockheed/Palo Alto, University of Iowa, Los Alamos, AFGL and a number of other institutions.

2. THE RADIATION ENVIRONMENT: EMPIRICAL DATA

For optimum design of the instrumentation built to measure geomagnetically trapped corpuscular radiation it is necessary to have some knowledge of the intensity of the fluxes likely to be encountered in different parts of the radiation belt region and other parts of geospace. This entails an assessment of the particle species, the dynamic range of the trapped fluxes and the probable directionality. One must also know the energy range of the different components. It is now known that particle energies in the radiation belts extend from thermal energies (below 1 eV) to hundreds of MeV; effectively nine orders of magnitude. Particles of even higher energies are also encountered, but these are cosmic rays on transit through geospace; their gyro-radii are generally too large to permit trapping in the radiation belts.

Information on the trapped radiation has been compiled by NASA based on early data collected during the first decade of in situ geospace monitoring and constitutes empirical statistical models of mean electron and bulk ion fluxes between 100 keV and tens of MeV. The most up-to-date of these models, the AP-8 proton (ion) and the AE-7 electron models give the empirical most probable particle fluxes as function of particle energy and location within the radiation belts; for details about the development and characteristics of these models, see Vette et al.⁷ and references therein. An example of the statistically average proton and other ion fluxes for solar minimum conditions is given in Figure 1 as integral, omnidirectional flux versus ion energy. This illustration shows the very large dynamic range requirement for adequate radiation belt ion measurements from well below 1 ion/cm²-sec-ster (integral flux) at several MeV energies in the outer radiation zone to well in excess of 10⁷ ion/cm²-sec-ster at L = 4 at tens of keV. These fluxes can become larger by orders of magnitude during magnetic storms and during solar maximum conditions.

In recent years we have learned that the ionic part of the radiation belts is not totally dominated by protons, but that heavier ions such as oxygen ions can be dominant at ≤ 10 keV energies as well as ≥ 1 MeV; for details, see the reviews of Shelley,⁸ Spjeldvik⁹ and Williams.¹⁰ The relative roles of heavier ions such as He⁺, He⁺⁺ and of carbon and oxygen ions are not well known for different geomagnetic conditions, although mass spectrometer results are now becoming available below approximately 20 keV. In an intermediate energy range from several tens of keV to several hundred keV per nucleon no composition measurements have yet been made; and at higher energies, primarily in the MeV range, composition measurements indicate a dominance of the heavier ions over protons.^{11,12,13}

Examples of omnidirectional radiation belt electron observations from OGO-1 and OGO-3 are given in Figure 2 and are taken from Vette et al.⁷ These data demonstrate the well known division of the radiation belts into an inner and an outer zone separated by a wide slot region, the location of which varies with electron energy (no two-zone structure applies to ions). These fluxes can vary from less than 10⁴ electrons/cm²-sec to approximately 10⁹ electrons/cm²-sec within the given energy range (>36 to <1970 keV); and can vary beyond these numbers at lower and higher energies. Thus, for electrons a very large dynamic range is also encountered. During disturbed times very large radiation enhancements are known to occur.

Because of the large number of references cited above, they will not be listed here. See References, page 205.

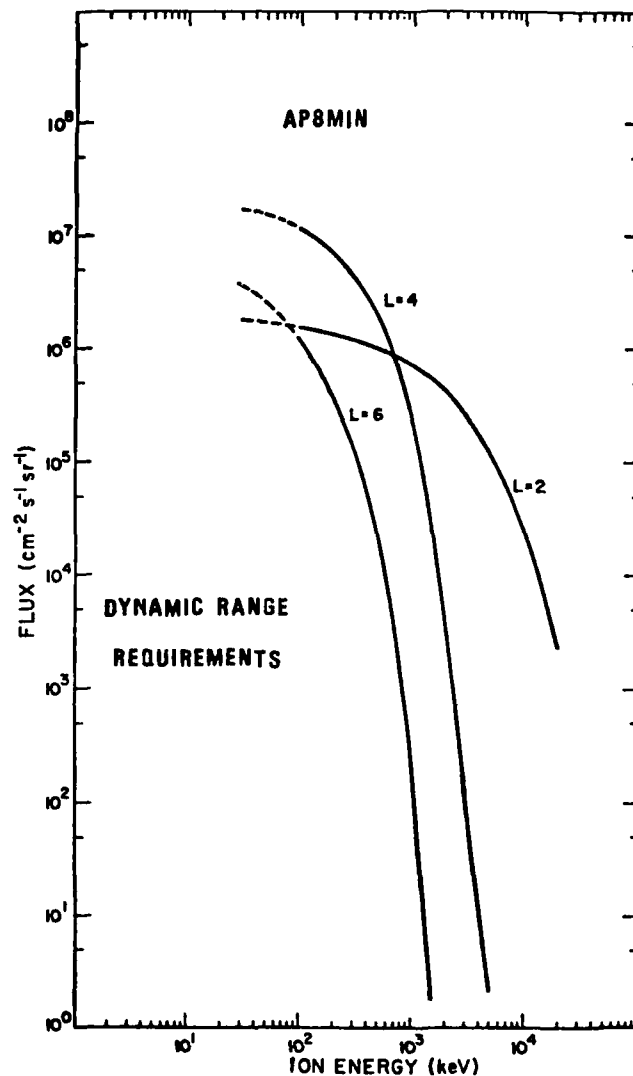


Figure 1. Empirical Radiation Belt Ion (Proton) Model for Solar Cycle Minimum Sunspot Conditions. The data are averages from measurements made during the 1960's and are given as integral flux above the indicated energy. The spectra at three sample L-shells are depicted: L = 2, 4, and 6. Notice the steep spectral gradients and the large dynamic range requirements for instruments designed to make these measurements. This is the NASA AP-8 bulk ion (usually labeled proton) model; see Vette et al⁷

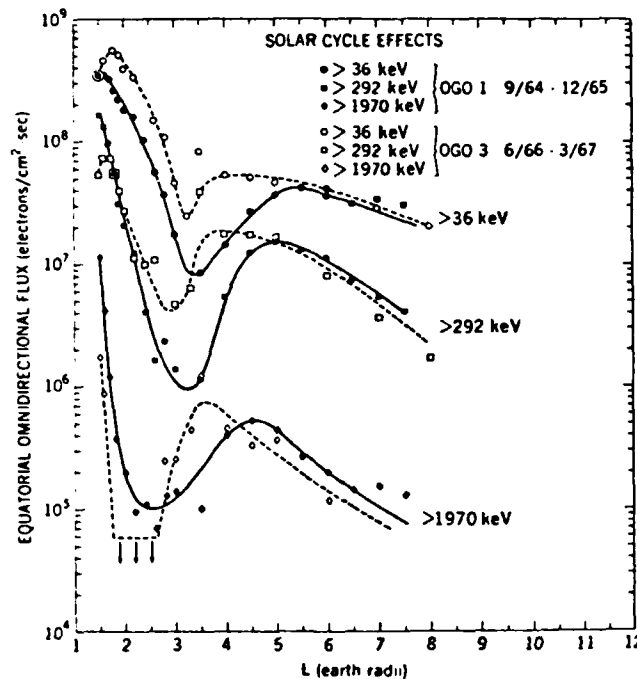


Figure 2. Radiation Belt Electron Observations Made with the OGO-1 and OGO-3 Satellites During Periods in 1965 and 1967. The data are given as integral flux above the indicated energy and are radial profiles through the radiation belts. The division of the radiation zone into two belts separated by a 'slot-region' for electrons is clear, and the division moves toward lower L-shells with higher electron energy. The variation from 1965 to 1967 is attributed to solar cycle effects. The data also indicate a significant dynamic range for radiation belt electrons; see Vette et al⁷

Of course, these empirical fluxes only tell about the radiation belt conditions during the period when the data were obtained. Great perturbations that strongly distort the magnetosphere^{14, 15} are known to occur, and orders of magnitude enhancement in the very energetic (>1 MeV) ion populations have been observed, including observations of ions heavier than oxygen.^{16, 17, 18} Thus it is necessary to have a much greater dynamic instrumentation range than what current empirical models would indicate.

Because of the large number of references cited above, they will not be listed here. See References, page 205.

3. REQUIREMENTS FOR RADIATION BELT MEASUREMENTS

From a directional point of view there are two kinds of corpuscular radiation detectors: One is the dose meter which measures the total radiation encountered by a spacecraft within a certain range of particle energies, and the other is the flux meter which measures the incident flux of selected particle species at selected energies arriving from a given spatial direction. The latter type of instrument comes in a variety of designs, and most of this paper is devoted to describing the characteristics of such instruments.

Corpuscular radiation is detected through its interaction with:

- (a) material substances;
- (b) fields;
- (c) combination of matter and fields;
- (d) multiple material substances for timing purposes; or
- (e) extended material substances for imaging purposes.

Interaction with matter leads to energy deposition in the target (detector) material, angular scattering of the incident particle, release of secondary particles (most often electrons) from the target, excitation of photon emission, and (after long radiation exposure) radiation damage to the detector system. Interactions with fields cause directional deflection, energization, or retardation; the first is commonly used for particle selection while the latter two (also known as post-acceleration or post-retardation) are used to increase resolution or insure measurability after particle selection.

Instrument design considerations depend on the type of particles to be measured. Ideally these considerations should include:

- (1) Sensitivity to:
 - (a) low fluxes;
 - (b) different elemental species; and
 - (c) different charge states for heavy ions.
- (2) Wide Dynamic ranges for instruments to avoid saturation or malfunction at high flux levels;
- (3) Sufficient coverage of the particle energy range;
- (4) Sufficient coverage of all angular directions;
- (5) Adequate resolution in:
 - (a) time;
 - (b) energy;
 - (c) angular orientation;
 - (d) particle species identification; and
 - (e) ion charge state identification;

- (6) High degree of background suppression;
- (7) Radiation damage minimization; and
- (8) Versatility through reprogramming capability.

Of course, information about the intended spacecraft orbit strongly impacts the design considerations so as to insure the proper instrument shielding by passive (thick walls) or active (for example, anti-coincidence logic) means in hostile or benign radiation environments.

Sensitivity and dynamic range are both important for the performance of an instrument: How low a flux can one measure? What is the upper limit of flux detectability before instrument fails due to saturation or damage? The longevity of the instrument is also important. The need for both high sensitivity as well as many orders of magnitude dynamic range are clearly demonstrated in the foregoing section.

The energy range of interest in radiation belt physics spans the interval from eV to hundreds of MeV energies: effectively 8-10 orders of magnitude range. No single instrument has been developed for space application that can cover such a wide range. Fortunately, a combination of several different instrumental techniques provides the required data coverage for electrons and ions. Within the ion group two severe difficulties have long been present: identification of ion species and determination of the ionic charge state. Techniques employed during the last decade have had success in such identification only in limited energy ranges, but more modern designs now being developed for the NASA/GALILEO, OPEN and SOLAR POLAR missions promise extensive energy coverage with good mass and charge resolution. Some of these new techniques are described below, as well as existing space tested methods.

Angular coverage is very important both for the study of the radiation belt pitch angle distributions (which give information about wave-particle interactions, and thus instability and loss mechanisms) and for the study of the high latitude sources of the radiation belts through the loss/source cone mechanism. Most often the angular coverage is provided by the spacecraft spin (detector mounted perpendicular to the spin axis) although some spacecraft employ an additional scan platform for angular coverage on a non-spinning spacecraft or for full 3-dimensional angular coverage.

Traditionally the fineness of the angular resolution was limited by the instrument aperture opening angle: Higher geometric factors which led to greater detector sensitivity to low fluxes (a particularly important consideration for the measurements of the very energetic radiation) gave poor angular resolution. A novel design utilizing the so-called "bullet-shaped" (toroidal or annular) aperture overcomes this problem by providing both a large geometric factor and fineness in angular definition. This design is described in the energetic ion composition section of this paper.

The concept of "background" is a quality of each individual instrument; it generally means contributions to the count rate from classes of radiation other than the one for which the measurement is designed. Background counts in an ion detector may stem from UV and X-ray photons triggering the counter, electrons, penetrating radiation through the detector shielding (for example, X-rays and cosmic rays), pile-up effects from particles that singly cannot trigger the detector response but where two or more particles in simultaneous incidence (within the resolution time of the instrument) can cause triggering, or from count contributions from adjacent data channels. The latter is a known shortcoming of some mass spectrometers. Background counts can also appear because of the generation of Bremsstrahlung X-rays and from nuclear reactions within the spacecraft structure induced by high energy cosmic rays. Penetrating radiation can also trigger the electronic discrimination and on-board microprocessor directly causing "bit-flip" and "latch-up" effects; the latter may be eliminated or at least minimized through redundant electronics design, component shielding or other methods. Finally, noise counts can appear because of faulty internal electronic connections, too high operating temperature and degradation of the detector elements.

Serious consideration must also be given to the effect of the volume of information acquired on the telemetry transmission rate. It is highly desirable to have the capability to command three telemetry transmission rates:

- (a) Low duty operation where only survey grade information is telemetered to the ground.
- (b) Normal operation of all instruments with standard bit-rate transmission.
- (c) High bit-rate data collection for the purposes of studying spatial and temporal structures, and events in great detail.

As an example one has the NOAA/WAPS instrument on ISEE-2 which in its normal operation gives eight spectral points of energetic particle information for both ions and electrons eight times per spacecraft spin period (of approximately 3 sec). For special event studies, the instrument can be commanded into a high bit-rate mode which doubles both the spectral coverage and the time resolution.

Clearly, the use of high bit-rate modes must be limited because of antenna resource limitations and because too many data points collected may hinder rather than help the data processing and thus hinder optimum scientific data utilization. On the other hand, well selected periods of high resolution data have proven to be of great value.

Design considerations also include an assessment of the variability/stability of the plasma and energetic particles to be measured. Obviously, a rapidly evolving plasma requires high time resolution diagnostics. In laboratory plasmas such

time scales of interest can be very short (microseconds to minutes). Experience from earlier magnetospheric measurements indicate, however, that major changes in the trapped radiation usually occur on time scales of minutes, hours, and days, and for the most energetic inner zone trapped particles, years to hundreds of years. Some acceleration and injection events are rapid and may require sub-second resolution, however, and precipitation of particles takes place on characteristic time scales of seconds (pulsating aurora, etc.), minutes (auroral break-ups and discrete arcs), and hours (mid-latitude post-storm electron precipitation).

Of utmost importance in the design of particle flux meters is the separation and identification of the ion and electron fluxes. This has now been accomplished through a number of different design techniques some of which are described in a subsequent section of this report. For example, when the incident particle flux has been cleansed of electrons, by using a "broom"-magnet or pulse height discrimination in thin solid state detectors, the problem remains to:

- (1) Measure the ion energy,
- (2) Identify the elemental ion species, and
- (3) Identify the ion charge state.

Usually, the angular directionality has already been determined through the collimator aperture system of the detector, although some techniques use multiple detectors for post-determination of the angle of incidence. While a slowly spinning spacecraft (such as SCATHA) makes an ideal platform for studies of the ambient pitch angle distributions of trapped particles, it precludes the detailed study of fast variations (such as in precipitation and upward jetting plasma phenomena). Instruments with high geometric factor and high time resolution on a rapidly spinning spacecraft could accomplish both requirements; however, a high data telemetry rate would be required, and the amount of data to be reduced would be large. Spacecraft with spin-rate adjustment capability and reprogrammable on-board instrument operation would be desirable, as well as a despun platform able to "look" towards the atmosphere along the magnetic field direction.

4. ENERGETIC ION (PROTON) DETECTORS: BULK MEASUREMENTS

Modern designs for energetic ion detection often employ solid state detectors, and frequently use a dual detector arrangement. In this arrangement, a thin front element detects a small fraction of the incident energy (from which the energy deposition rate dE/dx is deduced), while a thick rear element measures the total residual ion energy (E). Proper electronic pulse height discriminator electronics then process the signal into information about ion energy, and to some limited extent also ion mass. No information about the ionic charge state is obtained

since all residual bound electrons are stripped from the incident ion in the front detector.

An example of the solid state detector technique is shown in Figure 3; it may be labeled "passive $dE/dx - E$ " design and has been used on the ISEE-1 and ISEE-2 spacecraft.¹⁹ Two identical instruments are utilized, one with an open aperture and one covered with a thin aluminum foil which stops low energy protons (and other ions) but not electrons of 20 to 300 keV. The covered instrument thus measures electrons while the open instrument measures electrons and ions. When the detector properties are otherwise identical the difference should be the ion (proton) contribution. The obvious problem lies in the exceedingly accurate calibration required and in the fact that the ion flux is determined as a difference between two large numbers; when the ion flux is less than the electron flux it is difficult to measure these ions with acceptable accuracy. For that reason this design is not favored for radiation belt measurements although it seems to work well in the magnetotail plasma sheet and the outermost parts of the trapping region. The basic strength of this detector system comes from its great

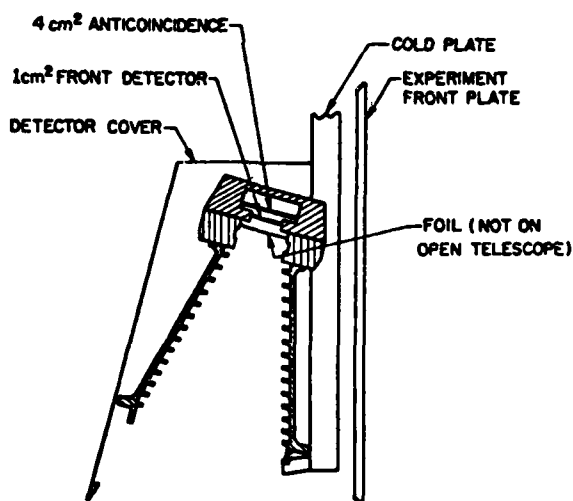


Figure 3. Simple Electron and Ion/electron Solid State Detector System. Two detectors like the one shown here are used; one with and one without a low energy ion stopping foil. This is an example of the passive $dE/dx - E$ design; see Anderson et al¹⁹

19. Anderson, K.A., Lin, R.P., Paoli, R.J., Parks, G.K., Lin, C.S., Reme, H., Bosqued, J.M., Martel, F., Cotin, F., and Cros, A. (1978) An experiment to study energetic particle fluxes in and beyond the earth's outer magnetosphere, IEEE Transactions on Geoscience Electronics, GE-16:213.

simplicity and light weight. The instrument can be built with different sensitivity properties by varying the collimator opening angle. However, the open aperture leaves the instrument vulnerable to sunlight contamination.

An example of the "active $dE/dx - E$ " technique employed by the Lockheed group²⁰ is depicted in Figure 4. Such instruments have been flown on many low altitude spacecraft. Some of the salient features of this design include a thin solid state detector front element, a stack of thicker detector elements operated in parallel and a coincidence detector. This illustrates some of the efforts one must make to insure effective ion measurements in the radiation belts. Shielding is very important as indicated here; this includes both passive shielding by thick walls which ideally stop electrons of energies up to several MeV and ions up to tens of MeV, and active shielding afforded by an anti-coincidence scintillator surrounding the solid state detectors. Such a technique removes much of the electron and high energy penetrating radiation background. This measuring technique uses the fact that electrons lose relatively little energy in the front detector while ions lose relatively much more energy there. Pulse height discrimination techniques thus provides relatively clear separation between ions and electrons. As with the previous instrument designs, the instrument sensitivity and angular resolutions can be varied by altering the collimator opening angles; high sensitivity and high angular definition are mutually exclusive, however. Radiation damage is minimized by mounting the front detector so that the aluminum side faces the environment and the gold side faces the interior of the instrument. With this technique, ions (protons) of energies in the range one to several hundred MeV are measured.

These heavy ions can be identified through analysis of the rate of energy deposition for ions of different masses as given by the classical Bethe formula applied to silicon detectors:

$$\frac{dE}{dx} = \frac{4\pi q^4 z^2}{mV^2} \times nZ \left[\ln \left(\frac{2mV^2}{I} \right) - \ln(1 - \beta^2) - \beta^2 \right] , \quad (1)$$

where

dE/dx = rate of energy loss of the particle,

q, m = charge and mass of electron,

z, V = atomic number and velocity of particle,

20. Reagan, J. B., Bakke, J. C., Kilner, J. R., Matthews, J. D., and Imhof, W. L. (1972) A high-resolution multiple-particle spectrometer for the measurements of solar particle events, IEEE Transactions in Nuclear Science, NS-19:554.

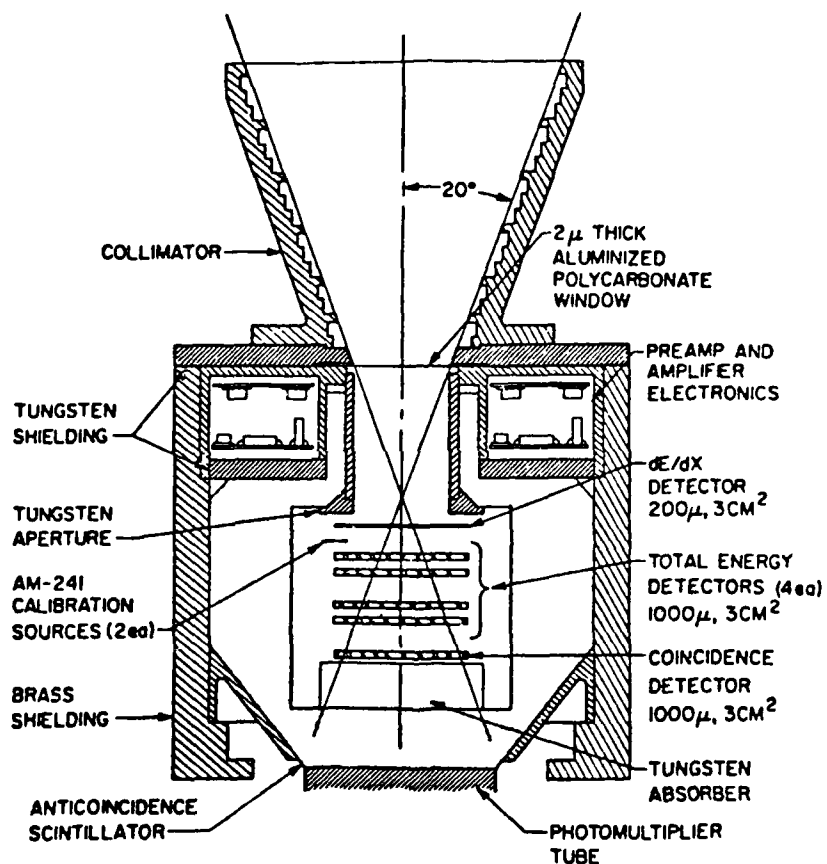


Figure 4. Solid State Detector Instrument Utilizing the Active dE/dx - E Design. This instrument uses an anticoincidence scintillator for background suppression and a stack of solid state detector elements. A tungsten absorber is placed between the detector elements and the scintillator, and a $2 \mu\text{m}$ aluminized polycarbonate window eliminates sunlight contamination (see Reagan et al, 1972)

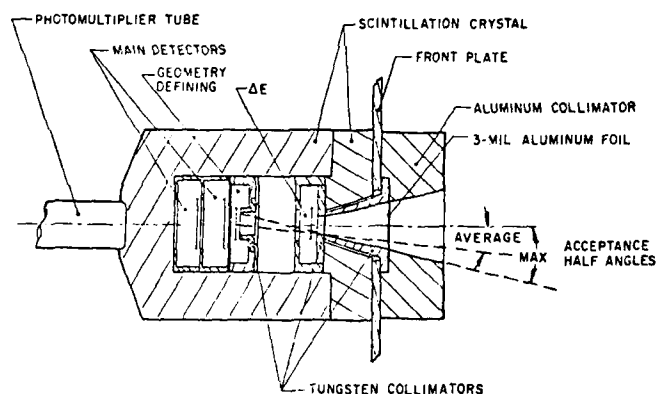
Z = atomic number of the absorber,
 N = number of atoms per cm^3 of absorber,
 β = particle velocity/velocity of light,
 I = average energy to ionize atoms of the absorber.

If $\beta \ll 1$, Eq. (1) simplifies to

$$\frac{dE}{dx} = K_1 \frac{Mz^2}{E} \ln \left(K_2 \frac{E}{M} \right) \quad (2)$$

where K_1 and K_2 are constants, and E , M , and z are the energy, mass, and atomic number of the particle.

From dE/dx and E measurements one can also determine the ion mass, and this technique has been applied in the tens of MeV range by Rubin et al.²¹ An illustration of their instrument is given in Figure 5. With such an instrument it is possible to use the dE/dx and E measurements to construct a particle identifier function (P) by the onboard spacecraft microprocessor. Such an approach leads to a P -function only weakly dependent on ion energy as illustrated in Figure 6; and



DETECTOR ASSEMBLY GEOMETRY

Figure 5. Solid State Ion Detector Used by Rubin et al.²¹ to Measure and Identify Alpha Particles (Helium Nuclei) at 18 to 70 MeV. The solid state detectors are surrounded by a large scintillator which gives good background rejection. The opening of the collimator is covered by a thin aluminum foil. Internal collimation is done with tungsten collimators

21. Rubin, A.G., Filz, R.C., and Rothwell, P.L. (1977) Geomagnetically trapped alpha particles from 18 to 70 MeV, *J. Geophys. Res.* 82:1938.

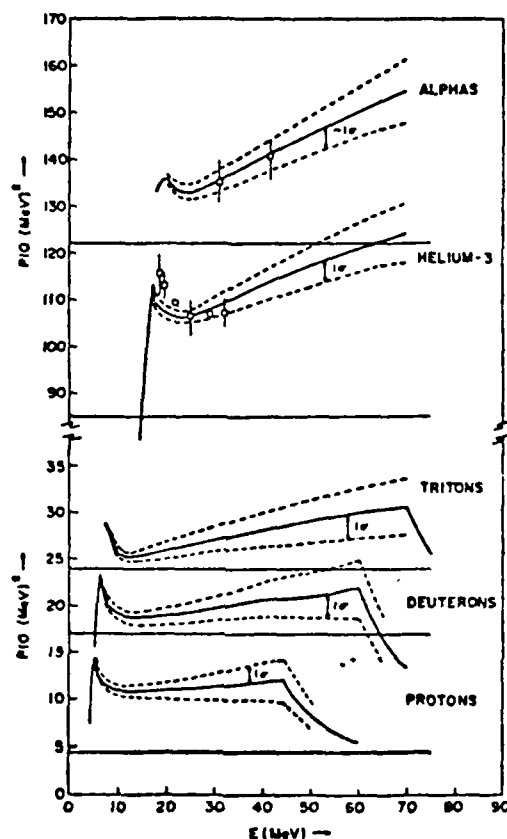


Figure 6. The Particle Identifier Function versus Particle Energy for Protons, Deuterons, Tritons, Helium₃ and Helium₄ (Alpha Particles). It can be seen that the particle identifier (mass signal) is only weakly dependent on particle energy, and this linearity is further insured by restricting the energy response²¹

separation between protons, deuterons, tritons, helium₃ and helium₄ (alpha-particles) becomes possible. This method has the great value that much of the first level data processing is carried out within the instrument itself, and only a small telemetry rate is needed; in contrast, the transmission of raw count information for subsequent processing at the ground would require a far higher bit-transmission rate. Rubin and his co-workers used six energy ranges and five particle identifier values totaling a matrix of only thirty numerical elements to obtain significant information about composition and energy spectra of the high energy

ion radiation. This type of solid state detector technique is generally limited to an ion energy range of 1 MeV to 200 MeV per ion, the precise limits being dependent on detector thickness and particle species.

Another technique employed by the Aerospace group is the Range Telescope shown in the upper portion of Figure 7. Here a stack of solid state detectors (five in this example) is interleaved by thick absorber plates (usually made from copper) which reduce the energy of the incident proton (ion) by known amounts. Such instruments have been flown on low altitude satellites and have proven effective up to 180 MeV. A large geometric factor is obtainable by using a large aperture opening angle.

At even higher energies Cerenkov Radiators are useful, and an example of this technique is shown in the lower portion of Figure 7. Here two pieces of Ne III scintillating plastic disks are used. The front and rear scintillators are coupled through lucite light-pipes to photomultipliers, and the rear scintillator is also followed by a Cerenkov radiator coupled to a photomultiplier. The output of the

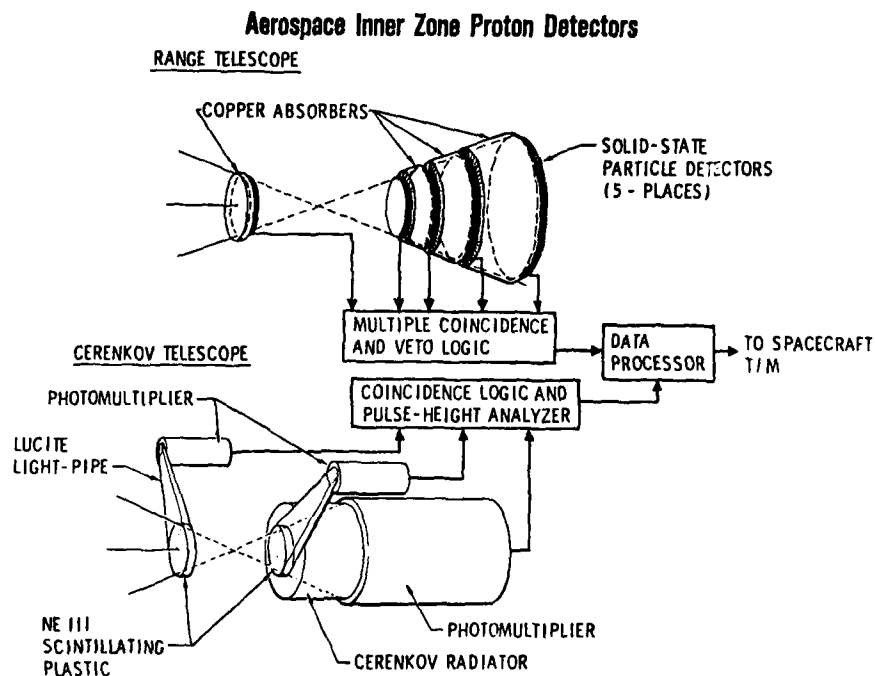


Figure 7. Upper Part: Range Telescope that Uses Copper Absorber Disks Between the Solid State Detector Elements Stacked as Indicated. Lower part: Cerenkov radiator detector with scintillators and photomultipliers

three photomultipliers form the basis for coincidence logic and pulse-height analysis. This instrument technique extends the energy coverage for protons (ions) to 200-500 MeV per ion, and several energy channels give spectral shape information.

In recent years magnetospheric physicists have placed greater emphasis on the understanding of the energetic particle populations at somewhat lower energies, in the keV to lower MeV range. The motivation is the desire to understand magnetospheric substorm and storm dynamics and the coupling between the magnetotail and the radiation belt trapping region. This is the energy range where solid state detectors are particularly useful. Figure 8 shows the schematics of a solid state ion detector utilized on SCATHA.²² It includes a "broom" magnet which sweeps away energetic electrons up to 300 keV (which is considered sufficient for use in the outer radiation zone, beyond $L = 5$). Ions are counted using two solid state detectors and pulse height discriminator technique, while the rear detector is used for anti-coincidence removal of background contaminations. By the use

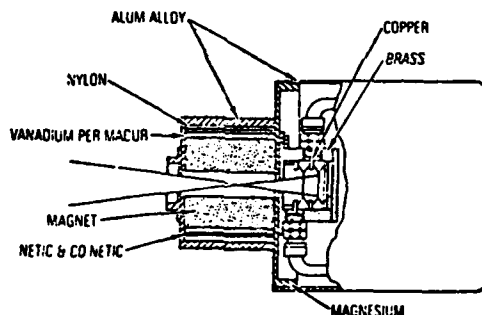


Figure 8. Energetic Ion Detector Used on the SCATHA Spacecraft. Through thermal design the instrument operates at -10°C and the solid state detectors are very low noise type which allowed measurement of the energy range from 14 keV to 3300 keV in differential energy passbands and >3300 keV in an integral passband. Electrons below ~ 300 keV are swept away by the broom magnet in the entrance aperture. The instrument uses dE/dx and E measuring and pulse height analysis in an on-board microprocessor. For details, see Stevens and Vampola²²

22. Stevens, J.R. and Vampola, A.L. (1978) Description of the Space Test Program P78-2 Spacecraft and Payloads, Space and Missile Systems Organization Report SAMSO TR-78-24, Los Angeles, California, p 26.

of low-noise detector elements and spacecraft thermal design which keeps the instrument at -10°C in orbit, protons (and other ions) are measured from 14 keV to 3.3 MeV energies in several differential energy passbands and above 3.3 MeV in an integral channel. It has been proposed that cryogenic cooling techniques be employed to cool solid state detector instruments to achieve an even lower operating energy rate; however, other existing instruments, such as electrostatic analyzers, cover these lower energies.

A somewhat different instrument that makes active use of magnetic deflection is illustrated in Figure 9. This instrument which was built cooperatively by the NOAA and MPAE groups was included on the ISEE-1 and ISEE-2 spacecraft;²³ it consists of a baffled collimator, a detector house with a permanent magnet whose field is perpendicular to the cross section of the drawing and solid state detectors arranged as indicated. This technique permits the simultaneous measurements

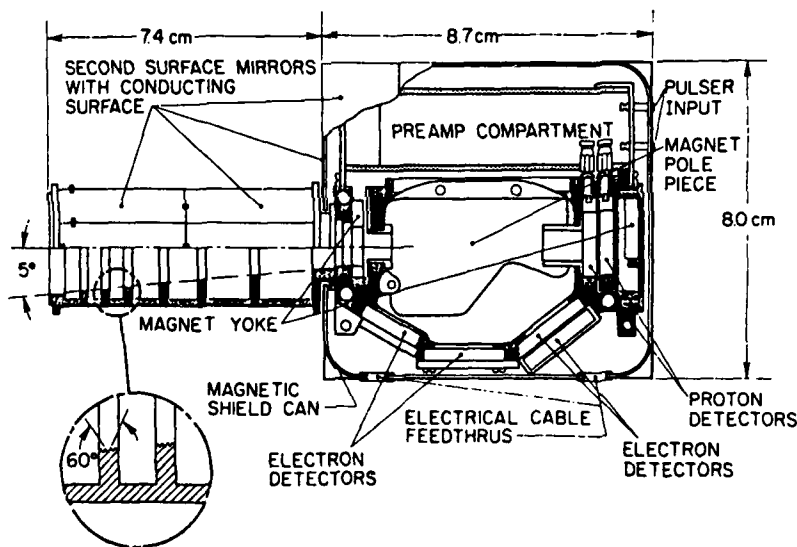


Figure 9. Magnetic Ion and Electron Spectrometer (WAPS) Effective from Tens of keV to Multi MeV Energies. Electrons are deflected towards the lower part of the instrument cavity by a static magnetic field and are detected by three solid state detector assemblies. Ions, because of their large mass, are essentially unaffected by the magnetic field and proceed through the instrument cavity to be detected in the rear ion detector elements. The collimator is well baffled to avoid electron scattering. This instrument was utilized on ISEE-1 and ISEE-2²³

23. Williams, D.J., Keppler, E., Fritz, T.A., Wilken, B., and Wibberenz, G. (1978) The ISEE 1 and 2 medium energy particle experiment, IEEE Transactions on Geoscience Electronics, GE-16:270.

of ions and electrons. Electrons are deflected by the magnetic field according to their energy and are detected by the solid state detectors in the lower part of the detector house; ions, which suffer very little magnetic deflection due to their much greater mass, go essentially straight through the detector house to be registered in the rear solid state detector stack. This instrument has provided excellent ion and electron data in the ranges 24-2081 keV for protons and 22.5-1200 keV for electrons throughout the radiation belts and the near-earth ($R \leq 23 R_E$) magnetotail region. The separation between ions and electrons is good, but no mass or charge identification of the ions is afforded by this technique. Background suppression is accomplished primarily by passive shielding and this is deemed sufficient over most of the radiation belts because of the relatively high count rates of the prime ions and electrons detected. A slight drawback in the design is the instrument's sensitivity to sunlight which makes flux measurements in the direction of the sun difficult; this problem (which is shared by several such instruments) can be overcome in the data analysis by interpolation across the data sector containing the sun-pulse. On ISEE-1 this instrument was mounted on a scan platform, the motion of which together with the spacecraft spin for the first time provided full 3-dimensional flux distributions. On ISEE-2 less extensive resolution in 3 dimensions was afforded by the multiple use of this instrument in a fan-shaped arrangement mounted in a plane containing the spacecraft spin axis. These mountings are illustrated in Figures 10 and 11.

Another example of instrumentation is an ion (proton) telescope used by the Los Alamos Group on a number of geosynchronous satellites.²⁴ A schematic diagram for this instrument is shown in Figure 12. The instrument consists of a collimator whose aperture is covered by a thin aluminized mylar window, three solid state detectors, thick aluminum shielding, an internal tungsten absorber to minimize X-ray effects, and an anti-coincidence plastic scintillator (surrounding the solid state detector stack) coupled to a photomultiplier tube. It is capable of measuring protons (ions) in the energy range above a few hundred keV to tens of MeV.

Another proposed design by the Los Alamos group which employs primarily very thick passive shielding that can stop electrons at up to 5 MeV from penetrating the detector assembly and a stack of five solid state detectors is shown in Figure 13. In addition to the outer shielding each detector element is surrounded by a guard ring which works as an anticoincidence element in lieu of an anti-coincidence scintillator. The front solid state detector is a relatively thin silicon detector ($d = 20 \mu\text{m}$) operated with the aluminum side facing out; the other detectors

24. Baker, D.N., Stauning, P., Hones, E.W., Jr., Higbie, P.R., and Belian, R.D. (1979) Strong electron pitch angle diffusion observed at geostationary orbit, Geophysical Research Letters 6:205.

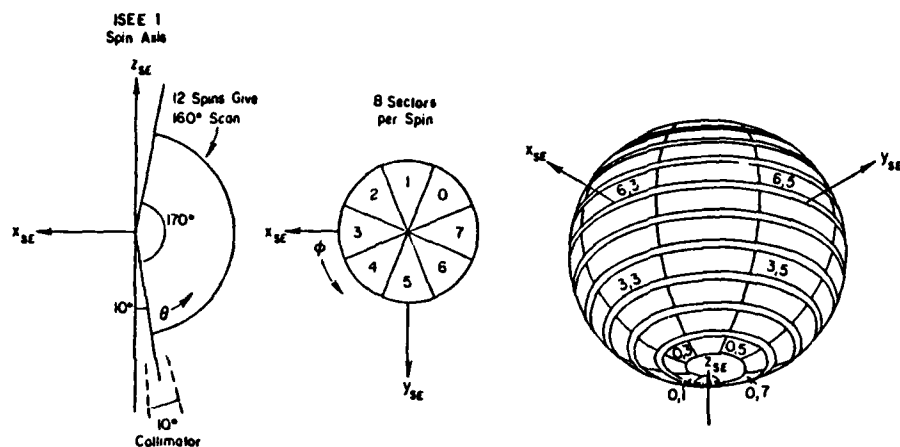


Figure 10. Mounting of the ISEE-1 Magnetic Particle Spectrometer (WAPS) on a Scan Platform Permits Detector Scan from 10° to 170° with Respect to the Spacecraft Spin Axis as shown in the Left Part. During the spin, 8 sectors are sampled in azimuth and in 12 spins the detector scans from north to south. This results in a spiral motion of the detector look direction as illustrated in the right part of this figure, and essentially all look directions are covered

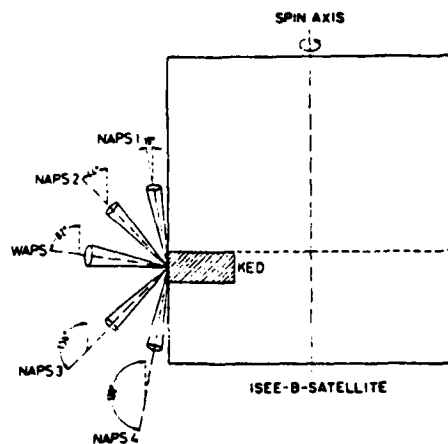


Figure 11. Mounting of the Five Particle Spectrometers on ISEE-2 in a Fanshaped Fashion in a Plane Containing the Spacecraft Spin Axis. The NAPS instruments are similar to the WAPS instrument but have a narrower acceptance angle. This mounting technique improves the time resolution but at a cost of a cruder spatial resolution

CPA HIGH-ENERGY PROTON TELESCOPE

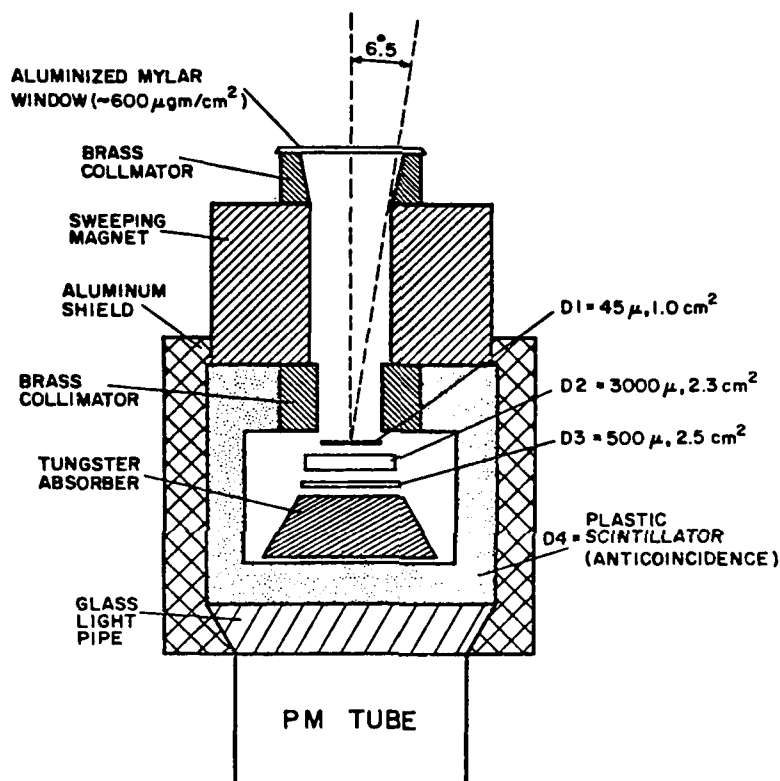


Figure 12. Solid State Detector Telescope of the Design Utilized by the Los Alamos Group. It uses both heavy passive shielding and a plastic scintillator for anticoincidence background rejection capabilities. For details, see Baker et al²⁴

are thicker as indicated in this figure. The aperture opening is large (30°). With suitable pulse height discrimination techniques electrons can be measured from 140 keV to 3 MeV, ions (including protons) from 140 keV to 17 MeV, and helium ions (alpha particles) can be measured from 1.2 to 4.4 MeV. This design is proposed for the NASA/OPEN mission.

The discovery of upward jetting beams of ions leaving the auroral ionosphere has focused the attention on precise measurements of the particle angular distributions. Pitch angle resolution of $\leq 1^\circ$ is required for an equatorial satellite to resolve the source/loss cone distribution characteristics. The problems in earlier

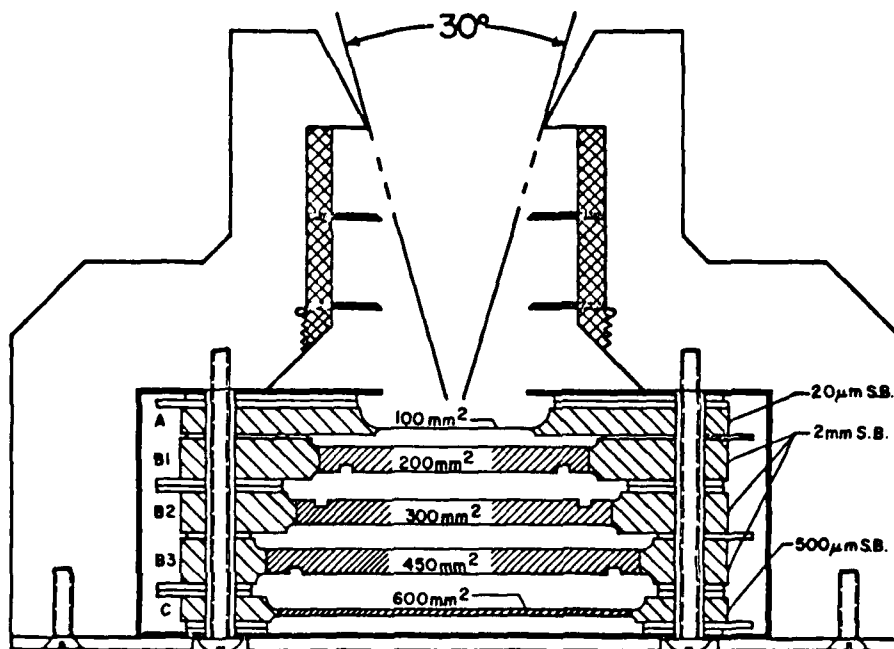


Figure 13. Solid State Ion and Electron Detector Proposed for the NASA/OPEN Mission by the Los Alamos Group. This instrument can measure electrons and ions from hundreds of keV to several MeV energies. The solid state detector elements are mounted on guard-ring scintillators which help reduce the background

design have been discussed by Spjeldvik.²⁵ An instrument package proposed by the Lockheed group for very fine angular resolution measurements on the NASA/OPEN mission is depicted in Figure 14. This is a multi-collimator, multi-detector design. The upper detector system has a narrow angle collimator (small geometric factor) and uses solid state elements as active detectors. The detector is most sensitive to electrons which can be measured from 20 keV to 3 MeV. The middle sensor system affords increased angular coverage. It measures ions from 200 keV to 17 MeV as well as electrons in the same range. The lower detector measures ions from 200 keV to 17 MeV and the electrons are excluded by a broom magnet in the collimator. This instrument package is also able to identify some of the heavier ions in the hundreds of keV to MeV range, but no charge state information is obtained. Aluminum and tungsten are used for shielding.

25. Spjeldvik, W.N. (1977) Radiation belt electrons: structure of the loss cone, J. Geophys. Res. 82:709.

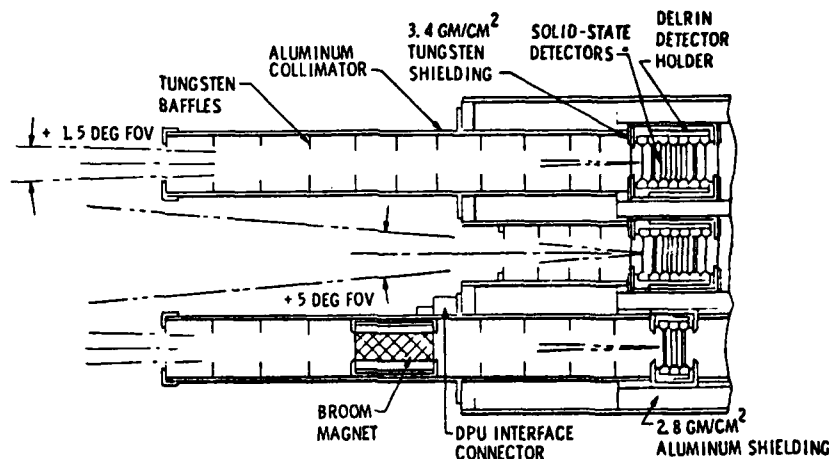


Figure 14. Multi Solid State Telescope System Design by the Lockheed Group to Measure Ions and Electrons With High Angular Resolution Proposed for the NASA/OPEN Mission

With the foregoing instruments the radiation belt ion fluxes above a few tens of keV can be measured with adequate angular and energy resolution. The present state of instrumentation for ion measurements can be summarized in eight points:

- (1) Magnetic deflection, $dE/dx - E$ measurements and Cerenkov detector systems provide good bulk ion measurement capability in the terrestrial radiation belts.
- (2) Excellent time and energy resolution are readily achieved with silicon solid state detectors (assuming the availability of reasonable telemetry rates in the kilobit/sec range).
- (3) Pitch angle distributions of energetic ions are normally measured with detectors mounted on rotating spacecraft, and for near-equatorial spacecraft the spin axis should lie in the orbital plane.
- (4) The large dynamic range needed for complete flux measurements requires multiple sensor systems; preferably there should be some overlap between the sensor energy ranges to insure compatible intercalibration.
- (5) Good electron and background suppression is achievable with passive shielding, scintillators and with guard-counter techniques.
- (6) Radiation damage to solid state detector systems can be minimized by design and sensor orientation.
- (7) Multi-parameter analysis can separate protons from helium ions and other heavy ions above a few hundred keV per ion (or above 50 to 100 keV per nucleon); at lower energies other techniques are needed.

(8) No ion charge state information is available with any of the foregoing designs.

5. LOW ENERGY ION COMPOSITION MEASUREMENTS

Ion composition measurements at energies below a few tens of keV have been included on a number of spacecraft in recent years. An instrument designed by the Lockheed group²⁶ has been flown on two low altitude, polar-orbiting satellites, and on the S3-3 satellite. The instrument covers the energy range from 0.5 to 16 keV and the mass range from 1 (protons or hydrogen ions) to 24. A further development of this instrument was included on the SCATHA spacecraft and covered the energy range from 0.1 to 32 keV. Figure 15 shows the schematics of this low energy ion mass spectrometer which utilizes a Wien velocity filter technique. The instrument has a collimator, a region of crossed electric and magnetic fields providing a selection of ion velocity (independent of mass) followed by an electrostatic analyzer. By varying the front electric field, ions of different velocities are accepted into the electrostatic analyzers where the ion mass per unit charge spectrum is determined at each ion velocity. This determines ion mass (per unit charge) and energy. For the lighter ions such as H^+ (protons), He^+ and He^{++} the relative contributions are determined; the instrument resolution decreases rapidly at the higher ion masses, greatly limiting the ability to detect the minor ionic characteristics. Figure 16 illustrates the mass resolution obtainable with this instrument as seen in an actual inflight data sampling; it can be seen that this is a relatively low resolution spectrometer (compared at the lower masses to the University of Bern group design²⁷ or the mass spectrometer developed by Moore²⁸). In the low mass end of the mass range it is difficult to detect the presence of minor ions in the presence of the primary ion flux if the ratio of minor to primary ion flux falls below a few percent; the mass resolution progressively degrades towards the higher energies, and in the high end of the mass range little ion species separation is possible. This instrument has great historic significance, however, since it was the first to detect upstreaming atmospheric

-
26. Shelley, E.G., Johnson, R.G., and Sharp, R.D. (1972) Satellite observations of energetic heavy ions during a geomagnetic storm, J. Geophys. Res. 77:6104.
 27. Balsiger, H., Eberhardt, P., Geiss, J., Ghielmetti, A., Walker, H.P., Young, D.T., Loidl, H., and Rosenbauer, H. (1976) A satellite-borne ion mass spectrometer for the energy range 0 to 16 keV, Space Science Instrumentation 2:499.
 28. Moore, T.E. (1977) Spectrograph suitable for the mass and energy analysis of space plasmas over the energy range 0.1-10 keV, Reviews of Scientific Instruments 48:221.

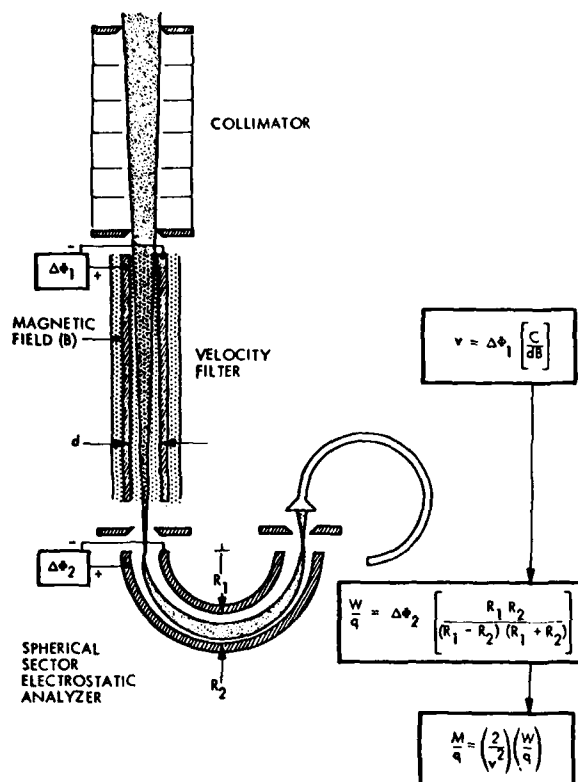


Figure 15. Low Energy Ion Mass Spectrometer Utilized by the Lockheed Group on Several Spacecraft. It used the Wien velocity filter technique and a spherical electrostatic analyzer²⁶

ions from the high latitude (auroral) ionosphere. Also, from the observations with such instruments we have learned that ions with mass $M = 16 \pm 2$ (usually labeled oxygen ions) at times can dominate the ion composition at lower ring current energies.⁸

A schematic illustration of the mass spectrometer developed by the University of Bern group is given in Figure 17. This instrument has an energy range from a few eV to 16 keV and the mass coverage extends from below 1 AMU to more than 100 AMU. The mass resolution at the center of the mass range is $\Delta M/M \sim 0.25$, slowly worsening towards both higher and lower ion masses. The instrument's sensitivity is good, and the transmission characteristics make the instrument (flown on GEOS-1 and GEOS-2) capable of measuring ion abundances of 10^{-4} to 10^{-5} of the dominant species at the lower end of the mass range. The design consists

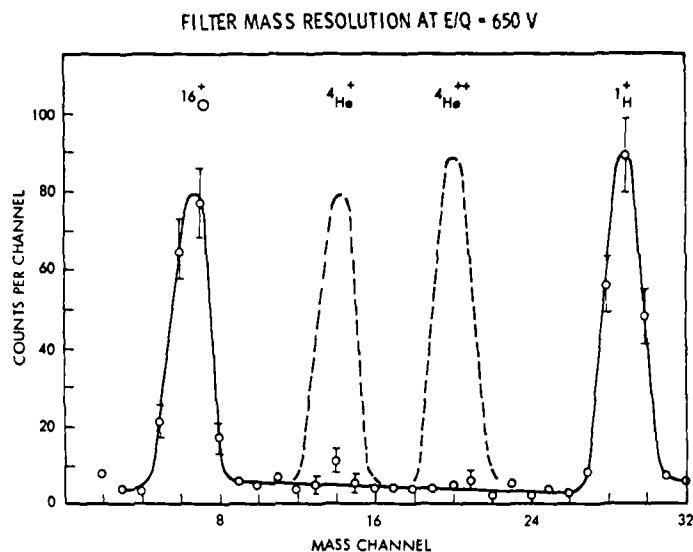


Figure 16. An Example of an In-Flight Mass Spectrum Obtained with the Lockheed Instrument Illustrated in the Foregoing Figure. This result was obtained with the SCATHA spacecraft at a radial distance of about 6 earth radii; the dotted lines depict the expected channel locations of H^+ and He^{++} ions

of a cylindrical electrostatic energy analyzer followed by a curved analyzer incorporating crossed magnetic and electric fields. In combination with the differential energy analyzer this functions as a mass analyzer. For details about the instrument design, see Balsiger et al.²⁷ Outstanding results obtained with this type of instrument include the identification of O^{2+} and O^{3+} ions in addition to O^+ at energies typically a few hundred eV. Examples of results obtained with this instrument flown on GEOS-1 are illustrated in Figure 18. Both He^+ and He^{2+} are detected in relative amounts that vary strongly. A further development of this instrument was included on ISEE-1.²⁹

A different type of ion mass spectrometer has been developed by Moore²⁸ who utilized a second-order double-focusing electric field geometry instrument with mass resolution sufficient to separate energetic space plasma ions such as C^+ , N^+ and O^+ as well as many molecular ions such as H_2O^+ , N_2^+ , O_2^+ , etc. (The schematic of this instrument is shown in Figure 19 and illustrates the principle of

29. Shelley, E.G., Sharp, R.D., Johnson, R.G., Geiss, J., Eberhardt, P., Balsiger, H., Haerendel, G., and Rosenbaum, H. (1978) Plasma composition experiment on ISEE-A, IEEE Transactions on Geoscience Electronics GE-16:266.

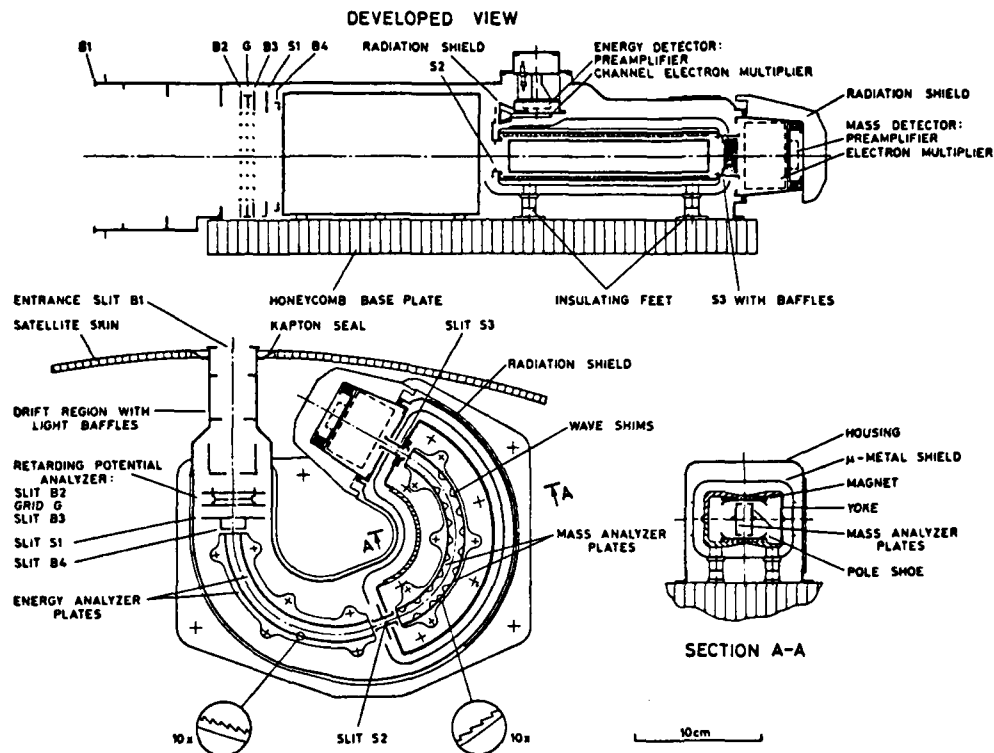


Figure 17. Low Energy Ion Mass Spectrometer Flown on GEOS-1 and Other Spacecraft by the University of Bern Group. This instrument covers energies below 16 keV. For details, see Balsiger et al.²⁷

the geometry, the mass-energy window and a sample of the mass resolution.) The mass range extends from 1 to 200 AMU. The energy range varies with ion mass and is typically 0.1 to 10 keV at 10 AMU. This instrument has been tested in the laboratory and flown on one auroral rocket, but so far it has not been utilized on a satellite. The instrument offers excellent mass resolution and the technique is flight ready.

It should be mentioned that atmospheric ions (H^+ , He^+ , O^+ , etc.) have been observed to be accelerated out of the auroral ionosphere within the atmospheric source/loss cone with energies in the lower keV range (about 4 keV for O^+ ions and 2 keV for protons). The precise measurements of the pitch angle distributions near $\alpha = 0^\circ$ for the different upstreaming ion species can give important information about the acceleration mechanisms themselves; such detailed, high angular resolution measurements should be made with future spacecraft. During magnetic storms high fluxes of keV O^+ ions are seen in the ring current and the dynamic

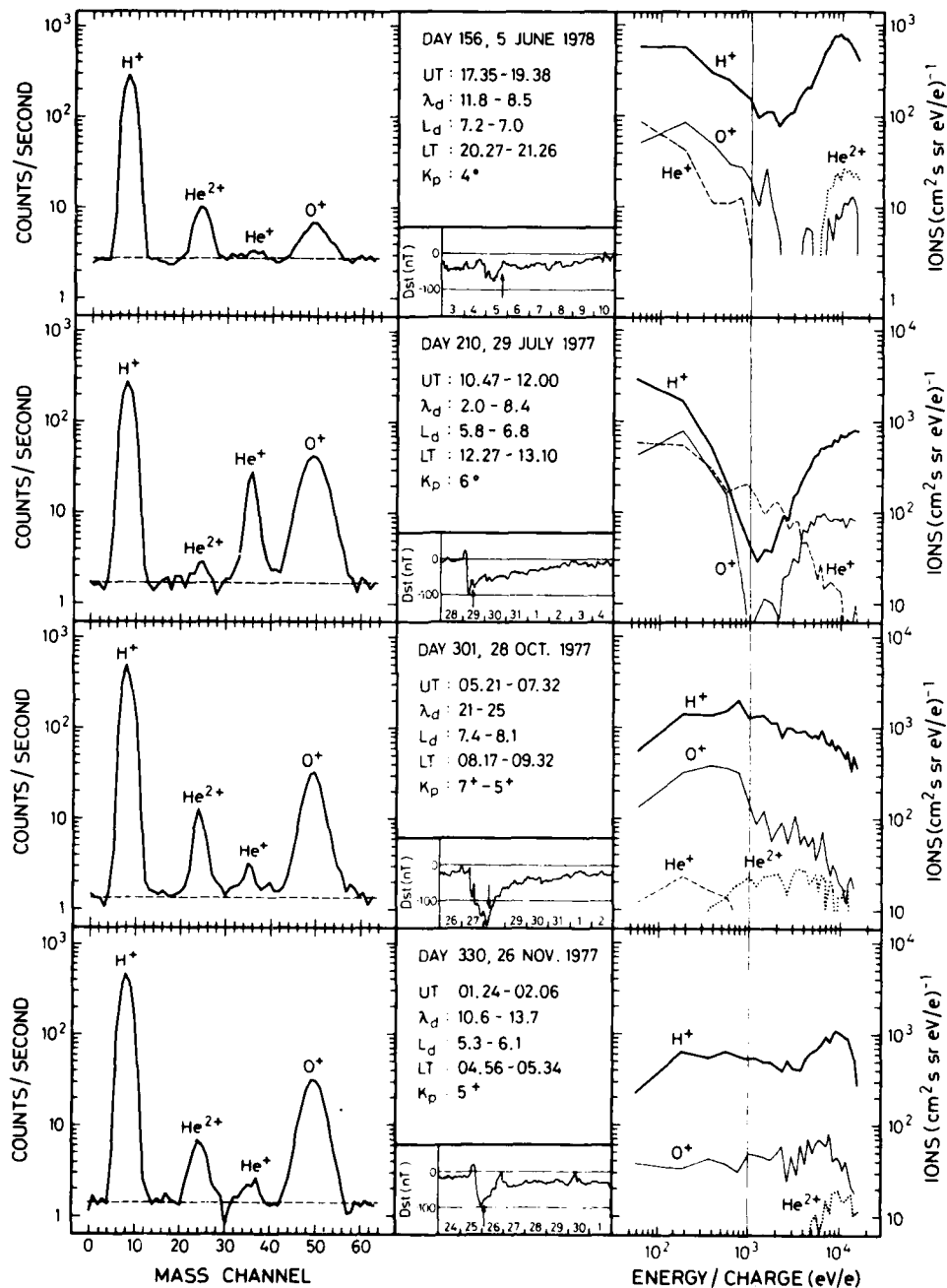
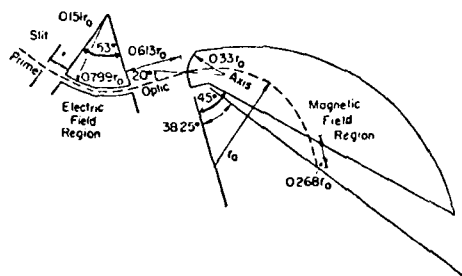


Figure 18. Examples of In-Flight Data from the University of Bern Mass Spectrometer on GEOS-1. Contributions to count rate from hydrogen ions (protons), helium ions in either charge state are well separated. A broad ion peak labeled O^+ is also seen in each of the data samples

Optimum Spectrograph Geometry. Dimensions from Hintenberger and Konig (1959).



The Geometry of a Double-Focusing Field Combination with Second-Order Aberration Coefficients Over a Wide Range of Gyro Paths.

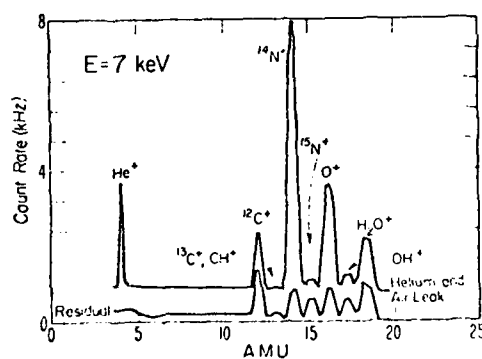
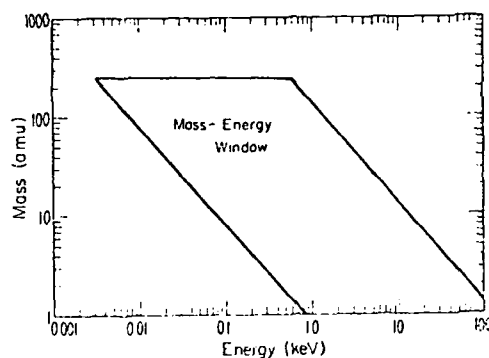


Figure 19. Double-Focusing, Second-Order Ion Mass Spectrometer Developed by Moore.²⁸ Upper section: Principle of the twin electric field design; middle panel: mass-energy window; and lower panel: an example of the instrument resolving power in a laboratory simulation using 7 keV ions

range of variability for O^+ is frequently greater than that of protons at comparable energies.

6. ENERGETIC ION COMPOSITION MEASUREMENTS

In previous sections, methods for bulk ion measurements without ion identification and a presentation of ion mass spectrometers effective in the upper eV and lower keV range have been described. With instrumentation for ion identification currently in use in space there is a significant gap in our ability to measure and identify ions; this gap extends from a few tens of keV (below which the ion mass spectrometers operate) to several hundred keV per nucleon (above which the simple solid state heavy ion telescope and proportional counter instruments are effective in the identification of the elemental species). This gap coincides with the energy range of the peak contribution to the ring current,¹⁰ and thus the energies where the dominant amount of the radiation belt particle energy is concentrated. A graph of the mean integral radiation belt ring current energy density is shown in Figure 20 (the steepest gradient in the curve implies the greatest contribution to the energy density at that energy); the gap in our composition information is clearly illustrated here. This is also the energy range where (energetically) the largest dynamic variations take place during geomagnetically disturbed times. The NOAA/MPAE/Aerospace ion detector package (CAMMICE) currently proposed for the NASA/OPEN mission uses newly developed technology to close this important gap in our knowledge of the ion composition; the coverage of this instrument package is indicated on the top of Figure 20, and the instruments are described later in this section.

A simplified genealogy of energetic composition instruments is shown in Figure 21. The first generation of ion detectors used either interaction with matter alone or deflection in fields alone; a second generation of instruments provided more complicated instrumentation based on either a combination of electric and magnetic field deflection to achieve focusing or by combining various methods using interaction with matter. Third generation instruments combine electric field and/or magnetic field deflection with the principle of interaction with matter. Instruments of this family allow for the first time simultaneous measurements of ionic and nuclear parameters of the ions. With suitable detector arrangements one can measure ion energy, pitch angle and also gain elemental identification through the nuclear charge as noted above. In recent years new instruments have been proposed that take advantage of advances in technology such as high time resolution (sub-nanosecond) pulse technology (which permits ion time-of-flight measurements within the instrument itself) together with devices which also permit

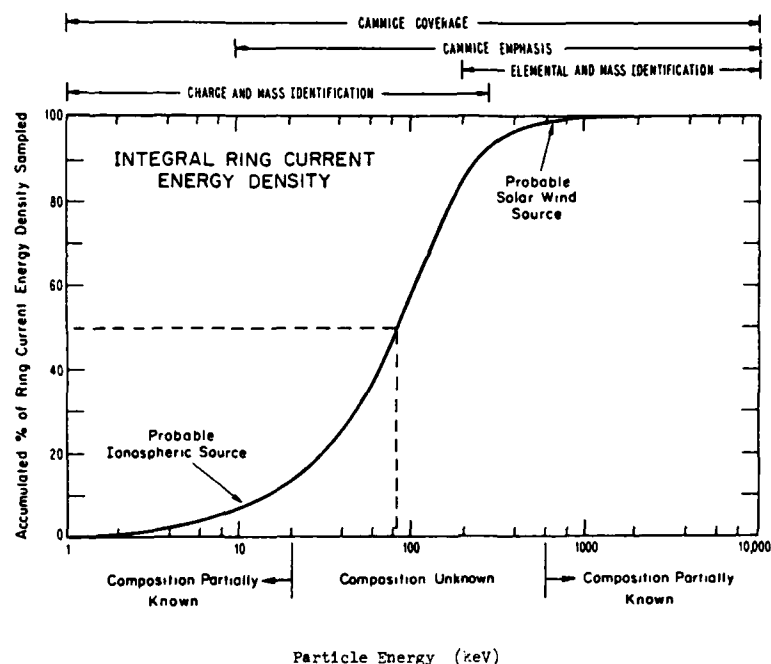


Figure 20. Integral Ring Current Energy Density versus Particle Energy (Recovery Phase) from Williams.¹⁰ The contribution to the energy density is greatest where the curve is steepest, and it can be seen that this occurs at 30 to 200 keV. It is thought that the ionosphere is the source of much of the lower energy (<20 keV) particles while the higher energy particles (>800 keV) may be of extraterrestrial origin; however, this is not firmly established. Also illustrated is the gap in our current knowledge of the ion composition at the intermediate energies where most of the energy density is located. The labels on the top of the figure indicate the mass and charge coverage of newly developed instruments (CAMMICE) proposed for the NASA/OPEN mission

the ionic charge state to be measured even up to hundreds of keV energies. Such instruments may be called energetic ion detectors of the third generation.

A more detailed illustration of this genealogy is shown in Figure 22 which is a block diagram indicating the various experimental techniques derived from the basic principles. Under this nomenclature solid state energetic ion detectors used to achieve ion identification and energy spectra can be said to be of the first generation. The schematic diagram in Figure 23 shows an example of such an instrument which is useful for ion identification above several hundred keV/nuc; it contains a collimator telescope, a thin aluminum foil (to shield from direct sunlight) and two solid state silicon detectors followed by suitable pulse height

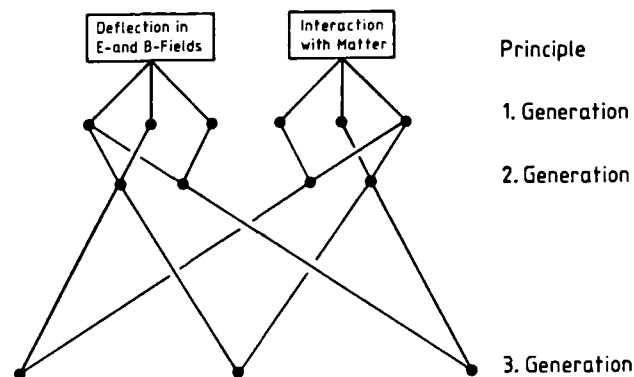


Figure 21. Simplified Genealogy of Satellite Instruments for Energetic Ion Composition Measurements. Further developments apply more sophisticated combinations of deflections in E and B fields and interactions with matter

discriminator logic. For heavy ion measurements the front element is very thin ($d \sim 3.4 \mu\text{m}$ on the NOAA instrument on ATS-6) and the rear element is substantially thicker. The thin front element is a necessity for the heavy ion detection and identification, and the lowest energy detectable depends on the front detector thickness. Currently commercially available silicon solid state detectors can have thickness as low as $\leq 2 \mu\text{m}$. In this instrument the shielding against penetrating radiation is primarily passive using lead and copper. This instrument type has been flown on a number of spacecraft including ATS-6 and Explorer 45,³⁰ and a wealth of heavy ion information has become available within the Explorer 45 orbit ($L \leq 5.25$) for energies in the lower MeV range.^{9, 31} The principle of the ion identification technique follows from the different rates of energy deposition in the silicon detectors for ions of different nuclear charges as noted in Eq. (1). This is illustrated in Figure 24 which depicts the energy deposited in the front detector element of the heavy ion telescope on ATS-6 versus incident ion energy for different ion species. By pulse height discrimination one can exclude contributions from protons (H^1) by accepting only pulses higher than a certain level (labeled A1 in Figure 24). Similarly, contributions from helium ions can be excluded by selecting pulses above level A3; pulses higher than level A5 must come from ions heavier

30. Fritz, T.A. and Cessna, J.R. (1975) ATS-6 NOAA Low Energy Proton Experiment, IEEE Transactions on Aerospace and Electronic Systems, AES-11: 1145.

31. Fritz, T.A. and Spjeldvik, W.N. (1981) Steady-state observations of geomagnetically trapped energetic heavy ions and their implications for theory, Planetary and Space Science, in press.

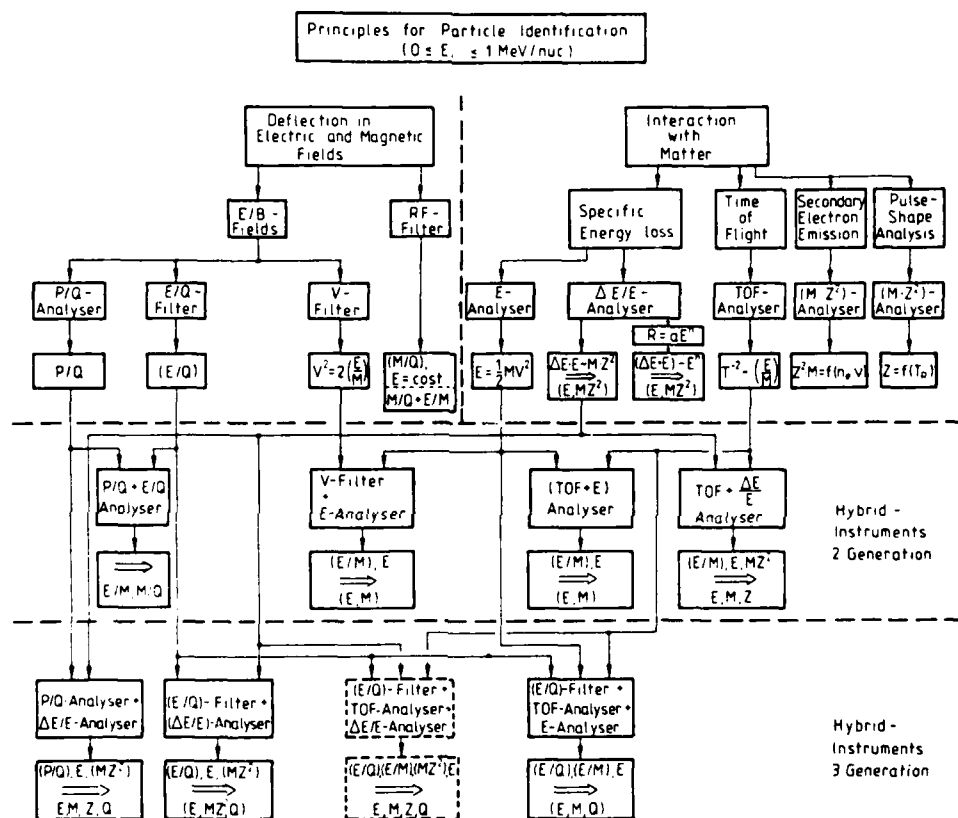


Figure 22. Block Diagram Illustrating the Genealogy of the Energetic Ion Composition Instruments. The quantities measured are noted in the boxes, and distinction is made between the two principles: field deflection and matter interaction. Hybrid methods using both principles and the addition of time-of-flight measurement techniques form the third generation instruments

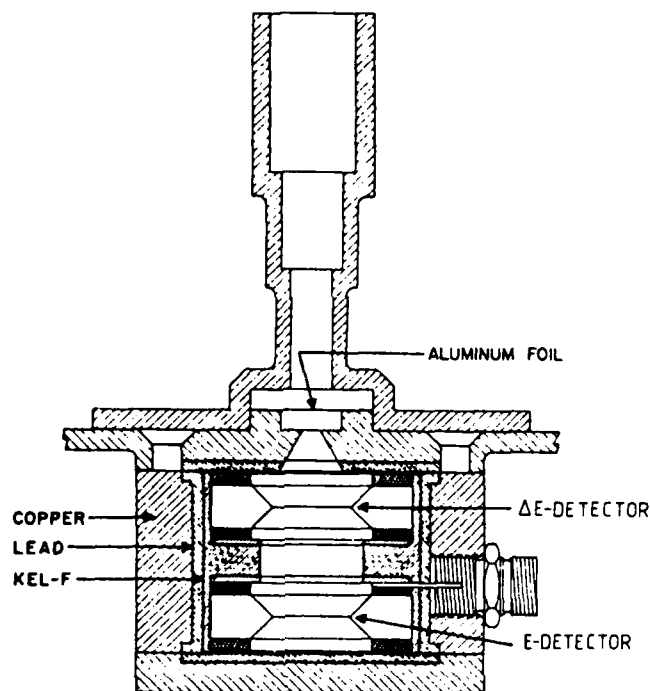


Figure 23. Solid State Detector Telescope With Two Silicon Detectors, a Thin Front Element for dE/dx Measurements and a Thick Rear Element to Measure the Total Ion Energy E . This type of instrument has been flown on ATS-6, Explorer 45 and other spacecraft. When the front element is very thin ($3.4 \mu\text{m}$ on ATS-6) heavy ions can be measured without proton contamination³⁰

than oxygen ions. Pulse height analysis of this type can also be applied to the rear detector element, and the two sets of discriminator levels can be combined to yield passbands for selected ion species and energies. This is shown in Figure 25, and one can define passbands for helium ions only ($\Delta\alpha 3$ and $\Delta\alpha 4$ in Figure 25), for carbon, boron, beryllium and lithium (L2 in Figure 25), for carbon, nitrogen and oxygen ions (M2 in Figure 25) and for other ions. This method is not suitable for the determination of the ion charge states, however. With current detector technology the energy coverage is limited to the range above a few hundred keV per nucleon; no definite upper energy cut-off is indicated, although helium ions are difficult to detect above a few tens of MeV (Figure 24) while in principle, the heavier ions can be detected at much higher energies.

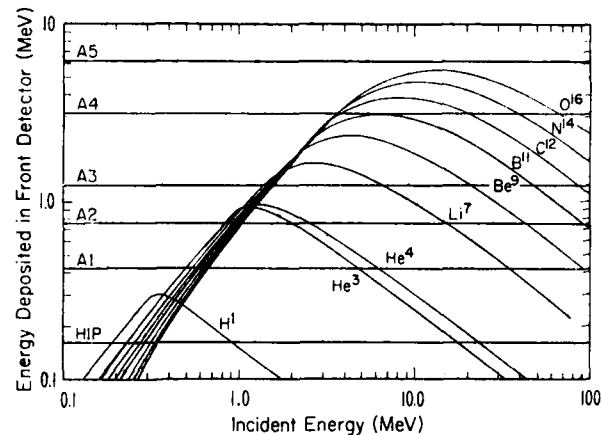


Figure 24. Energy Deposited in the Thin ($d = 3.4 \mu\text{m}$) Silicon Front Detector Element Versus Incident Ion Energy for Different Ion Species. There is a maximum deposited energy characteristic of each ion species, and protons (H^1) are excluded by pulse height discrimination

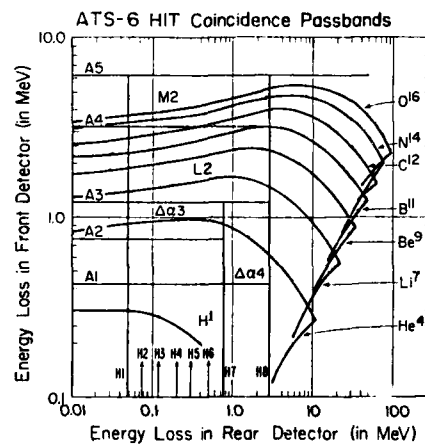


Figure 25. Energy Deposition in the Front Detector Element ($d = 3.4 \mu\text{m}$) versus Energy Deposition in the Rear Element of the ATS-6 Heavy Ion Detector Telescope Illustrated in Figure 23. The data are given for different ion species, and specific ion species may be selected by suitable pulse height discrimination using the signals from both detectors

With an instrument of this type one can also construct a particle identifier function PI given by $PI = \frac{dE}{dx} \cdot E M Z^2 f(v)$ where dE/dx and E are measured, M is the ion mass and Z is the nuclear charge; $f(v)$ is a weakly varying function of ion energy (or velocity). Such a quantity can be very useful if the instrument is required to have a large dynamic range (in counting rate). The ionic information may be sorted into separate passbands which may be selected for different particle species as illustrated in Figure 26. In the lower MeV range the response deviates from flat, however, and which worsens the mass resolution towards lower energies (near 1 MeV).

An example of an instrument of the second generation is shown in Figure 27. This instrument was flown on the ISEE-1 spacecraft by the NOAA and MPAE groups.²³ It uses a dE/dx and E measuring technique in the solid state detector elements in combination with a time-of-flight measurement for the energetic ions within the instrument itself. The instrument has a thin front detector and a thick rear detector, separated by 10 cm. The flight time information is obtained from the output signals of the two solid state detectors caused by the passing of the energetic ion. With the pulse height discriminator technique plus the time-of-flight measurement an improved particle identifier function can be devised which has a significantly flatter response than the simple $E \cdot dE/dx$ function, particularly in the lower MeV range as illustrated in Figure 28.

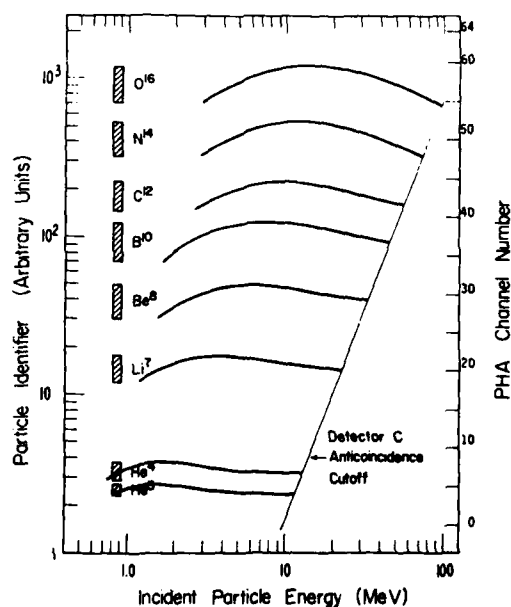


Figure 26. Linearity of the Pulse Height (PHA) Particle Identifier Function PI for the Two-Element Solid State Detector Flown on ATS-6 and Explorer 45³⁰

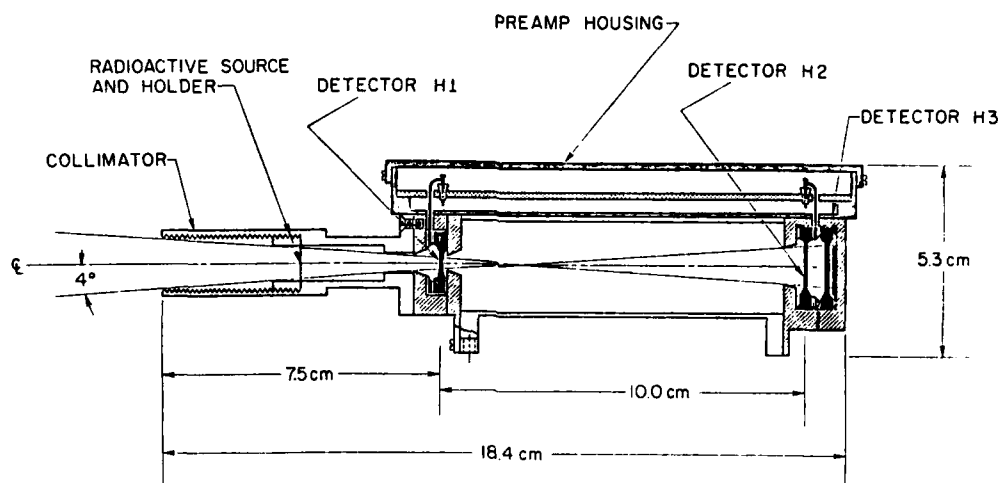


Figure 27. Time-of-Flight Solid State Detector Telescope Utilized on the ISEE-1 Spacecraft. Secondary electron emission from the front (H1) and first rear (H2) detectors are used for timing of the ion flight between these two detectors. The separation is 10 cm. A weak radioactive source in the collimator provides in-flight calibration. For details, see Williams et al²³

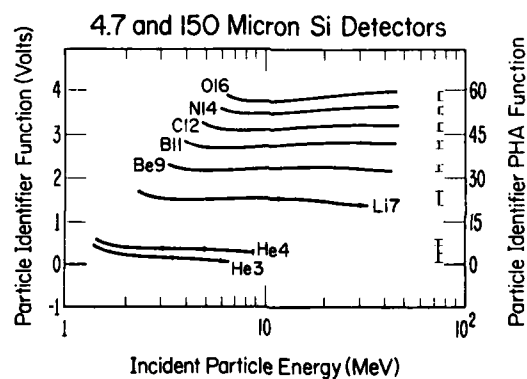


Figure 28. Linearity of the Particle Identifier Function for the Second Generation Time-of-Flight Instrument Used by the NOAA/MPAE Heavy Ion Detector on the ISEE-1 Spacecraft

A new type of time-of-flight instrument is shown in Figure 29. The principle utilized is that instead of a solid state detector as the front element (since these are limited to $>1 \mu\text{m}$ thickness) one utilizes a very thin foil (so that the incident ion loses extremely little energy there). Upon the passage of the energetic ion a few electrons are liberated from the foil, and in analogy with the workings of a vacuum tube these electrons are accelerated by a system of grids (carrying the proper electric potentials) so as to be detected in suitable electron detectors, here microchannel plates. This produces a (start) signal that marks the incident ion, and a similar arrangement is made after a certain path length of the ion (either another foil or the surface of a solid state detector) which then marks a (stop) signal for the time-of-flight measurement. This technique allows the detection and identification of much lower energy ions than is possible with the conventional two-element solid state telescope described earlier, at least down to 5 keV per nucleon (80 keV per ion for oxygen ions); the lower limit is in part controlled by the thickness of the front foil. From time-of-flight measurements together with the energy deposition information, ions can be identified and energy spectra calculated. This instrument is proposed for the NASA/OPEN mission by the NOAA/SEL in collaboration with a number of other institutions.

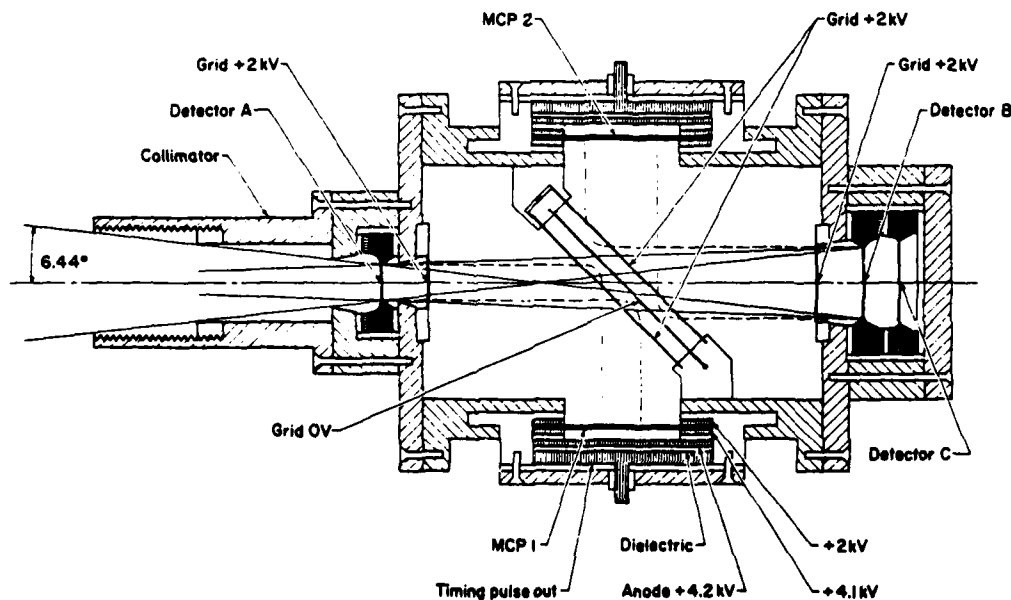


Figure 29. Time-of-Flight Instrument Using Grids to Control the Movement of Secondary Electrons Emitted by the Front Foil and the First Rear Solid State Detector. The electrons are measured by the two microchannel plate detectors, and these measurements generate a timing signal. This instrument has been proposed for the NASA/OPEN mission by a collaboration of several groups

The quality of timing that can be achieved with flight type electronics is illustrated in Figure 30. Here 200 keV protons, helium ions and heavier ions are depicted in a time spectrum from the time-of-flight and energy measurement made with this instrument in the laboratory. It can be seen that H_1^+ (protons), He_3^+ , He_4^+ , C_{12}^+ , N_{14}^+ and O_{16}^+ are readily resolvable, and would be resolved even for orders of magnitude differences in relative flux intensities. The widths of the ion peaks range from hundreds of picoseconds (400×10^{-12} sec for protons) to a few nanoseconds (2.5×10^{-9} sec for O^+ ions). Instruments with this kind of resolving power are expected to lead to significant advances in our knowledge of the magnetospheric heavy ion physics in the years ahead. The mass resolution of this instrument is illustrated in Figure 31; oxygen and carbon ions are clearly separated and nitrogen ions can also be identified. Isotopes of helium, He_3 and He_4 , can also be counted in separate channels.

An example of the energy versus time-of-flight resolution obtainable in the secondary electron emission instrument shown in Figure 29 is given in Figure 32. This is a result of a laboratory beam calibration of a prototype instrument recently built at MPAE/Lindau. The results for singly charged H_1 (protons), He_4 , N_{14} and A_{40} are shown.

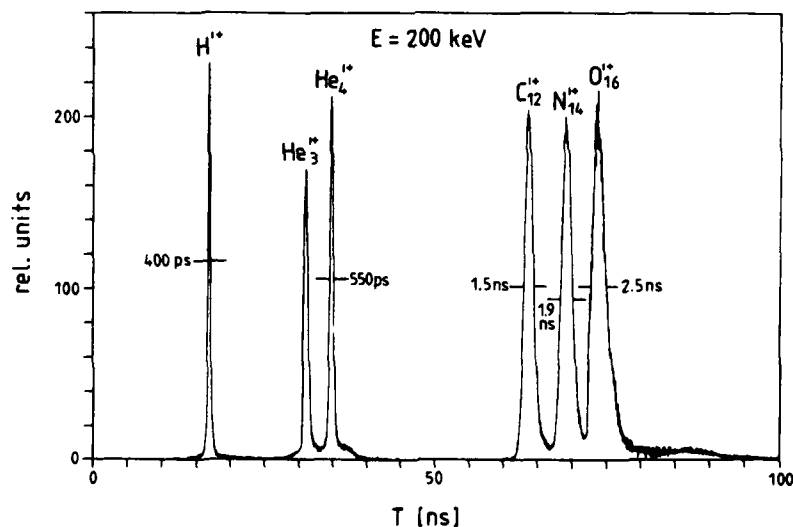


Figure 30. Timing Resolution for 200 keV Ions Within the Instrument Depicted in Figure 29. The full-width-half-max of the proton peak time resolution is 400 picoseconds, and for atomic oxygen ions this resolution is 2.5 nanoseconds. Notice that He_3^+ and He_4^+ are well resolved with this laboratory data

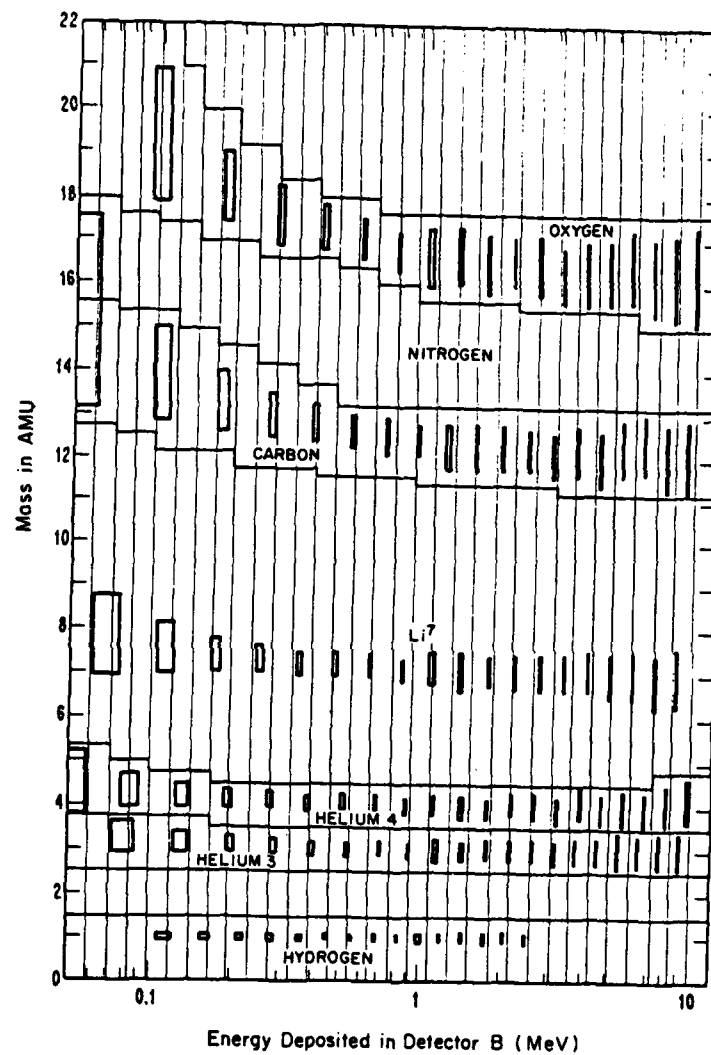


Figure 31. Elemental Resolution of the Time-of-Flight Instrument Depicted in Figure 29

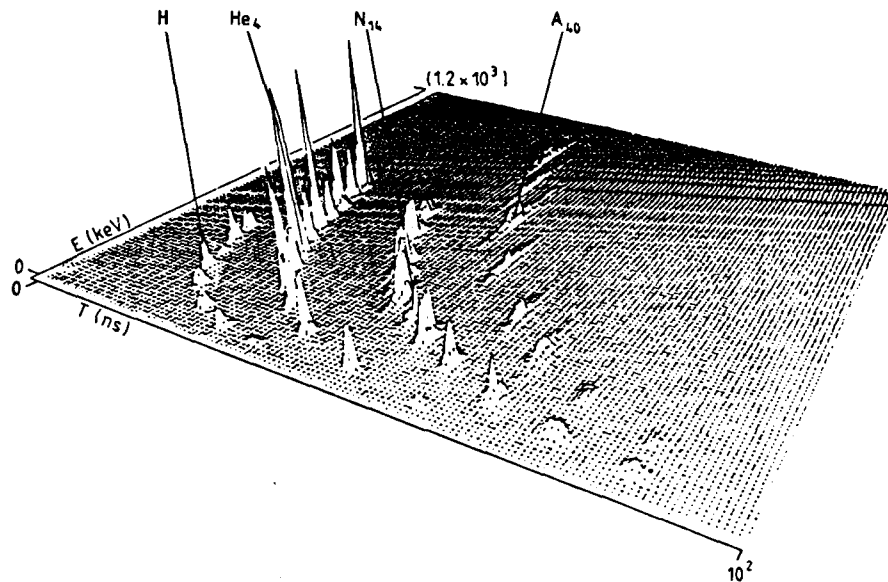


Figure 32. Examples of the Time-of-Flight versus Incident Ion Energy in the Detector Design Shown in Figure 29. The effect in the energy-time matrix is shown for hydrogen, helium, nitrogen and argon ions

An instrument of the second generation that has been tested in space is shown in Figure 33. This is an instrument that features a very large geometric factor: $g = 1.27 \text{ cm}^2\text{-ster}$. The instrument is sensitive to protons from 300 keV to 2.5 MeV, alpha particles from 200 keV/nucleon (800 keV) to 2.5 MeV/nucleon (10 MeV) and other ions including ions at $>100 \text{ keV/nucleon}$ ($\geq 6 \text{ MeV}$). The large geometric factor makes the instrument suitable for detection of rare ionic species such as those found in the 'low energy' cosmic rays. Such a detector has also been used on the S3-2 spacecraft to study precipitating heavy ions. From Figure 33 we notice that the detector has a gas-filled cavity, and a combination of a silicon surface barrier detector ($d = 800 \mu\text{m}$) and a flat two-chamber proportional counter is enclosed in an anticoincidence scintillator cup. The geometric factor is determined by the opening in the anticoincidence scintillator. The proportional counter is equally sensitive throughout the opening angle of the detector. A thin window foil ($d = 1 \mu\text{m}$) made of polypropylene separates the gas chamber ($p = 35 \text{ torr}$ isobutane gas) from the exterior. For more details about this instrument, see Hovestadt and Vollmer³² and Blake et al.³³ With a small gas tank the instrument can operate for years. The energy and charge state coverage of this instrument is

References 32 and 33 will not be listed here. See References, page 205.

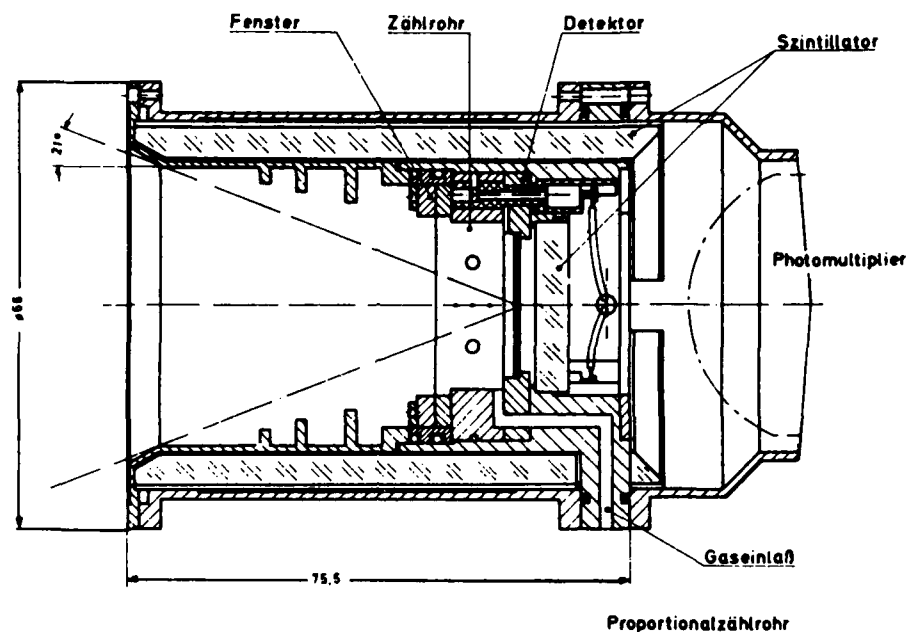


Figure 33. Energetic Iron Detector for the Measurements of Low Energy Cosmic Rays. The instrument features a large geometric factor $g = 1.27 \text{ cm}^2\text{-ster}$. It uses a proportional counter with a $1 \mu\text{m}$ polypropylene window and a 35 torr gas filled chamber. This instrument design was utilized on the S3-2 spacecraft³²

depicted in Figure 34 which shows the response of the detector system to different isotopes and elements.

An example of a third generation ion composition instrument is shown in Figure 35. This is a schematic diagram of the instrument flown by the MPE/Munich group on the ISEE-1 spacecraft. It combines electrostatic deflection with dE/dx and E measurements using a proportional counter. The position of incidence on the rear solid state detector element is also measured, and this position (because of the electrostatic deflection) is proportional to the quantity E/Q (energy per charge). Thus one determines E/Q , dE/dx and E , and from these quantities one can determine the ion charge state Q , ion mass and energy. In the same figure an in-flight example of the data obtained is shown. Carbon and oxygen ions are found in comparable quantities at MeV energies; this points to a solar, or at least a non-ionospheric, source for these energetic radiation belt ions. For more details see Hovestadt et al.^{12, 13}

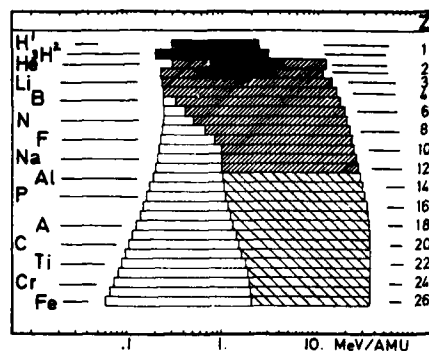


Figure 34. Response of the Cosmic Ray Composition Ion Detector System for Different Isotopes and Elements. The open boxes indicate the response to the various ions. The black boxes indicate the range of isotope separation and the densely shaded boxes show the regions of charge separation in groups

The principle of a time-of-flight mass spectrometer using secondary electron emission can be used to build a new type of instrument which uses an electrostatic deflection system as an integral part of the collimator aperture, post-acceleration, time-of-flight determination and energy measurements; it can be made to operate in the 1-300 keV range. This technique determines all the pertinent ionic parameters: the ion charge state Q , the ion mass M and the total ion energy E . Figure 36 shows the schematics of this instrument proposed for inclusion in the NASA/OPEN mission by the NOAA/SEL group in collaboration with a number of other institutions. The front electrostatic analyzer determines the ion energy per unit charge (E/Q) and the electric field may be stepped or swept continuously; the use of post-acceleration within the instrument (potential difference ϕ) helps to improve the resolution of the subsequent measurements, and the flight time (T) across the fixed internal distance (D) is measured. Finally the total energy (W) of the accelerated ion is measured with a solid state detector. The measured quantities: E/Q , W and T can be combined in an onboard microprocessor to yield the desired ionic characteristic quantities:

$$\frac{M}{Q} = 2 \left(\phi + \frac{E}{Q} \right) \frac{T^2}{D^2} \quad (3)$$

$$M = 2 W \frac{T^2}{D^2} \quad (4)$$

$$Q = W / \left(\phi + \frac{E}{Q} \right) \quad (5)$$

$$E = \frac{E}{Q} W / \left(\phi + \frac{E}{Q} \right) \quad (6)$$

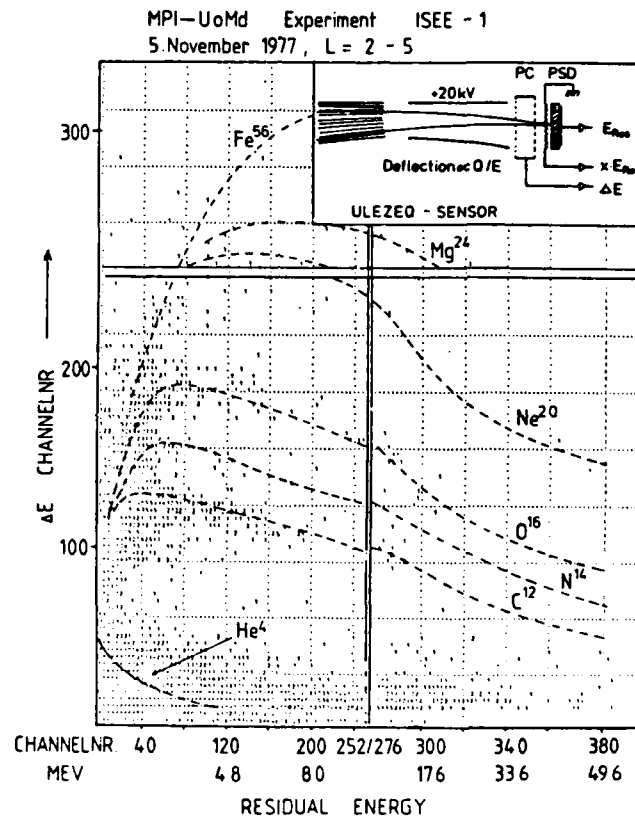


Figure 35. Principle of the MPE/Munich and University of Maryland ULEZEQ Sensor. Electrostatic ion deflection, dE/dx , E , and position sensitive rear detector permits separation of C, N and O ions and ion charge state information. This instrument was flown on the ISEE-1 spacecraft; for details, see Hovestadt et al^{12, 13}

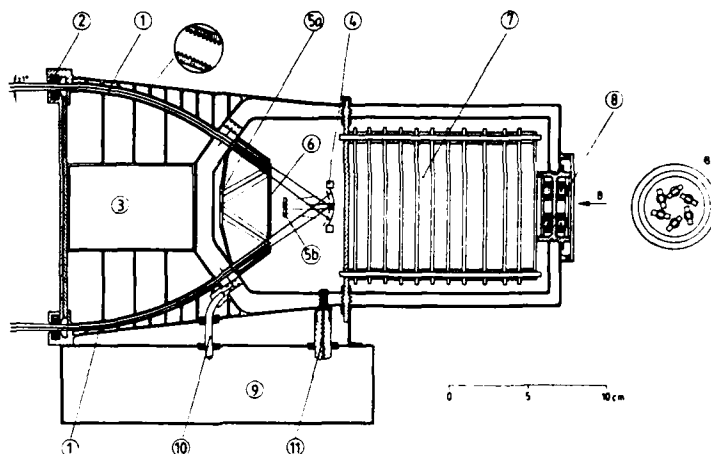


Figure 36. Instrument Capable of Measuring the Ion Mass, Energy, and Charge State in the Energy Range 1-200 keV. It features in-aperture electrostatic ion deflection and a ring-like aperture which permits both large geometric factor and high angular definition. Post-acceleration within the instrument makes solid state detectors effective for incident ion energies in the lower keV-range. This instrument is proposed for the NASA/OPEN mission by NOAA/SEL in collaboration with other institutions

An important aspect of the technique involves a collimator design which combines precise angular definition of the incident ion with a high geometric factor (in the older telescope-type collimator design these were mutually exclusive characteristics), and this feature permits high sensitivity to different ion species that are not necessarily very abundant in the magnetosphere. Figure 37 shows the logic of this instrument design, including time start/stop pulses for timing and the microprocessor characteristics.

The quality of resolution one may obtain with such an instrument is illustrated in Figure 38. This is a computer simulation based on experimentally determined detector and foil characteristics and shows the instrument M/Q versus M response matrix; the computation uses assumed magnetospheric ion population characteristics. It can be seen that the synthetic responses due to C^+ and O^+ are well separated from the responses due to the higher charge states of such ions. Thus this type of instrument is able to resolve all the important magnetospheric ion populations in the energy range that includes the "gap" in our present ion identification capability covering the entire ring current energy range.

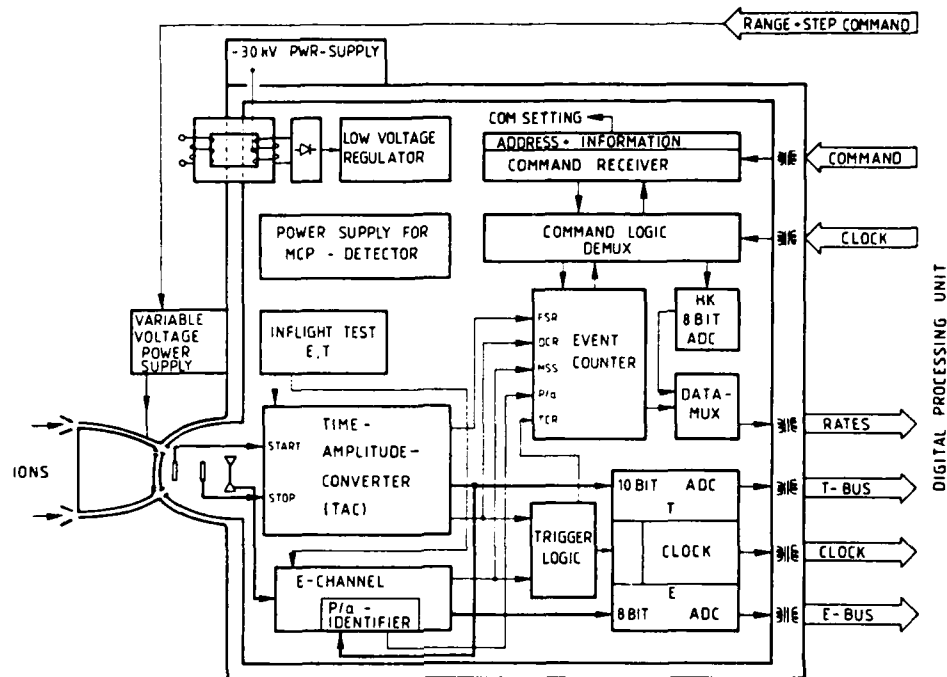


Figure 37. Microprocessor System for the Instrument Shown in Figure 36

To avoid contamination by energetic electrons and penetrating radiation the time-of-flight instruments rely on the fast timing characteristics (open time window is typically <100 nsec) and on substantial passive shielding of the instrument. The E/Q selection in the entrance aperture also severely limits the electron contamination. As such instruments come into use in space applications the concern about penetrating radiation effects and background suppression will be important. Fortunately, since at least two and sometimes more quasi-coincident detections are necessary in the time-of-flight instruments, these instruments have an intrinsic background rejection capability; of course, proper passive shielding is also important in excluding penetration of the lower energy ions and electrons of which high fluxes exist in the radiation belts. There is, however, a tendency for these instruments to produce their own internal background; this is illustrated in Figure 39 which shows a test result for a monoenergetic helium ion beam at 650 keV. Besides the effects of the prime ion beam there appears a number of "background" counts distributed in this energy-time matrix; one major reason for this stems from pulse pile-up effects in the rear solid state detector. This gives a spurious energy peak at the same time-of-flight as the primary signal. Pulse pile-up stems

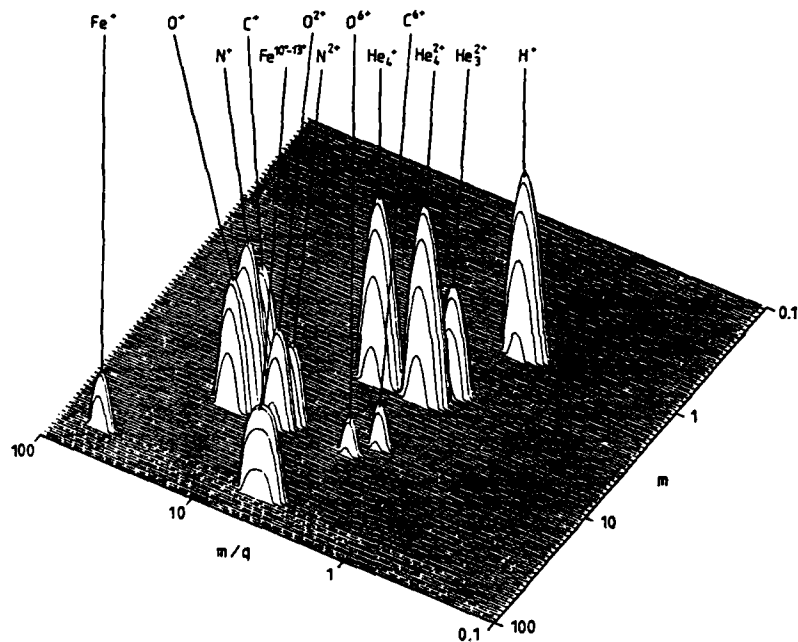


Figure 38. Computer Simulation of the Instrument Response to Different Ion Species Seen in the M versus M/Q Matrix. The instrument is shown in Figure 36

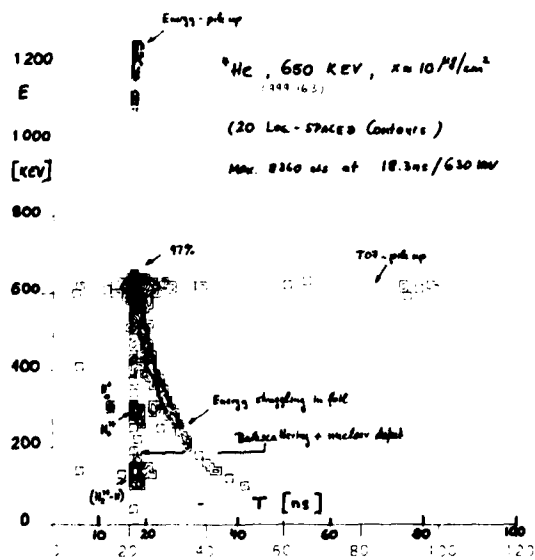


Figure 39. Laboratory Simulation of the Intrinsic "Background" Caused by a Number of Effects Within the Time-of-Flight Instrument

from the addition of two or more pulses that arrive faster than the electronics resolving time and is thus a function of the beam intensity (for very high incident fluxes) as well as the discriminator system time constants. Another source of error stems from the possibility that two or more ions can pass through the time-of-flight path on the time scale of a single particle passage. This gives rise to spurious counts at the correct particle energy but with an erroneous time-of-flight. A third error source stems from energy straggling (that is, statistical variation in the energy deposition rate) in the thin front detector element; this error source will not change ion mass determination, but will give some error in the precise energy measurement. Finally, the well-known 'nuclear defect' effect in the solid state detector elements coupled with possible ion backscatter from one of the detectors can also give rise to the 'internal background'. In a laboratory test of a prototype instrument it was found that approximately 97 percent of the beam was correctly registered and the other 3 percent was distributed over the various spurious count contributions. The best remedy for these problems are: (1) very fast electronic circuitry, sub-nanosecond resolution and fast rise and decay time for the pulses, (2) short time-of-flight path within the instrument and (3) use of a very thin front element.

Another important effect applicable to any time-of-flight ion mass spectrometer is angular scattering in the detector front element, which is particularly important for ions of such low energy that they barely penetrate the silicon detector. This means that the counting efficiency for lower energy and heavier mass ions becomes significantly reduced below unity in the lower part of the mass spectrometer range. For example, a 200 keV Argon ion was found to have only 10 percent counting efficiency (in a laboratory test using flight-grade silicon detectors). This points to the need for extremely careful pre-flight instrument calibration and assessment of the efficiency factors.

An interesting feature of this time-of-flight system is that it may be able to distinguish between a heavy atomic ion, for example Zn^{30} and an ionized molecule, for example, NO^+ with $M = 30$. A CO_2^+ molecule singly ionized passing through the front foil is fragmented by collisions with the foil atoms and continues through the instrument as individual (C + O + O) particles. Because of the breakup the molecular fragments lose more energy in the foil than a single heavy ionized atom, and slight velocity variations of the fragments occur. This gives rise to characteristic pulse signatures in the solid state detector.

New techniques that may come into use in the years ahead include the elimination of the spacing between the thin front detector and the rear detector in the classical solid state telescope. This would be done by growing the thin detector directly onto the thicker detector forming an integrated detector system. This will eliminate some of the angular scattering problems caused when the ions,

after having suffered scattering in the (separate) front detector, do not reach the rear element. An example of the kind of resolution achievable with an integrated detector system is given in Figure 40, here using beams of 1.63, 3.64 and 5.2 MeV alpha particles (He^{++}). The count distributions for the front layer and back layer are shown here; one finds similar resolution characteristics as for two separate detectors, but the advantages in handling and instrument design are clear.

Another principle that can be used in the kind of instruments described above is the analysis of the pulse shape which differs to some extent for incident ions of different nuclear charges.

A further example of a time-of-flight ion composition experiment that was developed for the Firewheel mission is shown in Figure 41. This is an ion composition telescope (detector head) which uses microchannel plate technology for secondary electron detection. Ions enter the baffled entrance aperture shown with an 11.4° opening angle. Within the collimator system a 'broom' magnet removes incident electrons, and the ions, in passing through a thin foil ($50 \mu\text{gm}/\text{cm}^2$), generate secondary electrons which are bent by a deflection magnet (100 Gauss) into

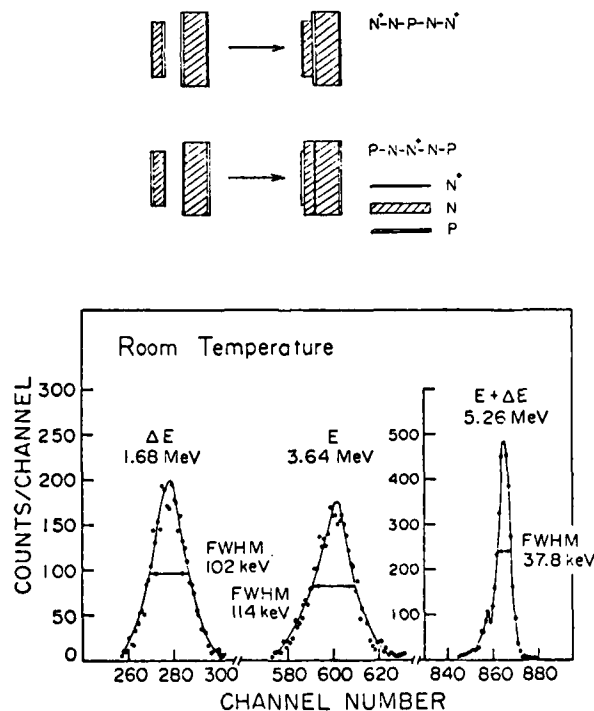


Figure 40. Resolution of Integrated Solid State Detectors

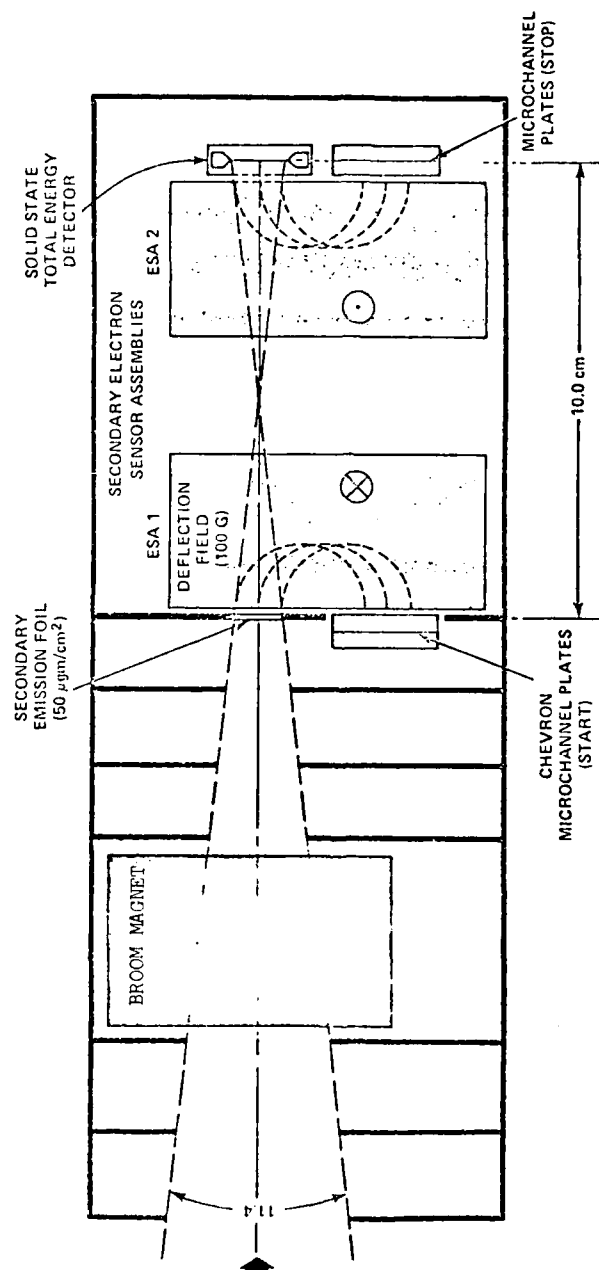


Figure 41. Firewheel Ion Composition Telescope Detector Head Utilizing Time-of-Flight Measurements in Conjunction with Solid State Detectors

a first set of microchannel plates; this marks the time of arrival, 'start' pulse. After a 10 cm flight path the ions enter a solid state detector which measures the total ion energy and liberates secondary electrons. The low energy electrons are bent in a magnetic field and are detected in a second set of microchannel plates; this produces the 'stop' pulse. Microchannel plates are very useful for the secondary electron detection because of the fast pulse rise time and large gain. The time resolution and energy range of this instrument, as determined in a laboratory calibration, are illustrated in Figure 42. The effective energy range extends from several tens of keV to several MeV per ion, and ions of hydrogen (protons), helium, the CNO group, neon and argon can be separated. The instrument electronics included a rotating priority system that insured adequate sampling of the different ion species and energies. The geometric factor of this instrument is about $6 \times 10^{-3} \text{ cm}^2\text{-ster}$ and can be increased somewhat, but at a cost of decreased instrument lifetime due to radiation damage. Electron contamination and penetrating radiation effects can be minimized by pulse height discrimination of the microchannel plate output; This method also eliminates contributions from protons since the number of secondary electrons emitted from the foil is proportional to the energy deposited there.

7. LOW ENERGY ELECTRON AND BULK ION MEASUREMENTS

While ions and electrons above 20 keV conveniently can be measured with solid state detector technology, particles of energies in the range from ten eV to tens of keV are currently monitored using electrostatic analyzers with various field configurations within the instrument. The energy range of this type of instrument makes it of particular interest for studies of the solar wind and the low energy part of the magnetotail plasma sheet, the radiation belts, the auroral precipitation and acceleration and the outer magnetosphere; it does not permit studies of the "cold" ($T \leq 1 \text{ eV}$) plasmaspheric and ionospheric plasmas.

Among the electrostatic analyzers in use there are five principal types of design; all of these use an electric field to deflect the incident ion and thus select a certain range of velocities of the incoming particle. Because of the opposite charges of ions and electrons these particles are easily separated (except for electron wall scattering effects). The five types are

- (1) cylindrical
- (2) parabolic with diverging geometry
- (3) spherical section
- (4) parabolic with parallel plates
- (5) toroidal (annular).

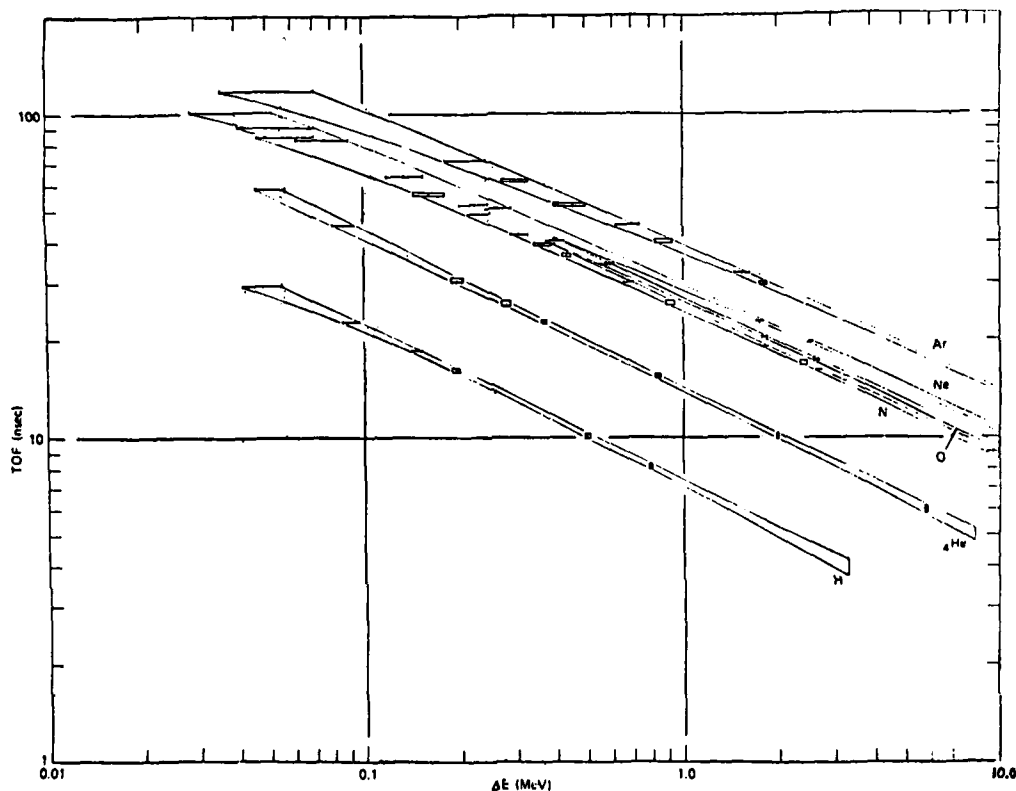


Figure 42. Resolution Characteristics of the Firewheel Time-of-Flight Solid State Detector System, as Determined in Laboratory Calibrations

Figure 43 shows a cylindrical electrostatic analyzer. This instrument is currently being used on the Air Force DMSP spacecraft. It consists of two parallel sections and has two collimators, one in front of and one following the deflector plates. The active measuring element is a particle channel multiplier. Within the deflection plates region the incoming particles are subject to the (radial) electrostatic force $\vec{F}_E = q\vec{E}$ where q = particle charge and \vec{E} is the instrument electric field. Particles with such energy that their centripetal force $F_S = MV^2/R = 2K/R$ (m = particle mass, V = velocity, R = radius of curvature and K = kinetic energy) balances the electric force ($K = 1/2 Rq \vec{E}$) will trigger the channel multiplier. The plate voltage is stepped and each voltage step provides

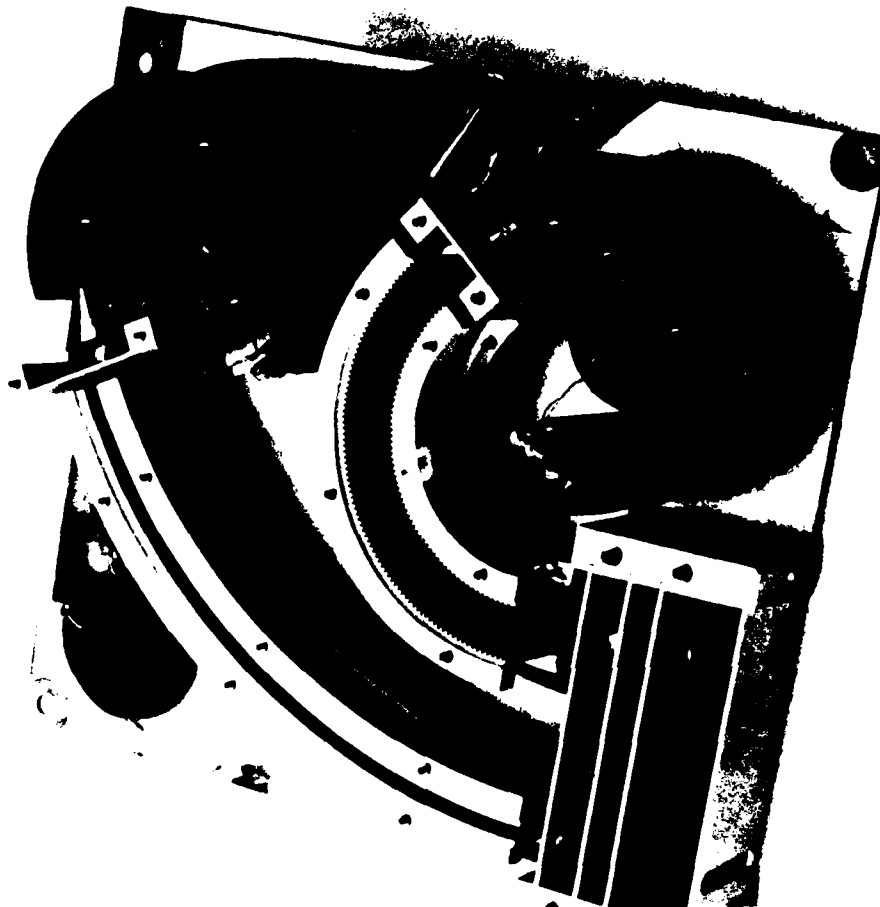


Figure 43. The Cylindrical Electrostatic Analyzer. This instrument type is used on the DMSP SSJ/3 spacecraft

an energy measurement. It is also possible to sweep the voltage continuously and to set the voltage to a fixed value for an extended period of time. The latter can greatly increase the time resolution at a cost of spectral information. Collimation determines both angular and energy response of the instrument. These considerations impose restrictions of the geometric factor obtainable and therefore on the sensitivity of the detector. Let A_1 and A_2 be the aperture cross section of the front and rear collimators, and let D be the mean distance (measured along the particle trajectory). For large distances D (compared to the radius of the largest of the aperture openings) the geometric factor is roughly given by

$$g \simeq A_1 A_2 / D^2$$

and this is the same approximate expression that applies to narrow angle solid state detector telescopes. When the particle acceptance angle becomes large ($\gg 10^\circ$) more precise determinations of the geometric factor must be made; for details see Thomas and Willis³⁴ and Paxton.³⁵ With this design the sensitivity can only be increased at a significant reduction in angular and energy definition. Increasing the front aperture A_1 enhances the acceptance angle and increasing the deflector plate separation enhances the energy band width (and also requires higher operating voltages to yield the same electric field strength). Decrease of the inter-aperture distance D enhances both energy bandwidth and acceptance angle, but short distances may lead to degradation of the instrument performance through susceptibility to electromagnetic radiation (such as sunlight) and particle scattering within the instrument. A commonly used version of this design has a 127° deflector plate curvature. This gives good particle focusing qualities into the channel multiplier (channeltron) device, and it also reduces contamination from scattering by requiring multiple scatter paths in order to reach the active detector. The cylindrical electrostatic analyzers have achieved geometric factors in the range 10^{-5} to 10^{-3} cm²-ster. Empirically this is adequate for radiation belt electrons, but not always for protons (ions) which may require greater sensitivity at some energies in this range. The shielding is primarily provided by passive means (thick walls of appropriate materials). The principal advantages are light weight (1-2 kg) and low power requirements (0.2 W).

Figure 44 shows the design characteristics of the parabolic electrostatic analyzer with diverging geometry. This type of instrument has been used on the ISIS spacecraft and auroral rockets. As with the previous instrument there are collimators both before and after the electrostatic deflection region. There are two active detectors, both channel multipliers. The deflection system acts as an electrostatic prism. Electrons and ions are deflected in opposite directions with deflection magnitudes dependent on the applied voltage. This permits the simultaneous measurement of ions and electrons with one instrument. Contamination due to scattering of particles or electromagnetic radiation is greatly reduced due to there being no direct scattering path between the front aperture and the channeltron detectors. A later design of this instrument for the Atmospheric Explorer (AE) satellite also includes a light-trap arrangement.

34. Thomas, G. R. and Willis, D. M. (1972) Analytical derivation of the geometric factor for a particle detector having circular or rectangular geometry, *Journal of Physics E: Scientific Instruments* 5:260.

35. Paxton, F. (1959) Solid angle calculation for a circular disk, *The Review of Scientific Instruments* 30:254.

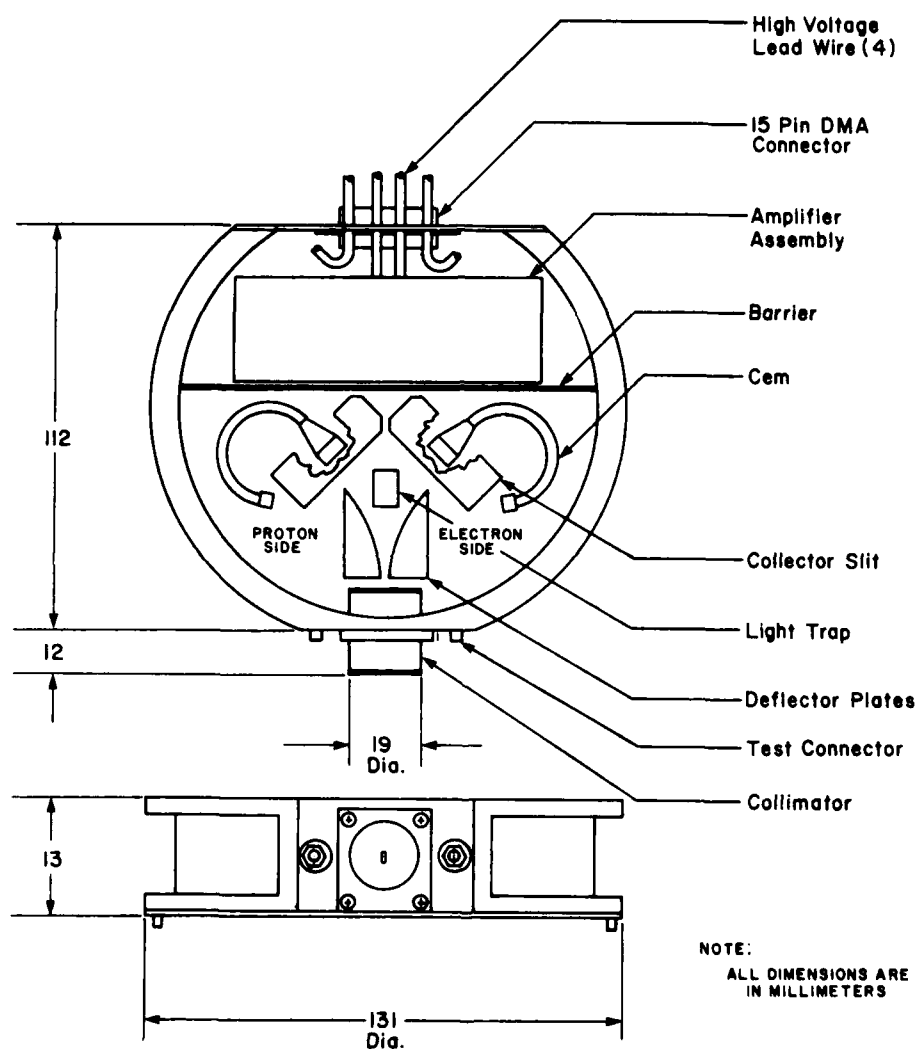


Figure 44. An Example of an Electrostatic Analyzer Using the Parabolic Diverging Geometry Principle. This instrument design has been used on many auroral rockets and on the ISIS spacecraft

A photograph of this detector system including the electronic on-board data processing system is shown in Figure 45; this was built for the DE-A spacecraft. The geometric factor of this instrument is 10^{-4} cm²-ster. In this satellite an array of 15 electrostatic detector systems are mounted on a separate platform in a fan-shaped array to provide detailed angular flux information; the platform is oriented according to the instantaneous magnetic field direction as determined from an onboard magnetometer.



Figure 45. An Electrostatic Analyzer for the DE-B Spacecraft Using the Parabolic Diverging Geometry

An example of the spherical section electrostatic analyzer design is shown in Figure 46. It consists of two concentric spherical sections forming the deflector surfaces across which the voltage is applied. One advantage of this design follows from the fact that particles entering the front aperture travel on great circles through the deflector system and thus, after 180° deflection, focus well for precise monitoring in the channel multipliers. This figure shows examples of particle trajectories within the instrument. Another major advantage is that it is possible to make many angular samples simultaneously by some variation in this design.

The principle behind the spherical type electrostatic analyzer has been applied by the University of Iowa group³⁶ to construct a quadra-spherical detector system used for the ISEE spacecraft. This instrument which is depicted in Figure 47 has an electrostatic deflector system consisting of three concentric shells using a 70° solid angle section of a sphere. The center shell is charged to a (variable) potential V and the other two shells are held at zero (ground) potential. This design allows simultaneous monitoring of ions and electrons over a wide range of incident angles. To achieve the latter property no entrance collimation is done other than that provided by the geometry of the deflector plates themselves. Seven sets of channeltron detectors mark the inner end of the deflection region. Particles with different incident angles will trigger different channel multipliers with angular resolution according to the number and size of such detectors. In the design of this instrument for the ISEE spacecraft the total angular acceptance angle spans 180° , and the mounting of the instrument in the plane of the spacecraft spin axis permitted the full 3-dimensional flux distribution to be studied. The voltage V is varied in 64 steps for high energy resolution. This capability has proven extremely valuable for research in regions of the magnetosphere where plasma flow and intermittent beams are important. Such high resolution measurements require high telemetry rates, and instrument reprogramming capability to switch from lower to higher duty cycles.

Another application of the spherical section design is the ISEE solar wind monitoring detectors. This instrument, which is shown in Figure 48, was built by the Los Alamos group³⁷ and uses two separate spherical section detectors each with a 135° solid angle segment. The detection technique is somewhat different than in the previous example. The deflection is done by the appropriate electric field and the selected ions are incident upon a series of active copper-beryllium

36. Frank, L.A., Yeager, D.M., Owens, H.D., Ackerson, K.L., and English, M.R. (1978) Quadrispherical LEPEDAS for ISEE's 1 and 2 plasma experiments, IEEE Transactions on Geoscience Electronics, GE-16:221.
37. Bame, S.J., Asbridge, J.R., Felthaus, H.E., Glore, J.P., Paschmann, G., Hemmerich, P., Lehmann, K., and Rosenbauer, H. (1978) ISEE-1 and ISEE-2 fast plasma experiment and the ISEE-1 solar wind experiment, IEEE Transactions on Geoscience Electronics, GE-16:216.

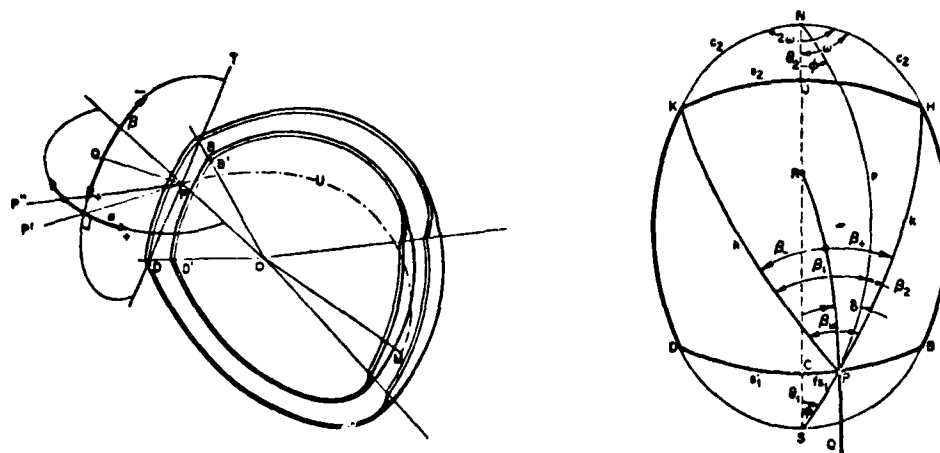


Figure 46. The Measurement Principle of a Spherical Section Electrostatic Analyzer

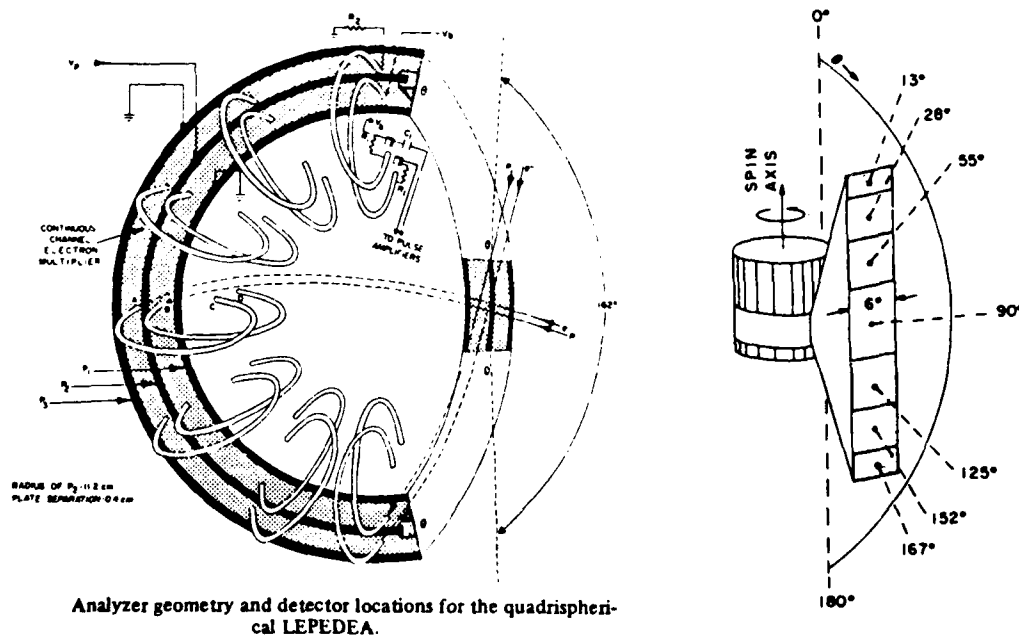


Figure 47. An Example of the Spherical Section Electrostatic Analyzer Utilized by the University of Iowa group on the ISEE-1 Spacecraft³⁶

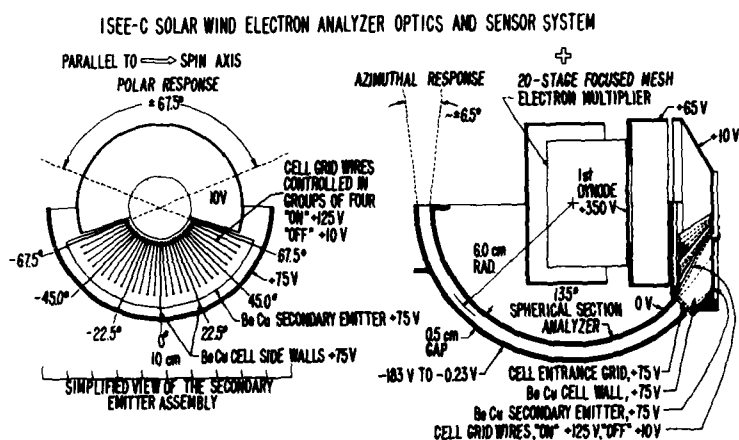


Figure 48. A Spherical Section Electrostatic Analyzer Used by the Los Alamos Group in Solar Wind Studies³⁷

secondary emitters. From these devices secondary electrons are released and these are steered and accelerated by the use of a grid system into a 20-stage dynode multiplier. By a series of such devices angular information is obtained through sequencing; simultaneous parallel measurements in all the devices give angle integrated observations and thus a higher signal which is advantageous in some applications. Figure 49 shows a different perspective of the workings of the secondary emitters and the controlling grid system.

The instrument response as a function of polar (incident) angle is illustrated in Figure 50 for incident electrons. The response characteristics for ions are similar. The principal disadvantage of the instrument is the need to sequence from one incident angle to another as well as over all the energy steps. This precludes simultaneity in measurements and reduces the time resolution obtainable.

The parabolic electrostatic design with parallel plates appears to have been initiated by the University of California at San Diego group and has been used on the ATS-5 and ATS-6 spacecraft, on SCATHA, and for Total Energy Detector on the operational Tiros spacecraft.³⁸ The principles of this instrument type are displayed in Figure 51. In order to achieve a large geometric factor the entrance aperture is large and only a small deflection of the plates in the energy analyzing direction is used (55 percent curvature). Focusing in the orthogonal direction is

38. McIlwain, C. (1971) UCSD Experiments, in: Operations Manual for the Environmental Measurements Experiment on the Applications Technology Satellite Mission ATS-F, pp 4-109, Westinghouse Defense and Space Center, Document 710667, Baltimore, Maryland.

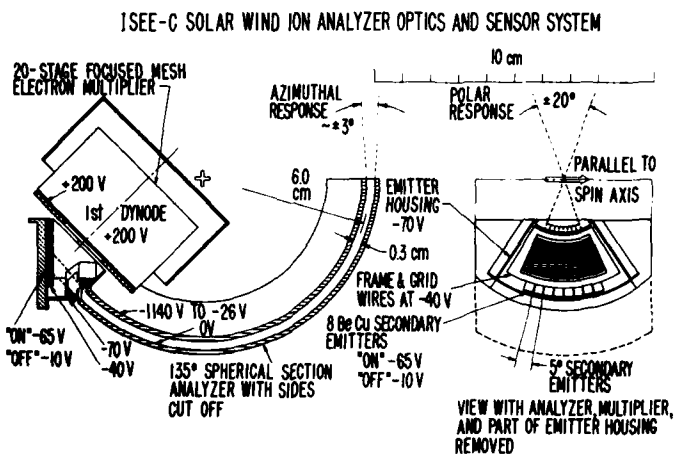


Figure 49. Principle of the Secondary Electron Emitters Utilized in the Instrument Depicted in the Foregoing Figure

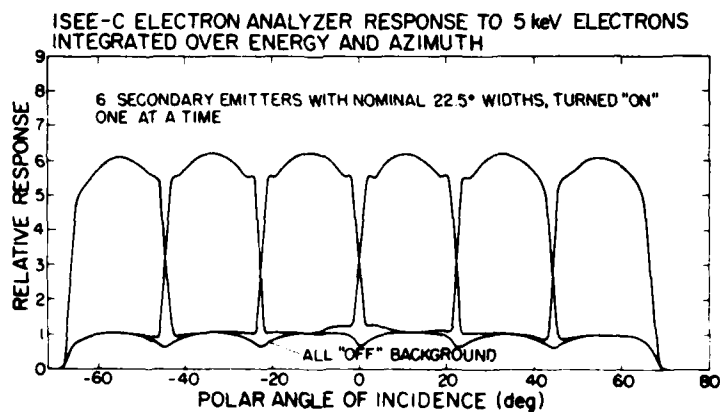


Figure 50. The Instrument Response Characteristics for Electrons in the Spherical Section Electrostatic Analyzer Shown in Figure 48

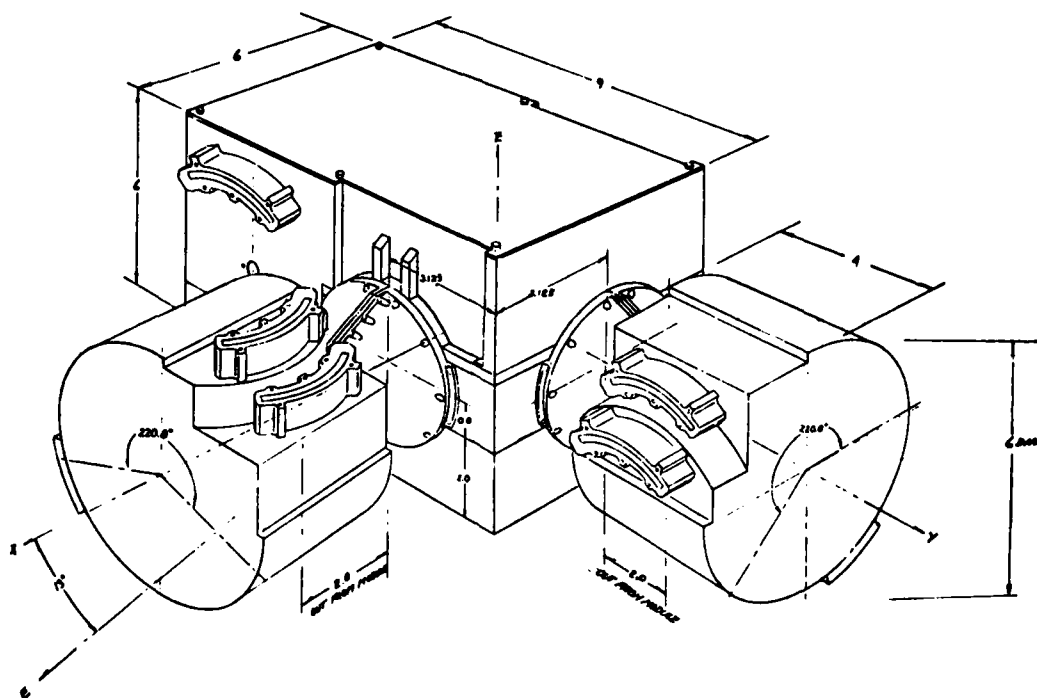


Figure 51. Parabolic Electrostatic Analyzer Designed by the U. C. San Diego Group Using the Parallel Plate Geometry³⁸

achieved by a 26 percent decrease in curvature in that direction. A special feature of this instrument concept is a set of two grids placed between the energy analyzer and the channel multipliers used as detector devices; these grids provide an electric field which further helps to focus the incident particles onto the channeltron detector. This instrument thus combines a small angular response with a reasonably large geometric factor. Separate detector systems for electrons and ions are required, however; and on the non-spinning ATS-6 satellite the instruments could be mechanically rotated to provide response to different pitch angles. This instrument has been used to study in detail the low energy geosynchronous radiation environment. One disadvantage of a stepping electrostatic particle energy analyzer is that it takes time to obtain a full particle spectrum and thus the finer details of temporal events such as certain injection events are difficult to resolve.

A new design which has not yet been flown in space is the toroidal (or annular) electrostatic analyzer. The main features of this type of instrument are shown in Figure 52; the design has been reported by French and Finnish scientists. Its

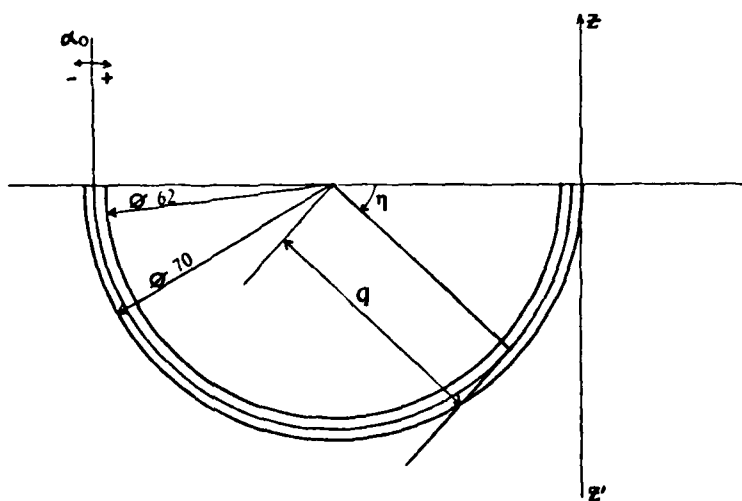
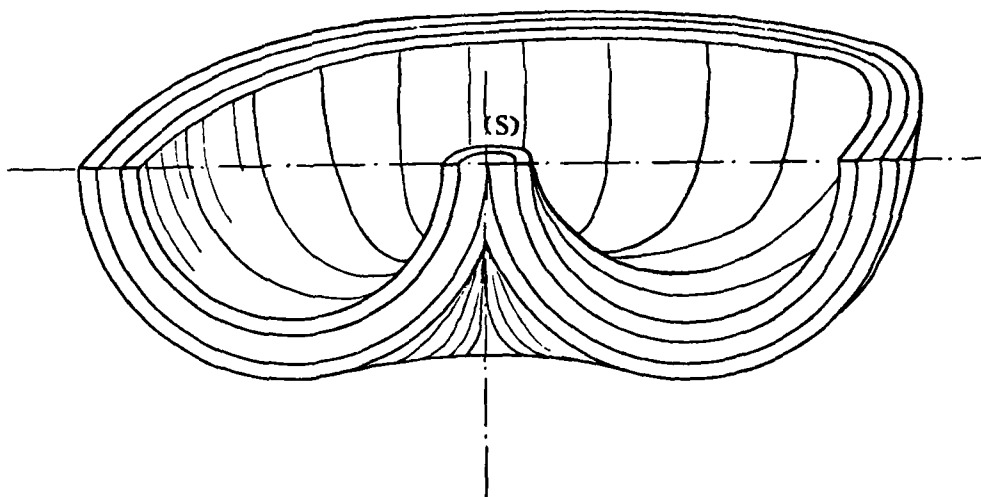


Figure 52. Principle of the Toroidal (Annular) Electrostatic Analyzer

prime advantage is that one can obtain a rather large geometric factor with a small instrument. The geometry arises from the rotation of a cylindrical system around an axis perpendicular to the radius of curvature for a particle in the deflection region. This increases the area of the front aperture (without opening the angular definition of the instrument) from the value of A_1 to the value A_1^* defined by $A_1^* = 4\pi^{3/2} R \sqrt{A_1}$ where $R(\gg \sqrt{A_1})$ is the radius of the axial rotation needed to make the toroidal apparatus. If the geometric factor itself is not the most significant consideration, one can make a tradeoff by reducing the geometric factor by narrowing the plate distance in the toroidal deflection system in favor of high energy resolution. Recent design has achieved energy resolution of $\Delta E/E$ of the order of 0.1 with a geometric factor of $2 \times 10^{-4} \text{ cm}^2\text{-ster}$. Spectral resolution of this quality may be needed to study certain types of field-aligned particle acceleration characteristics. One design characteristic of the toroidal electrostatic analyzer is the shape, which makes it difficult to shield behind the spacecraft skin; substantial passive shielding in the instrument walls would be needed.

8. ENERGETIC ELECTRON MEASUREMENTS

While magnetospheric electrons are well measured with electrostatic analyzers up to a few tens of keV, other techniques are employed at higher energies. The energy range 20 keV to >5 MeV is covered by instruments using solid state detectors, scintillators and magnetic deflection systems. Besides the known dynamic range as function of L-shell and electron energy mentioned in the beginning of this paper there are also dynamic variations by factors of 1 to $>10^3$, particularly in the radiation belt electron 'slot-region' located between $L = 2$ and $L = 4$ (depending on electron energy). Energetic electron spectra are frequently not describable by a power or exponential law, but exhibit significant peaks and valleys³⁹ as illustrated in Figure 53. This demonstrates the importance of making spectral measurements with high resolution in differential rather than integral passbands. Much can be learned about radiation belt physics and about electron precipitation into the atmosphere from spectral and temporal variations. Energy resolution of the order of 10 percent would be highly desirable in some applications, particularly at low altitudes where the work of the Lockheed group indicates that sharp peaks are regular features of the energetic electron spectra. Some of their findings are

39. Spjeldvik, W.N. and Thorne, R.M. (1975) The cause of storm after effects in the middle latitude D-region, Journal of Atmospheric and Terrestrial Physics 37:777.

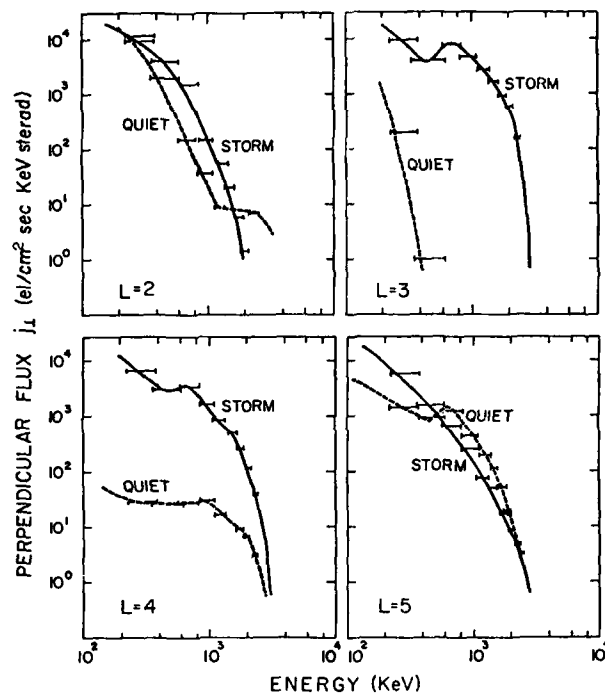


Figure 53. Radiation Belt Electron Spectra Prior to (Dashed Lines) and Following (Solid Lines) a Geomagnetic Storm. The data are given at L = 2, 3, 4 and 5; and it was obtained with the OV1-19 spacecraft³⁹.

shown in Figure 54, and the features may be interpreted in terms of electron-plasma wave resonance phenomena.⁴⁰

While wave-particle interactions for ions are thought to be primarily important in the tens of keV range, radiation belt electrons have significant interactions with ELF and VLF whistler mode turbulence up to MeV energies. In fact, these interactions, which are important for electrons both at keV and MeV energies, have been shown to control the structure of the quiet time radiation belt electrons within the plasmasphere.⁴¹ The resulting relativistic electron precipitation profoundly affects the ionospheric D-region at night for quiet times and at all times

40. Imhof, W.L., Gaines, E.E., and Reagan, J.B. (1981) Observations of multiple, narrow energy peaks in electrons precipitating from the inner radiation belt and their implications for wave-particle interactions, *J. Geophys. Res.* 86; in press.

41. Lyons, L.R. and Thorne, R.M. (1973) Equilibrium structure of radiation belt electrons, *J. Geophys. Res.* 78:2142.

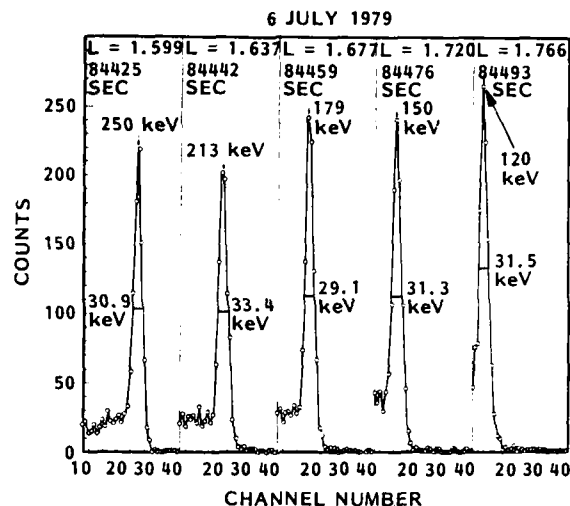


Figure 54. Examples of Some Very Narrow Peaks in the Energy Spectra of Precipitating Electrons Observed at Low Altitudes on the P78-1 Satellite. The narrow peaks are thought to result from cyclotron resonant interactions with VLF waves that must possess a bandwidth less than ~ 1 kHz⁴⁰

during storms.^{39, 42} It has been suggested that manmade waves (power-line harmonics, VLF transmitters, etc.) may have effects on the radiation belt electrons and cause electron precipitation. Studies of such a possibility require coordinated wave, and cold plasma particle measurements in space.

Besides the requirements for fine spectral resolution, research on the radiation belt electron processes require instruments with precise angular definition which must be a few degrees or better for loss cone studies and at most 10-15 degrees for studies of the trapped electron pitch angle distributions. Radiation belt electrons are known to exhibit sharp peaks near 90° equatorial pitch angles sometimes, and deep valleys at 90° at other times.^{24, 43, 44}

42. Reagan, J.B. (1977) Ionization Processes, in: Dynamical and Chemical Coupling Between the Neutral and Ionized Atmosphere, (ed. by: B. Grandel and J. A. Holtet), D. Reidel, Dordrecht, Holland.
43. West, H.I., Jr., Buck, R.M., and Walton, J.R. (1973) Electron pitch angle distributions throughout the magnetosphere as observed with OGO-5, J. Geophys. Res. 78:1064.
44. West, H.I., Jr., Buck, R.M., and Davidson, G. (1979) Study of Energetic Electrons in the Outer Radiation Belt Regions Using Data Obtained by the LLL Spectrometer on OGO-5 in 1968, Lawrence Livermore Report UCRL-52807, California.

Because of their small mass, energetic radiation belt electrons generally have relativistic velocities; at 511 keV the electron kinetic energy equals the rest mass energy and the kinetic velocity $v = \frac{1}{2} \sqrt{3} c \simeq 0.866c$ where c is the speed of light. This implies that instruments measuring dynamic variations and energy dispersion in electron injection and acceleration mechanisms must have the capability of great temporal resolution. Empirical data indicate that a time resolution capability of 10^{-2} sec or better is desirable for event studies.

Energetic electron detectors must have the capability of good background rejection. Cosmic rays, high energy protons and other ions and very energetic electrons can penetrate insufficient detector shielding and cause spurious counts in the instrument. Within the instrument, effects of secondary radiation such as Bremsstrahlung X-rays must be suppressed. This error source has caused severe problems in past measurements, and the elimination of the background is very important for achieving accurate measurements. Desirable features are a 10-30 percent absolute accuracy in the flux determinations and a few percent relative accuracy for precise angular and spectral measurements. Sensitivity requirements for energetic electrons range from a geometric factor of $\leq 10^{-3} \text{ cm}^2\text{-ster}$ at tens of keV energies to $\geq 1 \text{ cm}^2\text{-ster}$ to measure the most energetic, multi-MeV, electrons.

Two types of energetic electron detectors are used: omnidirectional (half of the 4π solid angle response) and directional spectrometers. A detector system built by the Aerospace group for the ATS-6 spacecraft is shown in Figure 55. Sensor 1 in this figure is a directional detector using a baffled collimator, and sensors 2-4 are omnidirectional detectors. For the omnidirectional detectors the back-hemisphere (unwanted) is heavily shielded while the front hemisphere (wanted) has lighter shielding which increases from sensor 2 through sensor 4 to yield different sensitivity to the electrons. The signal from the detector is electronically shaped and amplified and discriminated into different energy channels. This type of instrument works well. No pitch angle information is of course available from this detector design.

There exist a variety of directional energetic electron spectrometers. Many of them use magnetic deflection techniques. Figure 56 shows an instrument built by the Lawrence Livermore Laboratory group.⁴³ In it, a magnetic field bends the incident energetic electron trajectories into a series of solid state detectors. The field is weak enough to insure that protons and other ions do not suffer strong directional changes. A combination of two such instruments was built to span the range of electron energies from 79 keV to 2.8 MeV. When mounted on a spinning spacecraft or on a rotation platform on a non-spinning spacecraft this type of instrument also gives pitch angle information. The geometric factor depends on the aperture opening angle. A significant limitation on the use of this design results

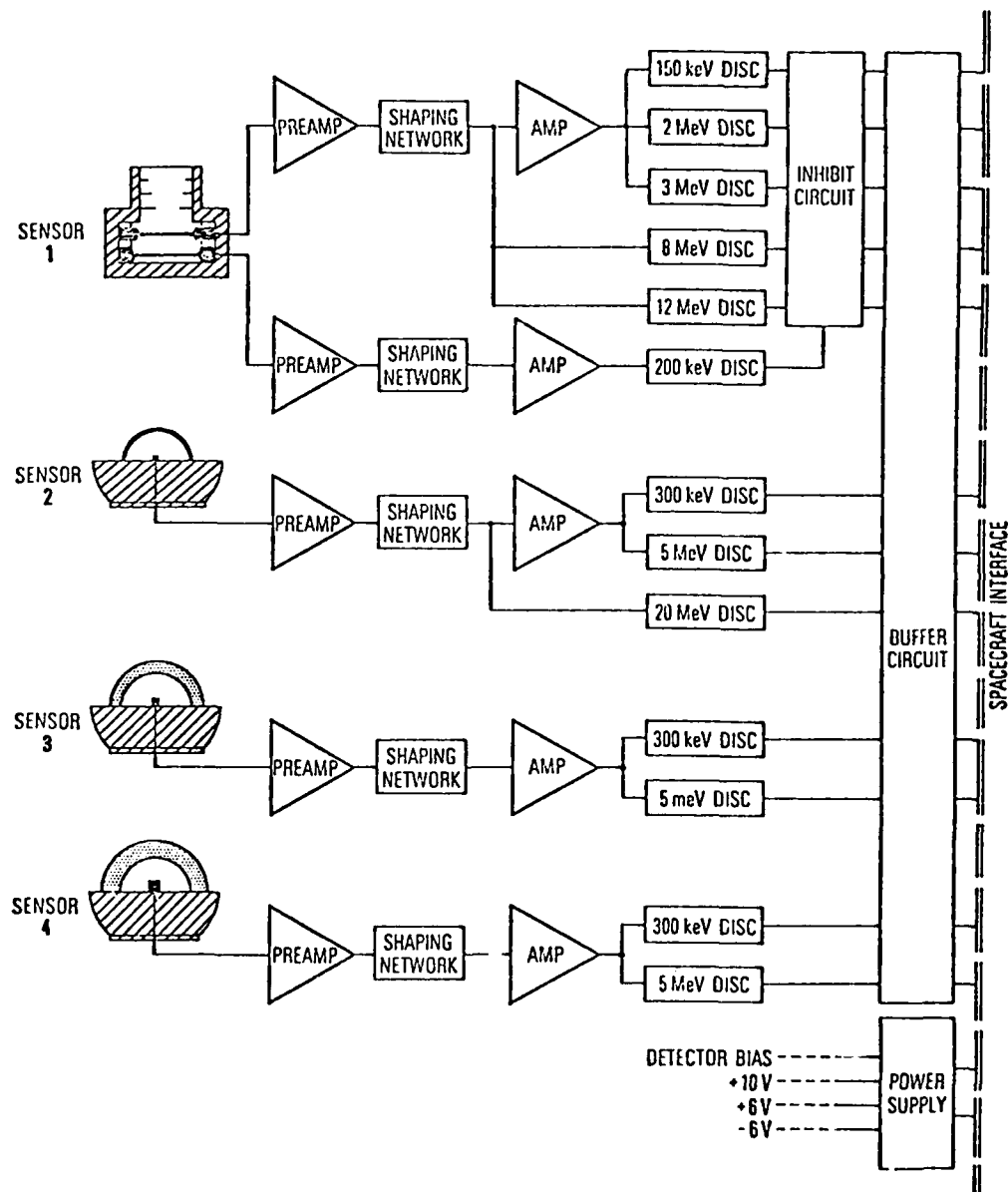


Figure 55. Omnidirectional Energetic Electron Detector System Built by the Aerospace Group and Utilized on the ATS-6 Satellite. Sensors 2-4 have different shielding

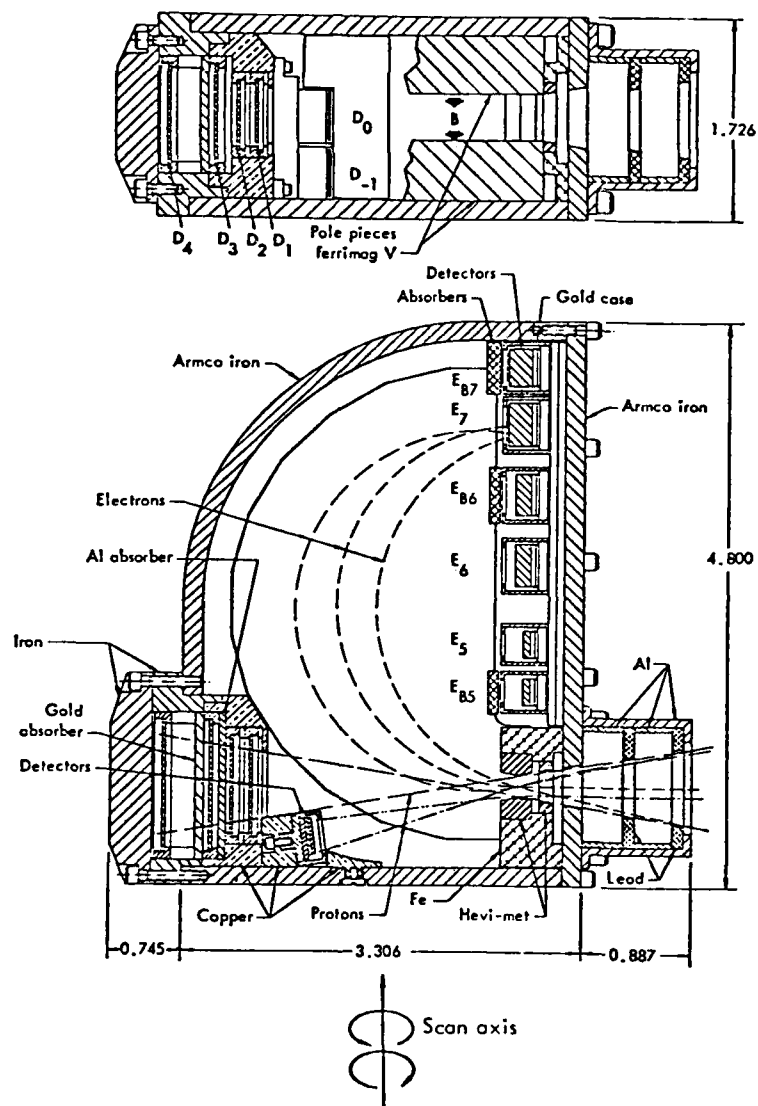


Figure 56. Magnetic Particle Spectrometer Built by the Lawrence-Livermore Group. The instrument is primarily sensitive to electrons although ions are also measured in a separate detector stack⁴³

from the large weight and size requirements. Another instrument of this type is shown in Figure 57. This instrument, which was built by the Aerospace group, was flown on the OV3-3 spacecraft. Both of these detector systems were well shielded by iron walls. A recent application of the magnetic spectrometer design is also depicted in Figure 9.

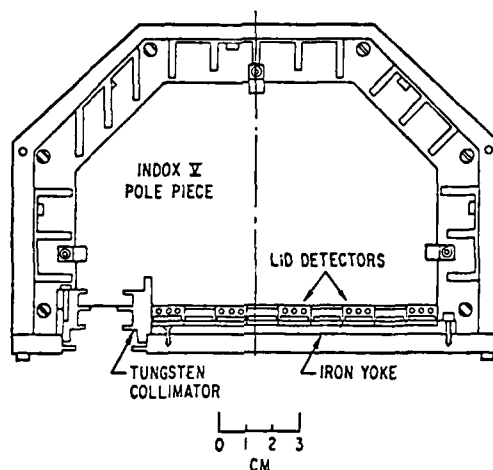


Figure 57. Magnetic Electron Spectrometer Built by the Aerospace Group and Flown on the OV3-3 Spacecraft. This instrument is insensitive to energetic ions

Scintillation electron spectrometers are of rather simple structure, consisting of a piece of scintillator followed by a photomultiplier. Current designs use plastic or Cesium iodide scintillators, and their performance characteristics are depicted in Figure 58. Basically, electrons have a much longer range (before stopping) in the scintillator material than do ions of comparable energies. The scintillator technique is useful from a few tens of keV to 10 MeV. A scintillator thickness of a few centimeters is sufficient to cover the electron energy range of interest in the radiation belts. This type of detector was much in use before the development of the solid state detector technology. The principal disadvantages are the requirement for a photomultiplier tube and the tendency for the instrument to be heavy.

A different type of instrument capable of measuring energetic electrons (and other particles) is shown schematically in Figure 59. This design is utilized by

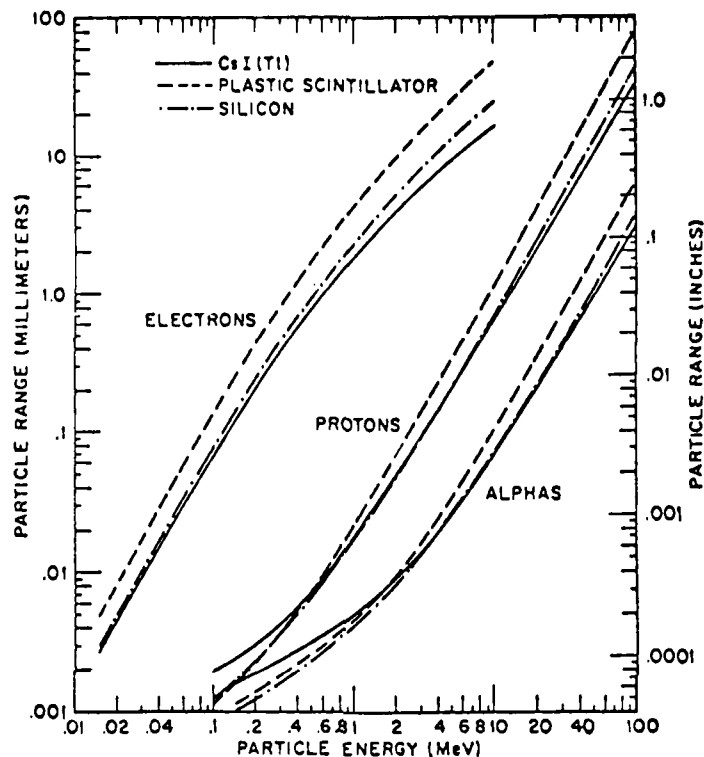


Figure 58. Performance Characteristics of Different Types of Scintillators. The particle ranges in the scintillator are given for CsI (Tl), silicon and plastic scintillators

the Los Alamos group and measures electrons at several tens of keV energies. The instrument is collimated for narrow angular acceptance and is heavily shielded against penetrating radiation. A window element eliminates protons (and other ions) up to 300 keV and solid state detectors measure the energy of the energetic electrons. This particular design has a multiple sensor system for simultaneous observations in several directions.

To measure the MeV electrons a series of solid state detector elements can be used, as illustrated in Figure 60. The principle of the electron energy measurement is similar to that of energetic ions described earlier, namely that of pulse height discrimination in multiple solid state detectors. The principal advantages of these solid state detector instruments are their small sizes and relatively light weights. In the outer radiation zone where most of the ion background is "soft" (that is, of energies in the low keV range) these instruments work quite

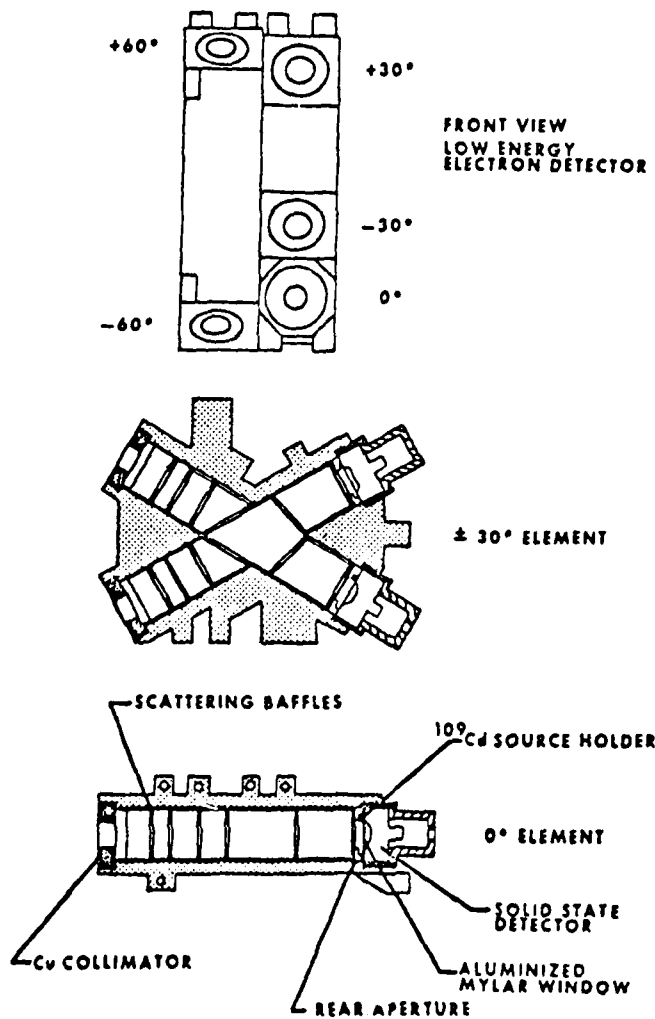


Figure 59. Charged Particle Analyzer Built by the Los Alamos Group to Permit Simultaneous Observations in Several Directions. The instrument is sensitive to electrons and ions in different pass-bands

AD-A113 959

AIR FORCE GEOPHYSICS LAB HANSCOM AFB MA
PROCEEDINGS OF THE AIR FORCE GEOPHYSICS LABORATORY WORKSHOP ON --ETC(U)
OCT 81 R C SAGALYN, W N SPJELDVIK, W J BURKE
AF6L-TR-81-0311

F/G 4/1

UNCLASSIFIED

NL

3 of 3
AD-A
113959



END
DATE
FILMED
5-82
DTIC

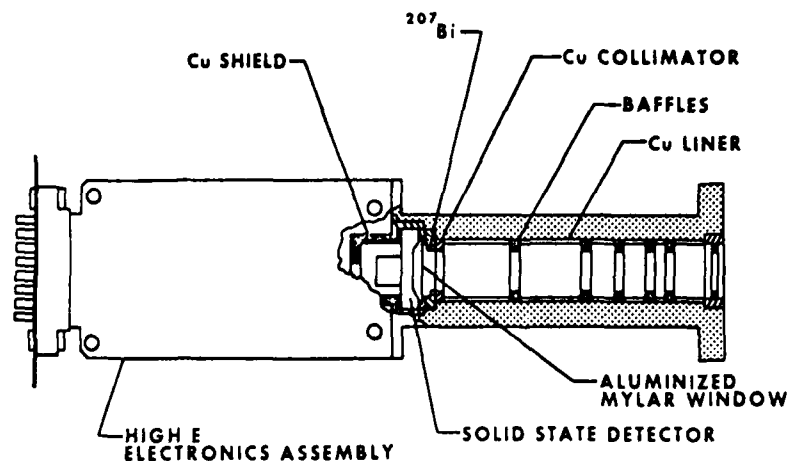


Figure 60. Energetic Charged Particle Analyzer Built by the Los Alamos Group. This instrument measures energetic electrons and ions to MeV energies

well, but in the inner radiation zone where most of the proton (ion) fluxes are "hard" (that is, in the MeV range) backgrounds may be substantial.

Such a technique is also used in the energetic particle telescope built for the SCATHA satellite by the Lockheed group. This instrument features a long collimator (with internal baffles) for narrow angular collimation to obtain fine pitch angle measurements, a "window" to remove contributions from the lower energy ions, and a stack of solid state detectors that form a dE/dx -E telescope. The detectors are surrounded by a plastic scintillator (followed by a photomultiplier tube) for anticoincidence suppression of background count contributions, and heavy shielding against X-rays and penetrating particles. Primarily, the instrument measures electrons from 47 to 5100 keV with a relatively high geometric factor of $3 \times 10^{-3} \text{ cm}^2\text{-ster}$, but also measures protons from 1 to 100 MeV and helium ions from 6 to 60 MeV. Energy spectra are obtained with a 12-channel pulse height analyzer. Figure 61 depicts the design of this instrument.

By operating scintillators and solid state detectors together one obtains a hybrid type of energetic electron detector system. An example of this design, built by the Los Alamos group, is shown in Figure 62. Two solid state detectors are located within the front aperture, and these are followed by a Bismuth Germanate ($\text{Bi}_4\text{Ge}_3\text{O}_{12}$) scintillator (with a photomultiplier tube) in coincidence with the front detectors. The geometric factor is large: $0.15 \text{ cm}^2\text{-ster}$ and the instrument is suitable for measurements of very high energy electrons (2.5 to 16 MeV) in four energy channels. Since the flux levels to be measured are very low, the main

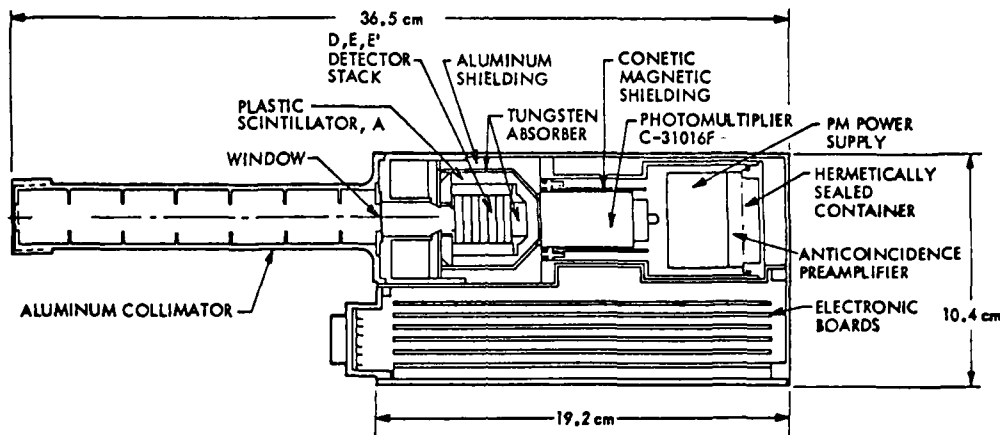


Figure 61. Energetic Particle Detector Telescope Built by the Lockheed Group and Flown on the SCATHA Spacecraft. The long collimator permits precise angular definition and fine pitch angle resolution

problems in detector systems for this energy range are significant background contributions due to Bremsstrahlung X-rays and cosmic rays. It is difficult to get enough shielding for clean measurements, and anticoincidence scintillators have not been very effective in reducing the X-ray background when good measurements of multi MeV electrons are required.

9. OTHER TYPES OF MEASUREMENTS

9.1 X-ray Cameras

Studies of the loss cone distributions of energetic electrons are difficult because of the high sensitivity and high background rejection requirements. In the auroral zone the loss cone population has very dynamic characteristics and at lower latitudes it can be extremely anisotropic. The relative flux intensities at equatorial pitch angles of $\pi/2$ and 0 can vary from nearly 1 (for strong pitch angle diffusion conditions) to $\ll 10^{-4}$ at low latitudes. For equatorial spacecraft the angular resolution requirements are formidable since the loss cone only spans a few degrees of pitch angle space,²⁵ and for low altitude polar orbiting satellites (which view a larger loss cone seen in local pitch angle) the rapid crossing of L-shells makes separation of temporal and spatial features difficult. It is well known that energetic electrons produce Bremsstrahlung X-rays upon precipitation into the atmosphere. Observations made on balloons are useful for such studies

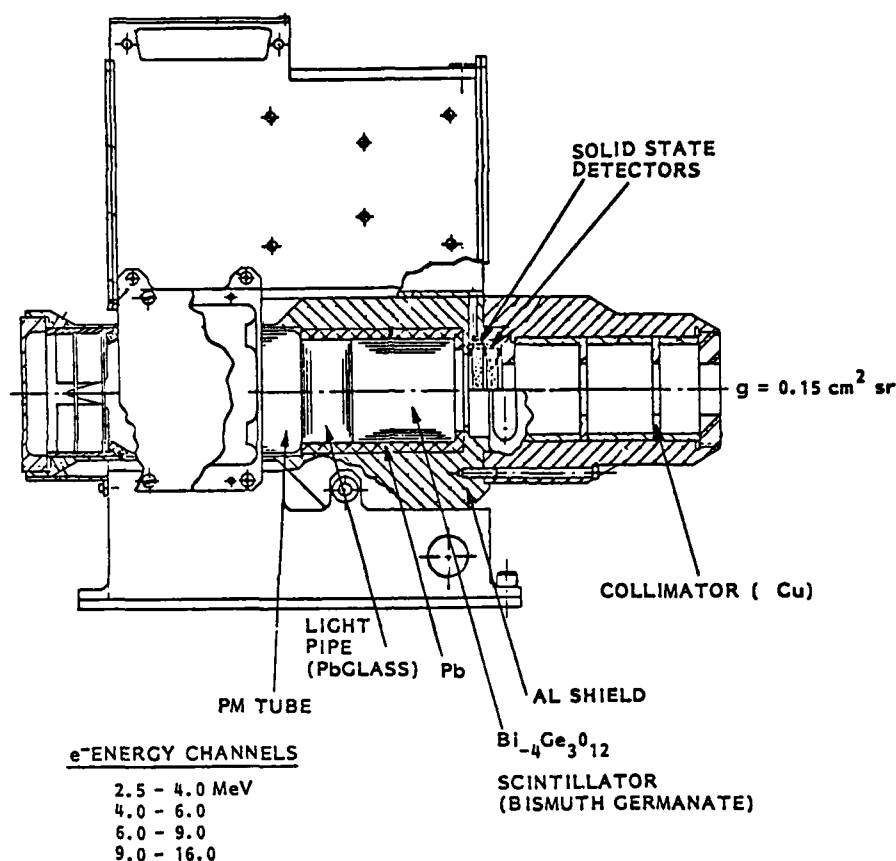


Figure 62. Hybrid Detector System that Utilizes Both Solid State Detectors and Scintillators. The instrument has a large geometric factor and is sensitive to electrons in the 2.5-16 MeV range

and much morphological information has already been gathered⁴⁵ using scintillation counter techniques. Wide field-of-view coverage can be achieved by measuring Bremsstrahlung X-rays from a satellite, a technique that has been demonstrated in orbit by the Lockheed and Aerospace groups. Another technique that permits X-ray imaging is the University of Washington pin-hole X-ray camera. This device is illustrated schematically in Figure 63. It is a variation of the scintillator technique where the scintillator is viewed by four photomultiplier tubes and is surrounded by a plastic scintillator for anti-coincidence background rejection. An

45. Trefall, H. (1973) Auroral Zone X-rays, in: *Cosmical Geophysics*, p 237, (ed. by: A. Egeland, O. Holter and A. Omholt), Universitetsforlaget, Oslo, Norway.

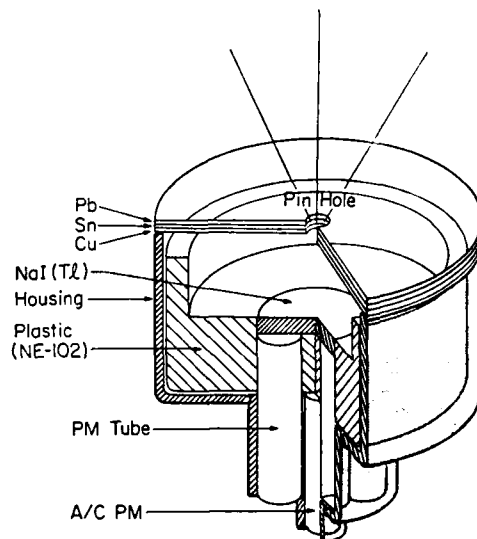


Figure 63. Pin-hole Type X-ray Camera Used by the University of Washington Group to study Bremsstrahlung X-rays from Precipitating Energetic Electrons. This instrument was flown on a balloon and can also be used on a satellite

incoming X-ray proton will generate a track of visible light photons in the scintillator and these are viewed by the photomultipliers. If the track is in the center of the scintillator all photomultipliers yield the same signal, but if the track is off center the signal will be registered differently by the four photomultipliers. A computer can process these photomultiplier signals to reconstruct the X-ray distribution over the sky as a function of time. By pulse height analysis of the four photomultipliers in parallel, energy distribution of the X-ray quantum flux can also be determined. An example of some of the results that can be obtained with this technique is shown in Figure 64. The top curve shows the overall count rate versus time and the bottom curve illustrates a crude measure for the energy spectrum; during a substorm event the spectrum becomes very soft. The actual X-ray pictures from such an event are shown in Figure 65. The upper part of this figure is prior to the enhanced activity; the bottom picture shows the event and that the X-rays were coming in from overhead. More detailed analysis can reveal X-ray spectra as function of location in the sky; one can distinguish between different X-ray energy components. Figure 66 shows that this event had both a 9 keV and a 30 keV component. The same technique can be used for a spacecraft looking down on the albedo X-ray coming up from the atmosphere; the simple pinhole

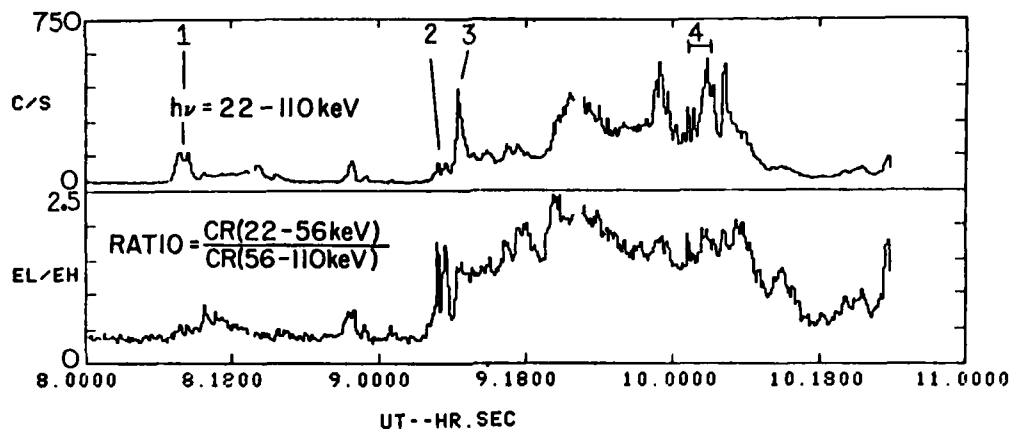


Figure 64. Examples of the X-ray Data Obtained with the Pin-Hole X-ray Camera

technique can be developed into multiple-hole or uniformly coated redundant systems. The sodium iodide, NaI(tl), scintillator crystal can also be replaced by proportional counters which will provide improved resolution. There are also other types of X-ray imaging detectors currently in use, and albedo X-ray from the aurora have been studied. The Lockheed group has proposed an X-ray camera for the OPEN mission.

The technique of measuring Bremsstrahlung X-rays from a satellite was first demonstrated with a collimated germanium spectrometer placed on a low altitude spinning satellite.⁴⁶ Local time distributions in X-ray (>50 keV) intensity, and hence electron precipitation, were derived from the counting rate variations with look direction and satellite position. More detailed spatial resolution was later achieved with the flight of an array of cadmium telluride X-ray spectrometers⁴⁷ on a spinning satellite. A threshold energy for satellite measurements of Bremsstrahlung X-rays has been lowered to 1.4 keV by the Aerospace group.⁴⁸ At low satellite altitudes only a portion of the auroral oval can be observed at any one time, but the entire polar zone can be mapped continuously with an X-ray

46. Imhof, W.L., Nakano, G.H., Johnson, R.G., and Reagan, J.B. (1974) Satellite observations of Bremsstrahlung from widespread energetic electron precipitation events, *J. Geophys. Res.* 79:565.
47. Imhof, W.L., Kilner, J.R., Nakano, G.H., and Reagan, J.B. (1980) Satellite X-ray mapping of sporadic auroral zone electron precipitation events in the local dusk sector, *J. Geophys. Res.* 85:3347.
48. Mizera, P.F., Luhmann, J.G., Kolasinski, W.A., and Blake, J.B. (1978) Correlated observations of auroral arcs, electrons and X-rays from a DMSP satellite, *J. Geophys. Res.* 83:5573.

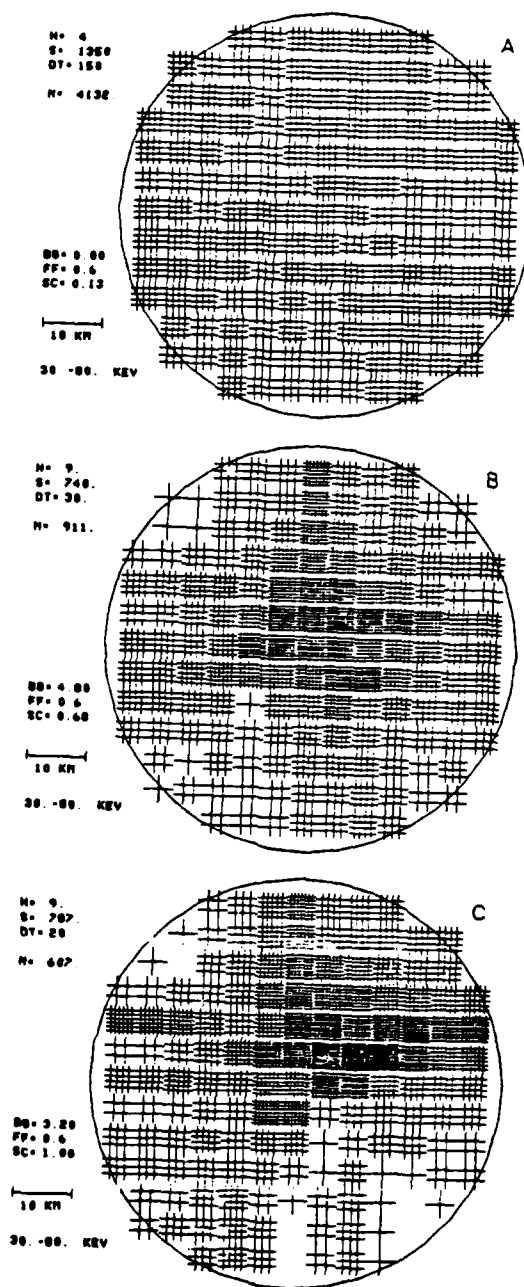


Figure 65. Example of an X-ray Picture of the Sky Taken with the Pin-hole X-ray Camera

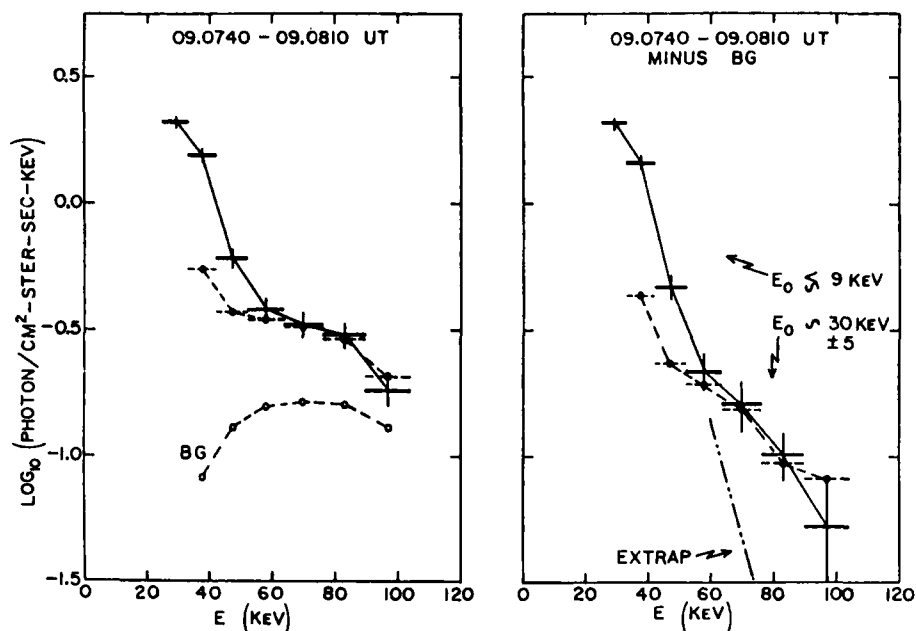


Figure 66. Examples of X-ray Spectra Deduced from the Pin-hole X-ray Camera

imager placed on a high altitude satellite such as the PPL vehicle proposed for OPEN. Fine angular resolution and high sensitivity are clearly needed and an X-ray spectrometer with these essential features and covering a broad range of X-ray energies has been jointly proposed for OPEN by the Lockheed and Aerospace groups.

9.2 High Energy Dose and Flux Meters

Of interest for low altitude spacecraft that traverse the innermost parts of the radiation belts is the radiation dose of high energy electrons and ions. For this purpose dose meters are designed to measure the total radiation at MeV energies impinging on a satellite. Figure 67 shows an example of such an instrument which is a further development of the instrument shown in Figure 55. It uses a dome of aluminum shielding material surrounding a solid state detector, and the angular acceptance is half of the full 4π steradian solid angle. The active element is a (photo-diode type) solid state detector with depletion depth of $\sim 400 \mu\text{m}$ and low noise characteristics. In-flight calibration is achieved by an alpha-particle-emitting radioactive source mounted within the instrument. The prime energy range is 1-10 MeV for electrons and ions which can be separated



Figure 67. High Energy Particle Dose Meter Sensitive in One Full 2π Steradian Hemisphere and Heavily Shielded in the Other Hemisphere

by pulse height analysis technique. The instrument also has the capability of measuring fission fragments (because of their larger mass) from nuclear detonations. A multi-dome configuration with different aluminum shielding ranging from 0.5 g/cm^2 to 6 g/cm^2 is being built for a DMSP satellite to be launched into an 835 km circular orbit in 1982. This shielding defines lower limits on the ions and electrons to be detected.

Another such instrument is the flux meter which has two solid state detectors in parallel (that is, working as one thick detector) and with a BGO-crystal scintillator for coincidence measurements. Empirically, measurements of the highest energy electrons can become contaminated by penetrating cosmic rays. To suppress this spurious background contribution two techniques are invoked. One technique involves the two solid state detectors operating in coincidence in addition to the scintillator coincidence. The other technique uses two photomultiplier tubes viewing a plastic scintillator surrounding the detector assembly (for anti-coincidence measurements). A 10-channel pulse height analysis of the prime signal gives energy information about the incident electrons from 1 to 10 MeV. Pulse height analysis of protons (ions) in 3 to 4 different channels can also be achieved for energies in the range 10 to 2000 MeV. The instrument is quite heavy (12.5 kg) with heavy tungsten shielding against Bremsstrahlung X-rays surrounded by an aluminum outer surface. The geometric factor is $10^{-2} \text{ cm}^2\text{-ster}$.

9.3 Nuclear Track Techniques

Nuclear emulsions have been flown on high altitude rockets early in the era of space exploration. Recovery of these emulsions after exposure to the inner edge of the radiation belts gave valuable insight into the composition and energies of the radiation. More recently the AFGL group has employed plastic emulsions that have superior performance characteristics and do not suffer the same saturation problems the earlier nuclear emulsions had. It is estimated that use of the plastics can allow inner radiation zone exposure of up to a year. Such techniques are very valuable since they can measure very high energy particles of low fluxes where the counts (tracks) are rare. The main drawback with the technique is that it requires recovery of the instrument rather than simply telemetry information.

Current dose measurements are made for MeV electrons and ions. It should be mentioned, however, that much lower energy electrons of 10-20 keV energy, for example, produce Bremsstrahlung X-rays that can penetrate thick shielding and affect the electronic circuitry and the detectors. These lower energy electrons have more intense fluxes by 2-4 orders of magnitude than those of MeV energies and can thus pose a significant problem to 'radiation-soft' spacecraft components. It is known that the X-ray dose a transistor on a spacecraft receives is not reduced significantly with shielding thickness for the range of shielding mass

acceptable (by weight limitation) for space applications. It is thus very difficult to shield against this radiation. As electronic components become smaller their susceptibility to radiation effects increases; this can cause bit-flips and latch-up effects in the logic circuitry. The development of safeguards and redundant design may be necessary to overcome these problems.

10. SUMMARY

Significant advances in spacecraft instrumentation for the detection and identification of energetic ions and electrons in the earth's space environment have been made during the last decade. Instruments already space tested or in various stages of development now cover essentially all energies from a few electron Volts to cosmic ray energies of hundreds of MeV. Electrostatic analyzers and mass spectrometers of various designs are generally effective up to a few tens of keV and are able to separate electrons and the different ionic components. Modern solid state detector instruments utilizing post-acceleration techniques are able to make detailed ion composition measurements from below 1 keV to above 200 keV with mass, energy and charge state identification. Energetic electrons are conveniently measured with solid state detector techniques from 20 keV up to tens of MeV; at energies above several MeV electron measurements become more difficult due to background suppression problems. Above a few hundred keV thin solid state detector techniques and time-of-flight measurements provide energy and ion mass measurements up to tens of MeV. Stacked solid state detectors, scintillators, Cerenkov radiations and nuclear emulsions extend the ion detection to cosmic ray energies. Thus for most of the ion and electron energies of interest in the earth's radiation belts the technology now exists to make the appropriate measurements.

References

1. Van Allen, J.A. (1957) Direct detection of auroral radiation with rocket equipment, Proc. National Academy Sci. 43:57.
2. Van Allen, J.A., Ludwig, G.H., Ray E.C., and McIlwain, C.E. (1958) Observation of high intensity radiation by satellites 1958 Alpha and Gamma, Jet Propulsion 28:588.
3. Van Allen, J.A. (1959) The geomagnetically-trapped corpuscular radiation, J. Geophys. Res. 64:1683.

4. Van Allen, J.A. (1962) Dynamics, composition and origin of the geomagnetically-trapped corpuscular radiation, Trans. International Astronomical Union, XIB:99.
5. Ögelman, H. and Wayland, R.H. (1970) Introduction to Experimental Techniques of High Energy Astrophysics, NASA/Goddard Space Flight Center, Washington, D.C.
6. Brown, W.L., Higginbotham, W.A., Miller, G.L., and Chase, R.L. (editors) (1969) Semiconductor Nuclear-Particle Detectors and Circuits, National Academy of Sciences, Publication 1594, Washington, D.C.
7. Vette, J.I., Teague, M.J., Sawyer, D.M., and Chan, K.W. (1979) Modeling of the earth's radiation belts; in: Solar-Terrestrial Predictions Proceedings, ed. by R. F. Donnelly, Vol II, p. 21. U.S. Dept. of Commerce, Washington, D.C.
8. Shelley, E.G. (1979) Heavy ions in the magnetosphere, Space Science Reviews 23:465.
9. Spjeldvik, W.N. (1979) Expected charge states of energetic ions in the magnetosphere, Space Science Reviews 23:499.
10. Williams, D.J. (1980) Ring current composition and sources, in: Dynamics of the Magnetosphere, ed. by S.I. Akasofu, D. Reidel, Boston, p. 407.
11. Fritz, T.A. and Spjeldvik, W.N. (1979) Simultaneous quiet time observations of energetic radiation belt protons and helium ions: The equatorial α/p ratio near 1 MeV, J. Geophys. Res. 84:2608.
12. Hovestadt, D., Gloeckler, G., Fan, C.Y., Fisk, L.A., Ipavich, F.M., Klecker, B., O'Gallagher, J.J., Scholer, M., Arbinger, H., Cain, J., Hofner, H., Kunne, E., Laeverenz, P., and Tums, E. (1978) The nuclear and ionic charge distribution particle experiments on the ISEE-1 and ISEE-C spacecraft, IEEE Transactions Geoscience Electronics, GE-16:166.
13. Hovestadt, D. and Vollmer, O. (1971) A satellite experiment for detecting low energy heavy cosmic rays, Proceedings of the 12th International Conference on Cosmic Rays, 4:1608.
14. Hoffman, R.A., Cahill, L.J., Jr., Anderson, R.R., Maynard, N.C., Smith, P.H., Fritz, T.A., Williams, D.J., Konradi, A., and Gurnett, D.A. (1975) Explorer 45 (S^3 - A) observations of the magnetosphere and magnetopause during the August 4-6, 1972 magnetic storm period, J. Geophys. Res. 80:4287.
15. Cahill, L.J., Jr. (1976) Response of the magnetosphere during early August 1972, Space Science Reviews 19:703.
16. Spjeldvik, W.N. and Fritz, T.A. (1981) Observations of energetic helium ions in the earth's radiation belt during a sequence of geomagnetic storms, J. Geophys. Res. 86:2317.
17. Spjeldvik, W.N. and Fritz, T.A. (1981) Energetic heavy ions with nuclear charge $Z \geq 4$ in the equatorial radiation belts of the earth: Magnetic storms, J. Geophys. Res. 86:2349.
18. Spjeldvik, W.N. and Fritz, T.A. (1981) Observations of ions with nuclear charge $Z \geq 9$ in the inner magnetosphere, J. Geophys. Res. 86:7749.
19. Anderson, K.A., Lin, R.P., Paoli, R.J., Parks, G.K., Lin, C.S., Reme, H., Bosqued, J.M., Martel, F., Cotin, F., and Cros, A. (1978) An experiment to study energetic particle fluxes in and beyond the earth's outer magnetosphere, IEEE Transactions on Geoscience Electronics, GE-16:213.

20. Reagan, J.B., Bakke, J.C., Kilner, J.R., Matthews, J.D., and Imhof, W.L. (1972) A high-resolution multiple-particle spectrometer for the measurements of solar particle events, IEEE Transactions in Nuclear Science, NS-19:554.
21. Rubin, A.G., Filz, R.C., and Rothwell, P.L. (1977) Geomagnetically trapped alpha particles from 18 to 70 MeV, J. Geophys. Res. 82:1938.
22. Stevens, J.R. and Vampola, A.L. (1978) Description of the Space Test Program P78-2 Spacecraft and Payloads, Space and Missile Systems Organization Report SAMSO TR-78-24, Los Angeles, California, p 26.
23. Williams, D.J., Keppler, E., Fritz, T.A., Wilken, B., and Wibberenz, G. (1978) The ISEE 1 and 2 medium energy particle experiment, IEEE Transactions on Geoscience Electronics, GE-16:270.
24. Baker, D.N., Stauning, P., Hones, E.W., Jr., Higbie, P.R., and Belian, R.D. (1979) Strong electron pitch angle diffusion observed at geostationary orbit, Geophysical Research Letters 6:205.
25. Spjeldvik, W.N. (1977) Radiation belt electrons: structure of the loss cone, J. Geophys. Res. 82:709.
26. Shelley, E.G., Johnson, R.G., and Sharp, R.D. (1972) Satellite observations of energetic heavy ions during a geomagnetic storm, J. Geophys. Res. 77:6104.
27. Balsiger, H., Eberhardt, P., Geiss, J., Ghielmetti, A., Walker, H.P., Young, D.T., Loidl, H., and Rosenbauer, H. (1976) A satellite-borne ion mass spectrometer for the energy range 0 to 16 keV, Space Science Instrumentation 2:499.
28. Moore, T.E. (1977) Spectrograph suitable for the mass and energy analysis of space plasmas over the energy range 0.1-10 keV, Reviews of Scientific Instruments 48:221.
29. Shelley, E.G., Sharp, R.D., Johnson, R.G., Geiss, J., Eberhardt, P., Balsiger, H., Haerendel, G., and Rosenbaum, H. (1978) Plasma composition experiment on ISEE-A, IEEE Transactions on Geoscience Electronics, GE-16:266.
30. Fritz, T.A., and Cessna, J.R. (1975) ATS-6 NOAA low energy proton experiment, IEEE Transactions on Aerospace and Electronic Systems, AES-11:1145.
31. Fritz, T.A. and Spjeldvik, W.N. (1981) Steady-state observations of geomagnetically trapped energetic heavy ions and their implications for theory, Planetary and Space Science, in press.
32. Hovestadt, D., Gloeckler, G., Fan, C.Y., Fisk, L.A., Ipavich, F.M., Klecker, B., O'Gallagher, J.J., and Scholer, M. (1978) Evidence for solar wind origin of energetic heavy ions in the earth's radiation belts, Geophysical Research Letters 5:1055.
33. Blake, J.B., Fennell, J.F., and Hovestadt, D. (1980) Measurements of heavy ions in the low-altitude region of the outer zone, J. Geophys. Res. 85:5992.
34. Thomas, G.R. and Willis, D.M. (1972) Analytical derivation of the geometric factor for a particle detector having circular or rectangular geometry, Journal of Physics E: Scientific Instruments 5:260.
35. Paxton, F. (1959) Solid angle calculation for a circular disk, The Review of Scientific Instruments 30:254.
36. Frank, L.A., Yeager, D.M., Owens, H.D., Ackerson, K.L., and English, M.R. (1978) Quadrispherical LEPEDAS for ISEE's 1 and 2 plasma experiments, IEEE Transactions on Geoscience Electronics, GE-16:221.

37. Bame, S.J., Asbridge, J.R., Felthausen, H.E., Glore, J.P., Paschmann, G., Hemmerich, P., Lehmann, K., and Rosenbauer, H. (1978) ISEE-1 and ISEE-2 fast plasma experiment and the ISEE-1 solar wind experiment, IEEE Transactions on Geoscience Electronics, GE-16:216.
38. McIlwain, C. (1971) UCSD Experiments, in: Operations Manual for the Environmental Measurements Experiment on the Applications Technology Satellite Mission ATS-F, pp 4-109, Westinghouse Defense and Space Center, Document 710667, Baltimore, Maryland.
39. Spjeldvik, W.N. and Thorne, R.M. (1975) The cause of storm after effects in the middle latitude D-region, Journal of Atmospheric and Terrestrial Physics 37:777.
40. Imhof, W.L., Gaines, E.E., and Reagan, J.B. (1981) Observations of multiple, narrow energy peaks in electrons precipitating from the inner radiation belt and their implications for wave-particle interactions, J. Geophys. Res. 86:in press.
41. Lyons, L.R. and Thorne, R.M. (1973) Equilibrium structure radiation belt electrons, J. Geophys. Res. 78:2142.
42. Reagan, J.B. (1977) Ionization Processes, in: Dynamical and Chemical Coupling Between the Neutral and Ionized Atmosphere, (ed. by B. Grandel and J.A. Holtet), D. Reidel, Dordrecht, Holland.
43. West, H.I., Jr., Buck, R.M., and Walton, J.R. (1973) Electron pitch angle distributions throughout the magnetosphere as observed with OGO-5, J. Geophys. Res. 78:1064.
44. West, H.I., Jr., Buck, R.M., and Davidson, G. (1979) Study of Energetic Electrons in the Outer Radiation Belt Regions Using Data Obtained by the LLL Spectrometer on OGO-5 in 1968, Lawrence Livermore Report UCRL-52807, California.
45. Trefall, H. (1973) Auroral Zone X-rays, in: Cosmical Geophysics, p 237, (ed. by: A. Egeland, O. Holter and A. Omholt), Universitetsforlaget, Oslo, Norway.
46. Imhof, W.L., Nakano, G.H., Johnson, R.G., and Reagan, J.B. (1974) Satellite observations of Bremsstrahlung from widespread energetic electron precipitation events, J. Geophys. Res. 79:565.
47. Imhof, W.L., Kilner, J.R., Nakano, G.H., and Reagan, J.B. (1980) Satellite X-ray mapping of sporadic auroral zone electron precipitation events in the local dusk sector, J. Geophys. Res. 85:3347.
48. Mizera, P.F., Luhmann, J.G., Kolasinski, W.A., and Blake, J.B. (1978) Correlated observations of auroral arcs, electrons and X-rays from a DMSP satellite, J. Geophys. Res. 83:5573.

Contents

1. Introduction	210
2. Magnetic Field Measurements	211
3. Low Energy Plasma Measurements in the Magnetosphere	214
3.1 Passive Wave Measurements	214
3.2 Active Wave Measurements	216
3.2.1 Relaxation Sounder	216
3.2.2 Mutual Impedance	216
3.3 Electrostatic Probes	218
3.4 Electrostatic Analyzers	218
3.5 Ion Mass Spectrometers	222
3.6 GEOS-1: Intercomparison of Technique	222
3.7 A Minimal Cold Plasma Package	226
4. Wave Measurements in the Radiation Belts	230
4.1 Wave Measurement Systems	230
4.1.1 Spectrum Analyzers	234
4.1.2 Sweep Frequency Analyzers	235
4.1.3 Wideband Receiver	235
4.2 Wave-Particle Time Resolution	240
References	241
List of Symbols	242

6. Magnetic Fields, Low Energy Plasma and Wave Measurements in the Radiation Belts

by

William J. Burke
Air Force Geophysics Laboratory
Hanscom AFB, Massachusetts 01731

and

David T. Young
University of Bern
Bern, Switzerland

based on oral presentations by

R.R. Anderson (The University of Iowa)
T. Chang (Massachusetts Institute of Technology)
P.M.E. Decreau (CRPE, Orleans)
J. Etcheto (CRPE, Issy les Moulineaux)
T.A. Potemra (Johns-Hopkins, Applied Physics Laboratory)
R.B. Torbert (University of California Berkeley)
D.T. Young (University of Bern)

1. INTRODUCTION

Radiation belt particles affect Air Force systems in many ways. A growing awareness of the damage that they can cause to essential integrated circuit components has emerged from this workshop. Energetic particle radiation is the main source of electronic component damage. Thus, the measurements of energetic particle spectra are of prime concern for the development of engineering models of component lifetimes and the specification of spacecraft environments.

Particle environments in the radiation belts are quite dynamic. Fluxes increase rapidly during main phase injections. Their persistence and decay are reflected in the relatively long time scales (on the order of days to months) of magnetic storm recovery. Rates at which particles are lost from the ring current are essential for models. Interactions between waves and particles are obvious and important loss mechanisms.

In the magnetosphere both electrostatic and electromagnetic waves cause energetic particles to pitch-angle scatter into the atmospheric loss cone. They are subsequently lost within a bounce period. Direct measurements of wave modes and intensities are necessary for calculating empirical pitch-angle diffusion coefficients. Which waves are excited depends on the dispersive characteristics of the plasma. The waves are produced as long as there is free energy available in the plasma to maintain them against dissipation and propagation losses. Two commonly cited sources of free energy are contained in pitch angle anisotropies and positive slopes in distribution functions. In both instances knowledge of the magnetic field and low energy ($E < 100$ eV) plasma backgrounds is essential for understanding energetic particle dynamics.

In recent years we have come to understand that the ionosphere is a source for ring current particles. The ion contributors must have energies in the kilovolt range. How are they heated? One suggestion is the lower hybrid resonance whose frequency is

$$\omega_{LH} \approx \omega_{pi} \left(1 + \frac{k_{\parallel}^2}{k^2} = \frac{m_i}{m_e} \right)$$

where ω_{pi} is the ion plasma frequency, m_i and m_e are the ion and electron mass. These electrostatic waves are generated by field-aligned electron beams and, in laboratory plasmas, heat ions perpendicular to \vec{B} . Whether such waves heat space plasmas has not yet been studied. They deserve both observational and theoretical attention.

This chapter addresses questions pertaining to subsidiary measurements of magnetic fields, low energy plasma, and waves in the radiation belts. Emphasis is placed more on instrumentation requirements than on the physics of the belts.

2. MAGNETIC FIELD MEASUREMENTS

Measurements of the magnetic field provide unifying information for our understanding of near-earth space. The geomagnetic field guides the motions of charged particles, traps thermal and energetic particles, transmits hydromagnetic stresses, links the solar wind and magnetosphere, projects magnetospheric processes onto the auroral "viewing screen," and defines the various magnetospheric regions. Through a variety of cartoon and model representations, investigators draw magnetic field lines to represent magnetospheric processes. Thus, a spacecraft should carry a magnetometer, at least, for orienting all other experiments.

Satellites designed to measure the properties of the radiation belts are in low inclination orbits. For most particle studies pitch angle determination with a 1 percent attitude accuracy is required. This translates into knowing attitude to within $\pm 0.5^\circ$. As shown below such accuracy is easily achieved by contemporary magnetometers. In low inclination orbits extending out to $10 R_E$, satellites may pass through various magnetospheric boundaries; radiation belts; plasma sheet; neutral sheet, and occasionally into the lobes of the magnetotail. Magnetic field information with an accuracy of better than 1 to 10 nT are needed to identify the magnetospheric region in which the satellite is moving. Magnetic field measurements provide information on many time scales, from seasonal effects due to the tilt of the Earth's dipole, and from ring current, substorm, and wave turbulence effects whose time scales are days, hours, and seconds, respectively.

Ness¹ has reviewed the characteristics of five types of magnetometers flown on spacecraft. These are: (1) search coils, (2) fluxgates, (3) proton precession, (4) alkali vapor and (5) helium. Search coils are simply wire coils that respond to magnetic induction, $\partial B/\partial t$ effects. They are useful for measuring high frequency magnetic field fluctuations but cannot be used to measure dc magnetic fields. These are discussed in the section of this chapter dealing with waves. Fluxgate magnetometers are most useful for measuring the dc magnetic field of the earth as well as its low frequency (≤ 100 Hz) fluctuations. Characteristics of fluxgates are discussed in detail in the paragraphs immediately following. The last three types of magnetometers provide very high resolution magnetic fields using atomic processes. They have been most recently flown on the low altitude

1. Ness, N.F. (1970) Magnetometers for space research, Sp. Sci. Rev. 11:459.

MAGSAT satellite. Within the radiation belts, fluxgates are the simplest devices for providing the required magnetic field information.

Fluxgate magnetometers use the hysteresis characteristics of saturable transformers to determine the second harmonics of a primary input frequency. This turns out to be a direct measure of the magnetic field, ΔH , in which the transformer is immersed. The principles of fluxgate magnetometers are illustrated in Figure 1. The hysteresis loop of the transformer is shown in the upper left corner. A triangular shaped signal with frequency $1/T$ is applied to a primary coil. The amplitude of the signal H_D is much greater than H_C required to saturate the core. The resultant magnetic flux B_R through the secondary coil as a function of time is given in the upper right corner of Figure 1. The voltage in the secondary coil is proportional to dB_R/dt which is alternately switched or gated to $\pm B_s$, the saturation magnetic flux. Identical \pm signals of width of αT in the secondary coil are nonuniformly spaced in time. Successive pulses are separated by βT or $(1 - \beta) T$. The expression for the voltage in the secondary coil is given in the lower right corner of Figure 1. The ratio of the second to the first harmonic for $\alpha \ll 1$ is (following Ness¹)

$$r = \frac{1 - 1 + i \sin\left(\frac{2\pi\Delta H}{H_D}\right)}{1 + 1 - i \sin\left(\frac{\pi\Delta H}{H_D}\right)} = \frac{i\pi\Delta H}{H_D}$$

This shows that the second harmonic is 90° out of phase with the primary signal. The sign is dictated by whether the measured magnetic field component is parallel or antiparallel to the core axis.

The problem to be solved designing a fluxgate magnetometer with the accuracy required for space missions is to isolate the first harmonic from the secondary coil as much as possible. Figure 2 is a sketch of four core designs for fluxgates. The simplest geometry uses only a single core. Since the measured signal is about 10^{-6} of the driving field, the measurement could be improved by going to a double core system in which the windings are designed to cancel the primary signal in the secondary coil. In practice the two core system is not used because the cores would have to be identical in physical characteristics. The "heliflux," a trade name of Schonstedt Co., is a type of magnetometer flown by many spacecraft. The primary and secondary coils are wound perpendicular to each other in such a way that the fundamental harmonic cancels. Thus, the second harmonic is measured. The ring-core fluxgate has been successfully flown on MAGSAT and Voyager. The primary is wound around a toroidal core. The measured field depends only on the direction of the secondary coil windings. By adding a second

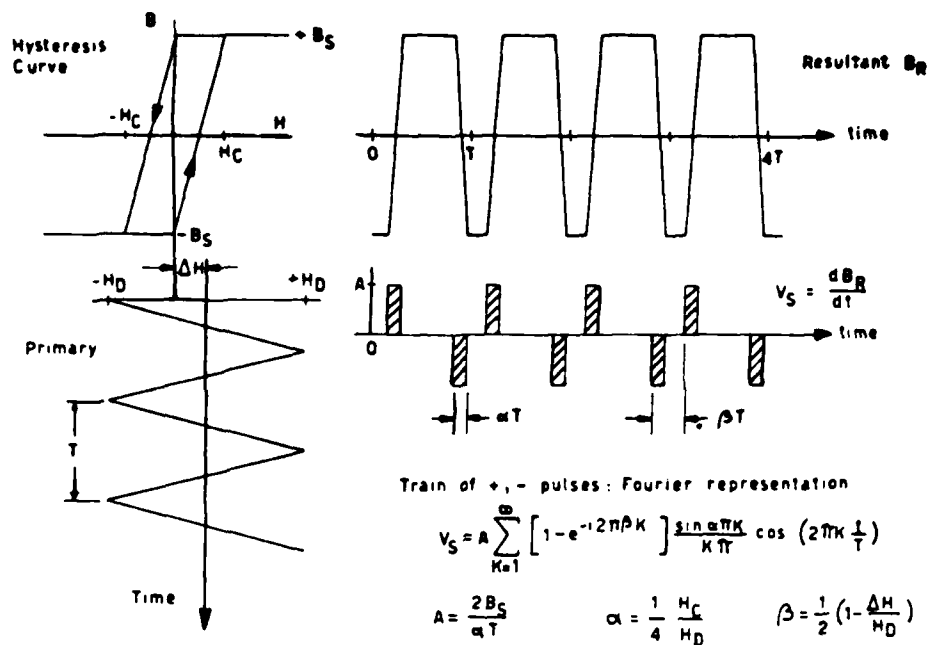


Figure 1. Diagram Illustrating Principles of Operation of Fluxgate Magnetometers

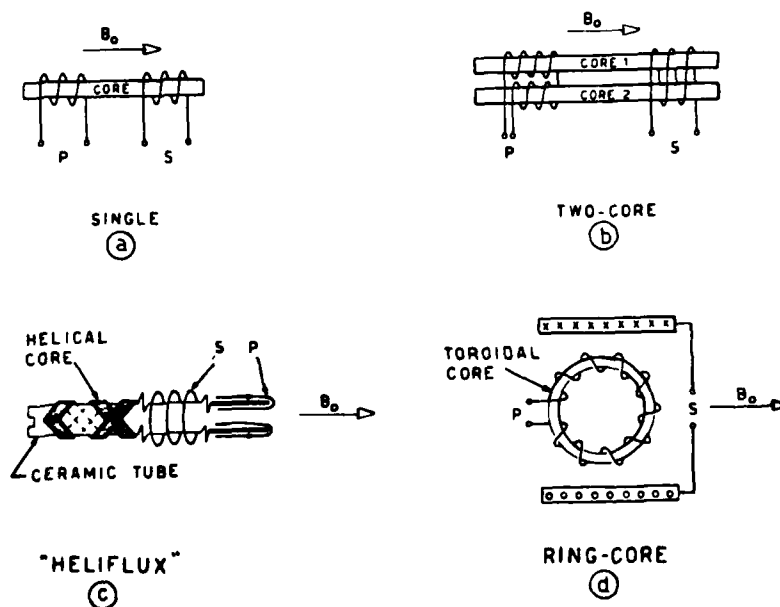


Figure 2. Various Geometries of Saturable Core Sensing Elements for Fluxgate Magnetometers

secondary coil, perpendicular to the first, it is possible to measure two components with a single sensor head.

Fluxgate magnetometers have an accuracy of better than 1 percent and have sensitivities down to 0.01 nT. With a sampling rate of > 100 Hz the magnetometer on Dynamics Explorer will be able to measure low amplitude waves. There are limiting considerations. Electromagnetic interference from the spacecraft and other sensors produce contamination which can be reduced by putting the sensor on booms. However, booms introduce problems with alignments. For example with a 12 bit plus sign word to measure a field of ± 6 nT (such as Triad) out of a $\pm 50,000$ nT field the alignment of the sensor must be known to an accuracy of $\pm 0.007^\circ$, about 25 arc-sec. This compares with the 0.5° accuracy required for particle experiments. Fortunately this type of accuracy can and has been achieved.

To summarize: A satellite in the radiation belt should carry a magnetometer to make sense of the primary, energetic particle measurements. A triaxial fluxgate magnetometer is adequate for meeting these mission requirements. Such a magnetometer was flown successfully on board the Explorer 45 satellite² through the radiation belts to an equatorial distance of $5.6 R_E$.

3. LOW ENERGY PLASMA MEASUREMENTS IN THE MAGNETOSPHERE

In this section the words "low-energy" describe both the "cold" (< 1 eV) and suprathermal populations. Table 1 is a list of some uses for cold plasma measurements. Instruments are designed to measure certain properties of the low energy plasma, for example, density, bulk motion, ion composition, etc. Table 2 lists the five different techniques that have been employed to measure aspects of the low energy plasma. Also listed are satellites³⁻¹⁵ employing the various techniques. In this subsection the techniques are described, along with their advantages and limitations. Examples of data are also provided. A direct comparison is made of five independent methods for measuring cold plasma density and three methods for measuring temperature on GEOS-1. Finally a minimum cold plasma package for a future, radiation-belt satellite is suggested.

3.1 Passive Wave Measurements

Technique: Cutoff of electromagnetic radiation trapped within the magnetosphere observed at the local value of the plasma frequency f_p .^{3,4}

Useful parameters: N_e = electron number density.

Because of the large number of references cited above, they will not be listed here. See References, page 241.

Table 1. Some Uses of Cold Plasma Data (and Required Parameters)

- Spacecraft potential, Debye length (N_0, T_0)
- Plasmapause location (N_0, V_0, T_0)
- Magnetospheric convection (N_0, V_0)
- Plasma wave propagation and amplification (N_j)
- Plasma transport between ionosphere and magnetosphere (N_j)
- Environment contamination, for example, by ion thrusters or spacecraft outgassing (N_j)
- Total plasma environment ($f_j(v)$)

Symbols

N_0, V_0, T_0 = Density, bulk velocity \perp to B, and temperature.
Measured for electrons and ions without distinguishing ion species.

$N_j, f_j(v)$ = Density, distribution function of jth species,
for example, $e^-, H^+, He^+, O^+, \dots$

Table 2. Magnetospheric Cold Plasma Measurement Techniques

Measurement of Bulk Properties

- Passive wave measurement (IMP-6,³ ISEE⁴)
- Active wave measurement
 - Relaxation sounder (GEOS,⁵ ISEE⁶)
 - Mutual impedance (GEOS⁷)
- Electrostatic (Langmuir) probes (GEOS,⁸ ISEE⁹)

Measurement of Differential Particle Distributions

- Electrostatic analyzer (ATS-6,¹⁰ GEOS,¹¹ ISEE¹²)
- Ion mass spectrometer
 - With energy/angle analysis (GEOS,¹³ ISEE¹⁴)
 - Without energy/angle analysis (OGO-5¹⁵)

Advantages: Continuous measurement possible in principle; useful as plasma diagnostic tool. Measurement not disturbed by local spacecraft environment.

Disadvantages: Location of cutoff subject to interpretation and is dependent on presence of natural emissions. No direct information about plasma ions and composition.

Comments: No systematic use of this method has yet been made for N_e .

Data example: Figure 3. Note that emissions are not continuously present and that f_p identification can be difficult.

3.2 Active Wave Measurements

3.2.1 RELAXATION SOUNDER^{5, 6}

Technique: Short duration (3 msec), large amplitude (10 to 100 V_{RMS}), narrowband (300 Hz) radio waves are transmitted from a long dipole antenna, then the receiver is connected for 100 msec and the return signals are monitored. This is repeated over a frequency range of 0 - ω_p (max). At frequencies near the characteristic frequencies of the plasma a resonance is excited and the returned signal strength increases. In the plasmasphere ω_p (max) = 300 kHz.

Useful parameters: N_e , $|B|$

Advantages: Continuous measurement with positive identification of wave parameters. Receiver functions as passive experiment. Measurement not disturbed by satellite environment.

Disadvantages: Transmitted signal will disturb particles in local plasma environment causing interference with low energy plasma analyzers. The radio frequency waves can cause noise pickup in solid state detectors.

Comments: Method has been used systematically on GEOS and ISEE in density range 0.1 - 70 cm⁻³. Experiments on GEOS and ISEE are nearly identical, with the ISEE experiment being more flexible.

Data example: Figure 4. Compare with Figure 3, and note continuous nature of data for f_p .

3.2.2 MUTUAL IMPEDANCE⁷

Technique: A current is injected on one set of dipoles and the signal voltage is measured on a second set. The ratio $V/I = Z_m(f)$ gives the plasma impedance as a function of frequency. Location of $Z_m(f)$ maximum give f_p and shape of curve gives λ_D . Accuracy is ± 500 Hz on f_p and ± 10 percent for λ_D .

Useful parameters: N_e , T_e ; ω_p , λ_D are the measured parameters.

Advantages: Signal strengths (1.7 V_{RMS}) are less than sounder method and cause smaller perturbations in local plasma. Continuous measurements are possible. Measurements are not disturbed by satellite environment.

JULY 6, 1977

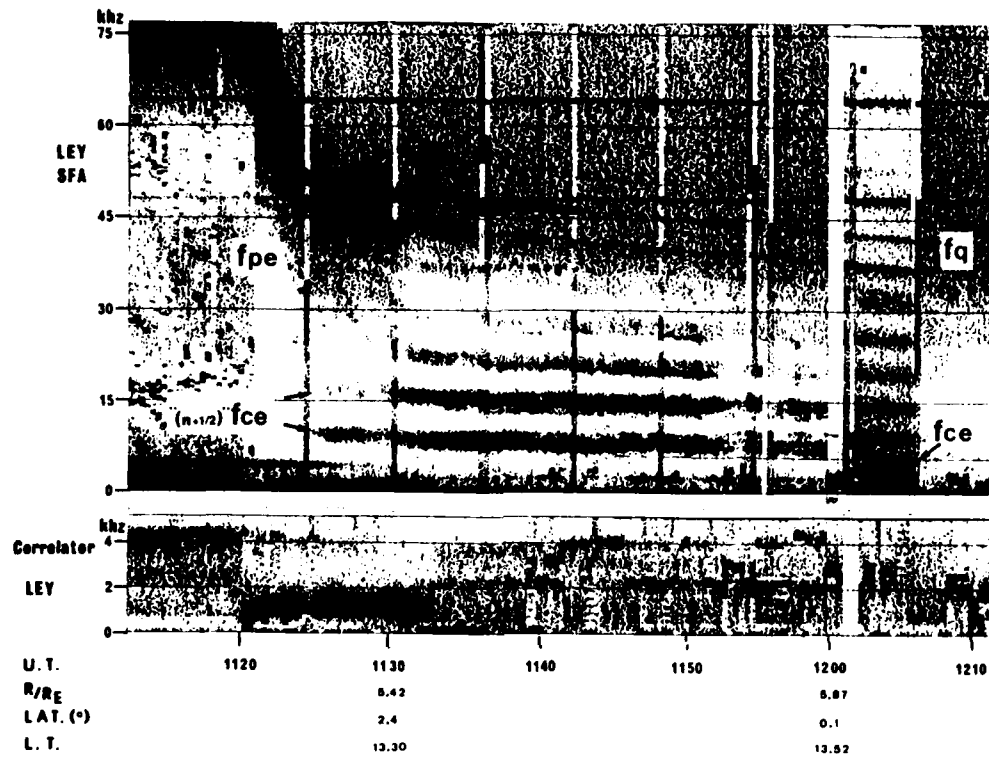


Figure 3. Frequency-time Spectrogram of Natural Emissions

SEPTEMBER 17, 1977

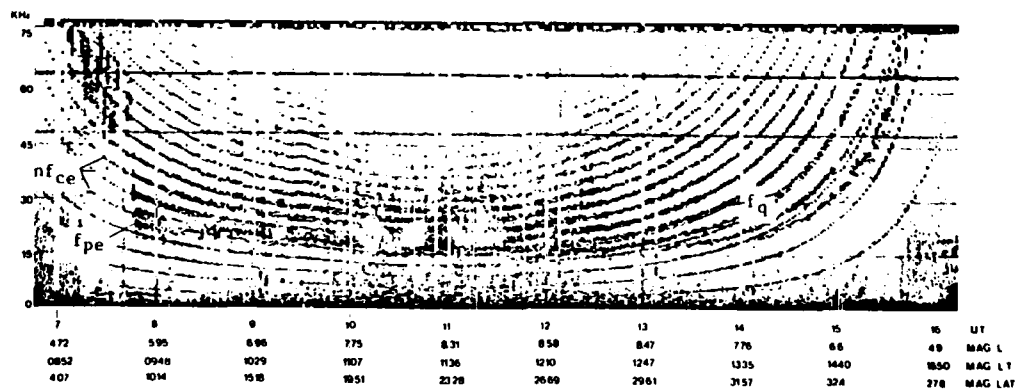


Figure 4. Frequency-time Spectrogram of Relaxation Sounder Data for an Entire Pass of GEOS-1

Disadvantages: Requires assumptions that plasma is homogeneous, Maxwellian and isotropic. Departures from these conditions make $Z_m(f)$ profile difficult to interpret. Will not work when $f_p \leq f_G$, where f_G is the electron cyclotron frequency.

Comments: Method has been used extensively on GEOS-1 and 2.

Data example: Figure 5 shows the case for a well-behaved Maxwellian distribution where f_p and λ_D can be determined accurately using a theoretical model of the plasma (dotted line). Figure 6 shows N_e and T_e deduced for a complete GEOS-1 pass. The mutual impedance and relaxation sounder experiment are able to follow rapid variations in plasma parameters.

3.3 Electrostatic Probes^{8,9}

Techniques: Double probes with length $L > \lambda_D$ inject a small negative current ($\leq 10^{-7}$ A) into the plasma, and I-V curve of probes is measured. From this the floating potential of the satellite relative to the plasma is determined. Probes also measure perpendicular electric field E_{\perp} from which plasma drift may be determined.

Useful parameters: E_{\perp} , ϕ_s . Estimates of N_e may be obtained from the probe I-V curve if electrons can be assumed to be in the 1 - 10 eV range.

Advantages: Continuous measurement of ϕ_s up to potentials of 50 V (for example, on ISEE-1). No disturbance to local plasma environment. Possible to estimate N_e empirically; also T_e under certain conditions.⁹

Disadvantages: Booms must be longer than λ_D , typically > 50 m tip to tip in outer magnetosphere. Limited to potentials ≤ 100 V unless larger bias current is used. N_e estimate is poor in a complex plasma or if T_e is outside expected range of 1 - 10 eV.

Comments: Technique has been used extensively only for E_{\perp} and ϕ_s data; no published survey of N_e or T_e . Conducting spacecraft surface is required.

Data example: Figure 7 shows an empirical curve relating N_e and the measured potential difference between probe and satellite body of GEOS (A. Pedersen, private communication, 1981). Examples of E_{\perp} measurements can be found in References 8 and 9.

3.4 Electrostatic Analyzers^{10,11,12}

Technique: Ion and electron differential fluxes are measured and converted into corresponding distribution functions. Fitting of the distribution with a theoretical function (for example, a Maxwellian) or averages (moments) over the measured distribution gives plasma parameters.

Useful parameters: N , \bar{v} , \underline{P} , detailed $f(\bar{v})$, ϕ_s .

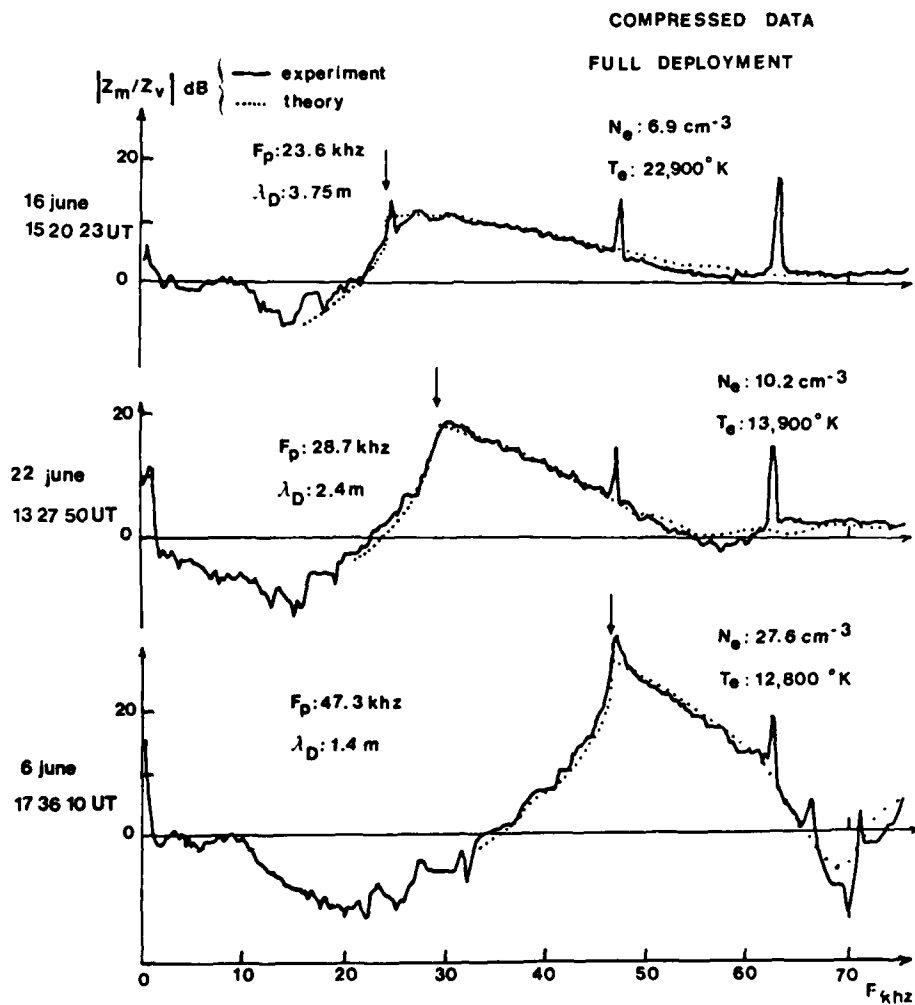


Figure 5. Variations of Mutual Impedance With Frequency Showing Examples of Fits to Maxwellian Distribution Data are from GEOS-1 and Dates Refer to 1977

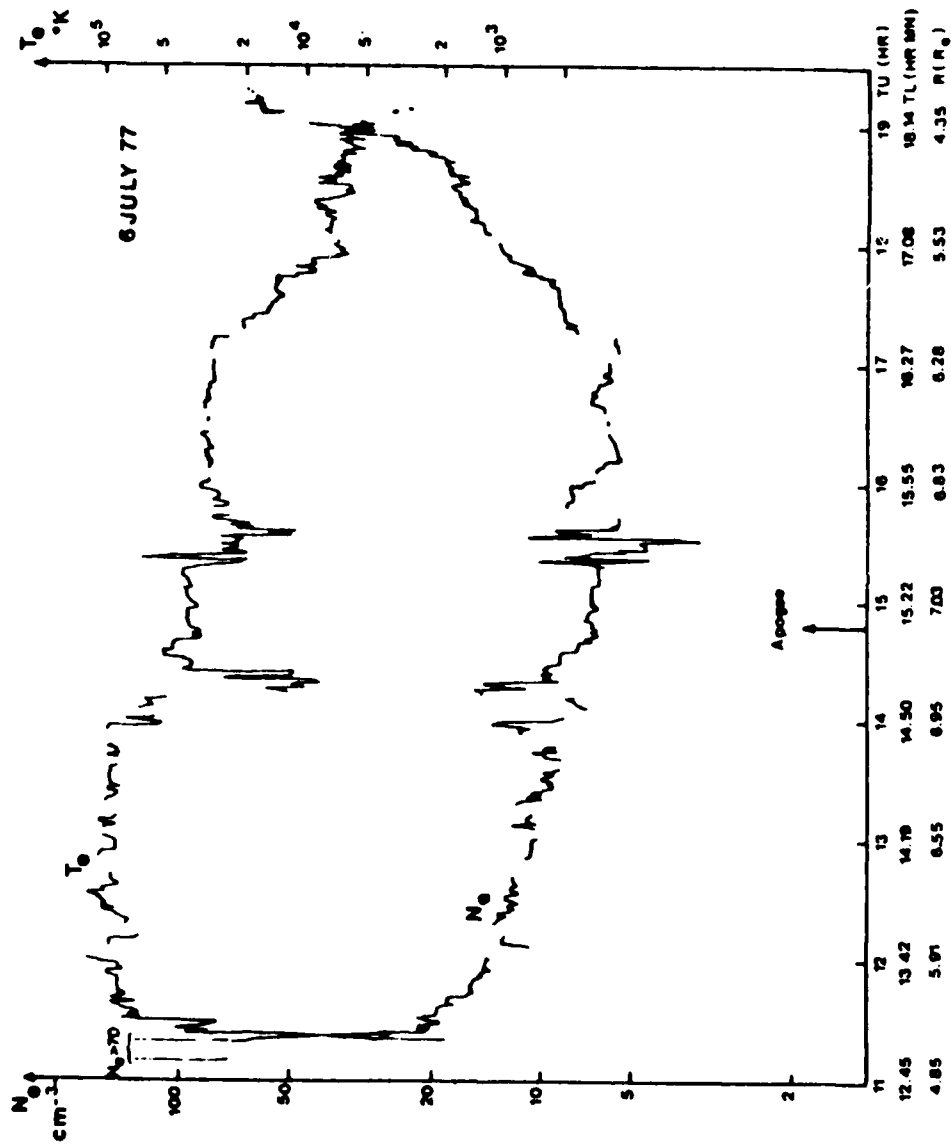


Figure 6. N_e and T_e Determined by the Mutual Impedance Method for a Complete Pass of GEOS-1. Note rapid variations in the two parameters in the region of 7 RE

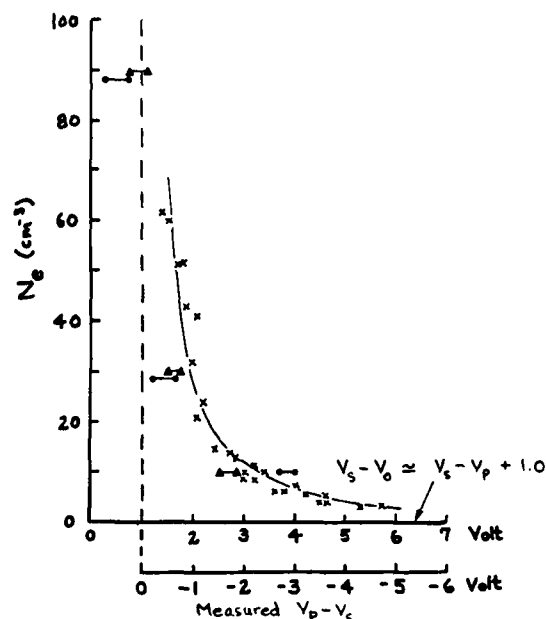


Figure 7. Empirical Relation Between N_e and Satellite Potential V_s Relative to the Plasma Potential V_0 . Comparison with laboratory data for photoemission characteristics of spacecraft body (solid symbols) suggests ≈ 1 Volt offset between the (biased) probes and the plasma. Crosses are measurements made by GEOS wave experiments of N_e .

Advantages: Electrons and ions are measured directly and without perturbation of the local environment. Details of $f(\vec{v})$ reveal free energy sources for plasma instabilities. Can determine ϕ_s if both electron and ion distributions are measured.

Disadvantages: Time resolution is often poor for obtaining full $f(\vec{v})$, typically several minutes. Distributions are suppressed or greatly distorted by acceleration when $|e\phi_s| > kT$. Measurements may be subject to background interference from photoelectrons, penetrating radiation, or both unless detectors are very carefully designed.

Comments: The above refers to curved plate analyzers with typically narrow (≤ 0.1 steradian) fields of view. So-called "ion traps" with more open geometry (≥ 1 ster) suffer even greater interference from photoelectrons and satellite potentials. Conducting spacecraft surface is desirable.

Data example: Figure 8a is a phase space density plot of electrons showing how the data are fit to determine N_e and T_e under the assumption of a Maxwellian velocity distribution.¹¹ Figure 8b shows densities with insets giving samples of ion pitch angle distributions to show complexity of $f(\vec{v})$. Data are from Reference 10.

3.5 Ion Mass Spectrometers^{13,14,15}

Technique: A magnetic momentum or velocity analyzer is used together with an electrostatic energy analyzer to obtain the velocity distributions of selected ion species, for example, H^+ , He^+ , He^{++} , O^+ , O^{++} . Analysis techniques are in principle the same as for electrostatic analyzers.

Useful parameters: For the j^{th} ion species N_j , \bar{V}_j , \underline{P}_j ; detailed $f_j(\vec{v})$.

Advantages: Same as for electrostatic analyzer but coverage can be extended to all ion species.

Disadvantages: Instrument is larger and more complex than an electrostatic analyzer due to addition of mass to measurement. Nature of ion optics restricts angular coverage in one dimension. Time resolution is reduced by the need to measure mass.

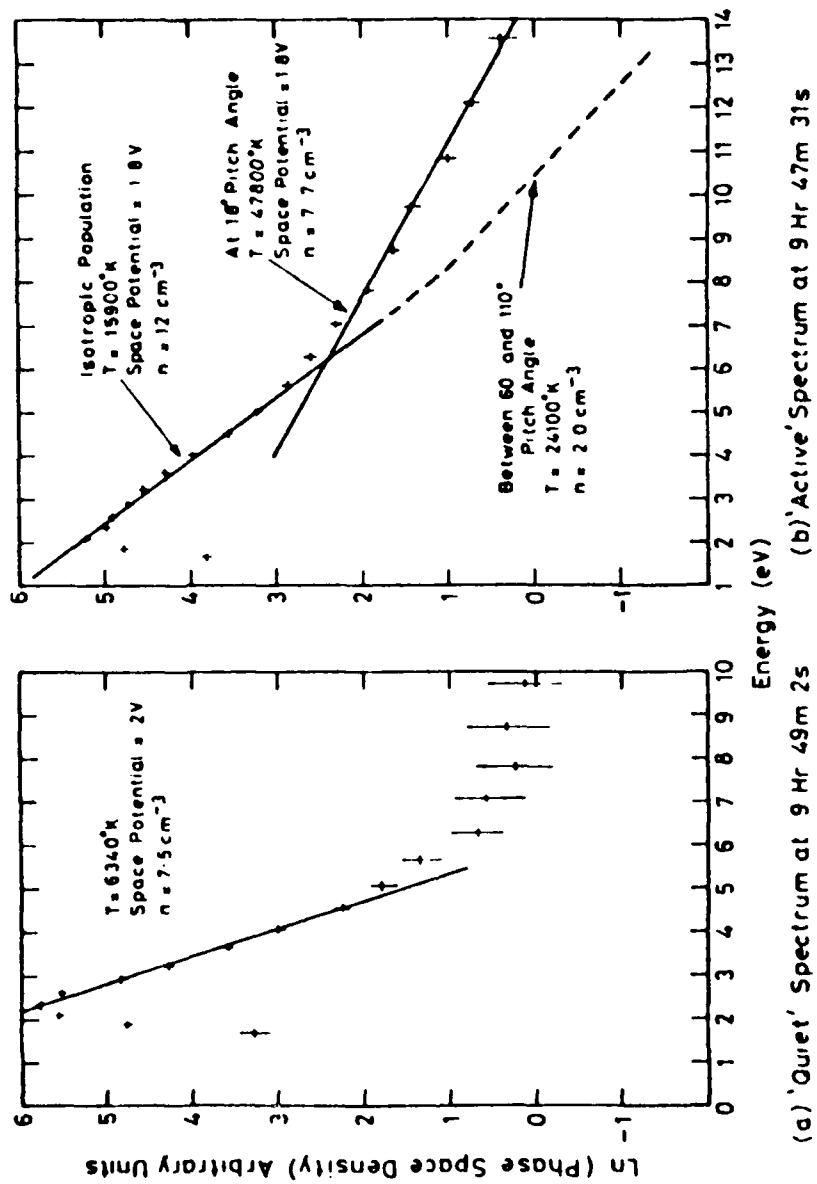
Comments: Low energy ion mass spectrometers with energy resolution are still in early stages of development, and more sophisticated versions are planned for OPEN. The OGO-5 spectrometer¹⁵ does not fall into the GEOS/ISEE class of instruments because it lacks energy and angular measurement capability. A modified version of OGO-5 flown on SCATHA is, however, comparable.¹⁵ Conducting spacecraft surface is desirable for all ion measurements.

Data example: Figure 9a shows a mass spectrum taken deep within the plasmasphere. Note the presence of five distinct ion peaks (there is an ambiguity with $M/Q = 2$ which could be either D^+ or He^{++} ¹³). Figure 9b shows the composition of 4 - 110 eV ions seen at geostationary orbit ($L = 6.6$) on GEOS-2. Data are plotted as a function of local time. Figure 9c shows an example of measurement contamination by satellite outgassing, in this case due to hydrazine during a satellite charging event.

3.6 GEOS-1: Intercomparison of Technique

An instructive intercomparison of five independent methods for measuring cold plasma density and three for temperature has been carried out with data from GEOS-1 by Decreau et al.¹⁶ GEOS-1 was an electrostatically clean spacecraft

16. Decreau, P.M.E., Etcheto, J., Knott, K., Pederson, A., Wrenn, G.L., and Young, D.T. (1978) Multi-experiment determination of plasma density and temperature, Sp. Sci. Rev. 22:633.



Spectra from 25 Aug., 1977.

Figure 8a. Electron Phase Space Density Plots Made With Two Detectors Oriented Parallel and Perpendicular to the Satellite Spin Axis. Note the existence of several Maxwellian populations simultaneously

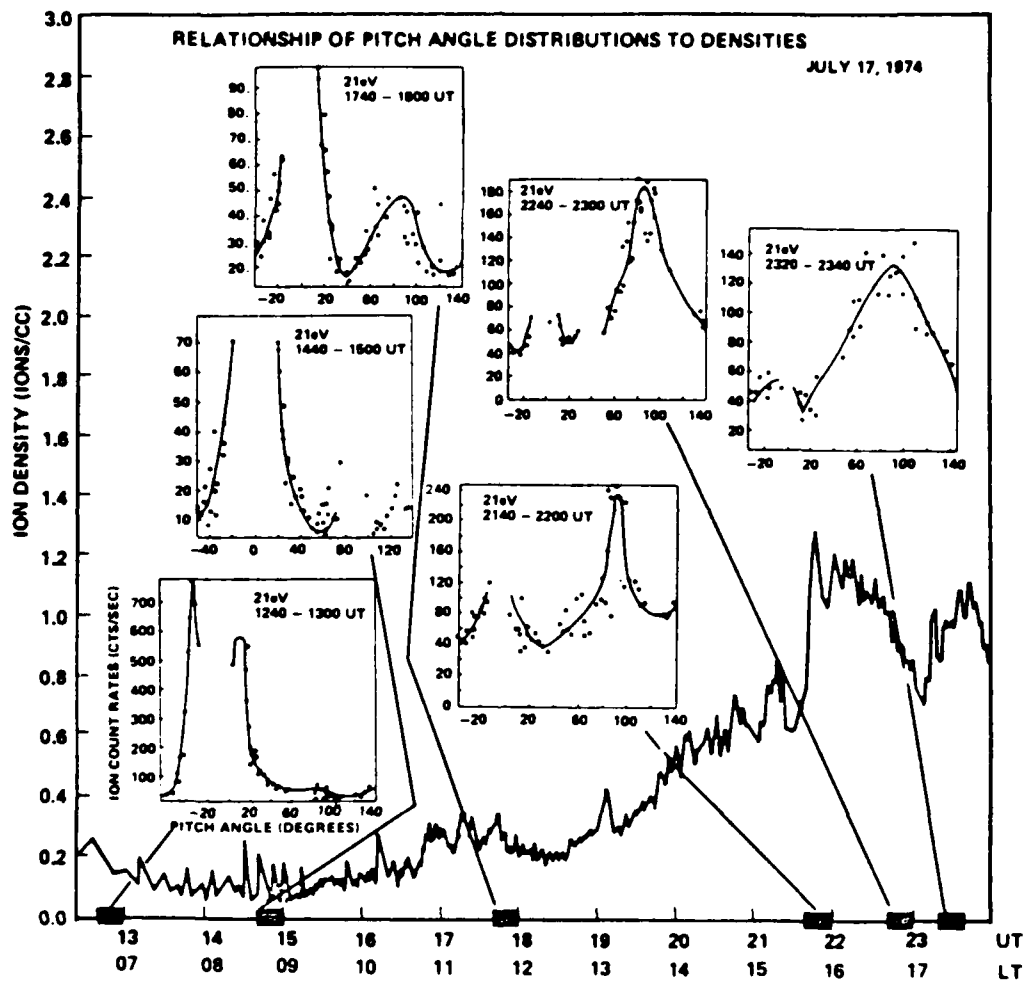


Figure 8b. Variety of Suprathermal Ion Pitch Angle Distributions Observed by the Auroral Particles Experiment on ATS-6

DAY 355 21 DEC. 1977 $\Sigma K_p = 11^+$
 ENERGY RANGE $2 \leq E/Q \leq 110 \text{ eV/e}$ T MODE

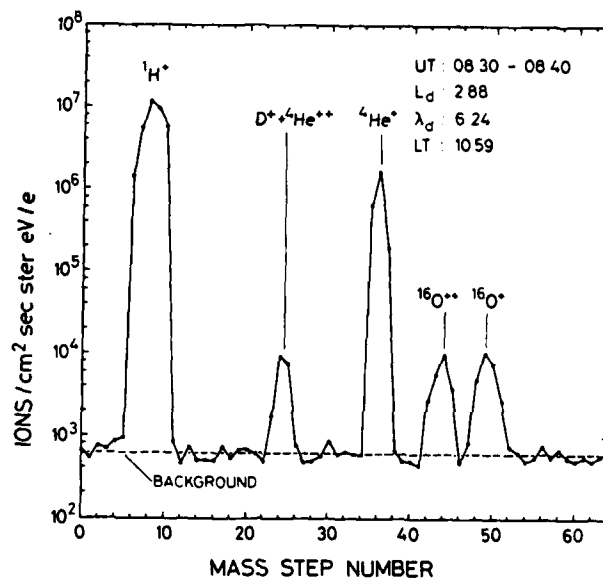


Figure 9a. Ion Mass Spectrum Measured Inside the Plasmasphere on GEOS-1. Ion temperatures were $\leq 1 \text{ eV}$

GEOS-2 ION COMPOSITION EXP.
 AVERAGE : 1 AUG. 1978 - 1 JULY 1979.
 $K_p = 0-1$ $4 \leq E/Q \leq 110 \text{ eV/e}$

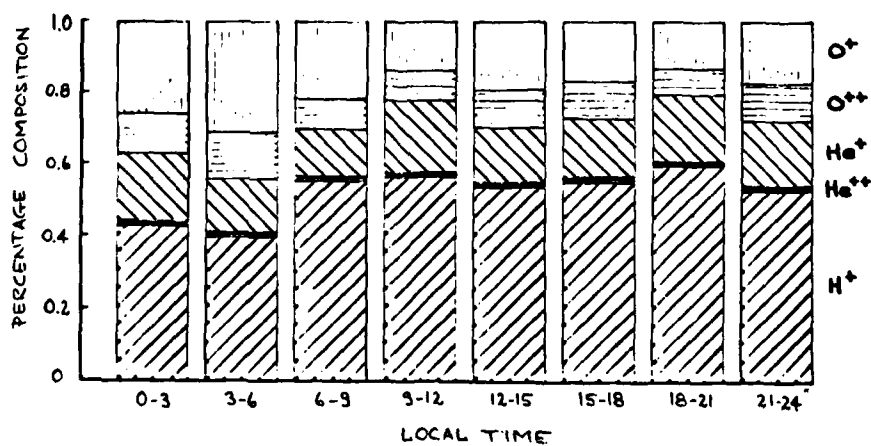


Figure 9b. Ion Composition Data Averaged Over 11 Months

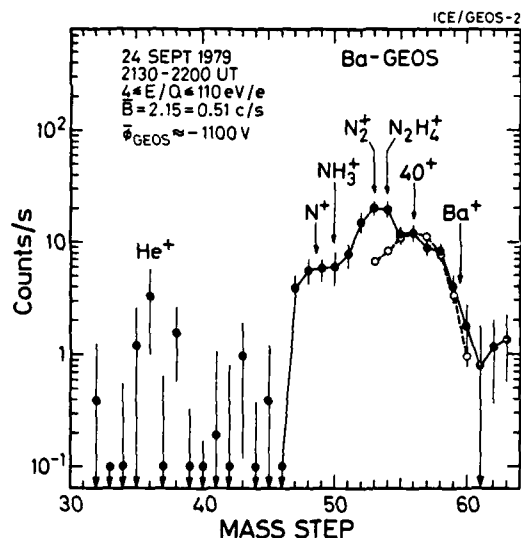


Figure 9c. Mass Spectrum of Spacecraft Environment during a Spacecraft Charging Event on GEOS-2

ideally suited for such a study, with a large array of plasma diagnostic equipment (cf. the GEOS-1 description by Knott¹⁷ and references therein). The various methods were found to agree reasonably well in measuring ϕ_s , T_e and T_i inside the plasmasphere (where $N_e \geq 10 \text{ cm}^{-3}$). However there was significant disagreement between wave and electrostatic probe experiments on the one hand and ion measurements on the other in determining density (Figure 10). It should be noted that no intercalibration of the two particle experiments was carried out nor were absolute preflight calibrations made against a standardized measurement such as that provided in situ by the wave experiment. Finally, no systematic investigation of the effect of the spacecraft sheath was made. The work reported in Reference 16 and displayed in Figure 10 was completed at an early stage of the GEOS data analysis and for a limited data set. A more comprehensive study is needed to resolve the apparent differences among the several experiments.

3.7 A Minimal Cold Plasma Package

From the brief instrumentation review presented above we find that the techniques tend more to be complementary than competitive. This is particularly true if we consider the group of active wave experiments vis a vis the particle

17. Knott, K. (1978) The GEOS-1 mission, Sp. Sci. Rev. 22:321.

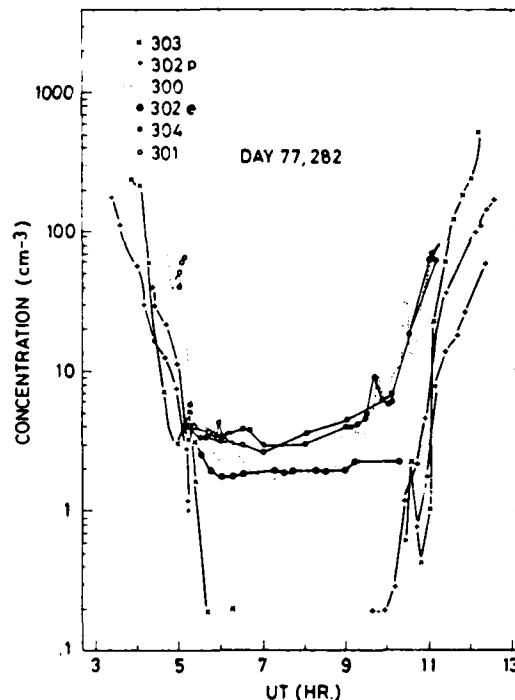


Figure 10. Cold Plasma Density as Measured by Five Different Experimental Techniques on GEOS-1. Experiment codes: 300, electrostatic probes; 301, relaxation sounder; 302, electrostatic analyzer; 303, ion composition experiment; 304, mutual impedance

experiments, which leads us to the following suggestion: Under most conditions an active wave experiment can easily provide the single piece of information on bulk plasma characteristics which the particle experiments have most difficulty in measuring, namely the total density N . Thus, in principle, all other parameters could be obtained from (differential) particle measurements and then be "normalized" to N , thereby eliminating questions of absolute calibration and the irksome problem of spacecraft potential. With this in mind we now examine some pros and cons of the several techniques and try to arrive at an optimum "model payload" for cold plasma measurements.

Since an active wave experiment by definition embodies a passive one (that is, there must be sensitive receiving equipment for both experiments) we discuss only the active experiment. A passive experiment alone, which is discussed in the following section, does not seem sufficiently reliable in providing measurements of N .

Furthermore, the resonance sounder appears preferable to the impedance experiment because it requires a dipole rather than quadrupole set of booms and because it is less sensitive to assumptions about the nature of the plasma.

By choosing a relaxation sounder experiment we can obtain high-time resolution (1 sec or faster) measurements of N without interference from the local environment. That is, the satellite need not be particularly clean electrostatically. In addition, we also obtain measurements of the natural plasma wave environment since the sounder can operate on a duty cycle of ≤ 10 percent depending on the time resolution required for N . Two drawbacks of an (active) wave experiment are its requirement for booms several meters in length (thus adding boom deployment mechanisms to spacecraft design problems) and the need for telemetry rates commensurate with frequency and time resolutions of the measurements. In this regard the method used by Higel¹⁸ for real-time tracking of plasma resonances could be put to use to reduce the bandwidth needed for measuring N . A third drawback of the sounder technique is the disturbance created in the local plasma environment by the large ($100 \text{ V}_{\text{RMS}}$) transmitted signal which interferes with low-energy (tens of eV) particle measurements (G. Wrenn, private communication, 1981). This can be overcome rather easily, however, by synchronizing the transmitter duty cycle (typically the transmitter is active for only a few milliseconds) with the particle experiment measurement cycle, for example, by having the transmitter on during the dead time that occurs when instrument voltages are switched and data are read out. It may also be possible to reduce the transmitted signal strength.

Given a reliable measurement of N , we turn now to the particle distribution aspects of the cold plasma. Here we find that the minimum requirement is for a 3-dimensional measurement of ions and electrons, particularly in the region of tenuous suprathermal plasma found outside the plasmasphere (Figure 8b).

Measurement of both electrons and ions allows the spacecraft potential to be calculated and corrected for. This can be checked against (and calibrated by) the true value of N provided by the wave experiment. Three-dimensional, ion-electron data are needed to properly determine plasma anisotropy and drifts. However, this can entail a considerable amount of data, which raises further questions of tradeoffs among resolution, sensitivity, telemetry, etc. If telemetry rates of 10^3 bits/sec are available then the time resolution for these measurements can be approximately 1 min (cf. Frank et al.¹²) which will provide sufficient detail to determine $f(\vec{v})$.

Taking the relaxation sounder and 3-dimensional electrostatic analyzer as our basic cold plasma package, we now turn to a possibly controversial point, namely

18. Higel, B. (1978) Small scale structure of magnetospheric electron density through on-line tracking of plasma resonances, Sp. Sci. Rev. 22:611.

whether an ion mass spectrometer should also be included in this category. In the first place, the contribution of heavy ($M/Q > 1$) ions to the total plasma content below 100 eV can be considerable as we have seen in Figure 9b. We also noted in Table 1 that plasma wave propagation and amplification depend on the composition of the plasma, a fact emphasized by recent studies carried out with wave and particle experiments on GEOS. Heavy ions may also serve as tracers of plasma transport processes, for example in the thermal diffusion and enrichment of O^{++} ions.¹³ From experience with GEOS and ISEE data we would therefore conclude that some form of ion mass spectrometer, perhaps a scaled-down version of those already flown, is required to make measurements roughly parallel and perpendicular to the local magnetic field. Because of the nature of magnetic mass spectrometers, a true 3-dimensional instrument comparable in angular coverage to electrostatic analyzers, is not presently feasible within reasonable mass, telemetry and power budgets.

To summarize, we suggest that an optimal cold plasma package would include the experiments listed in Table 3. These experiments form a hierarchy: more detail of the plasma distribution is provided as one proceeds from top to bottom. In addition, the upper experiment(s) serve as normalizing measurements for the experiment(s) below. Finally, we note that mass (excluding booms) and telemetry rate generally increase from top to bottom in Table 3, a possibly fortuitous circumstance for designers of spacecraft scientific payloads.

Table 3. Minimal Cold Plasma Measurements Package

- | |
|--|
| <ul style="list-style-type: none"> ● Relaxation sounder <ul style="list-style-type: none"> - Provides N_e independent of local plasma environment - Time resolution - 1 sec - Provides other characteristic plasma frequencies - Functions as passive wave experiment for 90 percent of time ● Electrostatic analyzer <ul style="list-style-type: none"> - Provides $f(\vec{v})$ for electrons and total ion population in 3-dimensions - Measurement normalized to N_e of waves - Time resolution - 1 minute ● Ion mass spectrometer <ul style="list-style-type: none"> - Provides measurement of composition of ions making up electrostatic analyzer fluxes - Gives details of $f_j(\vec{v})$ parallel and perpendicular to spin axis - Time resolution - 5 minutes |
|--|

4. WAVE MEASUREMENTS IN THE RADIATION BELTS

Wave-particle interactions are important radiation belt processes. Over the past two decades we have learned a great deal about waves in the equatorial region out to $10 R_E$.¹⁹ A wide variety of electromagnetic and electrostatic modes have been identified in the magnetosphere ranging in frequency from 10^6 down to 10^0 Hz.

The kind of waves present in a given region of the magnetosphere depends strongly on the distribution of particles. This is illustrated in data from the Explorer 45 satellite during a disturbed period in November 1971 (Figure 11). The top panels are electron measurements between 1.2 and 100 keV from Donald J. Williams' instrument. The bottom panels are data from the ac electric field experiment. During the period of interest the satellite was near apogee. There was a substorm injection at 1100 UT leading to a rapid increase in particle fluxes. The gyrofrequency line is given for reference. There are electrostatic emissions at $3/2 f_G$ and chorus emissions at $f < f_G$. Both of these types of emissions are important because of their interactions with radiation belt particles. Figure 12 is an example from another disturbed period in which count rates are enhanced only in the 1.2 keV electron channel and only electrostatic emissions above the gyrofrequency are detected. There is no evidence of electromagnetic chorus found during this disturbed period. Anderson and Maeda²⁰ showed that electrostatic emissions are associated with 1 keV electrons while electromagnetic chorus is associated with more energetic electrons.

The remainder of this section concerns the present state of wave measurements and suggests two areas for possible improvement. In the following subsection the ISEE and Helios wave experiments are described. The features of various system components are exemplified. The final subsection contains comments on high-time resolution requirements.

4.1 Wave Measurement Systems

Figures 13 and 14 are block diagrams of the plasma wave experiments on ISEE-1 and Helios-2, respectively.^{21,22} The basic philosophy of the plasma-wave

19. Shawhan, S.D. (1979) Magnetospheric wave research 1975-1978, Rev. Geophys. Sp. Phys. 17:705.
20. Anderson, R.R., and Maeda, K. (1977) VLF emissions associated with enhanced magnetospheric electrons, J. Geophys. Res. 82:135.
21. Gurnett, D.A., Scarf, F.L., Fredricks, R.W., and Smith, E.J. (1978) The ISEE-1 and ISEE-2 plasma wave investigation, IEEE Trans. Geosci. Elect. 16:225.
22. Gurnett, D.A., and Anderson, R.R. (1977) Plasma wave electric fields in the solar wind: initial results from Helios 1, J. Geophys. Res. 82:632.

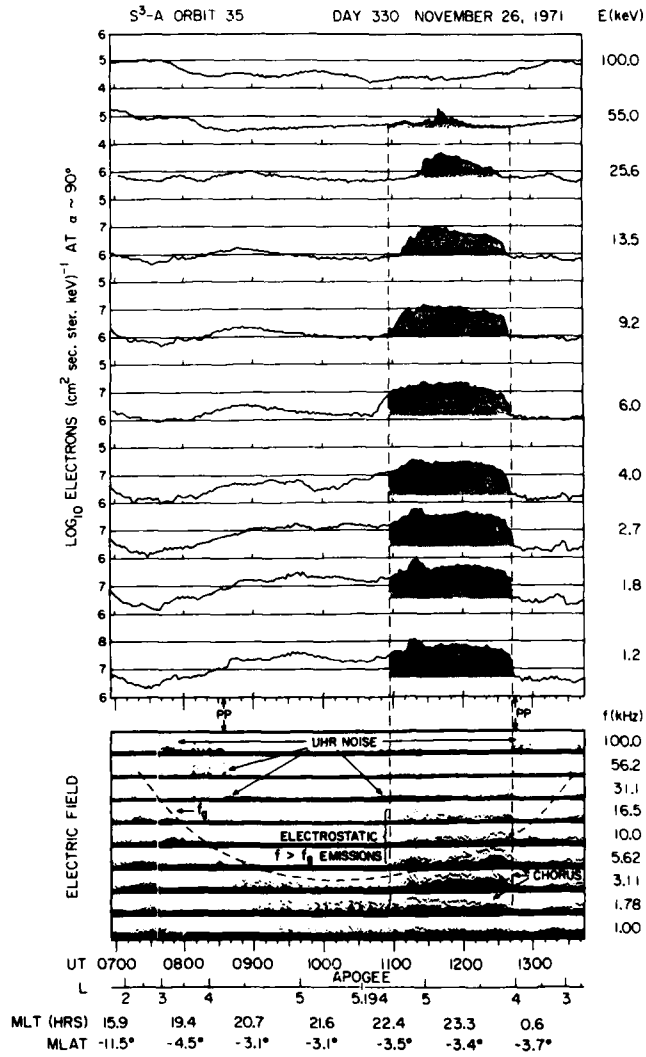


Figure 11. Simultaneous Electron (Top Panels) and Wave (Bottom Panels) Measurements by Explorer 45 (S³) in the Plasma Sheet Under Disturbed Conditions

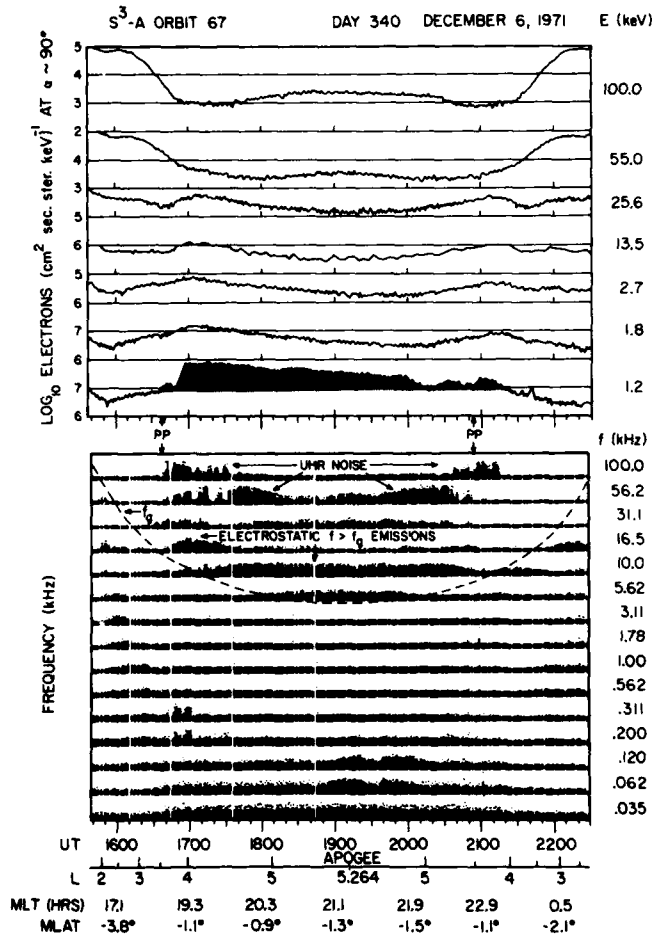


Figure 12. Explorer 45 Electron and Wave Measurements in the Quiet Time Plasma Sheet

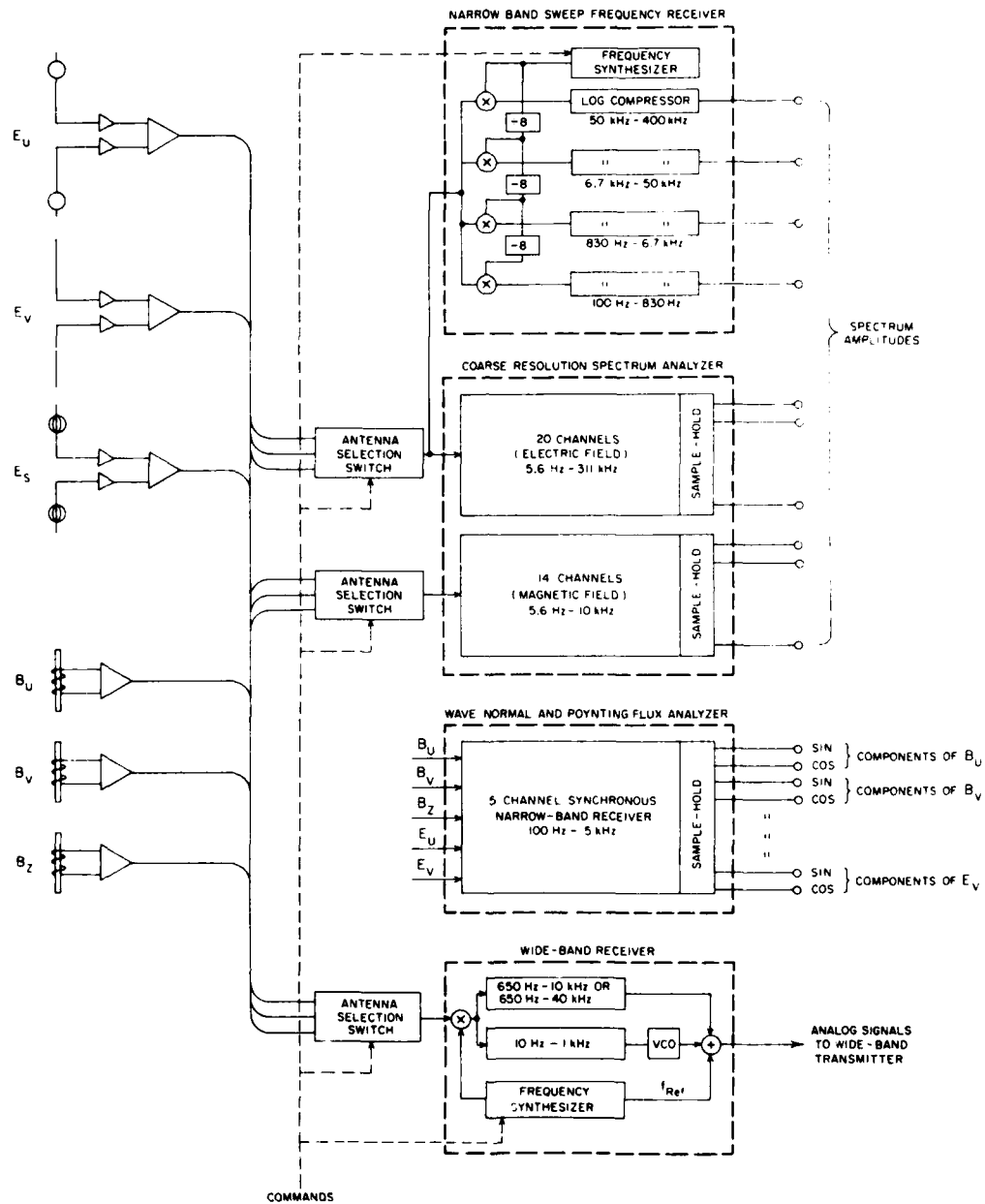


Figure 13. Block Diagram of the ISEE-1 Wave Experiment

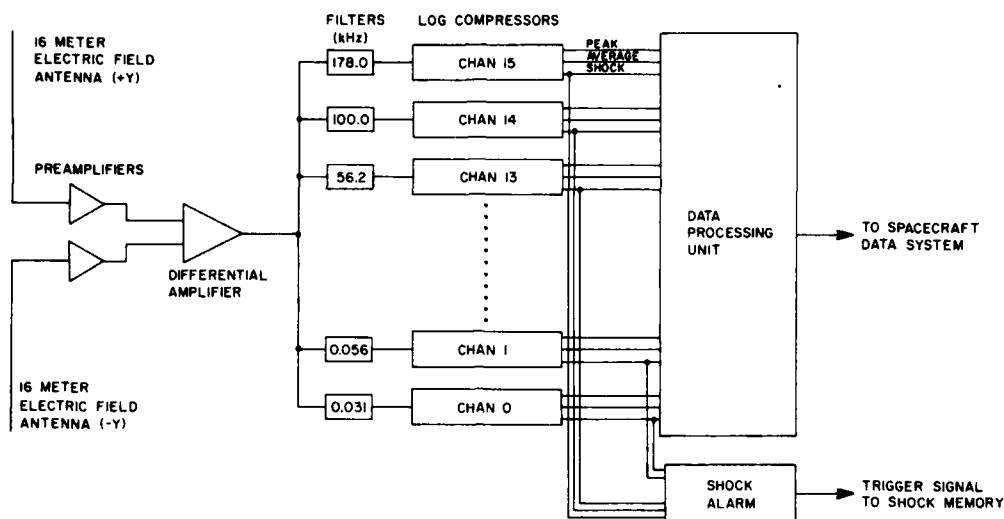


Figure 14. Block Diagram of the Helios-2 Wave Experiment

instrumentation design on the ISEE mission is to provide comprehensive measurements with ISEE-1 and only those measurements on ISEE-2 required to distinguish between spatial and temporal effects. The ISEE-1 experiment consists of three electric field dipoles and a triaxial search coil magnetometer. This complement allows a wave normal analysis of electromagnetic waves. The electronics package for the ISEE-1 experiments consists of four basic elements: (1) a spectrum analyzer, (2) sweep frequency analyzer, (3) a wideband receiver, and (4) a wave normal analyzer. Because the telemetry rate available for Helios is much less than ISEE the instrument consists of a single electric field dipole. It contains no wideband; it does possess peak average and shock detectors.

The next five figures were chosen to illustrate the features of spectrum analyzers, sweep frequency receivers and wideband receivers.

4.1.1 SPECTRUM ANALYZERS

Spectrum analyzers, because they have fairly broad bandwidths, can operate very rapidly. They can, conceivably, take 100 samples/second. The fastest used to date is 32 samples/sec across the entire frequency range. It is important if one flies a spectrum analyzer to include not only rapid time constant sampling but also a peak detector, which has an even faster time constant. If for example the detector has a sampling interval of 0.1 sec, the data tells what the average field was over that sampling interval. The peak detector however can catch very

rapid impulsive phenomena which are important in some studies. The Helios analyzer measured frequencies between 31 Hz and 178 kHz and had a dynamic range of 100 dB. Present state-of-the-art ranges of 120 dB can be achieved using logarithmic compressors. This represents 6 orders of magnitude in amplitude.

Figure 15 illustrates data from the Helios satellite sampled at a rate of 30/sec for 25 sec. Short bursts can be picked out in this representation. Figure 16 gives an example of an electron plasma oscillation burst in the solar wind. Here the wave amplitude jumps in 0.1 sec by 3 orders of magnitude. For some types of detailed studies it is important to get precisely this kind of resolution from spectrum analyzer data. The high time resolution data can be used to get a two (but not three) dimensional estimate of where the waves are coming from.

4.1.2 SWEEP FREQUENCY ANALYZERS

The power of a sweep frequency analyzer for diagnostic purposes is illustrated in Figure 17. This instrument has good frequency and amplitude resolution over a wide dynamic range. Data are sampled in 128 channels between 0.1 and 400 kHz. Frequently it is possible to identify the upper hybrid resonance which is approximately equal to the plasma frequency. Thus, sweep frequency plots give the plasma density. It is easy to identify continuum radiation, chorus, and the $(n + 1/2) f_G$ modes. The disadvantage of a sweep frequency receiver is that the time resolution is limited by the bandwidth of the 128 channels. The problem is particularly severe in the low frequency channels. The resolution can be improved by a factor of 10 or more by using different receivers for the low and high frequencies.

4.1.3 WIDEBAND RECEIVER

A wideband receiver provides the ultimate in frequency and time resolution. Figure 18 is an example of $(n + 1/2) f_G$ waves observed with the ISEE-1 wideband detector from 0 to 10 kHz. However, a bandwidth of 0 to 40 kHz is also available. One disadvantage of wideband data is the lack of absolute amplitude resolution. The receiver on ISEE automatically adjusts the gain (AGC). Wideband also has the disadvantage of needing a separate transmitter. To some extent this problem was circumvented on the Voyager mission to Jupiter. On this mission only a digital system, with no analog transmitter, was allowed. A 4-bit A-D conversion was done on the AGC wideband receiver data before transmission to ground. Through a computer, a D-A conversion was used to reproduce the analog signal. Detailed wave data were obtained during the Jupiter flyby. If further resolution is required on the ground, more resolution must be put into the A-D conversion. In the Voyager case 115 k bits/sec were used to get a bandwidth of 14 kHz.

Figure 19 is an example from Explorer 45 which points out the usefulness of combining high resolution wave and particle data. Prior to 1903 UT on November 26, 1971, the chorus emissions were only about one half the gyrofrequency. At

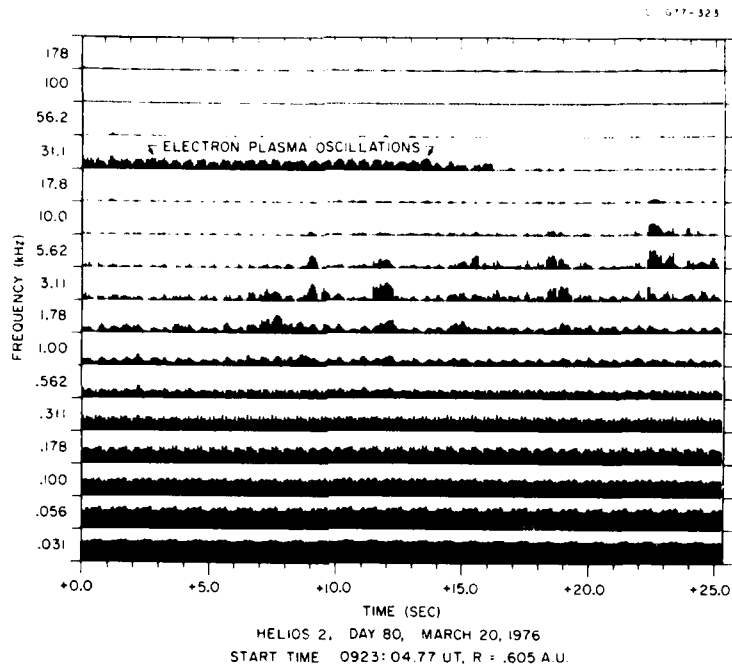


Figure 15. Twenty-five Second Example of Solar Wind Wave Measurements from Spectrum Analyzer on Helios 2

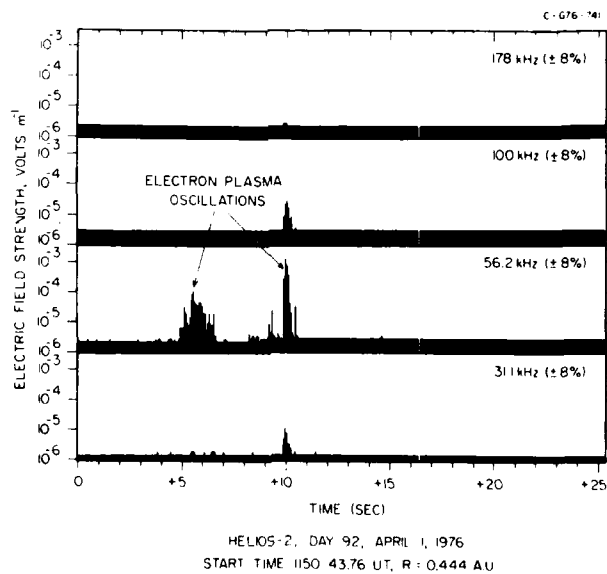


Figure 16. High Time Resolution Data from Spectrum Analyzer on Helios 2

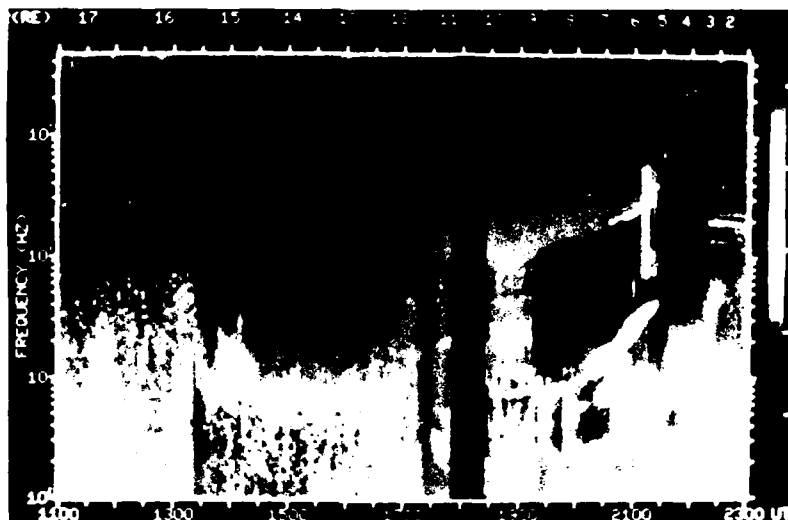


Figure 17. Twelve Hours of Measurements Between 0.1 and 400 kHz in 128 Channels as an Example from Sweep Frequency Receiver

C-G7B-350

ISEE-1 UNIVERSITY OF IOWA PLASMAWAVE EXPERIMENT
NOVEMBER 22, 1977 DAY 326 ORBIT 14

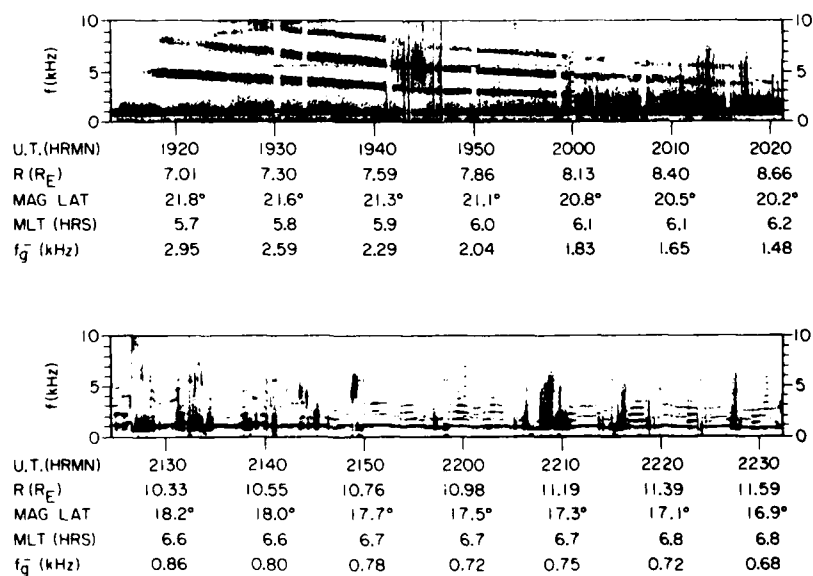


Figure 18. Example of Wideband Measurements Between 0 and 10 kHz from ISEE-1

S³-A ORBIT 36
 DAY 330 NOVEMBER 26, 1971
 ELECTRIC FIELD

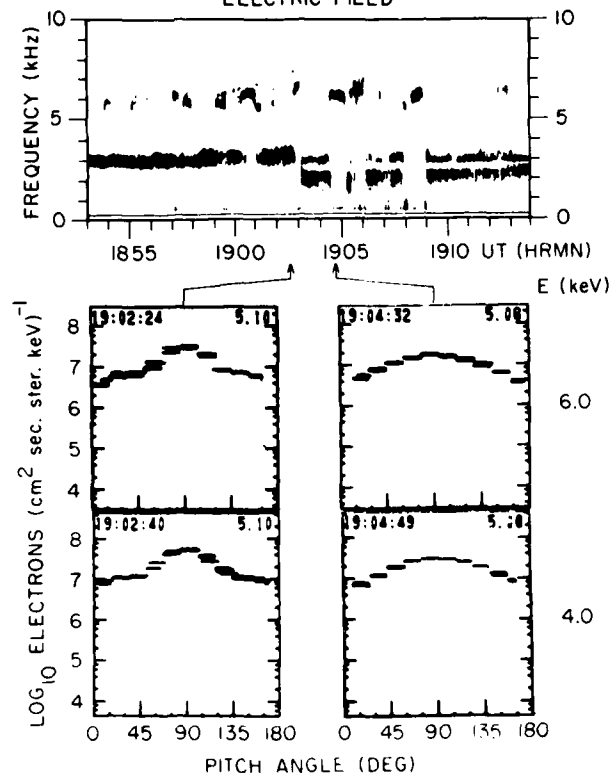


Figure 19. Simultaneous Electron Pitch Angle and Wideband Wave Measurement from Explorer 45

1903 there is an abrupt change as the anisotropy of the electron distribution was reduced. The frequency and intensity of the chorus dropped. The band split with no emissions at half the gyro-frequency. A comparison of wave and particle data shows that it takes a relatively large pitch angle anisotropy to generate the high frequency chorus component. This is an example of how wave and particle data can be combined. Higher time resolution must first be obtained. Further advances in measurements of wave-particle interactions in space requires improvement over present achievements in two areas: (1) determination of wave normals and polarization for both electromagnetic and electrostatic waves in order to identify wave modes and source locations, and (2) high-time resolution of simultaneous wave and particle measurements. The constraint imposed by the first requirement is the requirement for three orthogonal electric field dipoles and three orthogonal search coil magnetometers. The second requirement is discussed below.

4.2 Wave-Particle Time Resolution

One problem obstructing further advances in our understanding of space plasma processes concerns the temporal resolution of data sampling. The problem was alluded to in the tutorial presentation of M. Ashour-Abdalla. In part the problem is one of telemetry constraints. In part it reflects a duality of purpose in the space exploration philosophy. On one level there is a strong desire to understand the microphysics of space plasmas. There is also a desire to construct statistical or engineering models of the various region of space. The sampling requirements of the two modes are antithetical. To build statistical models on microphysics sampling rates involves the collection of inordinately large amounts of information — most of which would never be used. However, without high-time resolution the microphysics is unattainable. To overcome this duality the U. of California at Berkeley group has proposed an instrument for the OPEN project that does not measure any one physical parameter. Rather it measures them all in the most useful manner. They refer to it as a sort of "universal gizmo." This involves the mass storage of data collected from a large assortment of spacecraft instruments and at rates far exceeding that available with normal telemetry.

It is a rather remarkable fact that, despite the large distances involved in space, many of the most interesting and important phenomena occur at sharp boundaries (plasmopause, auroral arcs, magnetopause). These phenomena are important from the points of view of both the overall dynamics of the magnetosphere and of the specific plasma physics involved. In addition, other phenomena occur on time scales much faster than that associated with the overall dynamics of the magnetosphere. Examples include: microbursts, auroral kilometric radiation, and interactions between particle distributions and wave growth. A

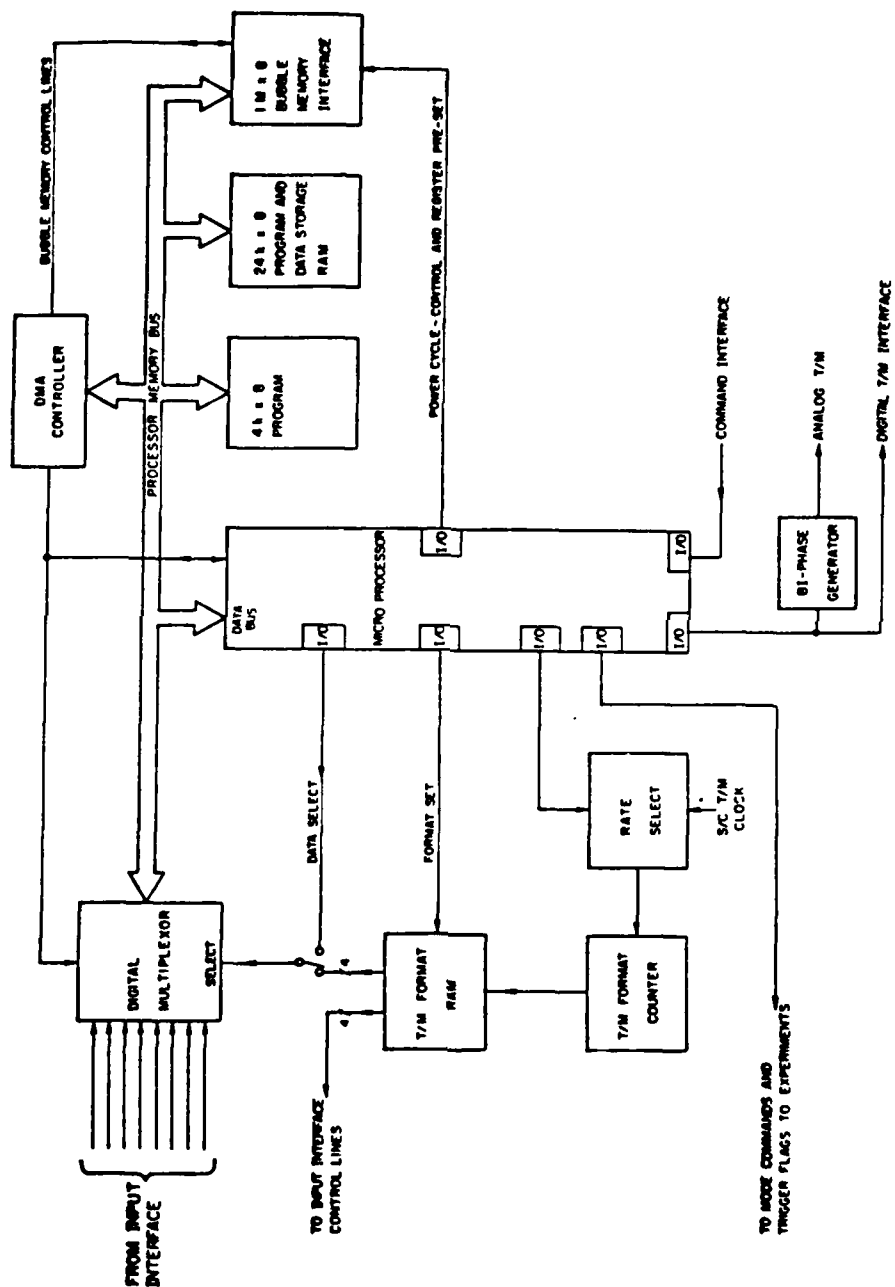


Figure 20. Digital Portion of Microprocessor Proposed for OPEN Project that Would Recognize Interesting Events and Record Them with High Temporal Resolution for Later Transmission to Ground

controller must be designed to recognize, *in situ*, the conditions of such special events, trigger the storage of very large amounts of data at variable rates from all relevant experiments and send this information down at a much slower rate. The digital portion of the instrument is diagrammed in Figure 20. The maximum storage capacity is 8×10^6 bits with a maximum storage rate of 1.02×10^6 bits/sec.

Now, the mass storage of data on board a spacecraft is not a new idea. What is new here is the integration of data from all the experiments under a central, scientifically controlled and programmable "trigger" mechanism. The physics of the problems under study would dictate unique "trigger" programs. The scientific results derived from such a mission depend crucially on how well science is designed into the hardware and software of such an experiment.

References

1. Ness, N.F. (1970) Magnetometers for space research, Sp. Sci. Rev. 11:459.
2. Longanecker, G.W., and Hoffman, R.A. (1973) S³-A spacecraft and experiment description, J. Geophys. Res. 78:4711.
3. Gurnett, D.A. and Shaw, R.R. (1973) Electromagnetic radiation trapped in the magnetosphere above the plasma frequency, J. Geophys. Res. 78:8136.
4. Gurnett, D.A., Anderson, R.R., Scarf, F.L., Fredricks, R.W., and Smith, E.J. (1979) Initial results from ISEE-1 and -2 plasma wave investigation, Sp. Sci. Rev. 23:103.
5. Etcheto, J., and Bloch, J.J. (1978) Plasma density measurements from GEOS-1 relaxation sounder, Sp. Sci. Rev. 22:597.
6. Harvey, C.C., Etcheto, J., DeJarvel, Y., Manning, R., and Pettit, M. (1978) The ISEE electron density experiment, IEEE Trans. Geosci. Elec. 16:231.
7. Decreau, P.M.E., Beghin, C., and Parrot, M. (1978) Electron density and temperature as measured by the mutual impedance experiment on board GEOS-1, Sp. Sci. Rev. 22:581.
8. Pedersen, A., Grard, R., Knott, K., Jones, D., and Gonfalone, A. (1978) Measurements of quasistatic electric fields between 3 and 7 earth radii on GEOS-1, Sp. Sci. Rev. 22:333.
9. Mozer, F.S., Torbert, R.B., Fablesen, U.V., Falthammer, C.G., Gonfalone, A., and Pedersen, A. (1978) Measurements of quasi-static and low frequency electric fields with spherical double probes on ISEE-1, IEEE Trans. Geosci. Elec. 16:258.
10. Horwitz, J.L., and Chappell, C.R. (1979) Observations of warm plasma in the dayside plasma trough at geosynchronous orbit, J. Geophys. Res. 84:7075.
11. Johnson, J.F.E., Sojka, J.J., and Wrenn, G.L. (1978) Thermal suprathermal plasmas observed by the S-302 experiment on GEOS-1, Sp. Sci. Rev. 22:567.

12. Frank, L.A., Ackerson, K.L., DeCoster, R.J., and Burek, B.G. (1978) Three-dimensional plasma measurements within the magnetosphere, Sp. Sci. Rev. 22:739.
13. Geiss, J., Balsiger, H., Eberhardt, P., Walker, H.P., Webster, L., and Young, D.T. (1978) Dynamics of magnetospheric ion composition as observed by the GEOS mass spectrometer, Sp. Sci. Rev. 22:537.
14. Shelley, E.G., Sharp, R.D., Johnson, R.G., Geiss, J., Eberhardt, P., Balsiger, A., Haerendel, G., and Rosenbauer, H. (1978) Plasma composition experiment on ISEE-A, IEEE Trans. Geosci. Elect. 16:266.
15. Harris, K.K., Sharp, G.W., and Chappell, C.R. (1970) Observations of the plasmopause from OGO-5, J. Geophys. Res. 75:219.
16. Decreau, P.M.E., Etcheto, J., Knott, K., Pederson, A., Wrenn, G.L., and Young, D.T. (1978) Multi-experiment determination of plasma density and temperature, Sp. Sci. Rev. 22:633.
17. Knott, K. (1978) The GEOS-1 mission, Sp. Sci. Rev. 22:321.
18. Higel, B., (1978) Small scale structure of magnetospheric electron density through on-line tracking of plasma resonances, Sp. Sci. Rev. 22:611.
19. Shawhan, S.D. (1979) Magnetospheric wave research 1975-1978, Rev. Geophys. Sp. Phys. 17:705.
20. Anderson, R.R., and Maeda, K. (1977) VLF emissions associated with enhanced magnetospheric electrons, J. Geophys. Res. 82:135.
21. Gurnett, D.A., Scarf, F.L., Fredricks, R.W., and Smith, E.J. (1978) The ISEE-1 and ISEE-2 plasma wave investigation, IEEE Trans. Geosci. Elect. 16:225.
22. Gurnett, D.A., and Anderson, R.R. (1977) Plasma wave electric fields in the solar wind: initial results from Helios 1, J. Geophys. Res. 82:632.

List of Symbols

A	$\frac{2B_S}{T}$
B	Magnetic field
B_R	Residual magnetic field
B_S	Saturation magnetic field
E	Electric field
E_{\perp}	Perpendicular electric field
e	Charge on an electron
f_G	Electron cyclotron frequency
f_p	Plasma frequency

$f(\bar{v})$	Velocity distribution function
$f_j(\bar{v})$	Velocity distribution function for j^{th} species
H	Magnetic intensity
H_C	Magnetic intensity required to saturate core of transformer
H_D	Driving signal (magnetic intensity) for saturable transformer
I	Current
k	Wave number
k_{\parallel}	Number of wave parallel to magnetic field
k	Boltzmann constant
L	Length
L	L-shell number
M	Mass of a particle (electron or ion)
M_e	Mass of electron
M_i	Mass of ion
N	Total (number) density
N_e	Number density of electrons
N_j	Number density of j^{th} species
$\underline{\underline{P}}$	Pressure tensor
$\underline{\underline{P}}_j$	Pressure tensor for j^{th} species
Q	Charge of a particle
R_e	Radius of the earth
T	Temperature
T_e	Electron temperature
T_i	Ion temperature
V	Voltage
V_s	Satellite potential
V_0	Bulk velocity perpendicular to magnetic field
\bar{V}	Bulk or drift velocity
\bar{V}_j	Bulk velocity of j^{th} species
$Z_m(f)$	Plasma impedance as a function of frequency

$$\alpha = \frac{H_C}{4H_D}$$

$$\beta = \frac{1}{2} \left(1 - \frac{\Delta H}{H_D} \right)$$

λ_D Debye length

ϕ_s Spacecraft potential

ω_p Plasma frequency

ω_{pi} Ion plasma frequency

ω_{LH} Lower hybrid frequency

Contents

1. Introduction	246
2. Statistical Models of the Radiation Belts	246
2.1 Electron Models	248
2.2 Ion (Proton) Models	248
3. Models of the Low Energy Trapping Region	249
3.1 A Particle and Field Self-Consistent Model	249
3.2 Application to Substorms	251
3.3 Application to Magnetic Storms	252
3.4 Model Limitations	253
4. Ion Composition of the Radiation Belts	255
4.1 Composition at Ring Current Energies	255
4.2 Composition at MeV Energies	256
5. Quasi-Empirical Modelling	257
6. A Model for an In Situ, Storm-Time Ring Current Source	259
7. High Energy Trapping Region	260
7.1 Radiation Belt Electron Model	262
7.2 Radiation Belt Proton Model	264
7.3 Radiation Belt Heavy Ion Model	265
References	269

7. Modelling of Magnetically Trapped Radiation in the Inner Magnetosphere of the Earth

by

Walther N. Spjeldvik
 Nordmann Research Ltd.
 Boulder, Colorado 80303
 and
 Cooperative Institute for
 Research in Environmental Sciences
 University of Colorado
 Boulder, Colorado 80309

based on presentations given by

James I. Vette (NASA/Goddard Space Flight Center)
 Richard A. Wolf (Rice University)
 Richard G. Johnson (Lockheed Palo Alto Research Laboratories)
 Stanley M. Kaye (Princeton University)
 Lawrence R. Lyons (Space Environment Laboratory)
 Walther N. Spjeldvik (Nordmann Research Ltd. and
 CIRES/U. of Colorado)

1. INTRODUCTION

The earth's radiation belts consist of geomagnetically trapped, energetic, charged particles which occupy a magnetically confined region of geospace from the top of the terrestrial atmosphere to about $L = 10$, L being the McIlwain parameter. Beyond this approximate boundary the magnetopause is found on the dayside magnetosphere. Existence of this trapped corpuscular radiation was first established through Geiger-Muller tube detectors on early satellites such as Explorer 1.¹ The early detectors primarily responded to energetic electrons which were later found to exhibit a low flux region (the "slot") in the middle of the trapping region. For that reason the characterization of the trapped radiation zone as the radiation belts (a two-belt structure when detecting > 100 keV electrons) came into use. The trapped radiation range of particle energies extends from thermal energies (approximately 1 eV) to above tens of MeV per particle. Examples of the radiation belt particle fluxes are found in the instrument session review contained in this volume. In some applications the radiation belts are considered to be the more energetic of the trapped particles (for example, $E > 100$ keV) while particles of lesser energies are referred to as being from the ring current. Such a division represents a rather arbitrary nomenclature, however. Figure 1 shows an overview of the earth's radiation belts as seen in energetic electrons; typical trapped particle spiral trajectories and the plasma wave propagation characteristics of plasmaspheric whistler mode hiss, which plays a major role in the control of radiation belt electrons, are also indicated.

This paper is organized into sections on statistical radiation belt models and a particle-and-field convection and electrical current model; there are also sections on ion composition observations which yield critical constraints on future modelling. Further sections demonstrate simplified, quasi-empirical modelling. They show how low-energy, radiation belt particles can become energized, providing a source of radiation belt energetic particles, and finally how the high energy radiation belts are modeled for electrons, protons and heavy (very abundant) ions.

2. STATISTICAL MODELS OF THE RADIATION BELTS

In many practical applications the question of the specific physical processes responsible for maintaining the earth's radiation belts is less important than the

1. Van Allen, J.A., Ludwig, G.H., Ray, E.C., and McIlwain, C.E. (1958) Observation of high intensity radiation by satellites 1958 Alpha and Gamma, Jet Propulsion, 28:588.

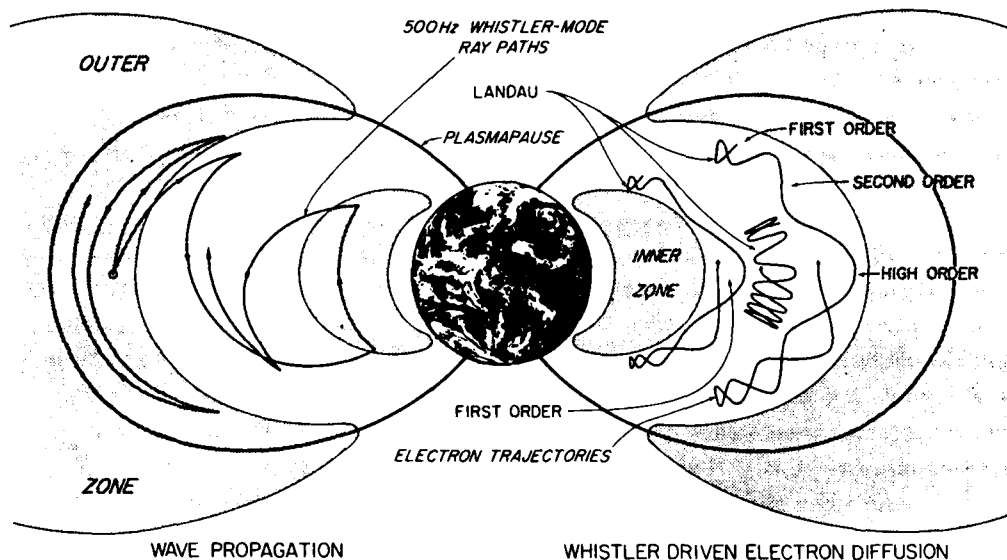


Figure 1. Cross Section of the Earth's Radiation Belts as Seen in Energetic (Hundreds of keV) Electrons. Left side: 500 Hz whistler mode wave paths. Right side: Examples of electron bounce trajectories. Indicated are the spatial regions in which the whistler wave-electron resonant interaction takes place for different harmonics. The average location of the plasmapause is also indicated.

intensity of the current radiation. Such applications include design considerations for new instrumentation, engineering aspects of the spacecraft, and radiation dose expectations for manned space flights. To meet this need for information, statistical models of radiation belt electrons and ions have been constructed based on accumulated space data from earlier spacecraft recordings. Several such models have been compiled at the NASA/Goddard Space Flight Center. These include the energetic electron ($E > 40$ keV) and ion (usually labeled proton) models. Particles of thermal plasma energies and much of the ring current population are excluded from these models. A practical reason for this lower energy cut-off in the models is that the lower energy particles are more easily shielded against and thus are of less importance in many engineering considerations.

The global coverage of the models extends over an L-shell range from $L \sim 1.2$ to $L \sim 11$. These models are not concerned with short-term radiation variations such as sporadic particle "bursts," substorms or even the 27-day solar rotation. Local time is averaged over; therefore no day/night sector variations are included.

Curves fitted to the data constitute the models. This provides a great simplification since a model user may specify the orbit of a proposed (or existing) spacecraft and receive a model estimate of the radiation exposure. Accuracy of the

model prediction is important. Clearly it would be desirable to have a probable error within 10 or 20 percent of the predicted values. However, because of inaccuracies in the data used in the model compilation, stemming from calibration problems as well as natural variations in the environment itself, it is estimated that the model yields predictions with no greater accuracy than a factor of 2.

The basic coordinates over which the modeled flux values are given are: L-shell, B-field and particle energy. Time variations are only used in producing models at different phases of the 11-year solar cycle such as solar maximum models and solar minimum models. In certain regions of space systematic, quiet-time particle flux variations by a factor of 3 are apparent between solar maximum and minimum models. Examples of the NASA/Goddard Space Flight Center statistical models are given in the instrument section of these proceedings. Over the years there has been steady progress in the model development, and this is described in Vette et al.² It would be highly desirable to incorporate data from SCATHA and other spacecraft in the future refinement of these statistical, applications oriented models.

2.1 Electron Models

The most up-to-date of the NASA/Goddard Space Flight Center statistical energetic electron model is the AEI - 7 model. This model covers electron energies from 40 keV to 4 MeV. One difficulty with this model is the energy range 2 to 4 MeV where data extrapolation is necessary; also the L-shell range is limited to beyond $L = 2.8$. A further refinement of this model is currently underway incorporating new data, and it is expected that a fully documented final model (AE-7) will soon be made available to users. The electron models are based on data gathered with a large number of spacecraft starting with Explorer 6 in 1959 and terminating with ATS - 1 in 1968. This time interval spans almost a full solar cycle. It was found that clearly discernable solar cycle effects for the energetic electrons were present from $L = 2.8$ to $L = 5$. The problem with electron observations at low L-shells (for example, $L \leq 2.2$) is that much of this data set was recorded between 1964 and 1967 while there was a significant contamination residue from nuclear explosion fragments.

2.2 Ion (Proton) Models

Large amounts of data have been compiled to yield the current statistical AP-8 model for protons (ions). This model uses data from 35 different instruments on numerous spacecraft, starting with Explorer 4 in 1958 and continuing until 1969.

2. Vette, J.I., Teague, M.J., Sawyer, D.M., and Chan, K.W. (1979) Modeling the earth's radiation belts, in Solar-Terrestrial Predictions Proceedings II, ed. R.F. Donnelly, U.S. Dept. of Commerce, Washington, D.C., p 12.

The reason for the lack of more recent data is that most ion detectors on newer spacecraft that traverse the inner magnetosphere have been designed to study the less energetic ions. ATS-6 in a geostationary orbit is an exception.

Solar cycle effects are quite apparent in low-altitude, radiation belt ion data. These solar cycle effects are caused by significant density variations at a given height in the uppermost parts of the atmosphere due to the solar control of the thermal conditions. The innermost parts of the radiation belts are controlled by collisions with the atmospheric particles. This leads to temporal variations in the energetic ion spectra. These variations determine the radiation exposure of low altitude spacecraft used for survey purposes.

3. MODELS OF THE LOW ENERGY TRAPPING REGION

Three major processes act to transport energetic charged particles in the inner magnetosphere: Convection (or drift motion) due to persistent electric and magnetic fields, diffusion (stochastic transport) due to intermittent small amplitude field fluctuations, and injection (sudden appearance of particles within a finite energy range in a region of space) due to external particle sources, or acceleration mechanisms, either *in-transit* or *in-situ*. In-transit acceleration is used as a label for unknown transport processes and is of particular importance during disturbed times, including magnetic storms and substorms. Convection is a dominant transport mode at up to several tens of keV energies, depending on particle species and location in the inner magnetosphere. Diffusion is the controlling transport mechanism at energies greater than a few hundred keV below the geostationary altitude. To first order, diffusion may therefore be neglected in models of the ring current and associated current systems in the lower energy end of the radiation belts.

3.1 A Particle and Field Self-Consistent Model

A numerical model that solves the physical equations describing the convection-dominated energy range (1-100 keV particles) has been developed by Richard Wolf and his coworkers at Rice University.^{3,4,5} This model computes both particle and

3. Harel, M., Wolf, R.A., Reiff, P.H., Spiro, R.W., Burke, W.J., Rich, F.J., and Smiddy, M. (1981) Quantitative simulation of a magnetospheric substorm, 1. Model logic and overview, J. Geophys. Res. 86:2217.
4. Harel, M., Wolf, R.A., Spiro, R.W., Reiff, P.H., Chen, C.K., Burke, W.J., Rich, F.J., and Smiddy, M. (1981) Quantitative simulation of a magnetospheric substorm, 2. Comparison with observations, J. Geophys. Res. 86:2242.
5. Spiro, R.W., Harel, M., Wolf, R.A., and Reiff, P.H. (1981) Quantitative simulation of a magnetospheric substorm, 3. Plasmaspheric electric fields and evolution of the plasmopause, J. Geophys. Res. 86:2261.

field behavior under externally imposed conditions. It is an almost self-consistent model in the sense that although the major particle and field quantities are derived self-consistently, such quantities as electrical conductivity and boundary potential distribution are added from auxiliary information. From comparisons of the model results for specific simulations with observable data, and from the agreement or disagreement with these data, knowledge of the interacting physical system may be assessed. Special emphasis is placed on the dynamic behavior of the ring current and adjoining current systems in the inner magnetosphere. To incorporate the effects of magnetospheric electric fields over the region of interest, boundary conditions are assigned both at the ionospheric and magnetotail limits of the simulation regions, and model calculations are carried out for L-shells below $L = 10$.

The most important external parameters for this convection model are the time-dependent polar cap potential drop and the electrical conductivity, estimated from observed electron fluxes during the event period. Also needed are a magnetic field model and an estimate of the plasma sheet particle population at the start of the simulation period.

The principal physical relation utilized is the assumption of an identically vanishing divergence of the current density vector: $\vec{\nabla} \cdot \vec{j} = 0$ where the local current density \vec{j} is a combination of the Birkeland current, the height integrated ionospheric current, and the ring current. The numerical solution of this equation, subject to Maxwell's field equations, the boundary conditions, and the initial conditions, yields the predicted current distributions in the magnetosphere. Ionospheric electric fields are self-consistently computed using Ohm's law. These electric fields are mapped to locations in the magnetosphere assuming that the magnetic field lines are equipotentials. The mapped electric fields are then used to simulate the motion of the different charged particle populations in the earth plasma sheet and in the inner magnetosphere.

The time variation of the large scale computed electric field controls the separatrix between open and closed electric equipotential lines around the earth and thus the location of the plasmapause. The total field is a combination of the "corotation" and the "convection" electric fields. Convective motion ceases to be the dominant transport mode at energies above 100 keV and thus this convection model, in its present state of development, has been used primarily for particles below 200 keV. Other derived physical predictions are simulated magnetograms for given locations on earth. These can be compared with actual magnetograms recorded for the event under study. The AFGL magnetometer chain is useful for this purpose. The model information about the strength of the horizontal

Figure 2 shows an overview of the intercoupled physical processes considered in the Rice University model. Notice the number of feed-back loops necessary to make field and particle flux quantities consistent. The model is deterministic and no stochastic mechanisms are included.

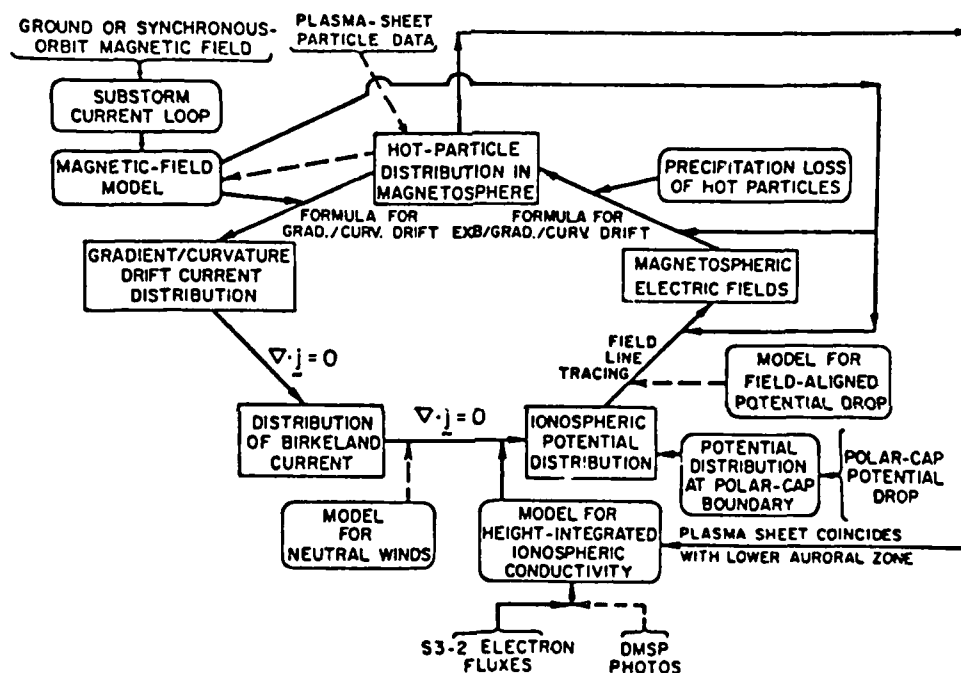


Figure 2. Overview of the Logic of the Rice University Convection and Current Model. Arrows indicate flow of model information and dashed lines indicate planned future improvements for greater internal consistency. The rectangles at the corners of the central pentagon represent basic computed parameters. Input models are indicated by rectangles with round corners; input data are indicated by curly brackets. The program cycles through the entire main loop (including all the rectangular boxes) every time step t (approximately every 30 sec). The basic equations that the computer uses or solves are described briefly by words or symbols next to the logic flow lines.

3.2 Application to Subterms

The model has been used to study the evolution and characteristics of the currents in the inner magnetosphere during an isolated substorm event.^{3,4,5} With the polar cap potential drop typical of quiet (pre-substorm) times the model yields

a rather shielded inner magnetosphere where the equipotential lines are far apart. With the substorm onset, the cross-polar-cap potential intensifies. This leads to development of an electric field distribution on a time scale shorter than that of the response time of the charged particle populations. It is interesting to note that during this transient phase the large-scale geoelectric field is computed to exhibit significant deviations from a nominal dawn-to-dusk structure. This is consistent with experimental observation of whistler behavior during substorms. As the simulated event progresses the particle populations in the near-earth plasma sheet and ring current redistribute themselves resulting in a lessening of the electric field structure in the inner magnetosphere.

To study the effect of parameter variations on the computed particle and field distributions appropriate for the substorm period, the model was perturbed by suddenly altering the electrical conductivity and at the same time reducing the cross-polar-cap potential drop. This leads to a significant alteration of the near-earth electric field configuration where a reversed local electric field and a potential minimum is found. Such effects have also been noted by observers using ground-based observations of the ionospheric current systems. Physically, these effects arise because of the different response time constants for the various components of the system. The model provides the first detailed description of the substorm effects in the inner magnetosphere and the low energy end of the radiation belt trapping region.

3.3 Application to Magnetic Storms

Recently a first attempt has been made to apply the Rice University model to the simulation of a magnetic storm.⁶ The time simulation was started in a similar fashion to that of the substorm simulation, namely with a relaxed distribution of particles and fields so that only a very weak convection electric field is present in the inner magnetosphere. Using polar-cap electric potential drop and electrical conductivities appropriate to the June 29, 1977 magnetic storm period, the simulation was carried out following the sudden commencement of this storm. The large increase in cross-polar-cap potential leads to a complete breakdown in the electrical shielding of the radiation belts and the ring current becomes highly perturbed. The inner edge of the plasma sheet was located near $L = 8$ in the evening sector prior to the storm. During the first hour of the main phase the plasma sheet moved earthward to $L = 5$. The model describes the injection of plasma sheet particles into the outer ring current following the storm onset. After 4 to 5 hours of simulated development the enhanced ring current was found in the outer radiation zone, extend-

6. Wolf, R.A., Harel, M., Spiro, R.W., Voigt, G.H., Reiff, P.H., and Chen, C.K. (1981) Computer simulation of inner magnetospheric dynamics for the magnetic storm of July 29, 1977, *J. Geophys. Res.* (submitted for publication).

ing in as far as $L = 4$. Also predicted is the eventual reestablishment of the shielding of the inner magnetosphere from the main convection electric field. It was also found that the sudden compression of the magnetosphere during the initial phase of the magnetic storm leads to an enhancement of the dawn-dusk convection electric field which produces a further intensification of the cross-polar-cap potential drop. This is the physical cause of the storm-time ring current injection. It also suggests that significant magnetic and electric impulses are not independent but that, in magnetic storms, the magnetic field variations cause the electric field impulses.

3.4 Model Limitations

The Rice University convection model represents a high degree of advancement in the modeling of the very complex, interacting lower energy particle radiation environment. There are, however, a number of physical limitations which affect its accuracy; these fall into two categories. One is the quality of the external input parameters, and the other stems from the physical approximations of the model itself. A major limiting factor in the accuracy of the model calculations is the limited knowledge of the polar-cap electric potential difference used as model input. This quantity is obtained from spacecraft observations which (because of the orbital period of polar orbiting satellites) is typically 50 minutes. Fast electric potential variations can thus not be resolved and are not represented in this crucial input data. In this context it should be noted that because of the sluggish response of the plasma sheet particle populations, fast potential changes tend to be passed through to the inner magnetosphere trapping region while slower variations give the particle populations enough response time to prevent the electric field penetration to low L -shells. Thus the near-earth plasma sheet acts as a high pass electric field frequency filter. Unfortunately, it is the important (and unknown) fast field variations that are inadequately represented in the input data.

In its present form the model does not allow for effects of neutral winds in the upper atmosphere. These winds can be quite strong and are known to create ionospheric charge separation and thus electric fields. It is possible that the ionospheric dynamo thus generates ionospheric fields stronger than those of purely magnetospheric electric fields. To include this effect would require the precise knowledge of the global wind systems at ionospheric heights as function of time including ionospheric composition variations, a rather formidable requirement.

Another physical process disregarded in the model is the sporadic existence of parallel (to the magnetic field) electric potential drops which have been observed to exist and to be substantial during at least some events.⁷ These parallel electric

7. Mozer, F.S. (1977) Relationships of electric fields to auroral forms, Report GA-533 Presented at the IAGA/IAMAP Joint Assembly, Seattle, Washington.

fields can accelerate ions or electrons (depending on the direction of the electric field) out of the ionosphere with energies typically 1 - 10 keV^{8,9} so that these particles may contribute to the ring current, provided that they are scattered sufficiently in pitch angle. These parallel particle beams are now thought of as important at auroral latitudes, although their precise roles are still subject to basic research. Thus, from a particle continuity point of view the model has only one particle source, located in the magnetotail plasma sheet.

A third limitation on the accuracy of this model is the neglect of any loss mechanism for the charge carriers either through particle-particle collisions or through wave-particle interactions. Collisions between an ion and an exospheric neutral hydrogen atom can lead to charge exchange, neutralizing the energetic ion (so that it is no longer trapped in the magnetic field). The charge is then carried by a much slower thermal ion which has a different response to the magnetic field (through the drift mechanism) than the energetic ion. Typical time scales for such processes may in some locations be comparable to the simulated event periods. When some of the energetic ions are heavier than the proton, the oxygen ion, for example, they may become multiply ionized and thus the fields will have a greater influence in their motion. Current knowledge of charge state chemistry indicates that the latter process would be primarily important above 100 keV although thermal O²⁺ ions are also observed. Particle-particle collisions that do not lead to changes in ionization state may cause energy exchange between the energetic charged particle and the thermal plasma particle (Coulomb collisions). This process also provides a natural resistance to the electrical current through the energy loss in the inner magnetosphere. Ions of ring current energies are also subject to wave-particle interactions which can lower the pitch angles of its charge carrying particles to the extent that they encounter the atmosphere during bounce motions. This constitutes an outright loss of the current carrying ions or electrons.

The time scales of these neglected processes are frequently of the order of the simulated event time period; thus future development of the Rice University Convection/Current model will be directed at including such processes.

These model limitations notwithstanding, comparisons of magnetograms observed at the ground with model predictions show that it indeed simulates major characteristic features of the inner magnetosphere evolution. Further, *in situ*

8. Evans, D.S. (1975) Evidence for the low altitude acceleration of auroral particles, in *Physics of the Hot Plasma in the Magnetosphere*, eds. B. Hultqvist and L. Stenflo, Plenum Press, New York, pp 319-340.
9. Mizera, P., Fennell, J.F., and Vampola, A.L. (1977) Correlated charged particle and electric field measurements, Report GA-125 Presented at the IAGA/IAMAP Joint Assembly, Seattle, Washington.

observations of the strength of the ring current particle fluxes tend to support the overall model results although a number of features (such as the dusk side ring current) show some discrepancies. A complete agreement is not expected, however, since the model does not treat the compositional aspects of the trapped ion population (which varies strongly from H^+ dominance to O^+ dominance during substorm events¹⁰) but rather assumes a purely proton-electron composition.

4. ION COMPOSITION OF THE RADIATION BELTS

In the first decade of geospace exploration it was believed that the radiation belts primarily contained protons and electrons with only minute contributions from helium and other heavy ions. Research conducted during the seventies has revealed a significantly different picture. We have learned that helium and oxygen ions can be numerous and at times even dominate in the 1 - 20 keV energy range¹¹ as well as in the > 800 keV range¹² where the heavy ions appear to dominate. There is clearly a need for incorporating the compositional aspects of the trapped radiation into both statistical and physical models. Work is currently underway to remedy this situation.

4.1 Composition at Ring Current Energies

Synoptic studies of the ion composition at energies below ~20 keV have been made using data from GEOS and other satellites. This research has shown that ions of terrestrial origin (H^+ , O^+ , He^+) populate at least a part of the ring current region in the inner magnetosphere^{10, 13-16} while ions of solar origin (H^+ , He^{++} ,

10. Lundin, R., Lyons, L.R., and Pissarenko, N. (1981) Observations of the ring current composition of L-values less than 4, J. Geophys. Res. (in press).
11. Shelley, E.G. (1979) Heavy ions in the magnetosphere, Sp. Sci. Rev. 23:465.
12. Spjeldvik, W.N. (1979) Expected charge states of energetic ions in the magnetosphere, Sp. Sci. Rev. 23:499.
13. Sharp, R.D., Johnson, R.G., and Shelley, E.G. (1976) The morphology of energetic O^+ ions during two magnetic storms: Temporal variations, J. Geophys. Res. 81:3283.
14. Sharp, R.D., Johnson, R.G., and Shelley, E.G. (1976) The morphology of energetic O^+ ions during two magnetic storms: Latitudinal variations, J. Geophys. Res. 81:3292.
15. Ghielmetti, A., Johnson, R.G., Sharp, R.D., and Shelley, E.G. (1978) The latitudinal, diurnal, and altitudinal distributions of upward flowing energetic ions of ionospheric origin, Geophys. Res. Lett. 5:59.
16. Johnson, R.G., Sharp, R.D., and Shelley, E.G. (1978) Observations of ions of ionospheric origin in the storm-time ring current, Geophys. Res. Lett. 5:59.

etc.) also have been detected. The morphological features have been investigated, and results indicate that for some geomagnetic disturbance levels ($K_p \sim 3$) there is roughly an equal contribution from the two sources. At the geomagnetic equator there seems to be a significant compositional variation with location as exemplified in Figure 3 which depicts results from the PROMICS experiment on the Prognoz-7 spacecraft. Upward-streaming, accelerated ions are found to come out of the auroral ionosphere in large fluxes.^{11, 17} More terrestrial H^+ ions than O^+ ion are found in the upward beam, at least as a statistical average over close to a year of data. However, once injected onto stably trapped orbits there is a difference in the charge exchange loss rates which favors the longevity of O^+ over H^+ .¹⁸ and equatorial fluxes of O^+ ions have indeed been observed to be dominant at some L-shells.¹⁰ The injection region is clearly that of high (auroral) latitudes. When the composition observations obtained with the S3-3 spacecraft are projected from low altitudes to the geomagnetic equator it is found that much of the upstreaming ionospheric ions arrive onto L-shells of $L = 10 \pm 2$ during "quiet" and moderately disturbed ($K_p \leq 2$) times. This supports one of the fundamental assumptions made in the Rice University model (a divergence-free current system) where indeed most of the atmospherically contributed energetic particles enter their simulation region from outside of $L = 10$; this should be valid for at least moderately disturbed periods although for greater disturbances this may not be true.

4.2 Composition at MeV Energies

Even at MeV energies the radiation belt ion population are not predominantly protons. The observational findings of Fritz and Wilken¹⁹ show that when comparisons are made at equal total ion energies there are more helium, oxygen and carbon ions at high energies than protons. These findings have subsequently been verified and extended.¹² On the other hand, when compared at equal energy per nucleon the ion comparison at MeV energies favors protons. The ion composition in the energy range ten keV to a few hundred keV is still experimentally unexplored.

17. Mizera, P.F., and Fennell, J.F. (1977) Signatures of electric fields from high and low altitude particle distributions, *Geophys. Res. Lett.* 4:311.
18. Lyons, L.R., and Moore, T.E. (1981) Effects of charge exchange on the distributions of ionospheric ions trapped in the radiation belts near synchronous orbit, *J. Geophys. Res.* (submitted for publication).
19. Fritz, T.A., and Wilken, B. (1976) Substorm generated fluxes of heavy ions at geostationary orbit, in *Magnetospheric Particles and Fields*, Ed. B.M. McCormac, Reidel Dordrecht-Holland, p 171.

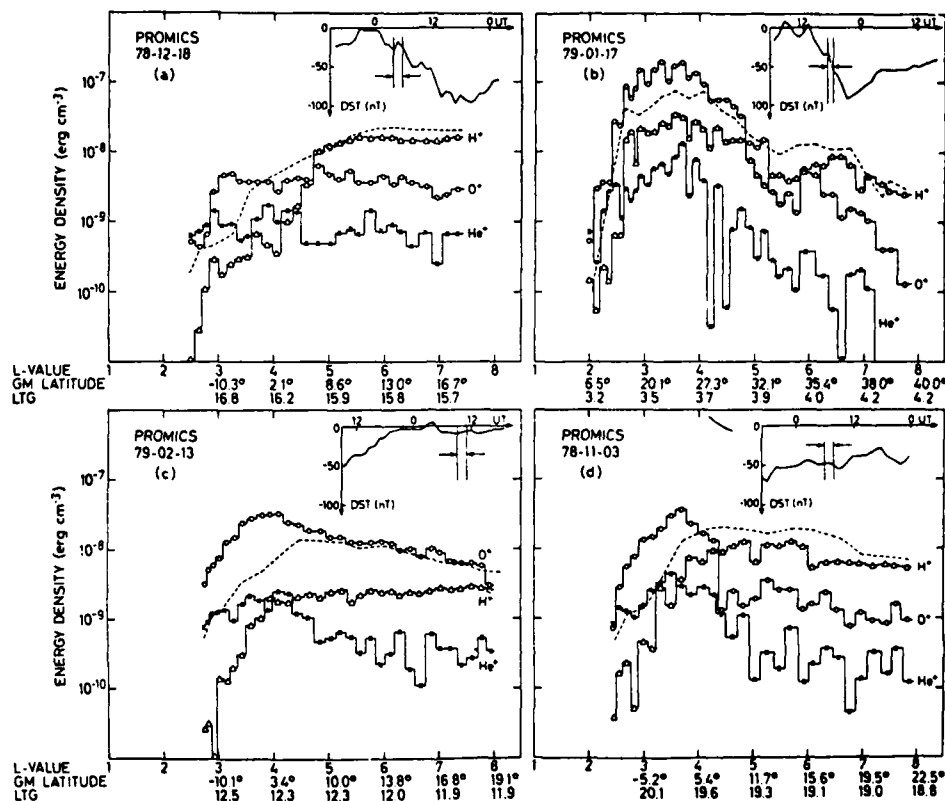


Figure 3. Examples of Near-equatorial Observations of the Ring Current Ion Composition at ~ 5 keV Energies. Triangles denote H^+ ions (protons), circles denote O^+ ions and crosses denote He^+ ions. The data were taken with the Swedish PROMICS ion composition experiment on one of the Soviet PROGNOZ spacecraft during four different periods. The D_{st} - index is also given; for further details, see Lundin et al¹⁰

5. QUASI-EMPIRICAL MODELLING

While the Rice University numerical model, which is directed towards a comprehensive, self-consistent treatment of electric fields and the trapped and quasi-trapped particle populations below 100 keV energies, has achieved noteworthy, successful simulations, the complexity of the model is a practical drawback. A number of much simpler approaches have been taken, such as single particle orbit tracking in specified field geometries.^{20,21} Such models are not derived

20. Ejiri, M. (1978) Trajectory traces of charged particles in the magnetosphere, *J. Geophys. Res.* 81:4798.

21. McIlwain, C.E. (1974) Substorm injection boundaries, in *Magnetospheric Physics*, Ed. B.M. McCormac, D. Reidel, Dordrecht-Holland, p 143.

from first principles of physics in a self-consistent fashion but rather use empirical relationships and/or given field values in lieu of the more complex physics. One such model has been developed by S. Kaye at Princeton University. It uses simplified physical conditions: an unperturbed purely dipolar magnetic field, a combination of corotational and convective electric field derivable from a scalar potential $E = -(U_{\text{cor}} + U_{\text{conv}})$, where U_{conv} is related to the polar cap potential drop, which in turn is empirically related to the location of the plasmapause and the K_p index. Such empirical relations are naturally subject to statistical deviations and thus probable errors. This model further incorporates an empirical shielding factor which depicts the estimated fall-off of the effective convective electric potential with lower L-shells. The model also adopts the existence of a sharp inner edge of the plasmasheet (the Alfvén layer) such that all particles considered are at or beyond the Alfvén layer and no particles at these energies reach into lower L-shells. The model then imposes the absolute constancy of the first and second adiabatic invariants, and the particle distributions can be studied in the quiet time, steady state limit or for imposed dynamical variations in the dawn-dusk convective electric field. Use of this model had led to a successful description of many characteristics of the Alfvén layer; most notably the so-called "nose-structure" that has frequently been observed with Explorer 45. This model has been used to explain the flux variations as seen by the spacecraft moving through a stationary or dynamic inner plasmasheet edge as function of particle energy, pitch angle and local time. This work has led to new insight into the radiation belt-plasmasheet interface processes. For details, see Kaye and Kivelson²² and Southwood and Kaye.²³ Specific application of this model has been made to study the motion and structure of the Alfvén layer during substorm events by assigning typical time dependent values to the cross-polar-cap potential difference. Comparison with the ATS-5 observations favor the validity of the computations made with this model.

Further development of this type of quasi-empirical modelling should utilize a more realistic magnetic field representation than the pure dipole configuration, include the effects of induction electric fields, and use the properties of the particle distribution function to arrive at quantitative spectral predictions. Particles can also be scattered in pitch angle and exchange energy with plasma waves; this is another avenue for future model development.

22. Kaye, S.M., and Kivelson, M.G. (1979) Time dependent convection electric fields and plasma injection, *J. Geophys. Res.* 84:4183.
23. Southwood, D.J., and Kaye, S.M. (1979) Drift boundary approximations in simple magnetospheric convection models, *J. Geophys. Res.* 84:5773.

6. A MODEL FOR AN IN SITU, STORM-TIME RING CURRENT SOURCE

It has been generally conceded that there are two significant contributing sources to the enhanced storm time ring current, inward convection of plasma sheet particles and upward acceleration of ions from the auroral ionosphere. Both of these sources are known to operate on L-shells beyond $L \sim 4$. There is, however, no reliable evidence that they are effective closer to earth, except during extreme conditions rarely attainable in the magnetosphere. A third possibility exists, namely the in situ acceleration of pre-existing lower energy charged particles in the outer radiation zone. A simple model describing this process was developed at the NOAA/Space Environment Laboratory by Lyons and Williams.²⁴

During the main phase of geomagnetic storms there are large increases in the fluxes of trapped ions and electrons in the radiation belts from $L \sim 7$ in to $L \sim 2$. It is well known that the electron slot region which extends in to $L \sim 2$ at some energies becomes substantially filled in during storms. These increases are observed at particle energies extending from less than 1 keV to above hundreds of keV. During magnetic storms the flux enhancements observed on L-shells beyond $L \sim 4$ are not significantly larger than those associated with substorm activity; however, below $L \sim 4$ the flux increases are only significant during major geomagnetic storms. It is the ring current flux increases on L-shells $L \leq 4$ that are responsible for most of the storm magnetic field decreases observed on the ground.

These particle flux increases at $L \leq 4$ can be explained from an inward, radial displacement of the trapped, low-energy outer-zone particles under the preservation of the first and second adiabatic invariants. To test if this source model has merit, data from Explorer 45 at the geomagnetic equator were studied. This spacecraft covers the L-shell range from the top of the atmosphere to $L \approx 5.2$. Presumably source mechanisms other than in-situ acceleration place particles onto L-shells beyond $L \sim 4$ so the model does not directly address the ultimate particle sources for the radiation belts. Data for two large geomagnetic storms in December 1971 and June 1972 were used in the testing. For equatorially mirroring particles the second adiabatic invariant is zero and is thus conserved. Conservation of the first adiabatic invariant μ yields $\Delta E/\mu \Delta B$ where the in-situ measured magnetic field values were used. Thus the energization is directly proportional to the increase in magnetic field induction during the inward radial displacement. The pre-injection fluxes as a function of energy were mapped to the post-injection location by the following method: For each post-injection L-shell the lowest pre-injection L-shell was determined from the equivalency of the flux

24. Lyons, L.R., and Williams, D.J. (1980) A source for the geomagnetic storm main phase ring current, J. Geophys. Res. 85:523.

intensities. This was done for both electrons and ions as a function of energy, and for all L-values for which the Explorer 45 data were available. Typically it was found that the post-injection fluxes at $L = 2.5$ correspond to pre-injection fluxes at $L = 3.5$ with an energization by a factor of $E(L = 2.5)/E(L = 3.5) = B(L = 2.5)/B(L = 3.5) \cong (3.5/2.5)^3 \sim 2.7$. Because of the steepness of the flux spectra this amounts to significant flux increases seen by detectors of finite energy bandwidth and thus, apparent injection. Results from this model²⁴ are displayed in Figure 4. The model mappings have been checked by using the results from the onboard dc electric field probe on Explorer 45. This probe saturates when it encounters a thermal plasma density of 60 particles/cm³ and is thus a measure of the location of the plasmopause. The orbit-to-orbit (period ~ 8 hours) motion of the plasmopause position in the equatorial plane allows determination of its radial motion. It was found that the observed radial displacement of the plasmopause corresponds to the deduced radial mapping of the radiation belt ion and electron fluxes. Thus, from this simple in situ magnetic storm acceleration model the most pertinent features of the storm main phase "injections" are reproduced for both ions and electrons over a wide range of radiation belt particle energies. Direct injections of "new" particles from a source external to the radiation belt trapping region are not required to explain the filling of the radiation belt slot region during magnetic storms. Other injection mechanisms are required to provide particles at $L > 4$ prior to the storm onset. The azimuthal electric field required to provide the cross-L transport must be of the order of 0.3 to 1 mV/m and must have lasted for a time span of approximately 3 hours. The Explorer 45 data indicate that it must have been effective over 270 degrees in longitude. The required magnitude of the electric field for the geomagnetic storms considered is only a factor of 2 or 3 higher than known electric fields during common substorm activity. This again suggests that a difference between magnetic storms and substorms is not so much the magnitude or duration of the electric field, but rather the longitude range over which it has to be effective. Further verification work for this model will require measurements from an equatorial spacecraft covering the L-shells from $L < 2$ to $L \sim 10$.

7. HIGH ENERGY TRAPPING REGION

Historically the high energy ($E > 100$ keV) geomagnetically trapped particle population was the first space plasma to be investigated in situ. The early geiger tube detectors primarily counted very energetic electrons. Later instruments were devised to monitor ions also. Much theoretical work was done during the

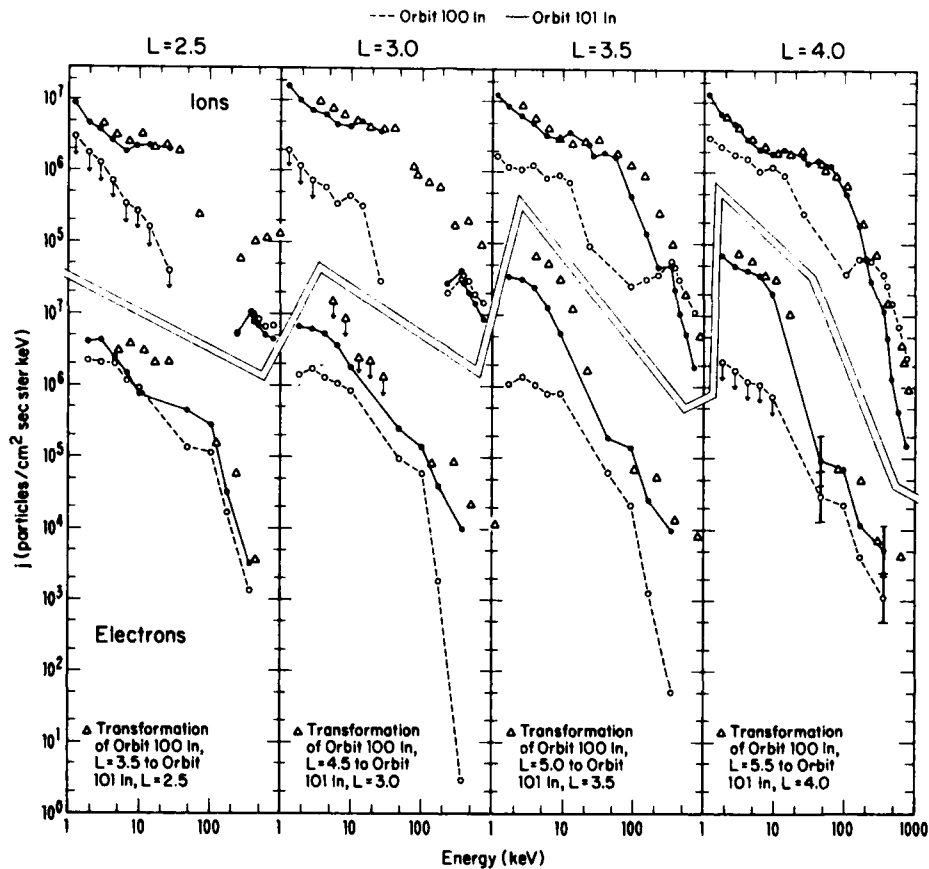


Figure 4. Results from the Inward Displacement Model Calculations Invoked to Explain Stormtime Trapped Flux Enhancements at $L < 4$. For specific details, the reader is referred to Lyons and Williams²⁴

first decade of the space era.²⁵ The understanding that was gained has been developed into working physical models that proved very successful in describing the high energy radiation environment, at least for quiet, steady state conditions. Current work in progress entails the development of time dependent, high energy models for applications to storm and substorm conditions. In the following, the most pertinent features of the radiation belt numerical modelling for electrons, protons, and heavy ions are outlined.

25. Schulz, M., and Lanzerotti, L.J. (1974) Particle Diffusion in the Radiation Belts, Springer Verlag, New York.

7.1 Radiation Belt Electron Model

The first successful model describing the steady state distribution of energetic radiation belt electrons was developed at University of California at Los Angeles.²⁶ From a ray tracing study of plasmaspheric whistler mode hiss it was concluded that plasma waves of this type, which can interact strongly with energetic electrons, propagate across the magnetic field lines to fill the entire plasmasphere with wave energy as illustrated on the left side of Figure 1. These waves scatter energetic electrons in pitch angle through a cyclotron resonant mechanism such that in a statistical sense they diffuse in pitch angle preferentially from high pitch angles and precipitate into the atmosphere. This mechanism works selectively in limited L-shell ranges²⁷ depending on electron energy and the characteristics of the whistler mode hiss turbulence. The efficiency of the interaction is illustrated in Figure 5 which depicts the energetic electron lifetimes for 20-2000 keV electrons in a 35 mV wave field. This mechanism does not operate beyond the plasmapause. From these lifetime calculations it is clear that energetic electrons are preferentially precipitated out of the trapping region on L-shells corresponding to the observed 'slot-region' between the two Van Allen radiation zones. To put the wave-particle interaction theory on a more quantitative footing Lyons and Thorne²⁸ developed a steady state equilibrium radiation belt electron model based on the following physical processes: Energetic electrons are injected into the outer radiation zone by an unspecified injection mechanism and so form a steady state boundary condition at $L \sim 5.5$. Radial diffusion due to electric fluctuations²⁹ was combined with electron losses due to the wave-particle interaction mechanism and Coulomb collisions, and the resulting electron diffusion equation averaged over the electron bounce period becomes

$$\frac{\partial f_e}{\partial t} = L^2 \frac{\partial}{\partial L} \left[D_{LL}^e L^{-2} \frac{\partial f_e}{\partial L} \right] - \frac{f_e}{\tau_w} - \frac{f_e}{\tau_c}$$

where f_e is the electron distribution function, L is the McIlwain L-shell parameter, D_{LL}^e is the electron radial diffusion coefficient, τ_w is the wave-particle scattering

26. Lyons, L.R., and Thorne, R.M. (1970) The magnetospheric reflection of whistlers, Planetary and Space Science, 18:1753.
27. Lyons, L.R., Thorne, R.M., and Kennel, C.F. (1972) Pitch angle diffusion of radiation belt electrons within the plasmasphere. J. Geophys. Res. 77:3455.
28. Lyons, L.R., and Thorne, R.M. (1973) Equilibrium structure of radiation belt electrons, J. Geophys. Res. 78:2142.
29. Cornwall, J.M. (1972) Radial diffusion of ionized helium and protons: A probe for magnetospheric dynamics, J. Geophys. Res. 77:1956.

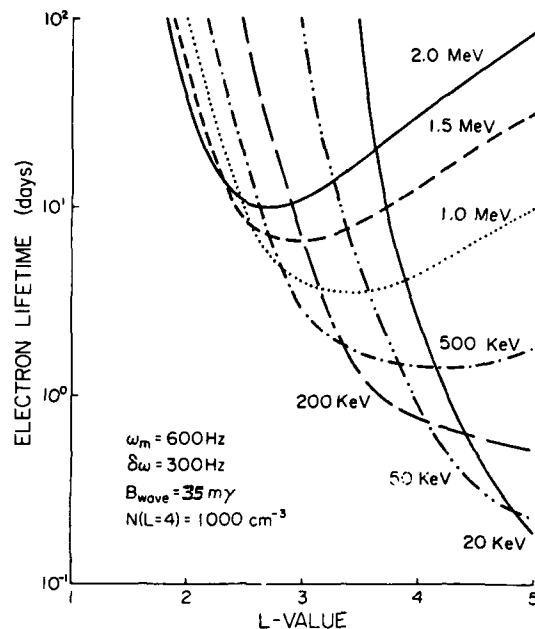


Figure 5. Electron Precipitation Lifetimes in the Radiation Belts Below $L \sim 5$ for 20 keV to 2 MeV Electron Energies. The results apply for a 35 m γ intense ELF whistler mode hiss turbulence, and the lifetimes scale with wave intensity following the relation $\tau_{bw} = \tau_{35} * (B_w/35)$ where B_w is the wave intensity (in milligamma). Typical electron lifetimes range from less than a day to hundreds of days. For details, see Lyons et al.²⁷

lifetime, and τ_c is the Coulomb collision lifetime. Only equatorially mirroring electrons were considered, and the diffusion equation was solved numerically, yielding the results depicted in Figure 6. It is noted that the comparison between this theory and pertinent data obtained with Explorer 45 is very good. This model also provided the definite answer to the long outstanding question of why radiation belt electrons were distributed into two distinct belts.

In subsequent works³⁰⁻³² this model was put to rather critical tests by calculating the energetic electron precipitation flux and by modelling in detail the interaction with the atmosphere. It was found that the predicted D region ionosphere (50 - 90 km) chemical changes computed from the precipitation flux were indeed those observed in the ionosphere. Later, an ionospheric prediction model was developed based on these combined mechanisms.³³

References 30 to 33 will not be listed here. See References, page 269.

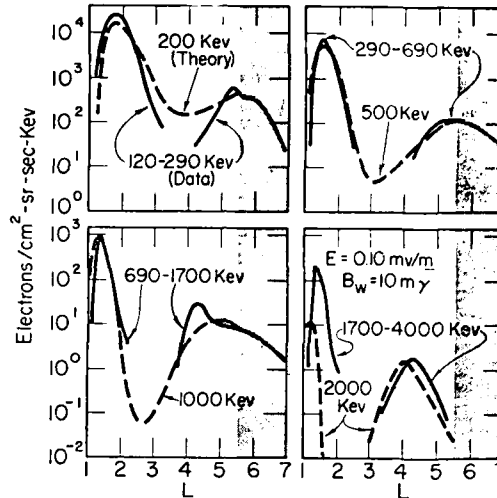


Figure 6. Comparison Between Theory and Observation for Radiation Belt Electrons. The theory simulates the radiation belt 'slot region' to a remarkable degree²⁸

7.2 Radiation Belt Proton Model

As with the electron model, the steady state equilibrium model for radiation belt protons utilizes a boundary condition on the proton flux assigned at an outer zone location. The radiation belt proton fluxes are computed as an equilibrium balance between radial diffusion from the outer zone boundary and losses due to Coulomb collisions and charge exchange ($\underline{H}^+ + H \rightarrow \underline{H} + H^+$), where underlining denotes the energetic particle. The former is not a simple loss of particles (as was approximated by Lyons and Thorne²⁸ for electrons) but rather provides a phase space transfer from higher to lower energies. The proton radial diffusion equation may then be written

$$\frac{\partial f_p}{\partial t} = L^2 \frac{\partial}{\partial L} \left[D_{LL}^p L^{-2} \frac{\partial f_p}{\partial L} \right] - \Lambda f_p + G_\mu^{-1/2} \frac{\partial f_p}{\partial \mu}$$

where

f_p is the proton distribution function,

D_{LL}^p is the proton radial diffusion coefficient,

$\Lambda = \langle \sigma_{10}^p V_p [H] \rangle$ is the charge exchange proton loss frequency per unit distribution function,

σ_{10}^P is the charge exchange cross section for the above mentioned process,

V_p is the proton speed

$[H]$ is the exospheric neutral hydrogen number density

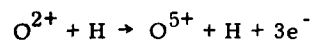
μ is the magnetic moment and

G is the Coulomb loss factor.

For details see Nakada and Mead,³⁴ Cornwall²⁹ or Spjeldvik.³⁵ The proton diffusion equation was solved by a finite difference numerical algorithm using boundary conditions obtained from ATS-6 at the geostationary altitude ($L \sim 6.6$). Some of the results are displayed in Figure 7 where a direct comparison with Explorer 45 data at lower L-shells is also made. Within the energy range covered by the valid data (which becomes less extensive in energy with lower L-shells) from this spacecraft the agreement is good. The validity of the model does not extend much below 100 keV. At ring current energies modes of transport other than pure stochastic diffusion (such as convection) and the importance of ion-cyclotron wave interactions³⁶ make for an incomplete physical description in the above model.

7.3 Radiation Belt Heavy Ion Model

By extending the physics described for the proton model to also allow for the higher charge states of heavy ions, models to describe helium ions^{29, 37} as well as models to describe oxygen ions have also been developed.^{37, 38} When the higher ionic charge states are considered one must allow for charge state altering processes other than pure neutralization of the ion. An example of these processes is:



34. Nakada, M.P., and Mead, G.D. (1965) Diffusion of protons in the outer radiation belt, J. Geophys. Res. 70:4777.
35. Spjeldvik, W.N. (1977) Equilibrium structure of equationally mirroring radiation belt protons, J. Geophys. Res. 82:2801.
36. Joselyn, J.A., and Lyons, L.R. (1976) Ion cyclotron wave growth calculated from satellite observations of the proton ring current during storm recovery, J. Geophys. Res. 81:2275.
37. Spjeldvik, W.N., and Fritz, T.A. (1978) Theory for charge states of energetic oxygen ions in the earth's radiation belts, J. Geophys. Res. 83:1583.
38. Spjeldvik, W.N., and Fritz, T.A. (1978) Energetic ionized helium in the quiet time radiation belts: Theory and comparison with observation, J. Geophys. Res. 83:654.

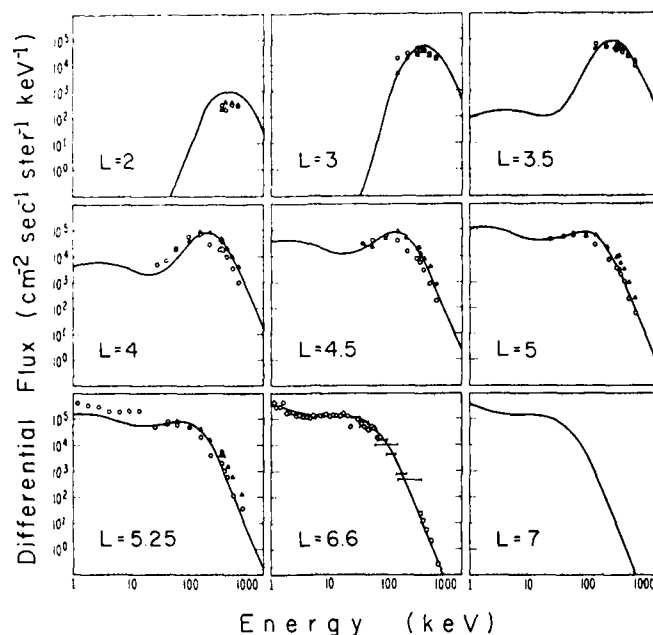
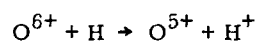


Figure 7. Comparison Between Theory and Observation for Energetic Radiation Belt Protons. The data points at $L \leq 5.25$ are from the Explorer 45 observations. The data at $L = 6.6$ were taken from ATS-6 and other spacecraft and used as boundary conditions³⁵

(triple charge state increase by the process of electron stripping); such processes are sometimes called 'internal' charge exchange. On the other hand the opposite process of electron capture can only proceed in unit charge state decreases because in processes such as



the exospheric neutral hydrogen atom has only one bound electron to lose. Thus a fully ionized oxygen ion (O^{8+}) will require a minimum of eight separate collisional encounters with the exospheric hydrogen atoms in order to become neutralized and thus lost from the radiation belts. A proper description of the radiation belt heavy ion physics thus requires the consideration of the ion distribution function for each charge state, or in compact form an ion distribution function which has the additional discrete parameter space corresponding to the available charge states.

When $\underline{F} = \{f_1, f_2, \dots, f_c\}$ is the ion distribution function for the c charge states, the heavy ion radial diffusion equation may be written in the form:

$$\frac{\partial \underline{F}}{\partial t} = L^2 \frac{\partial}{\partial L} \left[L^{-2} \underline{D}_{LL} \times \frac{\partial \underline{F}}{\partial L} \right] + \mu^{-1/2} \underline{G} \times \frac{\partial \underline{F}}{\partial L} - \underline{\Lambda}^* \underline{F} + (\underline{\Lambda} \underline{I}) \times \underline{F} - \underline{\Gamma} \times \underline{F}$$

where

$$\underline{D}_{LL} = \{D_{LL1}, D_{LL2}, \dots, D_{LLc}\}$$

$$\underline{G} = \{G_1, G_2, \dots, G_c\}$$

$$\underline{\Gamma} = \{\Gamma_1, \Gamma_2, \dots, \Gamma_c\}$$

\underline{I} is a column vector with unit elements, and the charge exchange matrix $\underline{\Lambda} = \{\Lambda_{ij}\}$. The symbols $*$ and \times denote vector transposition and direct matrix product respectively. For further details and the precise definition of these quantities, the reader is referred to Spjeldvik and Fritz.³⁷ A number of computer experiments have been carried out for the heavy ion characteristics, and the physics learned from this work may be summarized as follows:

- (1) Higher charge states are crucially important for the overall structure of the heavy ion component of the earth's radiation belts.
- (2) Charge state redistribution processes are of major importance throughout the radiation belts at essentially all energies.
- (3) Because of frequent 'internal' charge exchange the ionic charge state distribution deep within the radiation belts becomes largely independent of the ion source characteristics.
- (4) Below a narrow ($\Delta L \sim 1$) transition zone adjoining the outer zone boundary, the radiation belt ion charge state distribution is also largely independent of the radial diffusive transport rate.

For recent reviews of advances in radiation belt heavy ion physics, see Shelley¹¹ and Spjeldvik.¹²

References

1. Van Allen, J.A., Ludwig, G.H., Ray, E.C., and McIlwain, C.E. (1958) Observation of high intensity radiation by satellites 1958 Alpha and Gamma, Jet Propulsion 28:588.
2. Vette, J.I., Teague, M.J., Sawyer, D.M., and Chan, K.W. (1979) Modeling the earth's radiation belts, in: Solar-Terrestrial Predictions Proceedings II, ed. by: R. F. Donnelly, U.S. Dept. of Commerce, Washington, D. C., p 12.
3. Harel, M., Wolf, R.A., Reiff, P.H., Spiro, R.W., Burke, W.J., Rich, F.J., and Smiddy, M. (1981) Quantitative simulation of a magnetospheric substorm, 1. Model logic and overview, J. Geophys. Res. 86:2217.
4. Harel, M., Wolf, R.A., Spiro, R.W., Reiff, P.H., Chen, C.-K., Burke, W.J., Rich, F.J., and Smiddy, M. (1981) Quantitative simulation of a magnetospheric substorm, 2. Comparison with observations, J. Geophys. Res. 86:2242.
5. Spiro, R.W., Harel, M., Wolf, R.A., and Reiff, P.H. (1981) Quantitative simulation of a magnetospheric substorm, 3. Plasmaspheric electric fields and evolution of the plasmopause, J. Geophys. Res. 86:2261.
6. Wolf, R.A., Harel, M., Spiro, R.W., Voigt, G.-H., Reiff, P.H., and Chen, C.-K. (1981) Computer simulation of inner magnetospheric dynamics for the magnetic storm of July 29, 1977, J. Geophys. Res. (submitted for publication).
7. Mozer, F.S. (1977) Relationships of electric fields to auroral forms. Report GA-533 presented at the IAGA/IAMAP Joint Assembly, Seattle, Washington.
8. Evans, D.S. (1975) Evidence for the low altitude acceleration of auroral particles, in Physics of the Hot Plasma in the Magnetosphere, pp 319-340, eds.: B. Hultqvist and L. Stenflo, Plenum Press, New York.
9. Mizera, P., Fennell, J.F., and Vampola, A.L. (1977) Correlated charged particle and electric field measurements, Report GA-125 presented at the IAGA/IAMAP Joint Assembly, Seattle, Washington.

10. Lundin, R., Lyons, L.R., and Pissarenko, N. (1981) Observations of the ring current composition of L-values less than 4, J. Geophys. Res. (in press).
11. Shelley, E.G. (1979) Heavy ions in the magnetosphere, Sp. Sci. Rev. 23:465.
12. Spjeldvik, W.N. (1979) Expected charge states of energetic ions in the magnetosphere, Sp. Sci. Rev. 23:499.
13. Sharp, R.D., Johnson, R.G., and Shelley, E.G. (1976) The morphology of energetic O^+ ions during two magnetic storms: Temporal variations, J. Geophys. Res. 81:3283.
14. Sharp, R.D., Johnson, R.G., and Shelley, E.G. (1976) The morphology of energetic O^+ ions during two magnetic storms: Latitudinal variations, J. Geophys. Res. 81:3292.
15. Ghielmetti, A., Johnson, R.G., Sharp, R.D., and Shelley, E.G. (1978) The latitudinal, diurnal, and altitudinal distributions of upward flowing energetic ions of ionospheric origin, Geophys. Res. Lett. 5:59.
16. Johnson, R.G., Sharp, R.D., and Shelley, E.G. (1978) Observations of ions of ionospheric origin in the storm-time ring current, Geophys. Res. Lett. 5:59.
17. Mizera, P.F. and Fennell, J.F. (1977) Signatures of electric fields from high and low altitude particle distributions, Geophys. Res. Lett. 4:311.
18. Lyons, L.R. and Moore, T.E. (1981) Effects of charge exchange on the distributions of ionospheric ions trapped in the radiation belts near synchronous orbit, J. Geophys. Res. (submitted for publication).
19. Fritz, T.A., and Wilken, B. (1976) Substorm generated fluxes of heavy ions at geostationary orbit, in Magnetospheric Particles and Fields, p 171, ed. by B. M. McCormac, Reidel, Dordrecht-Holland.
20. Ejiri, M. (1978) Trajectory traces of charged particles in the magnetosphere, J. Geophys. Res. 81:4798.
21. McIlwain, C.E. (1974) Substorm injection boundaries, in Magnetospheric Physics, ed. by B. M. McCormac, D. Reidel, Dordrecht-Holland, p 143.
22. Kaye, S.M. and Kivelson, M.G. (1979) Time dependent convection electric fields and plasma injection, J. Geophys. Res. 84:4183.
23. Southwood, D.J. and Kaye, S.M. (1979) Drift boundary approximations in simple magnetospheric convection models, J. Geophys. Res. 84:5773.
24. Lyons, L.R. and Williams, D.J. (1980) A source for the geomagnetic storm main phase ring current, J. Geophys. Res. 85:523.
25. Schulz, M. and Lanzerotti, L.J. (1974) Particle Diffusion in the Radiation Belts, Springer Verlag, N.Y.
26. Lyons, L.R., and Thorne, R.M. (1970) The magnetospheric reflection of whistlers, Planetary and Space Science, 18:1753.
27. Lyons, L.R., Thorne, R.M., and Kennel, C.F. (1972) Pitch angle diffusion of radiation belt electrons within the plasmasphere, J. Geophys. Res. 77:3455.
28. Lyons, L.R. and Thorne, R.M. (1973) Equilibrium structure of radiation belt electrons, J. Geophys. Res. 78:2142.
29. Cornwall, J.M. (1972) Radial diffusion of ionized helium and protons: A probe for magnetospheric dynamics, J. Geophys. Res. 77:1956.

30. Spjeldvik, W.H. and Thorne, R.M. (1975) The cause of storm after effects in the middle latitude D-region, Journal of Atmospheric and Terrestrial Physics 37:777.
31. Spjeldvik, W.N. and Thorne, R.M. (1975) A simplified D-region model and its application to magnetic storm after effects, Journal of Atmospheric and Terrestrial Physics 37:1313.
32. Spjeldvik, W.N. and Thorne, R.M. (1976) Maintenance of the middle latitude nocturnal D-layer by energetic electron precipitation, Journal of Pure and Applied Geophysics 114:497.
33. Spjeldvik, W.N. and Lyons, L.R. (1980) On the predictability of radiation belt electron precipitation into the earth's atmosphere following magnetic storms, Proceedings of the International Symposium on Geophysical Predictions, IV, B-59.
34. Nakada, M.P. and Mead, G.D. (1965) Diffusion of protons in the outer radiation belt, J. Geophys. Res. 70:4777.
35. Spjeldvik, W.N. (1977) Equilibrium structure of equationally mirroring radiation belt protons, J. Geophys. Res. 82:2801.
36. Joselyn, J.A. and Lyons, L.R. (1976) Ion cyclotron wave growth calculated from satellite observations of the proton ring current during storm recovery, J. Geophys. Res. 81:2275.
37. Spjeldvik, W.N. and Fritz, T.A. (1978) Theory for charge states of energetic oxygen ions in the earth's radiation belts, J. Geophys. Res. 83:1583.
38. Spjeldvik, W.N. and Fritz, T.A. (1978) Energetic ionized helium in the quiet time radiation belts: Theory and comparison with observation, J. Geophys. Res. 83:654.

Contents

1. Introduction	273
2. Comparison of Models	274
2.1 Statistical Models	274
2.2 Numerical Models of Convection	276
2.3 Alfvén Layer Models	277
2.4 Radial Diffusion Models	278

8. Summary and Comparison of Radiation Belt Models

by

Stanley M. Kays
Plasma Physics Laboratory
Princeton University
Princeton, New Jersey 08540

Reporter's Review of Radiation Belt Modelling Panel

1. INTRODUCTION

In the Radiation Belt Modelling session, the various magnetospheric modelling efforts carried out to a certain degree of completeness or presently underway were brought together and presented. From the reports by the statistical, numerical and empirical modelers, the listener was left with the distinct impression that the modelers have achieved a high degree of sophistication and success, additional model development notwithstanding. The approaches to modelling are varied, and consequently they are based on different principles. For instance, the statistical models are based on long-time averages of observed fluxes, to present a picture of the base-line particle population in the magnetosphere. On the other hand, the numerical and empirical models, with the exception of the steady-state radial diffusion model, are geared towards understanding particle and field observations on an event basis. The statistical model is a time-independent model to first order, whereas the numerical and empirical models are used to simulate either

geomagnetically quiet (steady-state) times or times of enhanced geomagnetic activity when the magnetosphere may undergo drastic structural changes.

The key to modelling, as distinguished from pure theory, where on-principle aspects are considered, is that the modeler is not far removed from reality; reality here being data. This is by no means meant to imply that pure theory takes on a subsidiary role; certainly without the basic theory the models would not exist. It is, however, meant to point out that the models are a synthesis of theory and data, in that they aim to describe a part of nature based on known physics.

Most of the models attempt to model physical processes; yet the modeler finds that he can seldom start from first principles on all aspects of the problem. As an example, in certain models it is enough to know that an enhanced convection electric field is associated with storm or substorm onset. The modeler does not have to know the precise substorm triggering mechanism or the specific cause of the enhanced convection electric field; it suffices to say that substorms exist. It is up to the modeler to decide on the level of complexity in the physics to be incorporated; and then, often by trial and error, to discover what degree of sophistication is needed. In what follows, I will attempt to present a more detailed comparative picture of the various models being used, along with some feeling for the general theory and limitations of each of the models.

2. COMPARISON OF MODELS

2.1 Statistical Models

The statistical models were developed at the National Space Science Data Center (NASA/Goddard Space Flight Center), and are intended to give an overview of the radiation belt's trapped energetic particle population. The intent of the statistical model is not in any way to represent the physics of the radiation belts, but rather to represent the steady state energetic particle population to serve system users in such areas as orbit and radiation damage assessment. The models confine themselves to the more energetic particles, ≥ 40 keV electrons and ≥ 100 keV ions, and give a map of these particle fluxes in the (B, L) coordinate system out to distances of $L = 11$. The models were derived from long term averages (up to 1 year) of pre-1970 satellite data, and although the aim was to produce models to within 20 percent accuracy, so far the models are good to within a factor of 2. The various available models are summarized in Table 1 (courtesy of J.I. Vette).

Developing these statistical models, however, is not problem-free. Because past and future models are based on data from more than one spacecraft, there is a crucial need to standardize diagnostics and to cross-calibrate instruments. Care

Table 1. Current NSSDC Radiation Environment Models

Name of Model	Particle and Energy Range	L Range	Remarks
AE-4	Electrons 0.04 - 4 MeV	2.8 - 11.0	Flux values for epoch 1964 and 1967 corresponding to solar minimum and maximum conditions. Solar cycle effects only occur between $2.8 \leq L \leq 5$. Energies above 4 MeV are strictly extrapolations, and data above 1.9 MeV did not have proper calibration.
AE-5 (1975 projected)	Electrons 0.04 - 4 MeV	1.2 - 2.8	Flux values for October 1967, with Starfish residue subtracted and solar cycle effects used. The projected valid epoch is 1975, corresponding to solar minimum conditions.
AE-6	Electrons 0.04 - 4 MeV	1.2 - 2.8	Flux values for October 1967, with Starfish residue subtracted.
AP-8	Ions 0.1 - 400 MeV	1.17 - 6.6	Model has both solar minimum and maximum values; these changes only occur at low altitudes.
AEI-7	Electrons 0.04 - 5 MeV	2.8 - 11.0	Interim model with upper and lower limit for energies above 1.5 MeV to account for ATS 6 data at 3.9 MeV and OV1-19 data up to 5 MeV. Model is interim until discrepancies between Azur data at 4.5 MeV and OV1-19 data can be properly studied. At energies below 1.5 MeV, this model is same as AE-4 in the outer zone for solar maximum.

must be taken in interpreting the models as well. Residue from the Starfish atmospheric nuclear test affected particle flux levels for $L < 2.5$ for long periods of time. However, by mid-1970, practically all electron fluxes were again of purely natural origin. Stormtime particle injection events can generate misleading model comparisons. For instance, it was found that for $L = 3$, the 10 month averaged

fluxes from OV1-19 and OV3-3 in different epochs differed by a factor of 10, and the AE-4 electron model was about at the geometric mean. It was determined that this was caused by the different nature of the two injection events that occurred within both 10 month periods. Temporal dependencies are reflected in the model fluxes. One time variation was found to coincide with the solar cycle. Here the atmospheric density, modulated by solar effects, in turn affected ion lifetimes at low L, causing a modulation of model fluxes. One temporal effect, as yet unexplained and not related to the solar cycle, is a factor of 10 decay in 8-25 MeV ions from L = 1.2 to 1.9 over a 12-year (1964-1975) period. Finally, the statistical models treat trapped particles only. As yet there has been no attempt by the NASA group to statistically model precipitating particles, a more difficult effort.

2.2 Numerical Models of Convection

For ions of ring current energies the numerical model developed at Rice University (R. A. Wolf) is perhaps the most computationally sophisticated dynamical model used. It is a physically self-consistent, particles/fields model which deals with the region $L \leq 10$ within the magnetosphere and in the ionosphere. It determines how the magnetospheric particle impulsion is modified by changes in the earth's electric and magnetic fields, then determines the effect that the particle change has on the fields. Inputs to the model consist of the polar cap potential drop, ionospheric conductivity, magnetic field model, and particle fluxes at the outer boundary. The basic physics involve a solution of the relation, $\vec{\nabla} \cdot \vec{J} = 0$, where \vec{J} is the total current density including ionospheric Birkeland and ring currents, and the determination of a particle's total magnetic and electric drifts. The model is capable of computing the electric fields and current densities as functions of position and time in the ionosphere and magnetosphere, the ≤ 200 keV particle distribution in the equatorial plane, position, shape and time evolution of the plasmapause, ground magnetic perturbations, and ohmic heating. The specific details and general results of this model are well-documented in the literature. It is noteworthy to mention here the success that the model achieved in simulating the July 29, 1977 storm, an event chosen for a Coordinated Data Analysis Workshop held at NASA/Goddard Space Flight Center in October 1979. The results of the model represented one of the first real interactive syntheses of data models. Using a conductivity model estimated from the AE geomagnetic index, and a cross-polar cap potential drop estimated from solar wind data, the model was found to inject into the inner magnetosphere ring current particles whose corresponding D_{st} agreed very well with observations. This result suggested that the position and magnitude of the predicted ring current were close to those in reality. In addition, the position of the plasmasheet's inner edge, as predicted by the model, agreed for the most part with S3-3 and AE-C observations to within a few degrees invariant latitude.

Although this model is extensive, there are numerous features that can be added. At present, there are no neutral wind systems, reflecting the atmospheric dynamo region, or parallel electric fields incorporated in the model. Neither are particle losses, through charge exchange or wave-particle interactions, considered. These particle losses affect ring current development. Another limitation of the model is that ions other than protons are not considered. Recent observation has shown, without question, that O^+ and to a lesser extent He^+ constitute a good portion of the cold and hot ion population within $L = 10$, and during storms, O^+ may even be the dominant ion. These heavy ions can convect earthward from the tail ($L > 10$), or they may enter the magnetosphere directly from the ionosphere by flowing up field lines. Including the heavy ions in the Rice convection model may be straightforward. For the former case, the heavy ions can be incorporated directly into the particle population at the $L = 10$ outer boundary. In fact, this may be done even for the "upflowing" ions since, as was pointed out in the session that the majority of upflowing ion events occur in the vicinity of $L = 10$ on the nightside.

2.3 Alfvén Layer Models

The very large numerical model described above requires a large amount of computer time because of its complexity. Another approach to particle modelling in the ring current environment from $L = 4$ to $L = 10$ is to make some simplifying assumptions about the electric and magnetic fields and to treat the problem in a non-self-consistent manner. In such a model, the electric field (E) is assumed to be derivable from an electrostatic potential with the imposed feature that E decreases with decreasing radial distance. This electric field shielding is adopted as a result of both the self-consistent modelling and observations. The magnetic field is taken to be dipolar. The electric and magnetic drifts of particles define Alfvén layer boundaries which represent the inner limit of particle penetration and which are functions of the particles' first and second adiabatic invariants. Particles whose source is the plasmasheet cannot penetrate earthward of their Alfvén layer; consequently, a spacecraft passing outward across an Alfvén layer will see a flux increase of particles with the particular first and second invariants. In the steady state, the electric field magnitude is time-independent, and it can be determined from either K_p or plasmopause position. The Alfvén layers are also fixed in time. This modelling approach has interpreted particle flux increases observed at synchronous orbit, previously believed to be dynamic injection events, to be nothing more than Alfvén layer crossings by the satellite. In the time-dependent case, the initial Alfvén layers are first determined, and then to simulate storm or substorm onset the convection electric field is enhanced on a several minute time

scale. As the particles' drift velocities change in response to the change in convection electric field, their corresponding innermost penetration distances gradually move earthward. By keeping track of the satellite and penetration boundary positions as a function of time after onset, one can determine when and where the satellite will cross each penetration boundary and consequently can predict when and where flux increases and decreases should be seen. This time-dependent approach has been successful in explaining quantitatively several storm and substorm related observations in the synchronous orbit region. Future work with this model must include a realistic non-dipolar magnetic field, induction electric fields, and particle losses.

A common feature of the two models just discussed is that the source of ring current particles is the plasma sheet. However, another model presented at the workshop suggested that flux increases of trapped ions observed on Explorer 45 at $L \leq 4$ during two large geomagnetic storms could be accounted for by a 1-2 R_E inward adiabatic displacement of the pre-existing trapped particle distribution. In this model, the source of the observed particles is the in-situ population; no external source (plasma sheet or ionosphere) is required. The basic idea behind this model is that as a particle is displaced earthward after storm onset it is energized adiabatically. Assuming conservation of the first invariant without losses, a distribution function which depends on energy only (no L -dependence), and a negative energy slope ($\partial f / \partial W < 0$), then a consequence of the Liouville's theorem is that $\delta f(W) > 0$ as the distribution moves earthward. Consequently, a satellite will observe a flux increase at a given energy. For the observed $\delta f(W)$, the radial displacement necessary to cause the flux difference was determined to be 1-2 R_E ; the same magnitude displacement was also determined independently from the time history of the plasmopause position as measured by saturation of the DC electric field probe. In the absence of induction electric fields, Faraday's Law requires that inward convection over some azimuthal extent must be countered by outward convection over some other range of azimuth in order that $\oint \vec{E} \cdot d\vec{l} = 0$. Then the key question is, to what azimuthal extent does the inward convection take place? From the differences in δf as a function of energy, it was estimated that inward drift occurred over $\geq 270^\circ$, and it was suggested that this large azimuthal extent for inward convection may be a significant difference between storm and substorm processes.

2.4 Radial Diffusion Models

The models discussed so far take into account neither collision, charge-state transformation reactions due to the presence of cold plasma and exospheric gas, nor radial diffusion. Radiation belt diffusion models use these processes to

determine the radial and charge-state distributions of 10 keV - 100 MeV mirroring ions and electrons in a dipolar magnetic field. The ions are assumed to originate at a high-L source beyond the geostationary orbit. As boundary conditions, the charge states and energy spectrum of ions are specified. One needs to know as inputs for the model exospheric neutral hydrogen, the magnetic and electric diffusion coefficients, and the charge-state transformation reactions for energetic ions in an atomic hydrogen gas. For electrons, knowledge of wave-particle interactions is crucial. The radial diffusion transport equation then has to be solved subject to these physical processes. For electrons, excellent agreement between theory and observation has been obtained. For heavy ions, results of this calculation suggest that because of charge-state redistribution as the ions diffuse inward, taking higher charge states into account is of extreme importance for determining the overall structure of the heavy ion component. Near the source boundary, the ion component will reflect source characteristics since charge-state transformations there are infrequent. However, as the ions diffuse inwards, they redistribute in charge state leaving a population that becomes independent of the source charge-state characteristics. These calculations were made for quiet magnetic conditions, but more active steady state conditions were also simulated by modifying the radial diffusion coefficient. It was found after doing this that although the flux levels responded to changes in the transport coefficients, the relative distribution of ionic charge states was not affected. Current model development work aims for dynamic models.

In conclusion, models now exist for virtually all energetic trapped particles. These models have most often been successful in describing radiation belt phenomena, although further emphasis on sophistication and time-dependent dynamical models certainly is warranted. It is hoped that at some future time these models may be made into predictive tools for space operations within the earth's magnetosphere.

Contents

1. Introduction	281
2. The Tutorial Session	282
3. Radiation Effects on Electronic Systems	283
4. The Energetic Particle Detector Session	284
5. Magnetic Field, Cold Plasmas and Wave Diagnostics	285
6. Radiation Belt Modelling Session	287
7. Conclusions	289

9. A Summary Review of the Radiation Belt Workshop

1. INTRODUCTION

The Radiation Belt Workshop was highly successful in bringing together many of the world's foremost space scientists to assess the state of theoretical and experimental knowledge of the inner magnetosphere, and in particular, knowledge of the energetic particle populations of the earth's radiation belts. It also examined the status of existing inner magnetosphere models and outlined improvements needed in both statistical and physical models. The hazards to space systems electronics and sensors due to energetic particles in the environment were reviewed; design and test programs necessary to mitigate problems were addressed. Two decades of in-situ space research has led to substantial discoveries and the vast expansion of mankind's knowledge of the earth's space environment. In recent years geospace has become an increasingly important sphere of human endeavors as evidenced by a great number of spacecraft from many nations, including communication satellites, land and sea survey satellites, meteorological satellites, military surveillance platforms and scientific research satellites. Future plans include large, spaceborne solar power gathering facilities, manned space stations of several nations, active chemical, wave and beam experimentation and platforms for launches of interplanetary missions. It is therefore of great importance to know the precise mechanisms by which the different kinds of spacecraft interact with the natural plasma and radiation environment for all possible geomagnetic conditions. Of particular importance is the study of the

equatorial radiation environment for radial distances ranging from the inner radiation zone to 12 earth radii. This range encompasses the experimental research on a future radiation belt scientific spacecraft.

2. THE TUTORIAL SESSION (George Paulikas)

The papers in the tutorial session dealt with topics ranging from our knowledge of the space plasma transport coefficients to the effects of space radiation on space systems. Highlights of the session are summarized.

Substantial knowledge and understanding of the microphysics operating in space plasmas exists, to the point that some transport coefficients can be calculated or estimated. The major deficiencies result from a poor understanding of the role of electrostatic waves in determining transport coefficients. Experiments which fully describe wave-particle interactions (that is, measurements of the full particle distribution functions made simultaneously with measurements of the wave fields and polarizations) are required in order to make substantial progress in this area. Our knowledge of the transport coefficients is also deficient in the sense that virtually all analyses have dealt with localized regions of space and covered relatively short time intervals. Thus, we do not know how transport coefficients may depend on the boundary conditions imposed by the solar wind above and the atmosphere/ionosphere below.

While the static picture of the earth's radiation belts seems reasonably well in hand, the development of a quantitative understanding of particle injections and other classes of transient events is just beginning. Quantitative understanding of the role of magnetospheric boundary conditions and the coupling of the dynamics of the magnetosphere to the properties of the interplanetary medium is, in the main, still lacking. This lack is characterized both by gaps in our experimental knowledge (for example, we do not know the abundances of the constituent ions carrying the bulk of the energy in the storm-time ring current) as well as by gaps in our theoretical understanding of injection processes. On the more positive side, considerable progress has been made in understanding the processes which cause the decay of the charged populations injected into the inner magnetosphere. It also appears that at least some classes of transient events can be understood by recourse to simple adiabatic theory. To be sure, a host of non-adiabatic effects remains, but the dynamics of some fraction of the particle population associated with injection events may be explained by analytical tools and techniques well in hand.

The practical effects of the space radiations on spacecraft are many and varied. Static models of the magnetosphere exist which can provide guidance to

spacecraft designers. These static models have deficiencies; for example, the energetic electron population is very poorly known in many regions of space and energetic proton measurements have been virtually neglected for more than a decade. A more serious problem is the absence of quantitative representations of magnetospheric dynamics. Consequently, dose rate limits cannot be readily predicted.

The discussion in the session also highlighted the fact that substantial interaction between inaccuracies of the models of space radiation and deficiencies in our knowledge of the response of hardware to space radiation occurs. Thus, magnetospheric physicists and developers of micro-electronics must also learn to better characterize and test their devices. Progress in the areas of environment and hardware is necessary for improvements in the reliability of our space systems.

3. RADIATION EFFECTS ON ELECTRONIC SYSTEMS (P. J. McNulty)

In designing electronic systems for future flights in the radiation environments of space, designers must take into account the total dose and dose-rate vulnerability of circuit components, dielectric charging and discharging phenomena, and hard and soft errors induced by the traversal of individual energetic heavy ions and their interactions. There seems to be a consensus in the radiation-effects community that adequate laboratory procedures have been developed which, if followed, provide the data necessary to screen parts for total dose and dose-rate failures.

The dielectric charging and discharging phenomena are the result of exposure to large fluxes of energetic electrons. They occur primarily in cables and in the vicinity of irregularities and sharp corners of the spacecraft surface. Particles of keV and MeV energies incident upon a dielectric, such as the insulation of a connector cable, will penetrate below the material surface and can remain embedded there. This continues until a substantial spacecharge builds up and the dielectric medium breaks down. In addition to damaging the insulator, the discharge initiates large fast electronic pulses that then proceed to any devices connected to the cable. These cable effects and surface charging phenomena are currently being studied through the SCATHA spacecraft research program. Improved data on fluctuations in the flux of energetic (>100 keV) particles are needed to fully understand the environment-spacecraft interaction.

The single particle effects divide into hard errors (latch ups) and soft errors (bit upsets, anomalous signals, and incorrect logic execution). Both types result from the traversal or interactions of the energetic heavy ions in or near one of the sensitive microscopic volume elements on the devices. The problem becomes

increasingly serious as device geometries are scaled down to fit greater numbers of circuit elements on a chip. Present understanding is that a particle effect occurs if and only if at least some threshold amount of energy is deposited within one of the volume elements. It is therefore a micro dosimetry rather than a dosimetry problem. There is no threshold dose or dose-rate for soft or hard errors, only a probability of an event occurring per incident particle for a given incident energy. Space radiation has never been studied using microdosimetry techniques. It is particularly desirable that such a study be carried out which measures the energy-deposition spectra for volume elements typical of the radiation sensitive elements on LSI and VLSI devices.

Accelerated-testing procedures for single-particle effects are currently being developed. One difficulty is the fact that no single accelerator facility is adequate to represent the radiation environment of space. This radiation includes many components, each of which has a wide range of incident energies. There is good reason to believe that adequate testing procedures for single-particle effects will eventually be developed. What is needed is an agreed upon protocol for test exposures, from which the data can be put into an algorithm for estimating the expected error rate for different types of devices in space. The results of laboratory testing should be compared with at least one space trial. The devices compared should cover a range of sensitivities and different sensitive microelement geometries and sizes to validate the test procedure's predictive power.

4. THE ENERGETIC PARTICLE DETECTOR SESSION (R. McEntire for T. Krimigis)

Significant advances have been made in the energetic particle detector systems for spacecraft applications. This is particularly true for energetic ion composition detectors. These measurements are very difficult, particularly at energies in the ring current range: 10 keV to 500 keV. Sophisticated ion mass spectrometers have been shown to be effective up to tens of keV and have excellent resolution qualities. Prototype instruments to cover higher energies up to several hundred keV are now available, and flight-qualified instrumentation is being built for the upcoming Swedish Viking spacecraft and for the NASA OPEN Program. At energies in the MeV range, sophisticated solid state detector systems have been developed. The relatively high abundance of heavy ions were discovered with these instruments. Clean proton measurements, uncontaminated by electron and heavy ion contributions are badly needed, particularly because older ion measurements traditionally were labeled "proton observations" regardless of the ion identity. High quality electron detectors have also been developed which cover practically

all radiation belt energies. It is noted that electron detectors to study the most energetic, multi-MeV, electron population must be built with particular care in order to avoid contaminated measurements from penetrating radiation. This is also the case for the ion detectors where the ion energies may be as high as hundreds of MeV.

A spacecraft designed to study the earth's radiation belts should carry a payload of energetic particle detectors that covers electron energies from ≤ 1 keV to several tens of MeV and ion energies from ≤ 1 keV to hundreds of MeV. A combination of electrostatic analyzers and solid state detector systems cover the energies of importance. Because of the large spectral gradients it is useful to have a solid state detector system with a moderate geometric factor ($\sim 10^{-3}$ cm²-ster) for medium energy particles (20 to 500 keV) and a complementary solid state detector with a large geometric factor ($\geq 10^{-1}$) to cover the upper energy range (0.2 to ≥ 10 MeV). The ion detector systems should also cover up to 500 MeV. A spacecraft payload must also include modern ion detectors. Full ion identification is a necessary requirement for radiation belt studies in the 1980s. During the last few years it has become clear that energetic heavy ions in higher charge states are important in the radiation belts; there are both theoretical and experimental reports of their roles in the radiation belts. Fortunately, newly developed ion detector systems are now able to determine not only the mass (and thus elemental identity) of an ion, but also the ionic charge. Thus, the payload requirement for radiation belt ion detectors include ion energy, ion mass, and ion charge; this in contrast to electron measurements where only electron energy is sufficient.

5. MAGNETIC FIELD, COLD PLASMAS AND WAVE DIAGNOSTICS (M. C. Kelley)

The question that we are addressing is: Assuming that one has the appropriate complement of energetic particle detectors on radiation belt satellites, what minimal diagnostic tools are required to measure magnetic fields, cold plasma, and waves in the radiation belts?

A fluxgate magnetometer is required to give the aspect of particle measurements. Without this information pitch angle distributions are unknown. In regions such as the ring current where magnetic fields deviate significantly from the models the problem could be particularly severe. A sensitive fluxgate with high time resolution is also needed to give the gross features of magnetic boundary regions. For example, if currents in particle detectors are changing rapidly it may be that the satellite has passed out of the magnetosphere. Without a magnetometer such data would be very difficult to interpret. The sensitivity of a

fluxgate magnetometer should be improved, to measure low frequency (≤ 100 Hz) waves. The measurement of such waves, generated by heavy ions, is necessary to understand the role of energetic, heavy ions in the magnetosphere.

Cold plasma detectors are necessary to understand magnetospheric boundary effects, the plasma environment, and satellite charging. Without such detectors knowledge of the location of cold plasma boundaries, for example, is inaccessible. Knowledge of the cold plasma densities is also necessary to interpret the role of wave-particle interactions in altering the belt populations. That wave measurements are crucial for a radiation belt satellite is evident from our knowledge that whistler waves are responsible for the depletions producing two electron belts. Critical information concerning $\delta \vec{E}$ and $\delta \vec{B}$ can be gained from a simple swept frequency analyzer. The frequencies of the waves, in conjunction with the cold plasma measurement, are necessary to interpret the energetic particle measurements.

DC electric fields play an important role in particle acceleration. Particles gradient-curvature drift through potential drops, gaining kinetic energy. Equivalently, they $\vec{E} \times \vec{B}$ drift into regions of stronger B fields and gain energy to conserve their adiabatic invariant. Low frequency electric field measurements, in conjunction with similar magnetic field measurements will yield information on Alfvén waves and heavy ion cyclotron waves. It should be noted that there has been a recent technological development in measuring DC electric fields and magnetic field gradients utilizing electron beams. The use of this new technique in conjunction with probe measurements opens many possibilities for future space studies involving electric fields.

From the comments of several contributors it is obvious that in order to understand the radiation belt content through wave-particle interactions it is first necessary to know the ion composition. Pitch angle distributions must also be known. A new generation of particle analyzers offers the possibility of measuring full pitch angle distributions in short periods of time. These, in conjunction with cold particle measurements, allow us to determine if and where $\delta f / \delta \vec{v} > 0$ is a source of free energy for the generation of waves. The regions of positive slope in the distribution functions are probably quite gentle. Thus, high resolution detectors are not required. Conditions of marginal stability are hard to detect. The complexity of the instrumentation increases significantly if the mission objectives include increasing our understanding of the physics of the radiation belts. For example, because of the burst-like nature of certain phenomena, high data rates are needed for good wave measurements. Multicomponent measurements are required. Three magnetic fields and at least two electric field components are necessary to calculate the Poynting flux. To determine the direction of electrostatic wave vectors the third electric field component must also be measured.

The technology for making the required measurements exists. Primarily the problem is one of data handling techniques and the number of sensors that can be flown. High data rates for short periods of time are essential to understanding burst type events. This is not something unique to plasma physics. It goes on in the neutral atmosphere. The atmosphere is well mixed. The mixing, however, goes on in small regions of high turbulence such as those that airplanes run into from time to time. Most of the physics goes on in thin, turbulent regions.

Making the proper measurements requires smart data handling and sophisticated instruments. Roy Torbert pointed out that a considerable effort must go into the design of the satellite data acquisition systems; not just the engineering. It is not enough to say, "We need this much memory." We must also specify when to turn memory on and when to dump it. Thus, substantial scientific input must be made over and above the engineering of a data acquisition system.

Finally, in planning a radiation belt study it is very important, early in the program, to establish clear goals. The right parameters must be measured at the right sampling rates. Thus, it is necessary to include in the planning stage scientists who are interested in phenomenological modelling as well as those who are interested in the microphysics. The diagnostic technology for understanding the radiation belts already exists. The problems that must be solved are not easy. Those responsible for developing a radiation belt satellite must have a real commitment to the development of a satellite payload to obtain the data necessary for radiation belt modelling, microelectronic testing, and to advance the understanding of the dynamics of the radiation belt populations.

6. RADIATION BELT MODELLING SESSION (W. N. Spjeldvik)

Modelling of the Earth's Radiation Belts has brought forth a substantial body of knowledge during the preceding decade. It has been possible to test our physical understanding of the trapped radiation. For the high energy part of the radiation belts, emphasis has been placed on understanding the quiet time structure. The models, which assume a steady state balance between external sources and internal loss processes have utilized stochastic, diffusion processes as the prime plasma transport mechanisms within the trapping region. Based on existing data, which is incomplete for many ion species, these models simulate quite well the main characteristics of the quiet time radiation belts. Emphasis in the years ahead is now directed towards time dependent models to gain understanding of disturbed conditions such as magnetic storms and substorms.

Modelling of the extra-terrestrial ring current has become very sophisticated in recent years. A model has been developed at Rice University that self-consistently simulates both particle and field behavior. Other models treat, in a less complete but very useful way, the boundary between the plasma sheet and the radiation belt trapping region. These models use convection as the prime plasma transport mechanism for the lower energy particles.

There is a need for the development of a radiation belt model that is accurate at the intermediate energies of tens to hundreds of keV, where the plasma transport shifts from convection dominance at the lower energies to diffusion dominance at the higher energies. Research during the late 1970s has revealed that energetic particles are accelerated out of the high latitude ionosphere during geomagnetic active periods. This may constitute a very important source for the radiation belt particle population. It is expected that the basic research concerning ionospheric contributions, now being carried out, will lead to improved radiation belt models. Theoretical investigations of wave-particle interactions show that the understanding of plasma waves is vital to the precise modelling of the radiation belts. For radiation belt electrons, the dominant role of whistler mode wave turbulence in controlling the radiation belt structure is proven; for ions, our knowledge is more meager. For this reason it is strongly recommended that suitable electric and magnetic wave detectors be included in the payload of future radiation belt research spacecraft.

Data analysis must have high priority in the radiation belt program. It is clear that the full utilization of the spaceflight data is vital to solving existing problems, for testing and development of dynamic models and proving or disproving theories. High quality radiation belt observations will be of great interest to a broad scientific community.

A radiation belt satellite should ideally have its orbit in the equatorial plane (where it can sample the complete pitch angle distributions). It should cover the L-shell range from the top of the earth's atmosphere ($L \sim 1.2$) to well beyond the geostationary altitude. An apogee of $L = 9$ to 12 is highly desirable although a lesser apogee location of at least $L = 7$ to 8 would solve many problems. A slowly spinning spacecraft ($t \sim 1$ minute) is able to give detailed results on pitch angle distributions, while a faster spinning spacecraft is capable of high temporal resolution. Spin adjustment capability is desirable. This would permit model testing both for the detailed steady state models and for models of impulsive source and precipitation mechanisms.

7. CONCLUSIONS

Although magnetospheric physics has passed the stage where every observation constitutes a new discovery, much work remains to be done before our knowledge can be applied to predictive models. The most significant advances have come in areas where quasi-steady state approximations are valid. Our understanding is weakest in the most dynamical situations. A partial list of topics that must be further addressed in the 1980's includes:

- (1) Magnetic storm and substorm dynamics of the radiation belts.
- (2) The coupling processes responsible for the particle and energy flow between the plasma sheet and the radiation belts.
- (3) The simultaneous modelling of the radial and pitch angle diffusion.
- (4) The mass and charge composition of the extra-terrestrial ring current.
- (5) The role of electrostatic and electromagnetic plasma wave instabilities in the radiation belts.
- (6) The mechanisms by which the solar wind energy and particles are coupled to the magnetosphere and the radiation belts.

It will only be after these crucial areas are much more fully understood that we can hope to begin to develop physical models with predictive capabilities as good as those currently employed by our less than infallible tropospheric weathermen.

The second major concern of the Workshop was the effects of energetic particles in the radiation belts on electronic systems. This recognizes the fact that space systems of the future will rely more and more on microelectronics circuitry. That such circuitry is vulnerable to radiation damage is widely understood. The degree of vulnerability needs further, intensive study. Contributors to the Workshop have proposed a prescription that includes accelerated laboratory testing of critical components joined to a program of in situ verification.

The Workshop has provided us with a "first-cut" outline for radiation belt and electronic-component vulnerability research for the 1980s. Perhaps its most useful contribution was to provide the opportunity for two separate but interdependent communities to explain to each other their perceived needs for the coming decade.

DATE
ILME